UNIVERSITA' DEGLI STUDI DI GENOVA
Istituto Italiano di Tecnologia
PhD School in Sciences and Technologies of Chemistry and Materials
XXXI Cycle

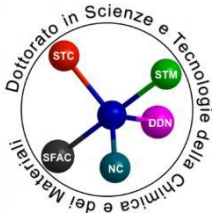

Colloidal Synthesis of Transition Metal Chalcogenides and Their Applications in Electrocatalytic Water Splitting

Supervisors: Prof. Liberato MANNA

Dr. Luca DE TRIZIO

Dr. Dipak V. SHINDE

Tutor: Maurizio FERRETTI

PhD thesis of:

Mengjiao Wang

Academic Year 2015-2019

一切都是命运

一切都是烟云

一切都是没有结局的开始

一切都是稍纵即逝的追寻

一切欢乐都没有微笑

一切苦难都没有泪痕

一切语言都是重复

一切交往都是初逢

一切爱情都在心里

一切往事都在梦中

一切希望都带着注释

一切信仰都带着呻吟

一切爆发都有片刻的宁静

一切死亡都有冗长的回声

——亦舒

Index

List of Figures

mL of OAm. After 1 mmol of OAm-Se was injected in the mixture, the reaction was heated up to 250 °C for 30 min.

Figure 3.5. Molecular structures of the solvent (a) ODE, (b) octyl ether, (c) TOPO and (d) OAm. XRD patterns and TEM images of the samples by solvent (a) ODE, (b) octyl ether, (c) TOPO and (d) OAm. Other experimental parameters: 0.5 mmol of $NiCl_2$, 0.5 mmol of $Co(acac)_2$, 5 mL of solvents (3 g of TOPO because it is solid), 6 mL of OAm. After 1 mmol of OAm-Se was injected in the mixture, the reaction was heated up to 250 °C for 30 min.

Figure 3.6. TEM images of samples with different kinds of surfactants: (a) ODPA, (b) HPA, (c) OAc, (d) OAc + OAm, (e) OAm, (f) no surfactants, (h) DDT. (g) XRD patterns of the samples using OAm as surfactant and without surfactant. (i) XRD pattern of the sample using DDT as surfactant. Other experimental parameters: 0.25 mmol of $NiCl_2$, 1 mmol of $Co(acac)_2$, 5 mL of ODE, some amount of surfactant ((a) 0.05g of ODPA, (b) 0.05 g of HPA, (c) 3 mL of OAc, (d) 3 mL of OAc + 3 mL of OAm, (e) 3 mL of OAm, (f) no surfactant and (h) 3 mL of DDT). After 1 mmol of OAm-Se was injected in the mixture, the reaction was heated up to 250 °C for 5 min.

Figure 3.7. XRD patterns and TEM images of the samples after the reaction time of (a) 1 min, (b) 5 min, (c) 30 min and (d) 60 min. Other experimental parameters: 0.25 mmol of $NiCl_2$, 1 mmol of $Co(acac)_2$, 5 mL of ODE, 3 mL of OAm. After degas 1 mmol of OAm-Se was injected in the mixture, the reaction was heated up to 250 °C for the specific time.

Figure 3.8. Schematic illustration of the probable change route of the chemical structures of the samples according to the reaction time.

Figure 3.9. XRD patterns and TEM images of the samples under the reaction temperature of (a) 150 °C, (b) 200 °C and (c) 250 °C. Other experimental parameters: 0.25 mmol of $NiCl_2$, 1 mmol of $Co(acac)_2$, 5 mL of ODE, 3 mL of OAm. After 1 mmol of OAm-Se was injected in the mixture, the reaction was heated up to the target temperature for 5 min.

Figure 3.10. XRD and TEM images of samples with (a) heat-up process and (b) hot injection. Other experimental parameters: 0.5 mmol of $NiCl_2$, 0.5 mmol of $Co(acac)_2$, 1 mmol of Se:OAm, 5 mL of ODE, 3 mL of OAm, After 1 mmol of OAm-Se was injected in the mixture, the reaction was heated up to 250 °C for 5 min; or the temperature reached to 250 °C then 1 mmol of OAm-Se was injected and the reaction lasted for 5 min.

Figure 3.11. (a-f) TEM images of the six samples listed in Table 3.2.

Figure 3.12. Polarization curves of (a) $Ni_{0.52}Co_{0.56}Se$ NCs with different electrolytes in HER and (b) CoSe NCs with different electrolytes in OER.

Figure 3.13. Polarization curves of $Ni_{0.52}Co_{0.56}Se$ NCs with different substrates in (a) HER and (b) OER.

Figure 3.14. (a) Polarization curves of electrodes comprising of CoSe NCs for HER with various catalyst loading amounts. Other experimental parameters: Ti foil as substrate and 0.5 M H_2SO_4 as electrolyte. The loading mass is 250 μL. (b) Polarization curves of electrodes comprising of $Ni_{0.3}Co_{0.74}Se$ NCs for OER with various catalyst loading amounts. Other experimental parameters: FTO as substrate and 1 M KOH as electrolyte. The loading mass is 20 μL.

Figure 3.15. (a) Polarization curves of electrodes comprising of CoSe NCs for HER with various catalyst loading amounts. (b) Polarization curves of electrodes comprising of $Ni_{0.3}Co_{0.74}Se$ NCs for OER with various catalyst loading amounts.

Figure 3.16. (a-e) TEM images and (f) XRD patterns of (a) CoSe, (b) $Ni_{0.3}Co_{0.74}Se$, (c) $Ni_{0.52}Co_{0.56}Se$, (d) $Ni_{0.78}Co_{0.28}Se$ and (e) NiSe NCs. The scale bar in each panel is 50 nm. (f) The bulk reflections of hexagonal NiSe (ICSD number 29310) and CoSe (ICSD number 53959) are also reported by means of light blue and black bars, respectively.

Figure 3.17. Polarization curves in HER of binary and ternary Ni-Co-Se NCs.

Figure 3.18. (a) LSVs measured at a sweep rate of 1 mV/s, (b) Tafel plots, (c) TOF values at η = 0.35 V, (d) CVs, (e) impedance spectra of electrodes measured at open circuit potential and (f) magnification of (e) in high frequency area of binary and ternary Ni-Co-Se NCs.

Figure 3.19. XRD patterns of CoSe, $Ni_{0.3}Co_{0.74}Se$ and NiSe NCs on FTO substrates after OER.

Figure 3.20. (a) SAED patterns of $Ni_{0.3}Co_{0.74}Se$ NCs before and after the OER. (b) HRTEM image of $Ni_{0.3}Co_{0.74}Se$ NCs before OER, exhibiting the expected hexagonal CoSe crystal structure and characterized by the absence of crystal defects. (c) EDS elemental mapping of a group of $Ni_{0.3}Co_{0.74}Se$ NCs before OER.

Figure 3.21. (a) TEM image and (b) HRTEM image of $Ni_{0.3}Co_{0.74}Se$ NCs after OER, showing the presence of both amorphous particles and a small fraction of tiny CoO or NiO NCs. (c) EDS elemental mapping and (d) EDS spectra of $Ni_{0.3}Co_{0.74}Se$ NCs after OER.

Figure 3.22. High-resolution (a) Ni, (b) Co and (c) Se spectra of $Ni_{0.3}Co_{0.74}Se$ NCs before and after OER.

Figure 3.23. FTIR spectra of $Ni_{0.3}Co_{0.74}Se$ NCs before (black line) and after (red line) five CVs of OER.

Scheme 4.1. Sketch of the Colloidal Synthesis of Ternary Ni-Co-Se and Quaternary Ni-Co-S-Se Alloy NCs Having the Same Hexagonal Crystal Structure.

Figure 4.1. (a) XRD patterns of various quaternary Ni-Co-S-Se NCs after different reaction time. TEM images of the samples after (b) 5 min, (c) 30 min, (d) 60 min, (e) 90 min and (f) 120 min.

Figure 4.2. (a) XRD patterns of various quaternary Ni-Co-S-Se NCs with different S/Se ratio. TEM images of the samples with (b) 3 mL of OAm-Se, (c) 3 mL of OAm-Se + 0.05 mL of DDT, (d) 3

mL of OAm-Se + 0.1 mL of DDT, (e) 1 mL of OAm-Se + 0.25 mL of DDT, (f) 1 mL of OAm-Se + 0.25 mL of DDT and (g) 5 mL of DDT. Other experimental parameters: 0.25 mmol of $Ni(acac)_2$, 0.75 mmol of $Co(acac)_2$, 10 mL of ODE. After the injection of S/Se precursors, the reaction was heated up to 250 °C for 1 h.

Figure 4.3. Low resolution TEM images of (a) $Ni_{0.3}Co_{0.73}S_{0.2}Se_{0.8}$ and (b) $Ni_{0.25}Co_{0.65}S_{0.4}Se_{0.6}$ NCs. The scale bar is 50 nm. (c) XRD patterns of $Ni_{0.3}Co_{0.74}Se$, $Ni_{0.3}Co_{0.73}S_{0.2}Se_{0.8}$ and $Ni_{0.25}Co_{0.65}S_{0.4}Se_{0.6}$ NCs. The pattern of $Ni_{0.3}Co_{0.74}Se$ NCs is also reported for a better comparison.

Figure 4.4. (a) LSVs measured at a sweep rate of 1 mV/s, (b) Tafel plots and (c) TOF values at η = 0.35 V of ternary and quaternary Ni-Co-S-Se NCs with various S/Se ratios.

Figure 4.5. Impedance spectra of electrodes measured at open circuit potential of ternary and quaternary Ni-Co-S-Se NCs with various S/Se ratios.

Figure 4.6. The EDLC measurements of (a) $Ni_{0,3}Co_{0,74}Se$, (b) $Ni_{0.3}Co_{0.73}S_{0.2}Se_{0.8}$ and (c) $Ni_{0.25}Co_{0.65}S_{0.4}Se_{0.6}$ NCs at different scan rates and the corresponding C_{dl} linear fitting and calculation (d).

Figure 4.7. Chronopotentiometry measurement at a current density of 10 mA/cm^2 for $Ni_{0.25}Co_{0.65}S_{0.4}Se_{0.6}$ NCs electrode.

Figure 4.8. CVs of quaternary Ni-Co-S-Se NCs with various S/Se ratios.

Figure 4.9. (a) SAED patterns of $Ni_{0.25}Co_{0.65}S_{0.4}Se_{0.6}$NCs before and after OER. (b, d-h) HRTEM images and (c) EDS elemental mapping of $Ni_{0.25}Co_{0.65}S_{0.4}Se_{0.6}$ NCs before OER. The NCs exhibit the expected hexagonal structure (ICSD number 53959) and they are characterized by a rich presence of defects.

Figure 4.10. (a) TEM micrograph, (b) HAADF-STEM image and (c,d) HRTEM image of $Ni_{0.25}Co_{0.65}S_{0.4}Se_{0.6}$NCs after OER. (e,f) Two regions of panel (d) are magnified to show the lattice fringes of the oxide NCs, which matching either NiO (ICSD number 9866) or CoO (ICSD number 9865). (g) EDS elemental mapping of $Ni_{0.25}Co_{0.65}S_{0.4}Se_{0.6}$ NCs after OER. (h) EDS spectrum and (i) XRD patterns on the FTO substrate of $Ni_{0.25}Co_{0.65}S_{0.4}Se_{0.6}$NCs after OER.

Figure 4.11. High-resolution (a) Ni, (b) Co, (c) S and (d) Se spectra of $Ni_{0.25}Co_{0.65}S_{0.4}Se_{0.6}$ NCs before and after OER.

Figure 4.12. (a) XRD patterns and TEM images of (b) $Co_{0,93}S_{0.39}Se_{0.61}$, (c) $Ni_{0,25}Co_{0,65}S_{0,41}Se_{0,59}$, (d) $Ni_{0.57}Co_{0.56}S_{0.38}Se_{0.62}$, (e) $Ni_{0.78}Co_{0.24}S_{0.42}Se_{0.58}$ and (f) $NiS_{0,41}Se_{0,59}$ NCs.

Figure 4.13. (a) LSVs measured at a sweep rate of 1 mV/s, (b) Tafel plots and (c) TOF values at η = 0.35 V of ternary and quaternary Ni-Co-S-Se NCs with various Ni/Co ratios.

Figure 4.14. Impedance spectra of electrodes measured at open circuit potential of ternary and quaternary Ni-Co-S-Se NCs with various Ni/Co ratios.

List of Tables

Chapter I Introduction

1.1 Electrocatalytic Water Splitting

The two industrial revolutions brought a "Big Bang" in the innovation of technology, while at the same time created a huge demand on energy. For hundred years, the main source of energy has been the fossil fuel, which is limited in storage and can raise environmental issues such as acid rain and smoke pollution. Therefore, the seek for the alternative energy sources, which are sustainable and eco-friendly, is in urgent requirements.

Hydrogen (H_2) as an energy carrier has attracted significant attention because it has the highest gravimetric energy density of any known fuel, and it is compatible with electrochemical processes for energy conversion free of CO_2 emissions.[1] Thus, finding a sustainable and low-energy-consuming way to produce H_2 became an important and significant topic in scientific research. Currently, most of the H_2 used for industrial purposes is made by steam reforming of natural gas or methane. At the moment this production technology is predominant because of the high availability and low price of natural gas, but natural gas is not a renewable energy source and the problem of CO_2 release is not solved.[2] Different from this traditional technique, solar energy for water splitting to produce H_2 presents an environmentally responsible, carbon-free alternative for the H_2 generation. However, restricted by a lot of disadvantages such as the limited absorption range of the photocatalysts on natural light and the high speed of the electron-hole recombination during photocatalysis processes, the efficiency of solar energy to chemical energy is fairly low during photocatalysis procedures. Compared to photocatalysis for water splitting, the electrocatalysis is an easier method with much higher efficiency, which can be as high as 100% and higher purity of H_2 and O_2. At the moment, the only disadvantage of the electrocatalysis is its cost. On one side, the source of electricity is mainly from water or coal which is a kind of non-renewable energy; On the other side, the traditional electrocatalysts are mainly noble metals and noble metal oxides. These drawbacks restrain the large-scale industrialization of electrocatalytic H_2 production. Based on this situation, searching for more efficient and economic electrocatalysts becomes a main problem to be solved.

1.2 Mechanism in HER and OER

The water splitting is composed by two simultaneous electrochemical half reactions, hydrogen evolution reaction (HER) and oxygen evolution reaction (OER). The reaction is performed in an

electrolytic cell with an external electric power source and the specific electrolyte which can provide H_2O for HER and OER. The HER and OER happen on the cathode and anode, respectively, when the potential is big enough (Figure 1.1).[3-4] The two half reactions can be written as following:

HER: $2H^+(aq) + 2e^- \leftrightarrow H_2(g)$ $\quad E_{cathodic} = 0\ V - 0.059(pH)\ V$ vs. RHE

OER: $2H_2O(l) \leftrightarrow O_2(g) + 4H^+(aq) + 4e^-$ $\quad E_{anodic} = 1.23\ V - 0.059(pH)\ V$ vs. RHE

Whole reaction: $2H_2O \rightarrow 2H_2 + O_2$ $\quad E = 1.23\ V$

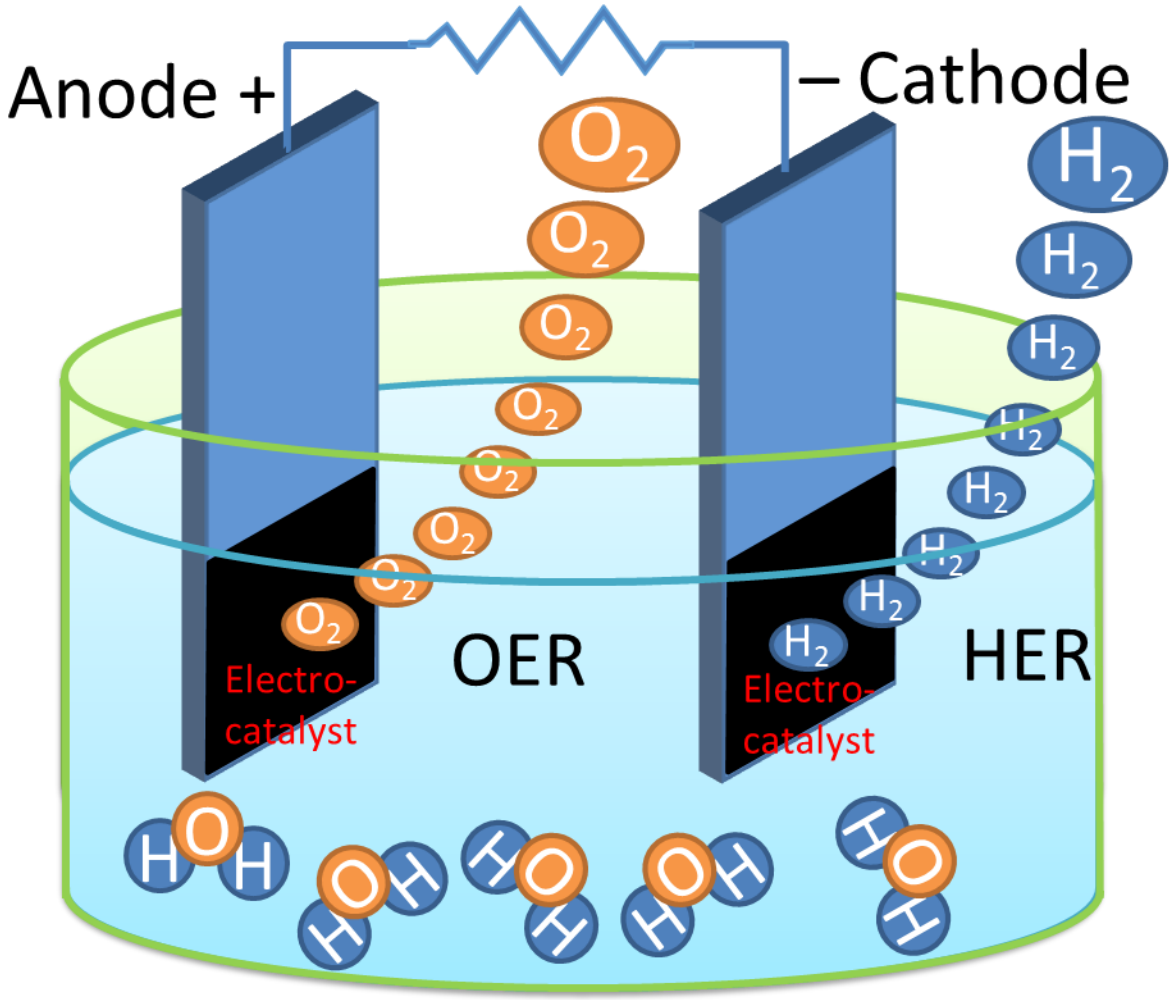

Figure 1.1. Schematic description of electrocatalysis of water splitting.

The redox potentials of the water splitting reactions strongly depend on pH values of the electrolytes. A potential-pH diagram, which is also known as the Pourbaix diagram, shows the area where, in theory, the potentials and pH values are suitable for HER and OER. As shown in Figure 1.2, line (a) and (b) stand for the equilibrium reaction of HER and OER, respectively. The HER is favored below line (a) and the OER is favored above line (b) (see Figure 1.2). Between line (a) and (b), the H_2O is thermodynamically stable.

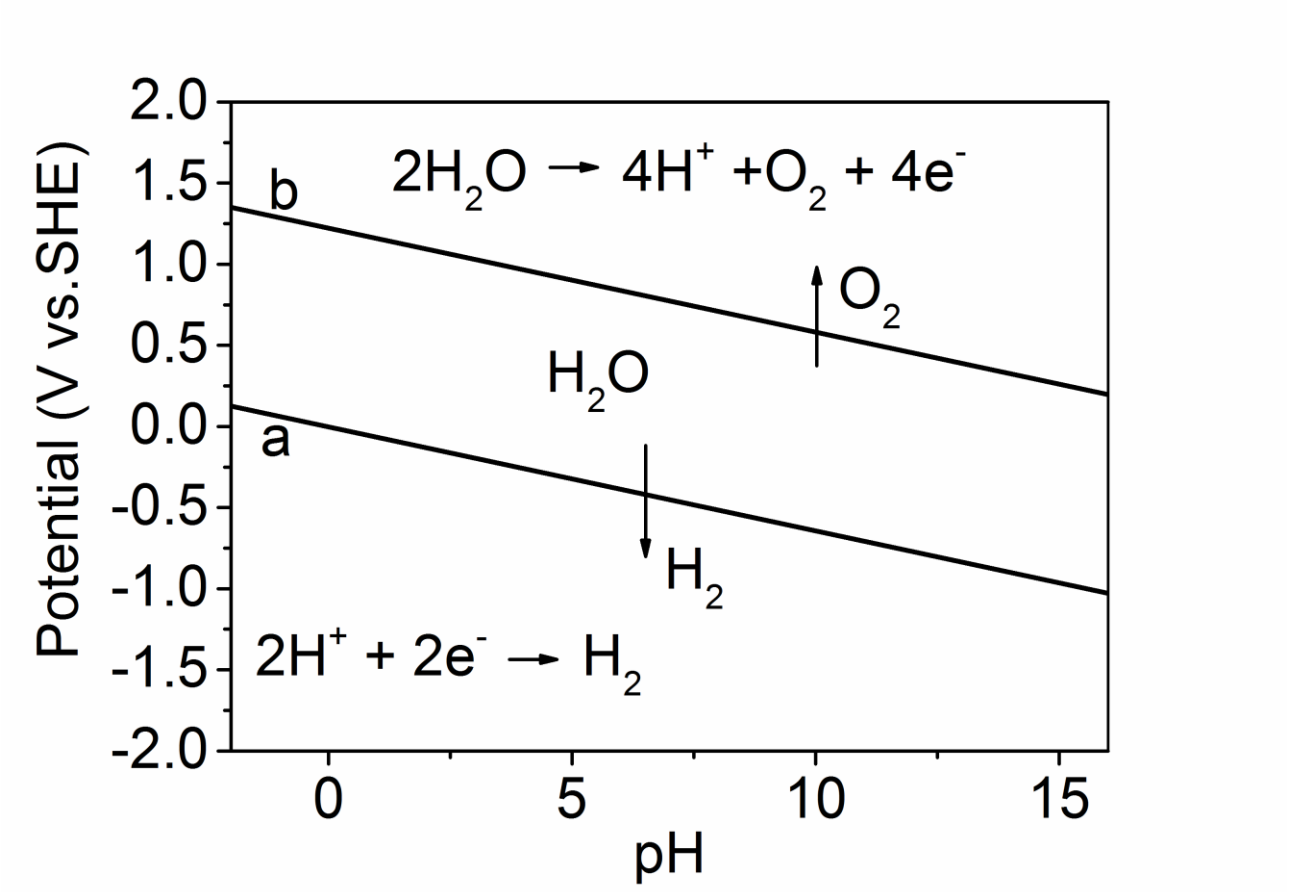

Figure 1.2. Pourbaix diagram of H_2O at 25 ºC.

Although these two half reactions are reversible, they cannot proceed strictly with the thermodynamic potential of reversibility. Instead, an extra potential is needed to trigger these reactions, and their required potential to start the reaction is different. For instance, when the pH of the electrolyte is 0, the potential is 0 V vs. reversible hydrogen electrode (RHE) for the HER; For the OER, the potential is 1.23 V vs. RHE. Hence, the OER requires a higher energy to overcome the thermodynamic barrier. Moreover, the OER is a four electron-proton coupled reaction while the HER is only a two electron-transfer reaction, thus it can be easily expected that OER requires a higher energy to overcome the kinetic barrier as well. Even if the production of pure H_2 is the main objective of electrochemical water splitting, one cannot neglect the counter-reaction (OER), as it is the sluggish step in the whole reaction. Based on these above situations, the challenges ahead in developing new, efficient catalysts both for HER and OER and opportunities are stressed.

1.2.1 Mechanism of HER

Table 1.1 shows HER reactions taking place either in acidic or alkaline conditions in which different electron transfer steps occur according to different pH environments. The first step, also called the Volmer reaction, under acidic conditions is characterized by the formation of H* species

on the surface of the electrode upon the reduction of H^+ ions (present in the acidic electrolyte) with the electrons present on the surface of the electrode. In alkaline electrolytes, because of the extremely low concentration of H^+ ions, the Volmer reaction happens together with the ionization of H_2O which produces enough H^+. This means extra energy is demanded to overcome this barrier. It is straightforward that the pH strongly influences the HER process and its kinetics. The second step of the HER, which leads to the actual formation of H_2 gas can occur in two different ways: in one route, also called the Heyrovsky reaction, an absorbed H* specie reacts with one e^- from the electrode and one H^+ from the electrolyte to form one H_2 molecule; another option, also called the Tafel reaction, consists in the reaction of two adjacent absorbed H* which combine to form one H_2 molecule.[5] While in alkaline electrolyte, the Heyrovsky reaction happens when the absorbed H* specie reacts with one e^- from the electrode and one H^+ from the ionized H_2O, which requires higher energy than in the acidic electrolyte. If the combination of two absorbed H* is dominant, namely Tafel reaction, the energy barrier will be less comparing to the Heyrovsky reaction. By calculating the Tafel slope which we will introduce in the next section, the determining step and the routes of HER can be deduced because the specific steps can refer to specific values of Tafel slope. For example, if a Tafel slope is approximately 120 mV/dec, it indicates that the discharge step (Volmer reaction) is rate limiting. A Tafel slope of about 40 mV/dec suggests that the Heyrovsky reaction is dominating, while Tafel slope of around 30 mV/dec suggests that Tafel reaction is dominating.[6]

Table 1.1. Process of HER in acidic and alkaline conditions.

Overall reaction (condition)	**Reaction pathway**
$2H^+ + 2e^- \rightarrow H_2$	$H^+ + e^- \rightarrow H^*$ (Volmer)
(Acidic solution)	$H^+ + e^- + H^* \rightarrow H_2$ (Heyrovsky)
	or $2H^* \rightarrow H_2$ (Tafel)
$2H_2O + 2e^- \rightarrow H_2 + 2OH^-$	$H_2O + e^- \rightarrow H^* + OH^-$ (Volmer)
(Alkaline solution)	$H_2O + e^- + H^* \rightarrow H_2 + OH^-$ (Heyrovsky)
	or $2H^* \rightarrow H_2$ (Tafel)

Based on these above mechanisms, the bonding energetics of the adsorbed H* on the active sites of the electrocatalysts play an important role in the HER. Indeed, the free energy of hydrogen adsorption (ΔG_{H^*}) should be suitable for the reaction, which, in simple terms, means that both the standard redox potential for HER and the associated standard ΔG_{H^*} should be zero. If the ΔG_{H^*} has a large negative value, it means the hydrogen adsorption bond is too strong, so the dissociation of

H_2 molecule is hard. On the contrary, if the ΔG_{H^*} has a large positive value, it means one the active sites the formation of hydrogen adsorption bond is not easy.

1.2.2 Mechanism of OER

Since the OER involves the transfer of four e^-, the kinds of intermediates vary in different experimental conditions, it is more complicated than the HER. It has been widely accepted that the OER is composed of five different sub-reactions. Table 1.2 shows the possible elemental steps involved in the OER both in acidic and alkaline conditions.[7] Similar as the situation in HER, if any of these intermediates (*OH, *O, OOH* or $*O_2$) is not favored by its standard free energy of bonding, the catalysts are not able to function for OER. On the other hand, if the intermediates are adsorbed too strongly or too weakly on the active sites, the total speed of the reaction on the catalysts will be influenced. Then a high overpotential is needed for the occurrence of OER. As in the case of the HER, the experimental values of Tafel slopes can reveal the rate-determining step at a certain extent, it is hard to build a corresponding relationship between the Tafel slope and the rate-determining step in OER. The kinds in the intermediates vary a lot so the models for the OER mechanism differ according to the specific kinds of active sites, for example the oxo groups have totally different reaction pathways from the terminal peroxide groups in catalyzing OER.[8] Besides, it has been demonstrated that that the OER reaction pathways are very sensitive to the surface structure of the electrodes, different materials or even different facets of the same material manifest different catalytic processes. Thus to determine the reaction routes is difficult.

Table 1.2. Process of OER in acidic and alkaline conditions.

Overall reaction (condition)	**Reaction pathway**
$2H_2O \rightarrow 4H^+ + 4e^- + O_2$	$* + H_2O \rightarrow *OH + H^+ + e^-$
(Acidic solution)	$*OH \rightarrow *O + H^+ + e^-$
	$*O + H_2O \rightarrow OOH* + H^+ + e^-$
	$*OOH \rightarrow *O_2 + H^+ + e^-$
	$*O_2 \rightarrow * + O_2$
$4OH^- \rightarrow 2H_2O + 4e^- + O_2$	$* + OH^- \rightarrow *OH + e^-$
(Alkaline solution)	$*OH + OH^- \rightarrow H_2O + e^- + *O$
	$*O + OH^- \rightarrow *OOH + e^-$
	$*OOH + OH^- \rightarrow *O_2 + e^-$
	$*O_2 \rightarrow * + O_2$

1.3 Parameters Used to Evaluate the Catalytic Activity

The following parameters are the widely recognized ones for evaluating and comparing the catalytic activities of electrocatalysts.

1.3.1 Overpotential (η)

In a real system, the electrochemical reaction occurs only when the potential predicted by the thermodynamics excluding the kinetic hindrances experienced.[9-11] To overcome these hindrances, an additional driving force which manifests as an extra potential is needed to influence such electrochemical reactions. This extra potential is called the overpotential (η). In both the HER and OER, usually three factors are considered to be the sources of overpotential, namely, the concentration overpotential, the activation overpotential, and the overpotential caused by the uncompensated or system resistance (R_s, mainly from the resistance of the other parts of the system except the electrodes for measurements, for example the resistance from the electrolyte). The activation overpotential only depends on the intrinsic property of the catalyst used in the electrocatalytic reaction and varies by the types of the materials. Hence, the more efficient the catalyst is chosen, the less activation overpotential it can get. The concentration overpotential occurs immediately after the electrode reaction begins since there is a sudden drop in ion concentration near the interfaces. By stirring the electrolyte this can be minimized. The last kind of overpotential can be removed by calibrating the data with Ohmic drop compensation, and this correction is now available in many electrochemical workstations.[12] This method, known as the *iR* correction, needs to be finished before further analysis of the data in order to reduce the influence from the surroundings to the data and make the data reflect the intrinsic properties of the electrocatalysts as much as possible.

In HER, the activation overpotential after *iR* correction can be considered as the onset overpotential, and it is more important than the other parameters, since the kinetics of the HER is more efficient than that of the OER.[13] This can be shown from the polarization curve acquired by plotting the potential versus the current density.

In contrast, the OER case differs from material to material in different test conditions. In order to calculate the overpotential, some other parameters should be taken into consideration too. Since all of the possible mechanisms of the OER proceed through a series of elementary steps, the kinetic barriers which are constructed by each of these steps will be contained in the overall activation overpotential for OER. Because of the different kinetics of these elementary steps, except the onset overpotential after *iR* correction, the overpotential at a certain current density (j) like 10 mA/cm^2 has now widely been used as an essential quantitative activity parameter for evaluating the performance of an electrocatalyst.[14] And this method to estimate the activity is also used for the

HER.

1.3.2 Tafel Slope

The Tafel plot is from the mathematic calculation of the polarization curve of the catalyst. In general, the polarization curve, which is a plot of j versus electrode potential (E), is replotted as a plot of log(j) versus η. The linear portion near the iR-corrected onset potential is chosen to be analyzed deeper and the slope is calculated as the Tafel slope. The Tafel slope is a reflection of the charge transfer property of the material, and the formula can be expressed as follows:

$$\frac{\mathrm{dlog}(j)}{\mathrm{d}\eta} = 2.303\mathrm{RT}/\alpha\mathrm{nF}$$

From the formula, it is clear that the Tafel slope is inversely proportional to the charge transfer coefficient (α), and the remaining other parameters are constants: R is the ideal gas constant, T is the temperature, F is Faraday constant, and n is the number of electrons transferred. In HER n is equal to 2, and in OER it is 4. According to the formula, a catalyst with a fast charge transfer ability should possess a low Tafel slope. Therefore, the Tafel slope is always used as a primary activity parameter to determine the activity of a catalyst. It has to be mentioned that the scan rate at which the polarization curve used for Tafel plot should be as low as possible (usually 1 mV/s). This is because when the electrocatalyst is highly capacitive, the capacitive current will strongly contribute to the whole current density which we can measure from the workstation and it is used for calculating the Tafel slope. In such a case the Tafel slope is influenced by the scan rate and this is not true.

1.3.3 Turnover Frequency (TOF)

The TOF is another quantitative parameter used to evaluate an electrocatalyst at a defined overpotential. The TOF of the catalyst is defined as the number of moles of O_2/H_2 evolved per unit time. The following formula is used to calculate the TOF for an electrocatalytic gas evolution reaction:

$$\mathrm{TOF} = \frac{jS}{AFn}$$

in which j is the measured current density, S is the geometric surface area of the electrode, F is Faraday's constant (96485.3 C/mol), A is the moles of the metal atom in the loaded catalysts, and n is number of electrons transferred, in HER it is equal to 2, in OER it is equal to 4.

1.3.4 Electrochemical Surface Area (ECSA)

Surface area is an importance parameter for catalysts as it is related to the active sites can be provided by the catalysts for catalytic reactions. For electrocatalysis, it is better to use ECSA to

characterize the surface area as it is more sensitive to the actual catalyst loading. Usually, the ECSA is determined by different scan rate of cyclic voltammetry in the non-faradaic region. The electrochemical double-layer capacitance (C_{dl}) extracted from the capacitive current as a function of scan rate serves as an estimate of the effective ECSA of the solid-liquid interface. Specifically, in this thesis for both HER and OER, the scan region of the cyclic voltammetry is a non-faradaic region from -0.02 to 0.08 V vs. Ag/AgCl (3M NaCl) The electrochemical double-layer capacitance (C_{dl}) was estimated by plotting $j = j_{anodic} - j_{cathodic}$ at -0.06 V vs. Ag/AgCl (3M NaCl) against the scan rate.

1.3.5 Stability

There are several kinds of method to test stability. Usually the following three methods are commonly used. The first one is to measure CV cycling at a higher scan rate and compare the change after hundreds of cycles. The other two methods are to expose the electrocatalysts to a fixed potential (chronoamperometry) or a fixed current density (chronopotentiometry) and test for durations of hours. In this thesis, we choose the chronopotentiometry method and set the current density at 10 mA/cm^2.

1.4 Electrocatalysts for Water Splitting

As introduced above, since the occurrence of electrochemical water splitting has to overcome the energy barrier, to find an electrocatalyst which can decrease reaction barrier and increase the energy conversion efficiency becomes a fundamental scientific problem to be solved in electrocatalysis of water splitting. Till now, much research has been devoted and people find that there are a variety of suitable electrocatalysts for HER and OER can not only decrease the energy barrier dramatically, but also increase the efficiency and stability of water splitting. For both HER and OER, the noble metals and their compounds were used as the electrocatalysts at the beginning. Then the emphasis was inclined to the non-noble electrocatalysts since people find some 3d transition metal compounds have promising potential in HER and OER as well but more economical compared to the noble metal catalysts.

1.4.1 Noble Metal Electrocatalysts for HER

Traditionally, platinum (Pt) metal is the best electrocatalyst for HER with a near-perfect overpotential close to 0 V vs. RHE.[15] Thus it is used as a reference HER catalyst in a lot of research work. The electrocatalytic activity differs on different facets of Pt crystals, and the tendency of activity in both acidic and alkaline is similar: (111) < (100) < (110),[16] and this role corresponds to the surface activation energy calculation according to the Arrenius curve.[17] Moreover, the surface

activation energy of Pt under alkaline situation is twice as that of Pt under acidic situation, which results in a better HER property of Pt in acidic situation than in alkaline situation. Similarly, palladium and iridium also show better activity in acidic solution than in alkaline solution.[18] The main reason of this difference is because in alkaline electrolyte, the metal-*OH bond and the ionization of H_2O influence the activity of HER. Except for Pt, other noble metals such as palladium, iridium,[19] gold,[20] silver, rhodium and ruthenium[21] and their alloys are also found to be active in HER. Similar as Pt, their properties also depend on the facets and pH environment. Moreover, although they are studied as HER catalysts, the performance is not as good as Pt.[22] Interestingly, people found that the alloy of several noble metals shows better performance than the single one by tuning the free energy of hydrogen adsorption (ΔG_{H^*}).[23] However, the drawback is still the price.

In order to reduce the utilization of expensive Pt, Pt alloys instead is studied as electrocatalysts for HER as well. These alloys mainly include Pt and 3d transition metals. In a lot of works, Pt can be synthesized as atomic layer in order to increase the surface active area and decrease the cost of the catalyst at the same time.[24] The induced another kind of atoms are helpful to optimize the ΔG_{H^*} on Pt thus optimize HER activity. For example, to construct 3d metal on the surface of Pt (111), namely 3d-Pt, can make the d-band center close to the Fermi level. On the contrary, the construction of Pt-3d-Pt (111) makes the d-band center far away from the Fermi level.[21] These calculations were proved by deposition of Pt or Pd on the single crystal surface of 3d metals.[25-26] Because of the influence of the ligand field or the stress between different atoms, the catalytic property of these alloys are better than the single metals.[27]

1.4.2 Noble Metal-Free Electrocatalysts for HER

From a sustainability and scalability perspective, the need for electrocatalysts composed of elements in high terrestrial abundance is evident. Based on this demand, people start to focus on the other alternative materials. At the beginning, 3d metals like nickel, molybdenum, and tungsten metals were tried to replace Pt, but all suffered from inferior activity and corrosion caused by the electrolyte.[28] Following the same route of improving the activity as noble metals, researchers began investigating the activity of transition metal alloys instead of single metals. The “volcano” plots of transition metal activity (Figure 1.3) suggested that there could be synergistic benefits of using alloy or multimetallic electrodes that could, through the cooperative interactions of metal species with differing ΔG_{H^*}, emulate or even improve upon the highly active surfaces of noble metal electrodes.[29-31] Specifically, alloying of transition metals is expected to tune the d-band center, Fermi level energy, and interatomic spacing, all of which could impact ΔG_{H^*} and then improve HER.[32] For instance, metal alloys including Ni-Mo, Ni-V, Ni-Fe, Ni-W, Co-Mo and Fe-Mo

exhibited higher activity toward the HER in alkaline conditions than their corresponding single metals.[33-34] Inspired by these results, people are trying alloys with more kinds of metals like ternary Ni-Mo-Cd,[35] Ni-Mo-Zn,[36-37] or even quaternary alloys.[38] Consequently, they also show improvement in HER though the stability is still a problem to be solved.

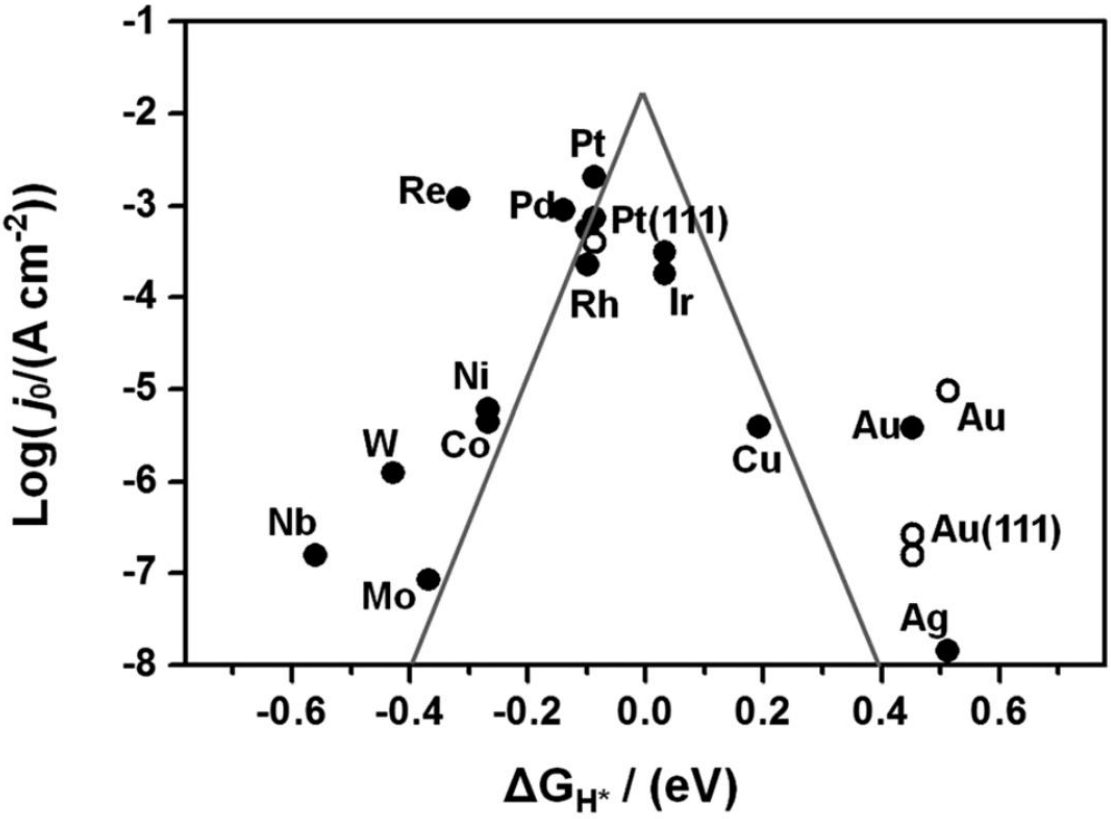

Figure 1.3. Exchange current density for the HER at different transition metal surfaces plotted as a function of the free energy for ΔG_{H^*}.[39]

To solve the problem of corrosion from the electrolyte with extreme pH environment, people try to replace the transition metals with the transition metal compounds. Despite their prevalence as industrial catalysts, the binary transition metal oxides generally do not find use as electrocatalysts in HER due to their poor electrical conductivity and low chemical stability particularly in acidic conditions.[40] Instead, most of the oxides were used as HER electrocatalysts together with other materials to improve the conductivity and avoid the low pH electrolyte such as NiO/Ni heterostructures[41] and CoO_x/N-doped carbon hybrids.[42] In order to avoid the disadvantages of oxides, other kinds of transition metal compounds are researched as well. Among these compounds, transition metal chalcogenides make up the largest class of electrocatalysts. For HER, the most well-known example among them is MoS_2. This layered material shows amazing performance in HER as bulk natural crystals or nanomaterials because its sulfided Mo-edges were active for the

HER with suitable $\Delta G_{H^*} \sim 0.1$ V, close to those of several efficient HER electrocatalysts including Pt.[43-44] Following the success of MoS_2, research attention has also been extended to several other layered transition metal chalcogenides such as WS_2, $MoSe_2$ and WSe_2.[45] Interestingly, $MoSe_2$ is found as the best one among these layered structures as proved by calculation and experiments because it has the most thermoneutral ΔG_{H^*} for both metal and chalcogen edges.[46-47]

Except these layered materials, other transition metal chalcogenides or their alloy chalcogenides were also investigated and emerged as new efficient electrocatalysts. In recent years, research attention has been extended to these various materials. These Ni-, Co- or Fe- based chalcogenides are synthesized into different shapes, sizes or combined with different structures in order to improve the catalytic properties.[48] As shown in Figure 1.4, these first-row transition metal chalcogenide electrocatalysts have low overpotential at 10 mA/cm^2 as HER electrocatalysts. To these chalcogenides, a similar mechanism should be responsible for the enhanced HER catalytic property like Mo and W chalcogenides. As to influence of the chalcogens, when the hydrogen desorption is considered as the determined step, selenides of Fe, Co and Ni stand ahead of sulfides, as the strength of Se-H bond is smaller than S-H bond, which means H_2 is easier to dissociate from Se. Moreover, the decreased electronegativity of Se makes the selenides more conductive, which is helpful for the charge transfer thus enhancing the HER activity.

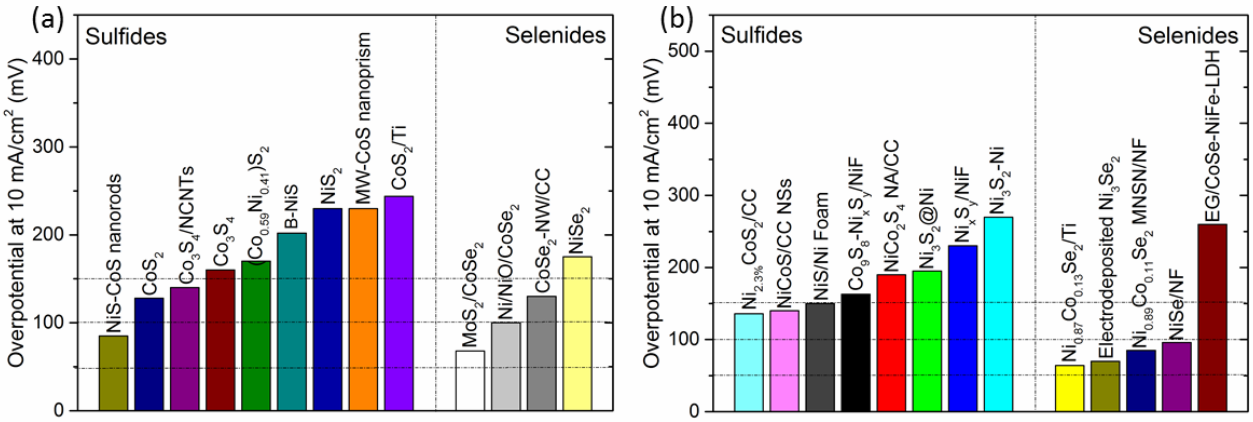

Figure 1.4. Comparison of the performance of various transition metal chalcogenides HER electrocatalysts in (a) acidic and (b) alkaline media.[48,49]

Besides, transition metal carbides, nitrides, phosphides, borides and even metal-free catalysts are also studied as HER catalysts with promising properties.[50] Figure 1.5 shows a brief summary of HER activities of different materials.[51]

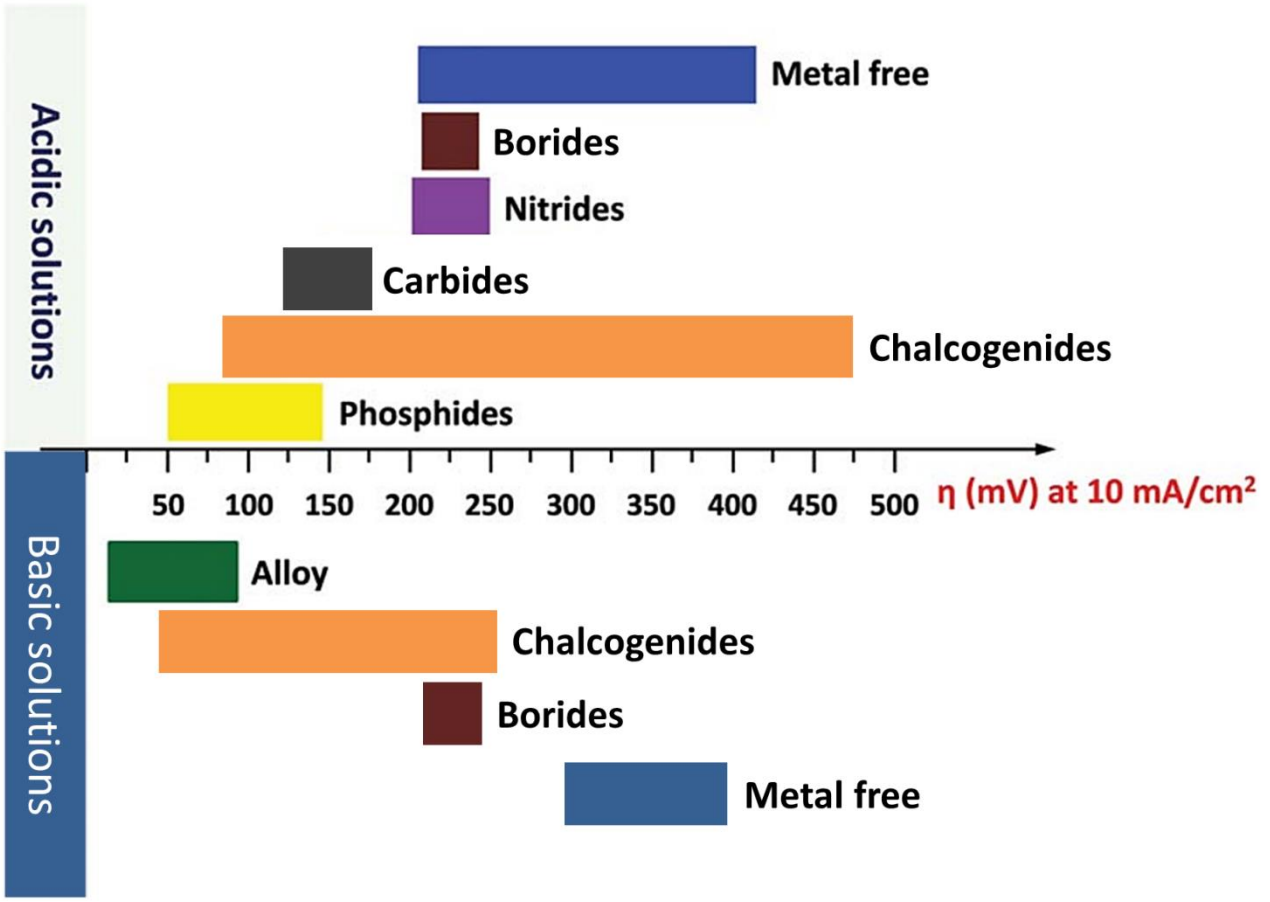

Figure 1.5. Summary of HER activities of different HER electrocatalysts.

1.4.3 Noble Metal Electrocatalysts for OER

The earliest research on electrocatalysts for OER traces back to 1960s, and most of the catalysts are noble metals. According to the experiments, different noble metals in acidic solutions display the following role on OER: Ru > Ir > Pd > Rh > Pt.[52] With high voltage, these metals are oxidized slowly. The oxides of these noble metals are still active in OER, while the stability from oxidization is the opposite of the catalytic activity of the corresponding oxides. For example, Pt is the most stable catalyst from being oxidized and Ru is the least stable. However, γ-RuO_2 shows better OER activity than any other materials till now in both acidic and alkaline solution, thus it is usually used as a reference catalyst in a host of researches.[53] Tremendous research was focused on the RuO_2 for OER and the results indicate that the catalytic activity of RuO_2 is strongly related to its physical and chemical properties such as local electron structure, phase, frictional factor and porosity.[54-55] When the voltage is more than 1.4 V, RuO_2 under acidic condition can be oxidized to RuO_4 which can be dissolved in the electrolysis slowly. Another kind of noble metal oxide, IrO_2, is more stable than RuO_2 under high voltage, but it needs more potential than RuO_2 with the same current density. Similar as the catalysts in HER, an important strategy to improve the properties is alloying. Ru-Ir alloy and the oxide alloys are also reported to have better catalytic activity and

stability than the single ones. In order to maintain a mixture of oxidation state of Ru (III-IV) and restrain the corrosion, tin (Sn) or tantalum (Ta) are also added to design ternary metal oxides with better catalytic activity and stability like $RuIr_{0.5}Ta_{0.5}O_x$ and $Sn_{0.5}Ru_{0.25}Ir_{0.25}O_2$.

1.4.4 Noble Metal-Free Electrocatalysts for OER

There are three main groups of inorganic electrocatalysts for OER except noble metal families. The first and the most widely studied group is the metal oxides. The metal oxides active for OER are mainly classified to three branches according to their structures: perovskites, spinels and layered transition metal oxide structures, and the main atoms behaving as active sites in these oxides are transition metals, mostly Ni, Co, Mn and Fe.[8] Meanwhile, a large amount of research also proves the introduction of different kinds of elements into the single structures can enhance the OER activity significantly. However, the poor conductivity and the stability in the acidic electrolytes limit their application, thus attention was focused on other compounds with promising properties.

The second group is metal chalcogenides. Till now, most of the metal chalcogenides for OER are Ni- or Co- based sulfides and selenides. These materials commonly exhibit robust properties and comparable OER activities to the oxides because of the better conductivity and stability in a wide range of pH values. Similar as transition metal oxides, the OER activity has a compact relationship with the structures of transition metal chalcogenides. It is found that the monochalcogenides and the dichalcogenides are very promising candidates for OER. In monochalcogenides, the reported overpotential arranges from 200 to 400 mV at 10 mA/cm^2, which is better than the transition metal oxides. Besides, the partial or total oxidation are usually observed by characterizing the catalysts after OER. For example, the formation of NiOOH was found on the surface of NiS microsphere after the long-term OER test, and the NiOOH@NiS was believed as the active center for the OER.[56] Similarly, the surface of $(Ni, Co)_{0.85}Se$ nanotubes is also oxidized to ion-permeable oxides/hydroxide, meanwhile the metallic $(Ni, Co)_{0.85}Se$ under the oxidized surface can boost electron transportation of the insulating oxides/hydroxide surface.[57] While in other literatures, the chalcogenides are found to become oxides totally with higher surface area compared to the directly synthesized oxide catalysts, resulting in a superior catalytic activity.[58] Oxidation phenomena were also found in dichalcogenides and similar mechanism is shared with monochalcogenides.[59] Inspired by this idea, the hybrid materials between oxides and chalcogenides were also synthesized for OER, and the results are promising.[60-62] It should be mentioned that the oxidation of the catalysts during OER is not always observed in metal chalcogenides. For instance, the ultrathin $CoSe_2$ nanosheets made by Liu et al. were reported to provide Co vacancies on the surface as active sites for OER instead of phase transformation.[63] Luo et al. investigated the NiS microarchitectures and verified that the phase was still NiS after OER.[64] Besides, other structures

like Ni_3Se_2,[65] Co_3S_4,[66] and Ni_3S_2[67] are also utilized for OER due to their excellent electroconductivities and chemical resistance against acid/alkaline electrolyte. However, most of these metal-rich compounds are not oxidized, instead in these chalcogenide deficient phases there are full of metal-metal bond which can be further modified through solid state chemistry approaches to optimize the catalytic efficiency.

Except for these binary chalcogenides, more and more multielemental transition chalcogenides are also designed for better performance in OER. They have the same structures as their corresponding binary materials but the performance was improved, and the synergistic effects of different elements might play critical roles in affecting the OER activity.[59, 68] Moreover, decoration,[60, 69] doping[70-71] or heterostructures[72] are also developed to modify the activity. The aims of these methods are either increasing the dispersion of the catalysts in order to increase the effective surface area, or tuning the electronic configuration to benefit the electron transfer efficiency. Figure 1.6 provides a summary of OER performance of some transition metal sulfides and selenides.[48, 68-69, 71, 73-78]

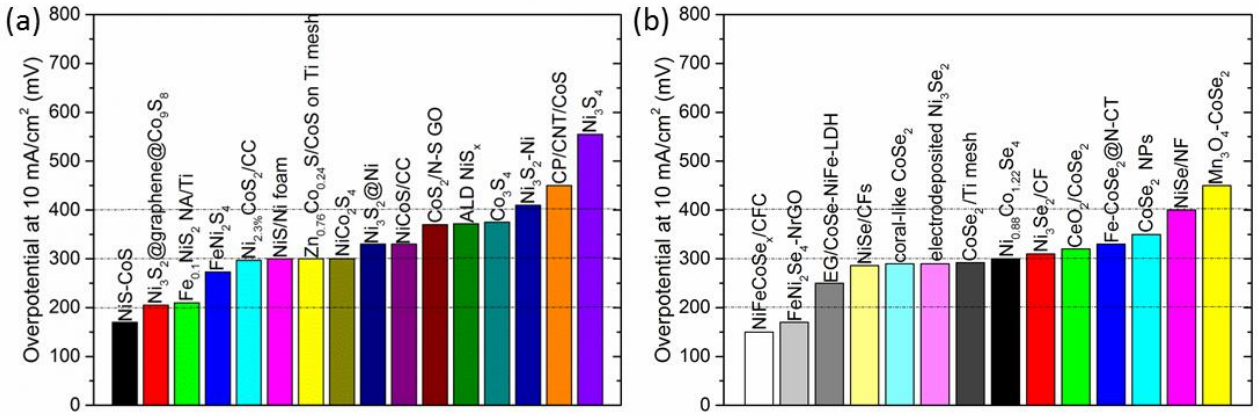

Figure 1.6. Comparison of the performance of various transition metal (a) sulfide and (b) selenide OER electrocatalysts in alkaline media.

The last group is transition metal pnictides. It was revealed that in some cases, a thin metal oxide layer forms during OER on the surface of the pnictides, which has similar mechanism as that in metal chalcogenides.[79-80] Also, people find that with higher ratio of metal inside the compounds, the electroconductivity can be increased and thereby more active for OER. For example, the electroconductivity and the OER performance of Co_2N, Co_3N and Co_4N follow the following role: $Co_2N < Co_3N < Co_4N$.[81] Some approaches are also tried to enhance the electrocatalytic performance such as combining with conductive substrates,[82] decoration,[83] doping[22] or alloying,[84-85] and a remarkable improvement was shown. Nevertheless, in some pnictides, the performance was found rapidly dropped and seems not stable, thus further study is still necessary on metal pnictides. Figure 1.7 shows a brief summary of OER activities of different materials.[53]

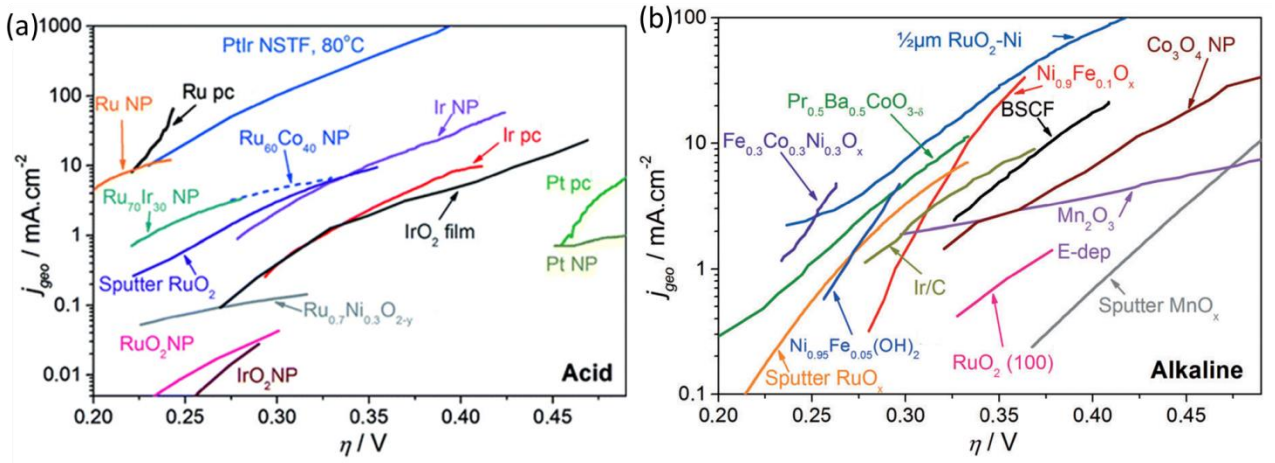

Figure 1.7. Overview of the state of the art for the oxygen evolution reaction in (a) acid media and (b) alkaline media of different materials.

1.5 Synthetic Strategies of Micro/Nano Transition Metal Compounds as Electrocatalysts

There are two main routes of synthesizing the micro/nano materials: top-down methods and bottom-up methods. For the noble metal-free electrocatalysts, many methods have been employed to prepare the materials with various kinds of structures, sizes, morphologies and compositions. Among them, liquid exfoliation is a typical top-down method, while hydrothermal or solvothermal method, colloidal synthesis, electrodeposition, template-direct method are all popular bottom-up approaches in nanotechnology. The synthesis of noble metal-free electrocatalysts has been achieved by following one or a mixture of these procedures in hope of a modification of the electrocatalysts in nanostructuring, chemical properties, structures and compositions.

1.5.1 Exfoliation

Exfoliation is a typical method used for synthesizing layered materials, such as MoS_2, WS_2, $MoSe_2$.[86-87] The main design thought is to break the relatively weak bond between the layers inside the bulk materials to obtain single-layer or multi-layer nanosheets. There are physical way and chemical way to achieve the exfoliation.[88] Physically, sonication is a commonly used method to split the bulk materials, and the results depend on the kinds of the solvents.[89] It was suggested that when the surface energy of the solvent matches with that of the layered material, the enthalpy of exfoliation minimized. Chemically, it is found in the lithium battery, when the layered materials are used as cathodes, the lithium interaction process allows Li atoms to insert in the structure of the layered materials (for example from MoS_2 to Li_xMoS_2).[90] Then the Li-contained compound reacts with water, and H_2 is generated between the layers and separate the layers. Exfoliation can produce the nanosheets with large quantity, but the reaction time is too long (for example 3 days).[91-92]

1.5.2 Colloidal Synthesis

Colloidal synthesis is a typical bottom-up method to acquire different kinds of nanocrystals. At the beginning, it was used to prepare inorganic semiconductors like CdSe.[93] Since then a lot of high-quality nanoparticles were developed based on the mechanism of this method and used in all the application field in nanotechnology including electrocatalysis in water splitting. In principle, the precursors of the products are mostly from organic compounds, which are easy to decompose under high temperature (100-400 °C) or dissolve in the organic solvent (for example 1-octadecene, ODE). Additional chemicals are needed in target of controlling the size, morphology, dispersion, or reducing or oxidizing the precursors, depending on the specific requirement. Mechanistic insights show that there are two main steps in the reaction: nucleation stage and growth stage. In the former step the monomers from the precursors aggregate to form nucleis, and in the later step the nucleis constantly collect the monomers in the mixed solvent to grow up (Figure 1.8). It should be highlighted that not all types of precursors can form the objective nanocrystals, the reaction follows the "HSAB" theory, namely hard/soft acid-base theory. The "acid" here refers to Lewis acid which means any species possessing a vacant orbital capable of accepting an electron pair, and the "base" is a Lewis base which refers to any species capable of donating an electron pair into a vacant orbital in a Lewis acid. In principle, hard Lewis acids prefer connecting with hard Lewis bases, while soft Lewis acids prefer soft Lewis bases. Furthermore, the key parameters like the amount of the precursors, ligands and solvents as well as the reaction time and temperature can be tuned to control the size distribution, composition and morphology.

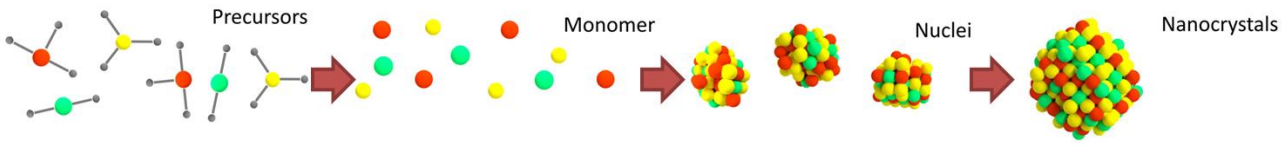

Figure 1.8. Scheme of the mechanism of colloidal synthesis.

Among the noble-metal free electrocatalysts, transition metal phosphides are commonly synthesized by colloidal synthesis. For example, Huang *et al.* reported the synthesis of Co_2P nanorods by the thermal degradation of cobalt(II) acetate and triphenylphosphine in the presence of oleylamine.[94] The obtained Co_2P nanostructures have relatively narrow size and shape distributions, which are controlled by oleylamine, a popular capping ligand used in colloidal synthesis. Besides, parameters like the kinds and amount of precursors, reaction time and temperature are also changed to acquire cobalt phosphides with different phases, sizes and morphologies, and all of them show good properties in either HER or OER.[95-96] Except for cobalt phosphides, iron phosphides and nickel phosphides are also investigated with different phases, sizes and shapes to improve the

properties in electrocatalysis.[97-98]

Although the colloidal synthesis is a very effective route for the synthesis of high-quality nano scale electrocatalysts, some disadvantages still exist. For example, the main drawback of the samples from colloidal synthesis is the organic ligands on the surfaces since large amount of organic solvents and surfactants are used in most syntheses. Fortunately, these organic ligands can be removed by annealing or ligand stripping. Nowadays, this simple one-step synthesis has received great of interest in fabricating chalcogenides such as $Cu_{2-x}Se$,[99] WS_2,[100] ZnS[101] Ag_2S[102] and $MoS_{2(1-x)}Se_{2x}$[103] with precisely controlled sizes and morphologies. This trend indicates that the colloidal synthesis may be one of the effective routes for the controlled preparation of chalcogenide nanocrystals which have a big potential in economic noble metal-free electrocatalysts.

1.5.3 Hydrothermal/Solvothermal Method

Hydrothermal/Solvothermal method has been used in nanotechnology for a long time to fabricate different kinds of materials applied in different fields. The scheme of this method is to create a sealed environment with high pressure and high temperature by special reaction vessels (for example Teflon-lined stainless steel autoclaves) for the monomers to promote the reaction. The only difference between hydrothermal method and solvothermal method is the solvents used. For hydrothermal method, H_2O is used to mix all the precursors, and the temperature is usually higher than 100 °C to sustain the pressure by the vapor from H_2O. A big advantage of using H_2O as solvent is some hydrophilic coordinating molecules like polyvinylpyrrolidone (PVP) can disperse in the mixture well to adjust the growth of the materials. In the field of noble metal-free electrocatalysts, this method is widely applied to synthesize transition metal compounds with different sizes, shapes and compositions including oxides/hydroxides,[104-106] chalcogenides,[107-108] phosphides,[109-110] nitrides, carbides, borides and so on. Except for H_2O, other organic solvents can be also chosen if the reactants are hydrophobic like long-chain ligands. Another difference of solvothermal method from hydrothermal process is that with the organic solvents the reaction temperature can be higher than that in hydrothermal method (usually 100-250 °C), so some reactions requiring high temperature can be performed. By solvothermal method, a wide range of electrocatalysts can be also fabricated like lamellar mesostructured $CoSe_2$ nanobelts,[111] CoP hollow microspheres,[112] Mo_2C microwires,[113] porous $NiCo_2S_4$ mircoflowers[77] and so on. Moreover, mixed solvent method is also applied based on the physical and chemical properties of the reagents. Actually, from the above examples it is not hard to notice that by hydrothermal/solvothermal method, the particles are usually on micro scale, and the size distribution is not easy to control (can be from nanoscale to microscale). Besides, the nucleation and growth process are not as clear as that of the colloidal synthesis. Because of the sealed “black box” system, the actual parameters like reaction temperature

and pressure are uncertain, thus the production of controllable nanoparticles is more dependent on experience.

1.5.4 Electrodeposition Method

Electrodeposition method is a widely used process for making films with high quality, and these films are usually constructed by nanoparticles. In general, the electrochemical process is made use of to attract the target ions to from the electrolyte to form specific nanomaterials including metals or metal compounds. The nucleation and growth step in electrodeposition are determined by several parameters. According to the literature, high cathode overpotential, high amount of adsorbed atoms on the substrate and low migration rate of the adsorbed atoms on the surface can cause a large amount of the formation of the crystal nucleus and hindrance of the growth thus resulting in particles with smaller size. Using electrodeposition method, a lot of interesting electrocatalysts are synthesized such as $Co(OH)_2$ nanosheets covered by polyaniline[114], Co-C-N film[115] and so on for HER, and Ni borate film,[116] Mn oxide films with different phases,[117] Ni_3Se_2 film[65] and so on for OER. However, the disadvantage is also apparent for this method: the voltage and the current are not stable enough to make materials with uniform structure, composition or morphology, which may influence the properties of the productions.

1.5.5 Chemical Vapor Deposition (CVD) Method

Different from the above methods which happen in liquid phase, CVD method is a kind of technique which the reaction happens between the solid precursor and the specific vapor. Basically three steps are included in the method: the formation of volatile substance, the transfer of the volatile substance and the reaction on the solid precursor. To synthesize transition metal compounds with this method, the ordinary route is to prepare metals or metal oxides as the solid precursor while the nonmetallic anions are vaporized from the simple substance (for example S and Se) or thermal decomposition of the compounds containing the required elements (for example the N in NH_3). The electrocatalysts prepared by this method can be classified by the source of several mainly used volatile reactants, since the chemicals with relatively low sublimation point /boiling point or easy to decompose are always the favorable choice. Nowadays there are a plenty of reports about electrocatalysts synthesized by CVD method, and most of them are transition metal nitrides from NH_3,[118] sulfides from H_2S,[119-120] selenides from Se powder.[121] Moreover, by partial reaction with the original materials, some heterostructures can be obtained like MoS_2-MoO_3 core-shell microwires.[119] It should be noticed that although the temperature for producing the vapor may be not so high, the temperature for the solid-vapor reaction can arrange from 400-800 °C. Under this temperature arrangement, the size of the materials is always on micro scale. Besides, the reaction speed is slow

comparing to other methods, which limits its application.

1.5.6 Other Synthesis Methods

Except for the above mentioned main groups, some other methods for nanomaterials are also reported for the synthesis of transition compounds electrocatalysts. For instance, Du *et al.* reported a template-assisted synthesis of CoP nanotubes for HER.[122] Zhang *et al.* obtained Co-Mo-N porous fil by N_2-plasma-activation method,[123] Zhang et al. constructed a hybrid of cobalt encapsulated by N, B codoped ultrathin carbon cages constructed by a bottom-up approach using metal organic frameworks.[124] All these methods provide new possibilities in synthesis of transition metal compounds in electrocatalysis.

Meanwhile, in order to obtain materials with better performance, scientists have designed combinations of several methods to fabricate electrocatalysts with better control of compositions, structures or morphologies.[125-127] These strategies are helpful to improve the properties but at the same time the multisteps increase the risk of reproduction and difficulty in synthesis of the materials.

1.6 Topic Basis & Thesis Structure

Based on the introduction in the above sections, in this thesis, different types of noble metal-free electrocatalysts for HER and OER are designed and synthesized. The colloidal synthesis is applied for fabricating the electrocatalysts with wanted modification. These catalysts are tested under different experimental conditions to research the electrochemical water splitting properties to prove their catalytic ability and stability in different electrolytes. Furthermore, the influence of the experimental factors and the mechanism behind the electrcatalytic reaction are studied to better understand the electrocatalytic water splitting system. Most important of all, the research on these noble metal-free electrocatalysts has great significance in relieving the energy crisis we are facing now.

In the third chapter, we explored the synthesis of binary and ternary transition metal chalcogenides (NiSe, CoSe and Ni-Co-Se) by colloidal synthesis. Via trying different parameters, we found the influence of these parameters on the structure and morphology. The experience from these trials are significant on the next design of fabrication of different kinds of transition metal chalcogenides electrocatalysts. Based on this experience, the experimental parameters are tuned to obtain the target samples. Then the electrochemical test was done for a group of samples with different Ni/Co ratio and the mechanism was studied.

In the fourth chapter, we alloyed the anions to make quaternary transition metal chalcogenides (Ni-Co-S-Se) and tested the electrocatalytic properties. By doing high resolution

transmission electron microscopy (HRTEM) characterization, we found that the quaternary system contains a lot of defects inside the nanoparticles, which may be the reason of the superb electrocatalytic performance.

In the fifth chapter, we used doping method and synthesized Ru doped CoSe NCs since Ru is a relatively cheaper one among the noble metals. The electrochemical test shows that with Ru dopant, the HER performance is improved dramatically, and the further analysis reveals that the addition of Ru improved the charge transfer speed thus improved the HER activity.

In the sixth chapter, we summarized the results of the previous experiments and provided the perspective of the development of inexpensive electrocatalysts for HER and OER.

References

1. Lewis, N. S.; Nocera, D. G. Powering the Planet: Chemical Challenges in Solar Energy Utilization. *Proc. Natl. Acad. Sci. U. S. A.* **2006,** *103*, 15729-35.
2. Coelho, B.; Oliveira, A. C.; Mendes, A. Concentrated Solar Power for Renewable Electricity and Hydrogen Production from Water—a Review. *Energy Environ. Sci.* **2010,** *3*, 1398-1405.
3. Walter, M. G.; Warren, E. L.; McKone, J. R.; Boettcher, S. W.; Mi, Q.; Santori, E. A.; Lewis, N. S. Solar Water Splitting Cells. *Chem. Rev.* **2010,** *110*, 6446-6473.
4. Yang, M. Q.; Wang, J.; Wu, H.; Ho, G. W. Noble Metal-Free Nanocatalysts with Vacancies for Electrochemical Water Splitting. *Small* **2018,** *14*, e1703323.
5. Conwaya, B. E.; Tilak, B. V. Interfacial Processes Involving Electrocatalytic Evolution and Oxidation of H_2, and the Role of Chemisorbed H. *Electrochim. Acta* **2002,** *47*, 3571-3594.
6. Faber, M. S.; Jin, S. Earth-Abundant Inorganic Electrocatalysts and Their Nanostructures for Energy Conversion Applications. *Energy Environ. Sci.* **2014,** *7*, 3519-3542.
7. Mom, R. V.; Cheng, J.; Koper, M. T. M.; Sprik, M. Modeling the Oxygen Evolution Reaction on Metal Oxides: The Infuence of Unrestricted DFT Calculations. *J. Phys. Chem. C* **2014,** *118*, 4095-4102.
8. Suen, N. T.; Hung, S. F.; Quan, Q.; Zhang, N.; Xu, Y. J.; Chen, H. M. Electrocatalysis for the Oxygen Evolution Reaction: Recent Development and Future Perspectives. *Chem. Soc. Rev.* **2017,** *46*, 337-365.
9. Fabbri, E.; Habereder, A.; Waltar, K.; Kötz, R.; Schmidt, T. J. Developments and Perspectives of Oxide-Based Catalysts for the Oxygen Evolution Reaction. *Catal. Sci. Technol.* **2014,** *4*, 3800-3821.
10. Man, I. C.; Su, H.-Y.; Calle-Vallejo, F.; Hansen, H. A.; Martínez, J. I.; Inoglu, N. G.; Kitchin, J.; Jaramillo, T. F.; Nørskov, J. K.; Rossmeisl, J. Universality in Oxygen Evolution Electrocatalysis on Oxide Surfaces. *ChemCatChem* **2011,** *3*, 1159-1165.
11. Bard, A. J.; Faulkner, L. R. Electrochemical Methods.
12. Shi, Y.; Zhang, B. Recent Advances in Transition Metal Phosphide Nanomaterials: Synthesis and Applications in Hydrogen Evolution Reaction. *Chem. Soc. Rev.* **2016,** *45*, 1529-41.
13. Zhu, Y. P.; Xu, X.; Su, H.; Liu, Y. P.; Chen, T.; Yuan, Z. Y. Ultrafine Metal Phosphide Nanocrystals in Situ Decorated on Highly Porous Heteroatom-Doped Carbons for Active Electrocatalytic Hydrogen Evolution. *ACS Appl. Mater. Interfaces* **2015,** *7*, 28369-76.
14. Gorlin, Y.; Jaramillo, T. F. A Bifunctional Nonprecious Metal Catalyst for Oxygen Reduction and Water Oxidation. *J. Am. Chem. Soc.* **2010,** *132*, 13612-13614.
15. Ding, Q.; Song, B.; Xu, P.; Jin, S. Efficient Electrocatalytic and Photoelectrochemical Hydrogen Generation Using MoS_2 and Related Compounds. *Chem* **2016,** *1*, 699-726.
16. Markovic, N. M.; B. N. Grgur; Ross, P. N. Temperature-Dependent Hydrogen Electrochemistry on

Platinum Low-Index Single-Crystal Surfaces in Acid Solutions. *J. Phys. Chem. B* **1997,** *101*, 5405-5413.
17. Zhang, T.; Anderson, A. B. Oxygen Reduction on Platinum Electrodes in Base: Theoretical Study. *Electrochim. Acta* **2007,** *53*, 982-989.
18. Durst, J.; Siebel, A.; Simon, C.; Hasché, F.; Herranz, J.; Gasteiger, H. A. New Insights into the Electrochemical Hydrogen Oxidation and Evolution Reaction Mechanism. *Energy Environ. Sci.* **2014,** *7*, 2255-2260.
19. Lamy-Pitara, E.; Barbier, J. The Electrocatalytic Reactions of Oxidation and Evolution of Hydrogen on Iridium Electrodes Modified by Sulphur Adsorption. *J. Electroanal. Chem.* **1996,** *416*, 47-51.
20. Xu, Y. The Hydrogen Evolution Reaction on Single Crystal Gold Electrode. *International Journal of Hydrogen Energy* **2009,** *34*, 77-83.
21. McCoustra, M. R. Water at Interfaces. *Phys. Chem. Chem. Phys.* **2008,** *10*, 4676-7.
22. Duan, J.; Chen, S.; Vasileff, A.; Qiao, S. Z. Anion and Cation Modulation in Metal Compounds for Bifunctional Overall Water Splitting. *ACS Nano* **2016,** *10*, 8738-45.
23. Greeley, J.; Norskov, J. K.; Kibler, L. A.; El-Aziz, A. M.; Kolb, D. M. Hydrogen Evolution over Bimetallic Systems: Understanding the Trends. *Chemphyschem* **2006,** *7*, 1032-5.
24. Esposito, D. V.; Chen, J. G. Monolayer Platinum Supported on Tungsten Carbides as Low-Cost Electrocatalysts: Opportunities and Limitations. *Energy Environ. Sci.* **2011,** *4*, 3900-3912.
25. Greeley, J.; Jaramillo, T. F.; Bonde, J.; Chorkendorff, I. B.; Norskov, J. K. Computational High-Throughput Screening of Electrocatalytic Materials for Hydrogen Evolution. *Nat. Mater.* **2006,** *5*, 909-13.
26. Kibler, L. A.; El-Aziz, A. M.; Hoyer, R.; Kolb, D. M. Tuning Reaction Rates by Lateral Strain in a Palladium Monolayer. *Angew. Chem., Int. Ed.* **2005,** *44*, 2080-2084.
27. Mavrikakis, M.; Hammer, B.; Nørskov, J. K. Effect of Strain on the Reactivity of Metal Surfaces. *Phys. Rev. Lett.* **1998,** *81*, 2819-2822.
28. Wu, M.; Ma, T. Platinum-Free Catalysts as Counter Electrodes in Dye-Sensitized Solar Cells. *ChemSusChem* **2012,** *5*, 1343-57.
29. Greeley, J.; Stephens, I. E.; Bondarenko, A. S.; Johansson, T. P.; Hansen, H. A.; Jaramillo, T. F.; Rossmeisl, J.; Chorkendorff, I.; Norskov, J. K. Alloys of Platinum and Early Transition Metals as Oxygen Reduction Electrocatalysts. *Nat Chem* **2009,** *1*, 552-6.
30. Jaksic, M. M. Hypo–Hyper-D-Electronic Interactive Nature of Interionic Synergism in Catalysis and Electrocatalysis for Hydrogen Reactions. *Int. J. Hydrogen Energy* **2001,** *26*, 559-578.
31. Highfield, J. G.; Claude, E.; Oguro, K. Electrocatalytic Synergism in Ni/Mo Cathodes for Hydrogen Evolution in Acid Medium: A New Model. *Electrochim. Acta* **1999,** *44*, 2805-2814.
32. Brooman, E. W.; Kuhn, A. T. Correlations between the Rate of the Hydrogen Electrode Reaction and the Properties of Alloys. *Elecytoanalytical Chemtstry and Interficial Electrochemistry* **1974,** *49*, 325-353.
33. Navarro-Flores, E.; Chong, Z.; Omanovic, S. Characterization of Ni, NiMo, NiW and NiFe Electroactive Coatings as Electrocatalysts for Hydrogen Evolution in an Acidic Medium. *J. Mol. Catal. A: Chem.* **2005,** *226*, 179-197.
34. Brown, D. E.; Mahmood, M. N.; Man, M. C. M.; Turner, A. K. Preparation and Characterization of Low Overvoltage Transition Metal Alloy Electrocatalysts for Hydrogen Evolution in Alkaline Solutions. *Electrochim. Acta* **1984,** *29*, 1551-1556.
35. Conway, B. E.; Bai, L. H_2 Evolution Kinetics at High Activity Ni-Mo-Cd Electrocoated Cathodes and Its Relation to Potential Dependence of Sorption of H*. *Int. J. Hydrogen Energy* **1986,** *11*, 533-540.
36. Nocera, D. G. The Artificial Leaf. *Accounts of Chemical Resesarch* **2012,** *45*, 767–776.
37. Reece, S. Y.; Hamel, J. A.; Sung, K.; Jarvi, T. D.; Esswein, A. J.; Pijpers, J. J. H.; Nocera, D. G. Wireless Solar Water Splitting Using Silicon-Based Semiconductors and Earth-Abundant Catalysts. *Science* **2011**, 645-648.
38. Raj, I. A. Nickel Based Composite Electrolytic Surface Coatings as Electrocatalysts for the Cathodes in the Energy Efficient Industrial Production of Hydrogen from Alkaline Water Electrolytic Cells. *Int. J. Hydrogen Energy* **1992,** *17*, 413-421.
39. Nørskov, J. K.; Bligaard, T.; Logadottir, A.; Kitchin, J. R.; Chen, J. G.; Pandelov, S.; Stimming, U. Trends in the Exchange Current for Hydrogen Evolution. *J. Electrochem. Soc.* **2005,** *152*, J23–J26.
40. Chen, Z.; Higgins, D.; Yu, A.; Zhang, L.; Zhang, J. A Review on Non-Precious Metal Electrocatalysts for

Pem Fuel Cells. *Energy Environ. Sci.* **2011,** *4*, 3167-3192.
41. Gong, M.; Zhou, W.; Tsai, M. C.; Zhou, J.; Guan, M.; Lin, M. C.; Zhang, B.; Hu, Y.; Wang, D. Y.; Yang, J.; Pennycook, S. J.; Hwang, B. J.; Dai, H. Nanoscale Nickel Oxide/Nickel Heterostructures for Active Hydrogen Evolution Electrocatalysis. *Nat. Commun.* **2014,** *5*, 4695.
42. Jin, H.; Wang, J.; Su, D.; Wei, Z.; Pang, Z.; Wang, Y. In Situ Cobalt-Cobalt Oxide/N-Doped Carbon Hybrids as Superior Bifunctional Electrocatalysts for Hydrogen and Oxygen Evolution. *J. Am. Chem. Soc.* **2015,** *137*, 2688-94.
43. Hinnemann, B.; Moses, P. G.; Bonde, J.; Jørgensen, K. P.; Nielsen, J. H.; Horch, S.; Chorkendorff, I.; Nørskov, J. K. Biomimetic Hydrogen Evolution: MoS_2 Nanoparticles as Catalyst for Hydrogen Evolution. *J. Am. Chem. Soc.* **2005,** *127*, 5308-5309.
44. Tributsh, H.; Bennett, J. C. Electrochemistry and Photochemistry of MoS_2 Layer Crystals. *J. Electroanal. Chem.* **1977,** *81*, 97-111.
45. Tsai, C.; Chan, K.; Abild-Pedersen, F.; Norskov, J. K. Active Edge Sites in $MoSe_2$ and WSe_2 Catalysts for the Hydrogen Evolution Reaction: A Density Functional Study. *Phys. Chem. Chem. Phys.* **2014,** *16*, 13156-64.
46. Wang, H.; Kong, D.; Johanes, P.; Cha, J. J.; Zheng, G.; Yan, K.; Liu, N.; Cui, Y. $MoSe_2$ and WSe_2 Nanofilms with Vertically Aligned Molecular Layers on Curved and Rough Surfaces. *Nano Lett.* **2013,** *13*, 3426-33.
47. Huang, X.; Zeng, Z.; Zhang, H. Metal Dichalcogenide Nanosheets: Preparation, Properties and Applications. *Chem. Soc. Rev.* **2013,** *42*, 1934-46.
48. Anantharaj, S.; Ede, S. R.; Sakthikumar, K.; Karthick, K.; Mishra, S.; Kundu, S. Recent Trends and Perspectives in Electrochemical Water Splitting with an Emphasis on Sulfide, Selenide, and Phosphide Catalysts of Fe, Co, and Ni: A Review. *ACS Catal.* **2016,** *6*, 8069-8097.
49. Kong, D.; Cha, J. J.; Wang, H.; Lee, H. R.; Cui, Y. First-Row Transition Metal Dichalcogenide Catalysts for Hydrogen Evolution Reaction. *Energy Environ. Sci.* **2013,** *6*, 3553-3558.
50. Wirth, S.; Harnisch, F.; Weinmann, M.; Schröder, U. Comparative Study of IVB–VIB Transition Metal Compound Electrocatalysts for the Hydrogen Evolution Reaction. *Appl. Catal., B* **2012,** *126*, 225-230.
51. Zeng, M.; Li, Y. Recent Advances in Heterogeneous Electrocatalysts for the Hydrogen Evolution Reaction. *J. Mater. Chem. A* **2015,** *3*, 14942-14962.
52. A. Damjanovic; A. Dey, I.; Bockris, J. O. M. Electrode Kinetics of Oxygen Evolution and Dissolution on Rh, Ir, and Pt-Rh Alloy Electrodes. *J. Electrochem. Soc.* **1966,** *113*, 739-746.
53. Frydendal, R.; Paoli, E. A.; Knudsen, B. P.; Wickman, B.; Malacrida, P.; Stephens, I. E. L.; Chorkendorff, I. Benchmarking the Stability of Oxygen Evolution Reaction Catalysts: The Importance of Monitoring Mass Losses. *ChemElectroChem* **2014,** *1*, 2075-2081.
54. Rossmeisl, J.; Qu, Z. W.; Zhu, H.; Kroes, G. J.; Nørskov, J. K. Electrolysis of Water on Oxide Surfaces. *J. Electroanal. Chem.* **2007,** *607*, 83-89.
55. Lee, Y.; Suntivich, J.; May, K. J.; Perry, E. E.; Shao-Horn, Y. Synthesis and Activities of Rutile IrO_2 and RuO_2 Nanoparticles for Oxygen Evolution in Acid and Alkaline Solutions. *J. Phys. Chem. Lett.* **2012,** *3*, 399-404.
56. Zhu, W.; Yue, X.; Zhang, W.; Yu, S.; Zhang, Y.; Wang, J.; Wang, J. Nickel Sulfide Microsphere Film on Ni Foam as an Efficient Bifunctional Electrocatalyst for Overall Water Splitting. *Chem. Commun. (Cambridge, U. K.)* **2016,** *52*, 1486-9.
57. Xia, C.; Jiang, Q.; Zhao, C.; Hedhili, M. N.; Alshareef, H. N. Selenide-Based Electrocatalysts and Scaffolds for Water Oxidation Applications. *Adv. Mater.* **2016,** *28*, 77-85.
58. Mabayoje, O.; Shoola, A.; Wygant, B. R.; Mullins, C. B. The Role of Anions in Metal Chalcogenide Oxygen Evolution Catalysis: Electrodeposited Thin Films of Nickel Sulfide as “Pre-Catalysts”. *ACS Energy Lett.* **2016,** *1*, 195-201.
59. Xu, X.; Song, F.; Hu, X. A Nickel Iron Diselenide-Derived Efficient Oxygen-Evolution Catalyst. *Nat. Commun.* **2016,** *7*, 12324.
60. McKendry, I. G.; Thenuwara, A. C.; Sun, J.; Peng, H.; Perdew, J. P.; Strongin, D. R.; Zdilla, M. J. Water Oxidation Catalyzed by Cobalt Oxide Supported on the Mattagamite Phase of $CoTe_2$. *ACS Catal.* **2016,** *6*, 7393-7397.
61. Yang, J.; Zhu, G.; Liu, Y.; Xia, J.; Ji, Z.; Shen, X.; Wu, S. Fe_3O_4-Decorated Co_9S_8 Nanoparticles in Situ

Grown on Reduced Graphene Oxide: A New and Efficient Electrocatalyst for Oxygen Evolution Reaction. *Adv. Funct. Mater.* **2016,** *26*, 4712-4721.
62. Zheng, Y. R.; Gao, M. R.; Gao, Q.; Li, H. H.; Xu, J.; Wu, Z. Y.; Yu, S. H. An Efficient CeO_2/$CoSe_2$ Nanobelt Composite for Electrochemical Water Oxidation. *Small* **2015,** *11*, 182-8.
63. Liu, Y.; Cheng, H.; Lyu, M.; Fan, S.; Liu, Q.; Zhang, W.; Zhi, Y.; Wang, C.; Xiao, C.; Wei, S.; Ye, B.; Xie, Y. Low Overpotential in Vacancy-Rich Ultrathin $CoSe_2$ Nanosheets for Water Oxidation. *J. Am. Chem. Soc.* **2014,** *136*, 15670-5.
64. Luo, P.; Zhang, H.; Liu, L.; Zhang, Y.; Deng, J.; Xu, C.; Hu, N.; Wang, Y. Targeted Synthesis of Unique Nickel Sulfide (NiS, NiS_2) Microarchitectures and the Applications for the Enhanced Water Splitting System. *ACS Appl. Mater. Interfaces* **2017,** *9*, 2500-2508.
65. Swesi, A. T.; Masud, J.; Nath, M. Nickel Selenide as a High-Efficiency Catalyst for Oxygen Evolution Reaction. *Energy Environ. Sci.* **2016,** *9*, 1771-1782.
66. Liu, Y.; Xiao, C.; Lyu, M.; Lin, Y.; Cai, W.; Huang, P.; Tong, W.; Zou, Y.; Xie, Y. Ultrathin Co_3S_4 Nanosheets That Synergistically Engineer Spin States and Exposed Polyhedra That Promote Water Oxidation under Neutral Conditions. *Angew. Chem., Int. Ed. Engl.* **2015,** *54*, 11231-5.
67. Ouyang, C.; Wang, X.; Wang, C.; Zhang, X.; Wu, J.; Ma, Z.; Dou, S.; Wang, S. Hierarchically Porous Ni_3S_2 Nanorod Array Foam as Highly Efficient Electrocatalyst for Hydrogen Evolution Reaction and Oxygen Evolution Reaction. *Electrochim. Acta* **2015,** *174*, 297-301.
68. Wang, H.; Tang, J.; Li, Y.; Chu, H.; Ge, Y.; Baines, R.; Dong, P.; Ajayan, P. M.; Shen, J.; Ye, M. Template-Free Solvothermal Preparation of Ternary $FeNi_2S_4$ Hollow Balloons as RuO_2-Like Efficient Electrocatalysts for the Oxygen Evolution Reaction with Superior Stability. *J. Mater. Chem. A* **2018,** *6*, 19417-19424.
69. Dong, Q.; Zhang, Y.; Dai, Z.; Wang, P.; Zhao, M.; Shao, J.; Huang, W.; Dong, X. Graphene as an Intermediary for Enhancing the Electron Transfer Rate: A Free-Standing Ni_3S_2@Graphene@Co_9S_8 Electrocatalytic Electrode for Oxygen Evolution Reaction. *Nano Res.* **2018,** *11*, 1389-1398.
70. Xu, Y.-Z.; Yuan, C.-Z.; Chen, X.-P. Co-Doped Nise Nanowires on Nickel Foam Via a Cation Exchange Approach as Efficient Electrocatalyst for Enhanced Oxygen Evolution Reaction. *RSC Adv.* **2016,** *6*, 106832-106836.
71. Li, J.; Liu, G.; Liu, B.; Min, Z.; Qian, D.; Jiang, J.; Li, J. Fe-Doped $CoSe_2$ Nanoparticles Encapsulated in N-Doped Bamboo-Like Carbon Nanotubes as an Efficient Electrocatalyst for Oxygen Evolution Reaction. *Electrochim. Acta* **2018,** *265*, 577-585.
72. Hou, Y.; Qiu, M.; Nam, G.; Kim, M. G.; Zhang, T.; Liu, K.; Zhuang, X.; Cho, J.; Yuan, C.; Feng, X. Integrated Hierarchical Cobalt Sulfide/Nickel Selenide Hybrid Nanosheets as an Efficient Three-Dimensional Electrode for Electrochemical and Photoelectrochemical Water Splitting. *Nano Lett.* **2017,** *17*, 4202-4209.
73. Ma, Z.; Zhao, Q.; Li, J.; Tang, B.; Zhang, Z.; Wang, X. Three-Dimensional Well-Mixed / Highly-Densed NiS-CoS Nanorod Arrays: An Efficient and Stable Bifunctional Electrocatalyst for Hydrogen and Oxygen Evolution Reactions. *Electrochim. Acta* **2018,** *260*, 82-91.
74. Han, X.; Tong, X.; Wu, G.; Yang, N.; Guo, X.-Y. Carbon Fibers Supported NiSe Nanowire Arrays as Efficient and Flexible Electrocatalysts for the Oxygen Evolution Reaction. *Carbon* **2018,** *129*, 245-251.
75. Umapathi, S.; Masud, J.; Swesi, A. T.; Nath, M. $FeNi_2Se_4$-Reduced Graphene Oxide Nanocomposite: Enhancing Bifunctional Electrocatalytic Activity for Oxygen Evolution and Reduction through Synergistic Effects. *Adv. Sustainable Syst.* **2017,** *1*, 1700086.
76. Shinde, D. V.; Trizio, L. D.; Dang, Z.; Prato, M.; Gaspari, R.; Manna, L. Hollow and Porous Nickel Cobalt Perselenide Nanostructured Microparticles for Enhanced Electrocatalytic Oxygen Evolution. *Chem. Mater.* **2017,** *29*, 7032-7041.
77. Jiang, J.; Yan, C.; Zhao, X.; Luo, H.; Xue, Z.; Mu, T. A Pegylated Deep Eutectic Solvent for Controllable Solvothermal Synthesis of Porous $NiCo_2S_4$ for Efficient Oxygen Evolution Reaction. *Green Chem.* **2017,** *19*, 3023-3031.
78. Chi, J.-Q.; Yan, K.-L.; Xiao, Z.; Dong, B.; Shang, X.; Gao, W.-K.; Li, X.; Chai, Y.-M.; Liu, C.-G. Trimetallic Ni-Fe-Co Selenides Nanoparticles Supported on Carbon Fiber Cloth as Efficient Electrocatalyst for Oxygen Evolution Reaction. *Int. J. Hydrogen Energy* **2017,** *42*, 20599-20607.
79. Ryu, J.; Jung, N.; Jang, J. H.; Kim, H.-J.; Yoo, S. J. In Situ Transformation of Hydrogen-Evolving CoP Nanoparticles: Toward Efficient Oxygen Evolution Catalysts Bearing Dispersed Morphologies with Co-

Oxo/Hydroxo Molecular Units. *ACS Catal.* **2015,** *5*, 4066-4074.
80. Stern, L.-A.; Feng, L.; Song, F.; Hu, X. Ni_2P as a Janus Catalyst for Water Splitting: The Oxygen Evolution Activity of Ni2p Nanoparticles. *Energy Environ. Sci.* **2015,** *8*, 2347-2351.
81. Chen, P.; Xu, K.; Tong, Y.; Li, X.; Tao, S.; Fang, Z.; Chu, W.; Wu, X.; Wu, C. Cobalt Nitrides as a Class of Metallic Electrocatalysts for the Oxygen Evolution Reaction. *Inorg. Chem. Front.* **2016,** *3*, 236-242.
82. Yuan, C.-Z.; Jiang, Y.-F.; Wang, Z.; Xie, X.; Yang, Z.-K.; Yousaf, A. B.; Xu, A.-W. Cobalt Phosphate Nanoparticles Decorated with Nitrogen-Doped Carbon Layers as Highly Active and Stable Electrocatalysts for the Oxygen Evolution Reaction. *J. Mater. Chem. A* **2016,** *4*, 8155-8160.
83. Xiong, X.; Ji, Y.; Xie, M.; You, C.; Yang, L.; Liu, Z.; Asiri, A. M.; Sun, X. MnO_2-CoP_3 Nanowires Array: An Efficient Electrocatalyst for Alkaline Oxygen Evolution Reaction with Enhanced Activity. *Electrochem. Commun.* **2018,** *86*, 161-165.
84. Mendoza-Garcia, A.; Su, D.; Sun, S. Sea Urchin-Like Cobalt-Iron Phosphide as an Active Catalyst for Oxygen Evolution Reaction. *Nanoscale* **2016,** *8*, 3244-7.
85. Hu, F.; Zhu, S.; Chen, S.; Li, Y.; Ma, L.; Wu, T.; Zhang, Y.; Wang, C.; Liu, C.; Yang, X.; Song, L.; Yang, X.; Xiong, Y. Amorphous Metallic Nifep: A Conductive Bulk Material Achieving High Activity for Oxygen Evolution Reaction in Both Alkaline and Acidic Media. *Adv. Mater.* **2017,** *29*, 1606570.
86. Coleman, J. N.; Lotya, M.; O'Neill, A.; Bergin, S. D.; King, P. J.; Khan, U.; Young, K.; Gaucher, A.; De, S.; Smith, R. J.; Shvets, I. V.; Arora, S. K.; Stanton, G.; Kim, H.-Y.; Lee, K.; Kim, G. T.; Duesberg, G. S.; Hallam, T.; Boland, J. J.; Wang, J. J.; Donegan, J. F.; Grunlan, J. C.; Moriarty, G.; Shmeliov, A.; Nicholls, R. J.; Perkins, J. M.; Grieveson, E. M.; Theuwissen, K.; McComb, D. W.; Nellist, P. D.; Nicolosi, V. Two-Dimensional Nanosheets Produced by Liquid Exfoliation of Layered Materials. *Science* **2011,** *331*, 568-571.
87. Cunningham, G.; Lotya, M.; Cucinotta, C. S.; Sanvito, S.; Bergin, S. D.; Menzel, R.; Shaffer, M. S. P.; Coleman, J. N. Solvent Exfoliation of Transition Metal Dichalcogenides Dispersibility of Exfoliated Nanosheets Varies Only Weakly between Compounds. *ACS Nano* **2012,** *6*, 3468–3480.
88. Wang, T.; Liu, L.; Zhu, Z.; Papakonstantinou, P.; Hu, J.; Liu, H.; Li, M. Enhanced Electrocatalytic Activity for Hydrogen Evolution Reaction from Self-Assembled Monodispersed Molybdenum Sulfidenanoparticles on an Au Electrode. *Energy Environ. Sci.* **2013,** *6*, 625-633.
89. Zhou, K. G.; Mao, N. N.; Wang, H. X.; Peng, Y.; Zhang, H. L. A Mixed-Solvent Strategy for Efficient Exfoliation of Inorganic Graphene Analogues. *Angew. Chem., Int. Ed. Engl.* **2011,** *50*, 10839-42.
90. Wang, H.; Lu, Z.; Xu, S.; Kong, D.; Cha, J. J.; Zheng, G.; Hsu, P. C.; Yan, K.; Bradshaw, D.; Prinz, F. B.; Cui, Y. Electrochemical Tuning of Vertically Aligned MoS_2 Nanofilms and Its Application in Improving Hydrogen Evolution Reaction. *Proc. Natl. Acad. Sci. U. S. A.* **2013,** *110*, 19701-6.
91. Matte, H. S.; Gomathi, A.; Manna, A. K.; Late, D. J.; Datta, R.; Pati, S. K.; Rao, C. N. MoS_2 and WS_2 Analogues of Graphene. *Angew. Chem., Int. Ed. Engl.* **2010,** *49*, 4059-62.
92. Miremadi, B. K.; Morrison, S. R. Exfoliated Mos_2 for Stabilization and Activation of Pt Oxidation Catalysts. *J. Catal.* **1991,** *131*, 127-132.
93. C. B. Murray; D. J. Noms; Bawendi, M. G. Synthesis and Characterization of Nearly Monodisperse CdE (E = Sulfur, Selenium, Tellurium) Semiconductor Nanocrystallites. *J. Am. Chem. Soc.* **1993,** *115*, 8706-8715.
94. Huang, Z.; Chen, Z.; Chen, Z.; Lv, C.; Humphrey, M. G.; Zhang, C. Cobalt Phosphide Nanorods as an Efficient Electrocatalyst for the Hydrogen Evolution Reaction. *Nano Energy* **2014,** *9*, 373-382.
95. Popczun, E. J.; Roske, C. W.; Read, C. G.; Crompton, J. C.; McEnaney, J. M.; Callejas, J. F.; Lewis, N. S.; Schaak, R. E. Highly Branched Cobalt Phosphide Nanostructures for Hydrogen-Evolution Electrocatalysis. *J. Mater. Chem. A* **2015,** *3*, 5420-5425.
96. Popczun, E. J.; Read, C. G.; Roske, C. W.; Lewis, N. S.; Schaak, R. E. Highly Active Electrocatalysis of the Hydrogen Evolution Reaction by Cobalt Phosphide Nanoparticles. *Angew. Chem., Int. Ed. Engl.* **2014,** *53*, 5427-30.
97. Callejas, J. F.; McEnaney, J. M.; Read, C. G.; Chance Crompton; Biacchi, A. J.; Eric J. Popczun; Thomas R. Gordon; Nathan S. Lewis; Schaak, R. E. Electrocatalytic and Photocatalytic Hydrogen Production from Acidic and Neutral-pH Aqueous Solutions Using Iron Phosphide Nanoparticles. *ACS Nano* **2014,** *8*, 11101–11107.
98. Popczun, E. J.; McKone, J. R.; Read, C. G.; Biacchi, A. J.; Wiltrout, A. M.; Lewis, N. S.; Schaak, R. E.

Nanostructured Nickel Phosphide as an Electrocatalyst for the Hydrogen Evolution Reaction. *J. Am. Chem. Soc.* **2013,** *135*, 9267-70.

99. Shen, H.; Wang, H.; Yuan, H.; Ma, L.; Li, L. S. Size-, Shape-, and Assembly-Controlled Synthesis of $Cu_{2-x}Se$ Nanocrystalsvia a Non-Injection Phosphine-Free Colloidal Method. *CrystEngComm* **2012,** *14*, 555-560.

100. Wan, C.; Regmi, Y. N.; Leonard, B. M. Multiple Phases of Molybdenum Carbide as Electrocatalysts for the Hydrogen Evolution Reaction. *Angew. Chem., Int. Ed. Engl.* **2014,** *53*, 6407-10.

101. Zhao, Y.; Zhang, Y.; Zhu, H.; Hadjipanayis, G. C.; Xiao, J. Q. Low-Temperature Synthesis of Hexagonal (Wurtzite) ZnS Nanocrystals. *J. Am. Chem. Soc.* **2004,** *126*, 6874-6875.

102. Wang, D.; Hao, C.; Zheng, W.; Peng, Q.; Wang, T.; Liao, Z.; Yu, D.; Li, Y. Ultralong Single-Crystalline Ag_2S Nanowires: Promising Candidates for Photoswitches and Room-Temperature Oxygen Sensors. *Adv. Mater.* **2008,** *20*, 2628-2632.

103. Gong, Q.; Cheng, L.; Liu, C.; Zhang, M.; Feng, Q.; Ye, H.; Zeng, M.; Xie, L.; Liu, Z.; Li, Y. Ultrathin $MoS_{2(1-x)}Se_{2x}$ Alloy Nanoflakes for Electrocatalytic Hydrogen Evolution Reaction. *ACS Catal.* **2015,** *5*, 2213-2219.

104. Long, X.; Li, J.; Xiao, S.; Yan, K.; Wang, Z.; Chen, H.; Yang, S. A Strongly Coupled Graphene and FeNi Double Hydroxide Hybrid as an Excellent Electrocatalyst for the Oxygen Evolution Reaction. *Angew. Chem., Int. Ed. Engl.* **2014,** *53*, 7584-8.

105. Gong, M.; Dai, H. A Mini Review of NiFe-Based Materials as Highly Active Oxygen Evolution Reaction Electrocatalysts. *Nano Res.* **2014,** *8*, 23-39.

106. Lu, Z.; Xu, W.; Zhu, W.; Yang, Q.; Lei, X.; Liu, J.; Li, Y.; Sun, X.; Duan, X. Three-Dimensional NiFe Layered Double Hydroxide Film for High-Efficiency Oxygen Evolution Reaction. *Chem. Commun. (Cambridge, U. K.)* **2014,** *50*, 6479-82.

107. Tang, H.; Dou, K.; Kaun, C.-C.; Kuang, Q.; Yang, S. $MoSe_2$ Nanosheets and Their Graphene Hybrids: Synthesis, Characterization and Hydrogen Evolution Reaction Studies. *J. Mater. Chem. A* **2014,** *2*, 360-364.

108. Zhang, W.; Wang, Y.; Wang, Z.; Zhong, Z.; Xu, R. Highly Efficient and Noble Metal-Free NiS/CdS Photocatalysts for H_2 Evolution from Lactic Acid Sacrificial Solution under Visible Light. *Chem. Commun. (Cambridge, U. K.)* **2010,** *46*, 7631-3.

109. Xu, Y.; Wu, R.; Zhang, J.; Shi, Y.; Zhang, B. Anion-Exchange Synthesis of Nanoporous FeP Nanosheets as Electrocatalysts for Hydrogen Evolution Reaction. *Chem. Commun.* **2013,** *49*, 6656.

110. Zhou, D.; He, L.; Zhu, W.; Hou, X.; Wang, K.; Du, G.; Zheng, C.; Sun, X.; Asiri, A. M. Interconnected Urchin-Like Cobalt Phosphide Microspheres Film for Highly Efficient Electrochemical Hydrogen Evolution in Both Acidic and Basic Media. *J. Mater. Chem. A* **2016,** *4*, 10114-10117.

111. Gao, M.-R.; Yao, W.-T.; Yao, H.-B.; Yu, S.-H. Synthesis of Unique Ultrathin Lamellar Mesostructured $CoSe_2$-Amine (Protonated) Nanobelts in a Binary Solution. *J. Am. Chem. Soc.* **2009,** *131*, 7486-7487.

112. Liu, M.; Li, J. Cobalt Phosphide Hollow Polyhedron as Efficient Bifunctional Electrocatalysts for the Evolution Reaction of Hydrogen and Oxygen. *ACS Appl. Mater. Interfaces* **2016,** *8*, 2158-65.

113. Liao, L.; Wang, S.; Xiao, J.; Bian, X.; Zhang, Y.; Scanlon, M. D.; Hu, X.; Tang, Y.; Liu, B.; Girault, H. H. A Nanoporous Molybdenum Carbide Nanowire as an Electrocatalyst for Hydrogen Evolution Reaction. *Energy Environ. Sci.* **2014,** *7*, 387-392.

114. Feng, J. X.; Ding, L. X.; Ye, S. H.; He, X. J.; Xu, H.; Tong, Y. X.; Li, G. R. $Co(OH)_2$@PANI Hybrid Nanosheets with 3D Networks as High-Performance Electrocatalysts for Hydrogen Evolution Reaction. *Adv. Mater.* **2015,** *27*, 7051-7.

115. Wang, Z. L.; Hao, X. F.; Jiang, Z.; Sun, X. P.; Xu, D.; Wang, J.; Zhong, H. X.; Meng, F. L.; Zhang, X. B. C and N Hybrid Coordination Derived Co-C-N Complex as a Highly Efficient Electrocatalyst for Hydrogen Evolution Reaction. *J. Am. Chem. Soc.* **2015,** *137*, 15070-3.

116. Bediako, D. K.; Surendranath, Y.; Nocera, D. G. Mechanistic Studies of the Oxygen Evolution Reaction Mediated by a Nickel-Borate Thin Film Electrocatalyst. *J. Am. Chem. Soc.* **2013,** *135*, 3662-74.

117. Ramírez, A.; Hillebrand, P.; Stellmach, D.; May, M. M.; Bogdanoff, P.; Fiechter, S. Evaluation of MnO_x, Mn_2O_3, and Mn_3O_4 Electrodeposited Films for the Oxygen Evolution Reaction of Water. *J. Phys. Chem. C* **2014,** *118*, 14073-14081.

118. Cao, B.; Veith, G. M.; Neuefeind, J. C.; Adzic, R. R.; Khalifah, P. G. Mixed Close-Packed Cobalt

Molybdenum Nitrides as Non-Noble Metal Electrocatalysts for the Hydrogen Evolution Reaction. *J. Am. Chem. Soc.* **2013,** *135*, 19186-92.

119. Benck, J. D.; Hellstern, T. R.; Kibsgaard, J.; Chakthranont, P.; Jaramillo, T. F. Catalyzing the Hydrogen Evolution Reaction (Her) with Molybdenum Sulfide Nanomaterials. *ACS Catal.* **2014,** *4*, 3957-3971.

120. Xu, K.; FengmeiWang; ZhenxingWang; Zhan, X.; QishengWang; Cheng, Z.; Safdar, M.; He, J. Component-Controllable $WS_{2(1-X)}Se_{2x}$ Nanotubes for Efficient Hydrogen Evolution Reaction. *ACS Nano* **2014,** *8*, 8468-8476.

121. Kong, D.; Wang, H.; Lu, Z.; Cui, Y. $Cose_2$ Nanoparticles Grown on Carbon Fiber Paper: An Efficient and Stable Electrocatalyst for Hydrogen Evolution Reaction. *J. Am. Chem. Soc.* **2014,** *136*, 4897-900.

122. Du, H.; Liu, Q.; Cheng, N.; Asiri, A. M.; Sun, X.; Li, C. M. Template-Assisted Synthesis of CoP Nanotubes to Efficiently Catalyze Hydrogen-Evolving Reaction. *J. Mater. Chem. A* **2014,** *2*, 14812-14816.

123. Zhang, Y.; Ouyang, B.; Xu, J.; Chen, S.; Rawat, R. S.; Fan, H. J. 3D Porous Hierarchical Nickel-Molybdenum Nitrides Synthesized by Rf Plasma as Highly Active and Stable Hydrogen-Evolution-Reaction Electrocatalysts. *Adv. Energy Mater.* **2016,** *6*, 1600221.

124. Zhang, H.; Ma, Z.; Duan, J.; Liu, H.; Liu, G.; Wang, T.; Chang, K.; Li, M.; Shi, L.; Meng, X.; Wu, K.; Ye, J. Active Sites Implanted Carbon Cages in Core-Shell Architecture: Highly Active and Durable Electrocatalyst for Hydrogen Evolution Reaction. *ACS Nano* **2016,** *10*, 684-94.

125. Wang, D. Y.; Gong, M.; Chou, H. L.; Pan, C. J.; Chen, H. A.; Wu, Y.; Lin, M. C.; Guan, M.; Yang, J.; Chen, C. W.; Wang, Y. L.; Hwang, B. J.; Chen, C. C.; Dai, H. Highly Active and Stable Hybrid Catalyst of Cobalt-Doped FeS_2 Nanosheets-Carbon Nanotubes for Hydrogen Evolution Reaction. *J. Am. Chem. Soc.* **2015,** *137*, 1587-92.

126. Zheng, X.; Xu, J.; Yan, K.; Wang, H.; Wang, Z.; Yang, S. Space-Confined Growth of MoS_2 Nanosheets within Graphite: The Layered Hybrid of MoS_2 and Graphene as an Active Catalyst for Hydrogen Evolution Reaction. *Chem. Mater.* **2014,** *26*, 2344-2353.

127. Wu, Z.; Fang, B.; Wang, Z.; Wang, C.; Liu, Z.; Liu, F.; Wang, W.; Alfantazi, A.; Wang, D.; Wilkinson, D. P. MoS_2 Nanosheets: A Designed Structure with High Active Site Density for the Hydrogen Evolution Reaction. *ACS Catal.* **2013,** *3*, 2101-2107.

Chapter II Experimental Section

This chapter introduces the chemicals, methods and measurement techniques that have been employed to synthesize and test all the transition metal based compounds shown in this thesis.

2.1 Chemicals

The chemicals used in this thesis are all listed in Table 2.1. It should be mentioned that all the chemicals are used directly without any further treatment unless it is declared in the thesis.

Table 2.1. Reagents used in the synthesis.

Chemicals	Suppliers	Functions	Reactions applied
Nickel(II) chloride ($NiCl_2$, 98% purity)	Sigma Aldrich	Ni precursor	Colloidal synthesis
Nickel(II) acetylacetonate ($Ni(acac)_2$, 95% purity)	Sigma Aldrich	Ni precursor	
Cobalt(II) chloride ($CoCl_2$, 97% purity)	Sigma Aldrich	Co precursor	
Cobalt(II) bromide ($CoBr_2$, 99% purity)	Sigma Aldrich	Co precursor	
Cobalt(II) iodide (CoI_2, 95% purity)	Sigma Aldrich	Co precursor	
Cobalt(II) acetylacetonate ($Co(acac)_2$, 97% purity)	Sigma Aldrich	Co precursor	
Selenium powder (Se, 99.99% purity)	Alfa Aesar	Se precursor	
1-dodecanethiol (DDT, 98% purity)	Sigma Aldrich	S precursor	
Ruthenium(III) chloride ($RuCl_3$, Ru content, 40.00-49.00%)	Sigma Aldrich	Ru precursor	
1-octadecene (ODE, technical grade, 90%,)	Sigma Aldrich	Solvent	
Octyl ether (99% purity)	Sigma Aldrich	Solvent	
Oleylamine (OAm, 70% purity)	Sigma Aldrich	Surfactant	
Oleic acid (OAc, technical grade, 90% purity)	Sigma Aldrich	Surfactant	
Octadecyl phosphonic acid (ODPA, >99% purity)	PCI Synthesis	Surfactant	
Hexyl phosphonic acid (HPA, >99% purity)	PCI Synthesis	Surfactant	
Trioctylphosphine (TOP, 90% purity)	Sigma Aldrich	Surfactant	
Trioctylphosphine oxide (TOPO, 90%	Sigma Aldrich	Surfactant	

Chemicals	Suppliers	Functions	Reactions applied
purity)			
Toluene (99.7% purity)	Sigma Aldrich	Dispersant	
Ethanol (99.8% purity)	Sigma Aldrich	Precipitator/ Solvent	Colloidal synthesis/ Electrochemical measurement
Distilled water (H_2O)		Solvent/ Electrolyte	Electrochemical measurement
Potassium hydroxide (KOH, 86% purity)	Sigma Aldrich	Electrolyte	
Sulphuric acid (H_2SO_4, 95-98% purity)	Sigma Aldrich	Electrolyte	
Nafion® 117 solution (~5% in a mixture of lower aliphatic alcohols and water)	Sigma Aldrich	Dispersant	
Carbon black (99+% purity)	Alfa Aesar	Conductor	
Fluorine-doped tin oxide glass substrates (FTO, surface resistivity ~7 Ω/sq)*	Sigma Aldrich	Substrate	
Titanium foil (99.7% trace metals basis)*	Sigma Aldrich	Substrate	

* The substrates are immersed in isopropanol and acetone (1:1) for at least one day before using.

2.2 Characterization of Samples

X-ray Diffraction (XRD). XRD patterns were obtained using a PANalytical Empyrean X-ray diffractometer equipped with a 1.8 kW Cu Kα ceramic X-ray tube and a PIXcel3D 22 area detector operating at 45 kV and 40 mA. The diffraction patterns were collected in air at room temperature using parallel-beam geometry and symmetric reflection mode. All XRD samples were prepared by drop casting a concentrated solution of NCs on a zero-background quartz substrate. XRD patterns were processed by HighScore 4.1 software from PANalytical and they were compared to the powder diffraction database from the inorganic crystal structure database (ICSD).

Elemental Analysis. Detailed elemental analysis was carried out via inductively coupled plasma optical emission spectroscopy (ICP-OES) using an iCAP 6500 Thermo spectrometer. All chemical analyses performed by ICP-OES were affected by a systematic error of about 5%. The samples were decomposed overnight in aqua regia (the ratio of HCl to HNO_3 was 3:1 (v/v)) prior to the ICP measurements.

Electron Microscopy. The samples were prepared by dropping dilute solutions of NCs onto carbon film-coated 200 mesh copper grids for low-resolution transmission electron microscopy

(TEM) and ultrathin carbon/holey carbon coated 400 mesh copper grids for high resolution TEM (HRTEM). Low-resolution TEM measurements were carried out on a JEOL JEM-1011 transmission electron microscope operating at an acceleration voltage of 100 kV. HRTEM, selected area electron diffraction (SAED) analyses and energy dispersive spectroscopy (EDS) were performed on a JEOL JEM-2200FS microscope equipped with a Schottky emitter operating at 200 kV, a CEOS spherical aberration corrector for the objective lens, an in-column energy filter (Omega-type), and a Bruker Quantax 400 EDS system with an XFlash 5060 detector. Scanning electron microscopy (SEM) with energy-dispersive x-ray spectroscopy (EDS) analyses were performed on electrodes coated with a 10 nm gold layer using a FEI NanoLab 600 dual-beam system.

X-ray Photoelectron Spectroscopy (XPS). XPS analyses were performed on samples before and after OER, using a Kratos Axis Ultra^{DLD} spectrometer equipped with monochromatic Al Kα source operated at 15 kV and 20 mA. Survey scan analyses were carried out with an analysis area of 300×700 μm and a pass energy of 160 eV. High-resolution analyses were carried out with and the same analysis area and a pass energy of 20 eV. The Kratos charge neutralizer system was used on all specimens. Spectra have been charge corrected to the main line of the carbon 1s spectrum (adventitious carbon) set to 284.8 eV. Spectra were analyzed using CasaXPS software (version 2.3.17).

Thermogravimetric analysis (TGA). The data were acquired using TA TGA-Q500 V20.13 Build 39 thermogravimetric analyzer at a heating rate of 5 °C/min under slow nitrogen flow.

Fourier Transform Infrared Spectroscopy (FTIR) Analysis. The samples were obtained by mixing the dry powder with a KBr powder using a sample/KBr ratio of 1% in weight (i.e. 1 mg of NCs and 100 mg of KBr). The resulting mixture of powder was put in a die and pressed for 3 minutes with 3 Tons, producing a 12 mm diameter disk. The disks were analyzed using a FTIR Vertex 70v, running 128 scans per sample in the 4000-600 cm^{-1} range, with a resolution of 4 cm^{-1}.

2.3 Electrochemical Measurement

The inks used to prepare the electrodes have been prepared by dispersing colloidal NCs in different solvents with the desired concentration. These parameters can influence the performance of the electrocatalysts and their influence of the final performance will be discussed for each system. As regarding the electrolyte, 1 M KOH or 0.5 M H_2SO_4 solution were chosen as the two main electrolytes according to different measurements.

2.3.1 Mechanism of the Electrochemical Workstation

An electrochemical workstation performs as the machine to characterize the electrocatalytic properties.

An IVIUM Compactstat was used for all the measurements at room temperature (25 °C). Briefly, inside the workstation, there is a circuit with the combination of potentiostat, galvanometer and electrochemical alternating current (AC) impedance test system. Outside the sealed circuit, a three-electrode electrolytic cell is provided for the electrochemical analysis with a reference electrode (RE), a counter electrode (CE) and a working electrode (WE) (Figure 2.1a). Figure 2.1b illustrates a schematic view of a typical electrochemical measurement circuit made of an adjustable voltage source (V_S), an ammeter (A_M), a voltmeter (V_M) and an electrolytic cell. There are two circuits in the three-electrode system: one, composed of a WE and a RE, is used to measure the electrochemical reaction; the second one, made of a WE and a CE, serves to transfer the electrons in order to form an integrated circuit. The potential (E) between the WE and the RE is measured with the voltmeter, and the V_S is adjusted to maintain the desired potential at WE with respect to RE. The resulting current (i) flowing to or from WE is measured with the ammeter (A_M).

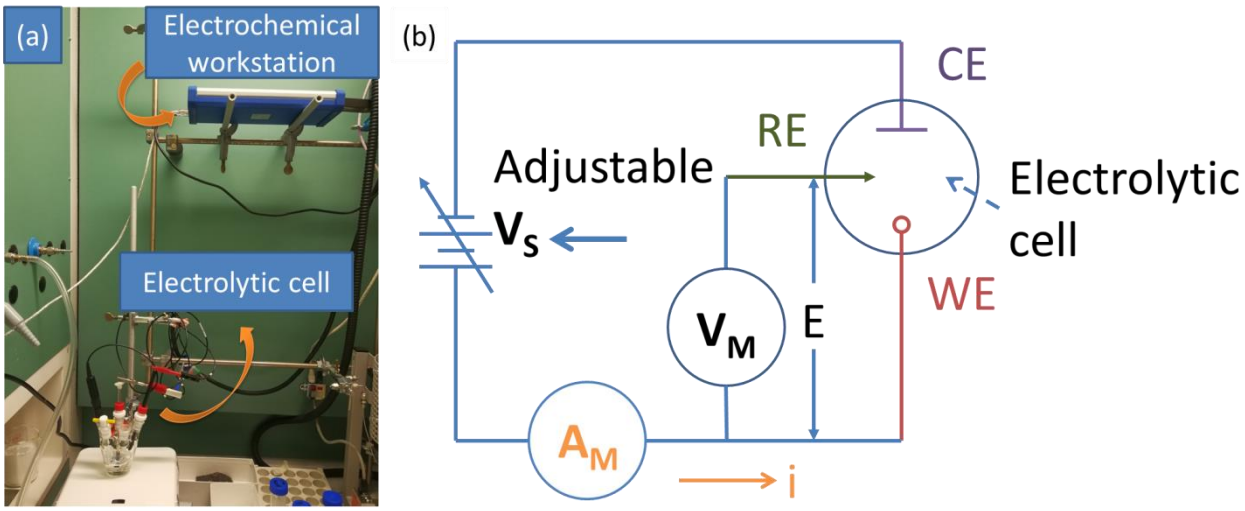

Figure 2.1. (a) The image of the electrochemical workstation. (b) A schematic representation of simplified measurement circuit of the electrochemical workstation.

Working electrode (WE). In electrocatalytic measurements, the electrodes composed of the active material (i.e. the samples under analysis) are called working electrodes. In this thesis, the WEs are made by drop casting the ink containing the NC electrocatalysts onto different substrates such as, FTO glasses or Ti foils, depending on different measurements.

Reference electrode (RE). The RE is an electrode used as a point of reference in the electrochemical cell for the potential control and measurement. Strictly speaking, the standard hydrogen electrode (SHE) is the primary standard electrode in electrochemistry, and the potential of SHE has already become the standard zero potential at all temperatures and a reference for all the

electrochemical oxidation and reduction half reactions. The concept of SHE is defined under ideal conditions: it is the electrode formed by platinized Pt electrode in an ideal solution with the hydrogen ion (H^+) activity of 1 M. In reality, the "solution with the hydrogen ion (H^+) activity of 1 M" does not exist. To avoid this strict requirement, a reversible hydrogen electrode (RHE) has replaced the SHE in recent years replaces becoming the well-accepted standard reference electrode.[1] It is related to the pH value and can be calculated by Nernst equation:

$E_{RHE} = E_{SHE}(0) - 0.059 \times pH$ (at 25 °C)

However, considering that the RHE is also hard to achieve during the actual measurement, some other electrodes which are stable are actually used as RE for evaluating the potential of the WE. First of all, the potential of these REs is precisely confirmed compared to the RHE. Then by comparing the potential difference of the RE with the WE, the potential of WE can be calculated. The commonly used REs include the calomel electrode and the Ag/AgCl electrode, with the latter being the one used in this thesis. To convert the voltage to RHE from Ag/AgCl electrode in different pH values of electrolytes, the following formula is applied:

$$E_{RHE} = E_{Ag/AgCl} + E^0_{Ag/AgCl} + 0.059 \times pH$$
$$= E_{Ag/AgCl} + 0.197 + 0.059 \times pH$$

Where 0.197 is the potential of Ag/AgCl electrode (KCl saturated solution, 3.5 M) at 25 °C.

Counter electrode (CE). CE constructs the circuit together with the WE and provides a fluent route for the electric current. In the cathode reaction, such as the OER, the CE functions as the anode, while for the anode reaction, like the HER, the CE functions as the cathode. The CE has to be inert in when immersed in the electrolyte in order to avoid any undesired electrochemical reaction. Also, the CE has to have a larger surface area than the WE to reduce the current density, thus the polarization of the CE becomes less possible. Typical electrodes, which fulfill these requirements are made of Pt wires, nets or plates. Sometimes metals such as Ag, Ni, W or Pb are also applied as CEs because they can keep stable in the specific electrolytes. In our measurements, the graphite rods are also used as CEs, thanks to their stability in both acidic and alkaline conditions.

2.3.2 Mechanism of the Electrochemical Measurements

Cyclic voltammetry (CV) measurements. CV measurements are performed at a certain potential to obtain a volt-ampere characteristic curve. For each cycle, the curve is divided into two linear segments. The segments are created by increasing or decreasing the potential with a voltage step at each interval, so that a staircase scan is applied to the cell with a defined scan rate. From the CV curve, we can observe some redox reactions according to the redox peaks. For example, Figure 2.2 shows a typical CV curve of amorphous $Ni(OH)_2$ nanospheres at various scan rates in 1 M

KOH.[2] When the potential increases, the amorphous $Ni(OH)_2$ nanospheres create a anodic peak because $Ni(OH)_2$ is oxidized to NiOOH, which, in turn, can be reduced "back" to $Ni(OH)_2$ when the potential decreases, as evidenced by the cathodic peak shown when the potential. Besides, the current of the peaks can increase when the scan rate increases, which is also clear in the figure.

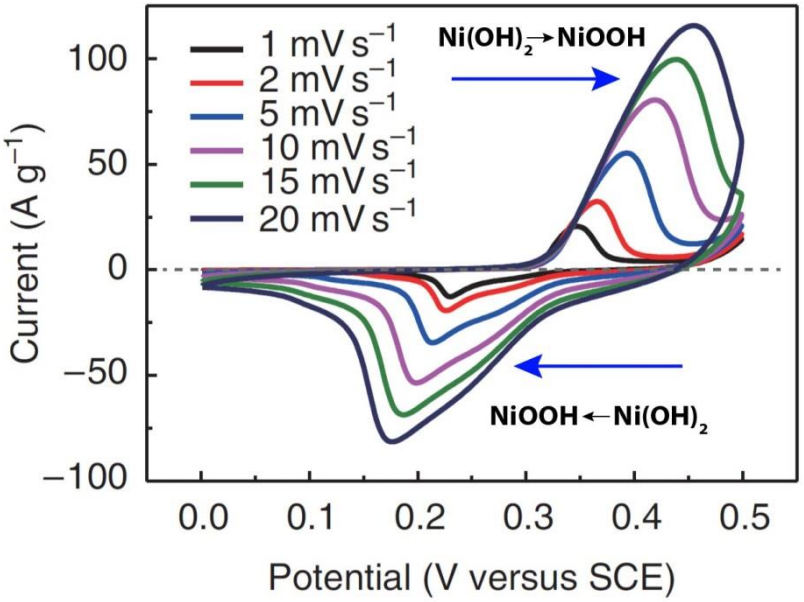

Figure 2.2. CV curves of the amorphous $Ni(OH)_2$ nanospheres at various scan rates in 1M KOH.

Linear sweep voltamogram (LSV) measurements. A linear potential sweep is created by updating the potential with a voltage step at each interval, so that a staircase scan is applied to the cell with a defined scan rate. Figure 2.3 shows a typical example of LSV graph from which we can see the change of current according to the potential.

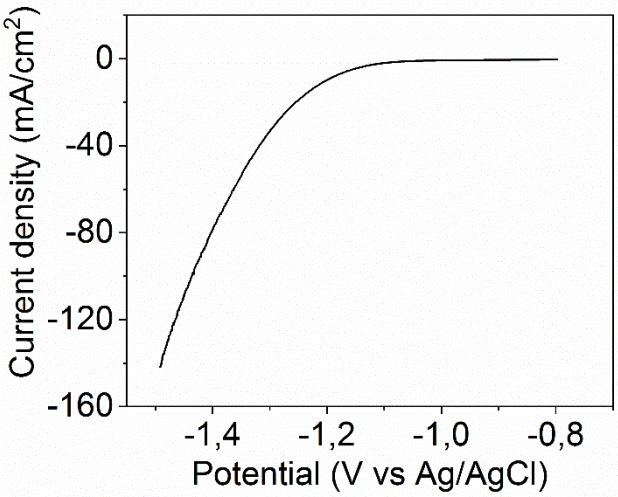

Figure 2.3. An example of LSV graph.

Electrochemical impedance Spectroscopy (EIS) measurements. To characterize the ability of the circuit to resist the flow of electrical current in the whole system, we use EIS measurements.[3] Usually, a sinusoidal test voltage or current is applied to measure the impedance over a suitable frequency range. In the EIS measurements of this thesis, a range of frequencies is applied at a sine-wave voltage, which can be expressed by the following formula:

$E_t = E_0 \sin(\omega t)$ or $E_t = E_0 \exp(j\omega t)$ (Eulers relationship)

Where E_t is the potential at time t, E_0 is the emplitude of the signal, and ω is the radial frequency. Additionally, ω has the following relationship with the frequency expressed in Hertz:

$\omega = 2\pi f$.

The response signal I_t is also in sinusoidal mode with a shift of phase (φ):

$I_t = I_0 \sin(\omega t + \varphi)$ or $I_t = I_0 \exp(j\omega t - \varphi)$ (Eulers relationship)

Then the impedance Z can be calculated as follows:

$$Z = \frac{E_t}{I_t} = \frac{E_0 \sin(\omega t)}{I_0 \sin(\omega t + \varphi)} = Z_0 \frac{\sin(\omega t)}{\sin(\omega t + \varphi)} = Z_0 (\cos\varphi + j\sin\varphi)$$

Eventually, Z can be represented as a complex number. By collecting the Z values under different frequencies and setting the real part (Z') and the imagination part (Z'') as x and y arrows, respectivley, we can obtain the Nyquist plot.[4] For instance, Figure 2.4a is a typical Nyquist plot recorded from an electrolytic cell with one plate electrode (for example the WE in electrocatalysis) with an applied potential. Each dot from the "half circle" is the value under specific frequency, and from left side to right side the frequency decreases according to the setting. Moreover, from the Nyquist plot, we can model an equivalent circuit by using the basic electric elements such as capacitor, resistor and inductors to fit the dots (see the line connecting the dots). The upper part of Figure 2.4a shows the corresponding equivalent circuit. When Z'' is equal to 0, the Z' values of the two dots correspond to R_s and $R_s + R_{ct}$, thus it is clear to obtain the values of R_s and R_{ct} which are important resistances for analyzing the property of the plate electrode. In order to match the real experimental environment with the modeling circuit, a scheme of a plate electrode is shown in Figure 2.4b. The C_{dl} stands for double layer capacitance which is formed by the electrolyte and the sample layer, R_s is the system resistance which is mainly form the electrolyte, and R_{ct} represents the resistance on the electrode.

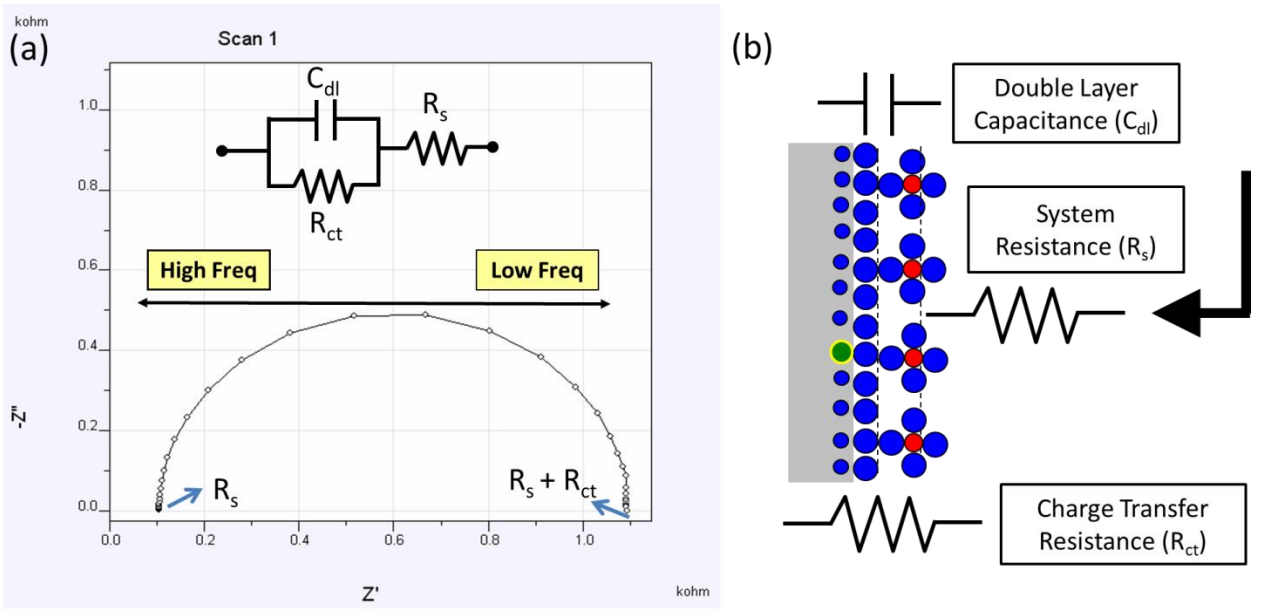

Figure 2.4. (a) A typical Nyquist plot of a electrolytic system contains one plate electrode. (b) The scheme of the plate electrode.

References

1. Marı´a, E.; Marco, J. F.; A´ngel, C., Surface Decoration at the Atomic Scale Using a Molecular Pattern Copper Adsorption on Cyanide-Modified Pt(111) Electrodes. *J. Phys. Chem. C* **2009,** *113*, 2340-12344.

2. Li, H. B.; Yu, M. H.; Wang, F. X.; Liu, P.; Liang, Y.; Xiao, J.; Wang, C. X.; Tong, Y. X.; Yang, G. W., Amorphous Nickel Hydroxide Nanospheres with Ultrahigh Capacitance and Energy Density as Electrochemical Pseudocapacitor Materials. *Nat. Commun.* **2013,** *4*, 1894.

3. Boukamp, B. A., A Package for Impedance-admittance Data Analysis. *Solid State Ionics* **1986,** *18 & 19*, 136-140.

4. Boukamp, B. A., A Nonlinear Least Squares Fit Procedure for Analysis of Immitance Data of Electrochemical Systems. *Solid State Ionics* **1986,** *20*, 31-44.

Chapter III Synthesis of Cation Alloyed Ternary Ni-Co-Se NCs and Their Application in HER and OER

3.1 Introduction

As previously discussed in Chapter I, Ni- and Co- based chalcogenides sparked great interest owing to their promising properties in both HER and OER. Till now, many efforts have been taken to synthesize binary and ternary transition metal chalcogenides and the alloy of the transition metal in the complexes were reported to be more catalytically active in HER and OER than the materials without alloy. For example, $NiCo_2S_4$ Nanowires,[1] $Ni_{0.89}Co_{0.11}Se_2$ nanosheets,[2] and $Co_{0.59}Ni_{0.41}S_2$ microcrystals[3] have been identified as promising candidate HER electrocatalysts, having higher performance than their binary compounds. On the other hand, it has also been shown that the OER performances of such materials can be tuned via composition control, namely by modulating the Co/Ni elemental ratio in the catalyst. Liu et al. reported that the OER catalytic activity of $NiCo_2S_4$@graphene core@shell nanosheets was considerably higher than that of Ni_3S_4@graphene and Co_3S_4@graphene counterparts.[4] Xia et al. showed that Ni-doped $Co_{0.85}Se$ nanotube arrays were much more efficient and durable electrocatalysts in alkaline media than undoped $Co_{0.85}Se$.[5] In a recent study by our group, we also found that ternary $NiCoSe_4$ hollow microparticles exhibited an improved OER activity with respect to the binary $CoSe_2$ ones.[6] The improved performances observed in these cases have been tentatively explained by considering that the presence of both Ni and Co causes a synergistic effect that can lead to the formation of more active sites with a lower activation energy.[7-9] Unfortunately, it is still unclear what the specific role of Ni and Co is in the HER or OER, and what the optimal Ni/Co ratio is in each system. For example, in some recent works on Ni-Co chalcogenide materials, improved OER performances have been reported both in Co-rich[6, 10-12] and in Ni-rich compounds.[2, 5, 13]

Furthermore, it is still being debated whether these materials act as the actual catalysts or as pre-catalysts, which undergo a chemical transformation under OER conditions, thus forming metal oxides/hydroxides.[14] For example, Nath and co-workers reported that Ni_3Te_2, $FeNi_2Se_4$ and $NiSe_2$ do not undergo any degradation, oxidation or compositional change upon OER.[14-16] Conversely, Chen et al. systematically investigated the structural evolution of different transition metal dichalcogenides (MX, M = Co, Ni, Fe; X = S, Se, Te) under OER, and found that they all underwent oxidation under operational conditions, forming the corresponding metal oxides.[17]

Similarly, Zhou et al. observed that Ni_3S_2 nanorods gradually transformed into hydrated nickel oxide when employed as OER catalysts.[18] Also, different authors reported that Ni-Co-S rods, NiSe nanowires and $NiCoSe_4$ hollow microcrystals were characterized by accumulated hydroxides or oxides species on their surface upon OER.[6, 14, 19-20] However, it is still unclear which factors control the transformation of metal chalcogenide catalysts into their corresponding oxide/hydroxides. All these recent findings have motivated us to investigate not only if optimized OER performances could be achieved via both a cation tuning Ni-Co-Se catalysts, but also what the specific roles of Ni and Co elements are.

In this chapter, we developed the colloidal synthesis to produce ternary Ni-Co-Se NCs which had the same crystal structure for the electrocatalytic HER and OER, respectively. Then, we systematically studied the transformations of such NCs during OER under alkaline conditions. Our findings revealed that Ni and Co based chalcogenide NCs were helpful to improve the performance of OER while HER was better with binary NiSe or CoSe NCs. Under OER conditions, completely transform into Co and/or Ni oxide/hydroxide materials, which are the actual active catalysts. It is of particular importance that the activity of such materials strongly depends on the composition of the starting chalcogenide NCs. According to species during the OER. CoSe NCs, on the other hand, completely transformed into active amorphous CoO_x and $Co(OH)_x$ materials. Ternary Ni-Co-Se NCs, upon OER, turned into amorphous Ni-Co hydroxides/hydroxides, which exhibited a higher catalytic activity than that of the Co hydroxides/hydroxides.

3.2 Exploration of Colloidal Synthesis of Ternary Ni-Co-Se NCs

The synthesis of the ternary Ni-Co-Se NCs is facile with only a mixture of Ni and Co precursors before the reaction. By tuning the different reaction parameters (precursors, solvents, surfactants, reaction time, temperature etc.) we tried to achieve control over size, shape and composition of the resulting NCs. XRD, TEM and elemental analyses were performed to characterize the crystal structure, the morphology, the size and the composition of the nanocrystals, respectively. The electrocatalytical properties of the most promising samples were studied

According to the ICSD database, Ni- and Co- based selenides NCs have a hexagonal structure belonging to the same space group and they have similar lattice parameters (Figure 3.1). Moreover, there are already some reports about the colloidal synthesis of NiS and CoSe NCs.[21-22] Inspired by these reports, the achievement of Ni and Co in the selenides may have a possibility and the relative colloidal synthesis were designed. In a standard synthesis, Ni and Co precursors with specific ratios were mixed with ODE, and/or OAm, and/or OAc in a 25 mL three-neck flask with a condenser. The flask was placed on a heating mantle with a temperature controller, and the thermocouple was

inserted between the flask and the heating mantle. The mixture was stirred by magnetic stirring apparatus during all the reaction. First, the mixture was degassed under vacuum at 120 °C for 1 hour to remove any moisture and oxygen. Then the N_2 or Ar atmosphere was inflated into the flask to replace the vacuum. After that, the Se precursor was injected into the flask and the temperature was increased to the reaction temperature for some designed time. The black product was dispersed by toluene and precipitated by ethanol for at least twice, then dispersed in toluene at last. In the following we introduced the influence of several key experimental parameters.

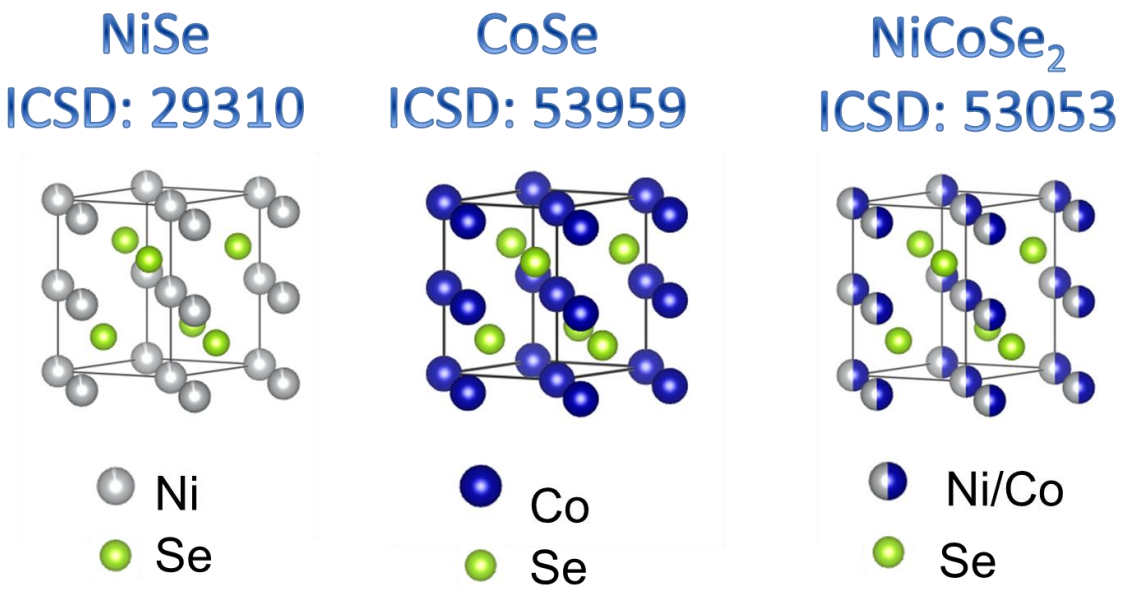

Figure 3.1. Crystal structures of NiSe, CoSe and $NiCoSe_2$.

3.2.1 Influence of Se Precursor

Based on published reports, there are several types of Se precursors used in colloidal synthesis.[23-24] We chose two kinds of Se sources with different Se═X (X = N, P) bonds for the experiments, and both of them are synthesized as uniform liquid complexes by simple processes. The synthesis methods are provided as follows:

Synthesis of TOP-Se. 1 mmol of Se powder is added to 1 mL of TOP. Then the mixture is stirred at 100 °C till the color turns transparent. It should be mentioned that all the operations should be in glove box.

Preparation of OAm-Se. 8 mmol of Se powder was mixed with 24 mL of OAm in a 3-neck flask, and the resulting mixture was degassed under vacuum at 120 °C for 1 h. The system was slowly heated up to 230 °C for 3 h in Ar atmosphere until the solution became transparent with an orange color. Eventually, the OAm-Se precursor solution was transferred to a glass vial and stored

in an N_2 filled glovebox for further use.

The molecular structures of these two Se precursors are shown in Figure 4.2a, b. In TOP-Se and OAm-Se, the Se atoms form Se═P and Se═N, respectively. While the kind of Se precursors is changed, other experimental conditions are the same in both experiments. The XRD and TEM characterizations of both samples are shown in Figure 3.2c-f. The XRD pattern of sample made by using TOP-Se fits the phase of a mixture of mainly NiSe and a tiny amount of Ni_3Se_2, while the sample made using OAm-Se fits $NiCoSe_2$ with a small shift to the higher degree of 2 theta. Also from Figure 3.2c it is clear that the sample using TOP-Se as the precursor is prone to form Ni_3Se_2 which contains less ratio of Se inside the NCs than NiSe. This means TOP-Se is probably less active in forming hexagonal metal monoselenide structure.

Moreover, according to the elemental analysis from ICP, the ratio of Ni/Co is 0.92:0.04 when TOP-Se is used as Se precursor, which means the ratio of Co is very small inside the NCs even considering that the ratio of the Ni and Co precursors are 1:1. This is because the combination of TOP and OAc might dissolve Co^{2+} and slow down its rate of forming the nanoparticles. This phenomenon is proved by both the literature and the experiment, in which the mixture is not able to from any NCs with only Co precursor in the synthesis while other experimental parameters are the same as the ones from the TOP-Se experiment (Sample 1 in Table 3.1).[25] Besides, it is also proved that the combination of TOP-Se and large amount of OAm is also possible to dissolve Co precursor very well resulting in not forming any NCs (Sample 2 and 3 in Table 3.1).

From the TEM images, it is clear that the sample made by TOP-Se is characterized by elongated crystals with a “rod-like” shape with the length about 5 μm, while the sample made using OAm-Se contains mainly rounded crystals with a diameter of about 100 nm.

Consequently, Co precursor is reactive when using OAm-Se leading, thus, to the formation of ternary compounds.

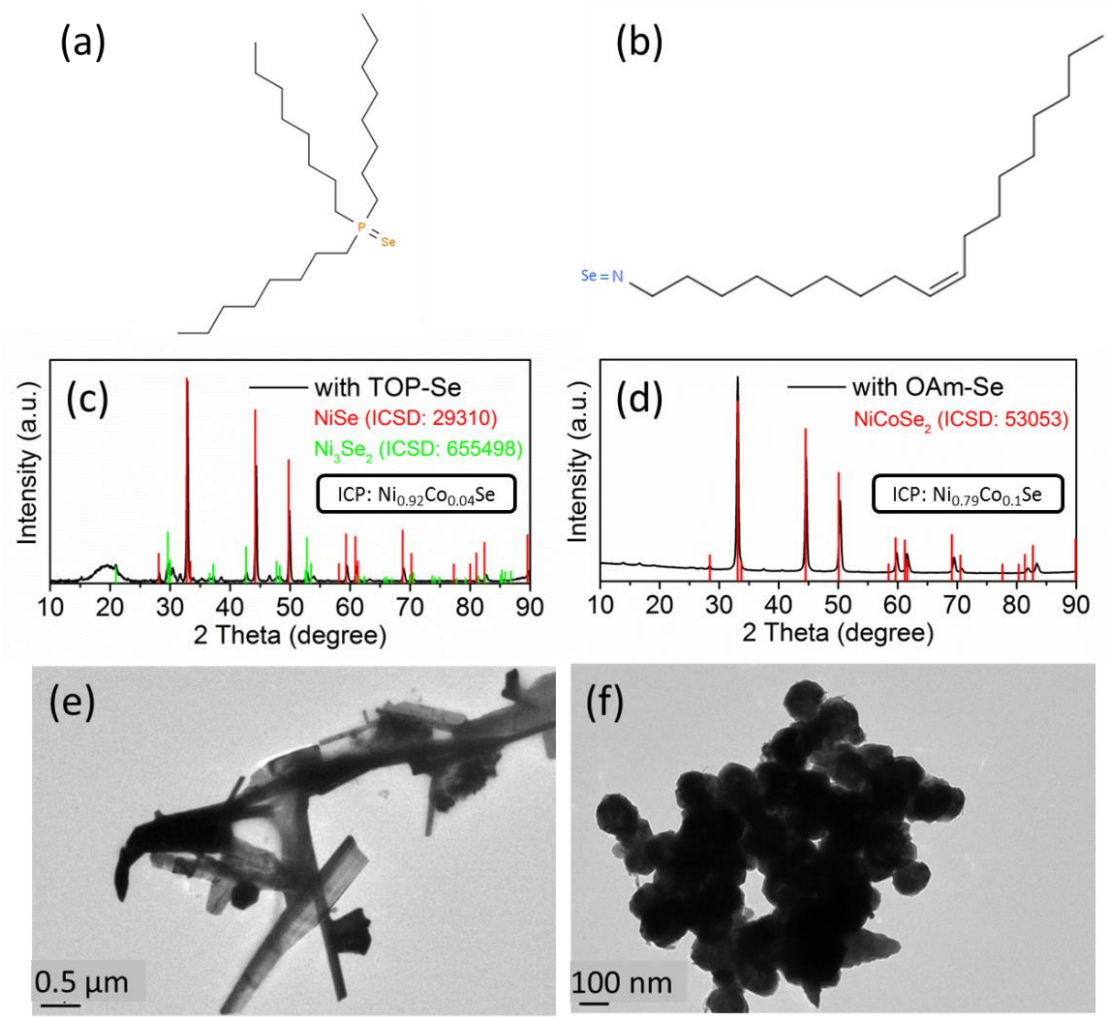

Figure 3.2. Molecular structure of (a) TOP-Se and (b) OAm-Se. (c) XRD pattern and (e) TEM image of NCs obtained using TOP-Se as Se precursor. (d) XRD pattern and (f) TEM image of NCs obtained using OAm-Se as Se precursor. Other experimental parameters: 0.5 mmol of $NiCl_2$, 0.5 mmol of $CoCl_2$, 5 mL of ODE, 3 mL of OAc. After the injection of 1 mmol of Se precursor, the reaction was heated up to 250 °C for 1 h.

Table 3.1. Some experimental conditions under which no NCs are formed.

Parameters	**Sample 1**	**Sample 2**	**Sample 3**
$CoCl_2$ (mmol)	0.5	0.5	0.5
TOP-Se (mmol)	1	1	1
ODE (mL)	5	5	5
OAc (mL)	3	0	3
OAm (mL)	0	8	0.5
Reaction temperature (°C)	250	250	250
Reaction time (h)	1	1	1

3.2.2 Influence of Co Precursors

Three different Co precursors were tested in the colloidal synthesis of Co-Ni-Se NCs: CoI_2, $CoCl_2$ and $Co(acac)_2$. The molecular structures of these Co precursors are shown in Figure 3.3, and the basicity of the anions follows the trend: $I^- < Cl^- < acac^-$. Three comparative experiments are performed with only the types of Co precursors changed from CoI_2, $CoCl_2$ to $Co(acac)_2$, and the other parameters being the same. It should be mentioned that according to the analysis of the last section, since the combination of OAc and TOP can slow down the activity of Co, the surfactant Se precursor are changed to suitable amount of OAm and OAm-Se, respectively. The XRD patterns of these three samples obtained with different kinds of Co precursors have the same crystalline structure corresponding to hexagonal NiSe (ICSD: 29310) with a slight shift to higher 2 theta, which is consistent with the shrinkage of the crystal structure which occurs when replacing Ni^{2+} (0.69 Å) with smaller Co^{2+} (0.61 Å) cations. The ICP elemental analysis shows that the content of Co increases from 7% (compared to Se), 15% to 20% when the Co precursors changes from CoI_2, $CoCl_2$ to $Co(acac)_2$. This increase of the ratio of Co in the content might result from the different basicity of the anions. Probably the basicity of $acac^-$ is the most suitable one in the same experimental condition so $Co(acac)_2$ is the most active one among these three Co precursors.

The TEM pictures show that all the samples have smaller size comparing to the last experimental group (Figure 3.2). This is probably because the reaction time is reduced, as it will be discussed afterward. Specifically, by using CoI_2 and $CoCl_2$, the size of the NCs is around 50 nm, while the size can be reduced to ~30 nm when $Co(acac)_2$ is used as the Co precursor.

According to the above analysis, although the crystal structure and morphology have no clear change, the $Co(acac)_2$ which is helpful to alloy more ratio of Co inside the compound is chosen as the Co precursor eventually.

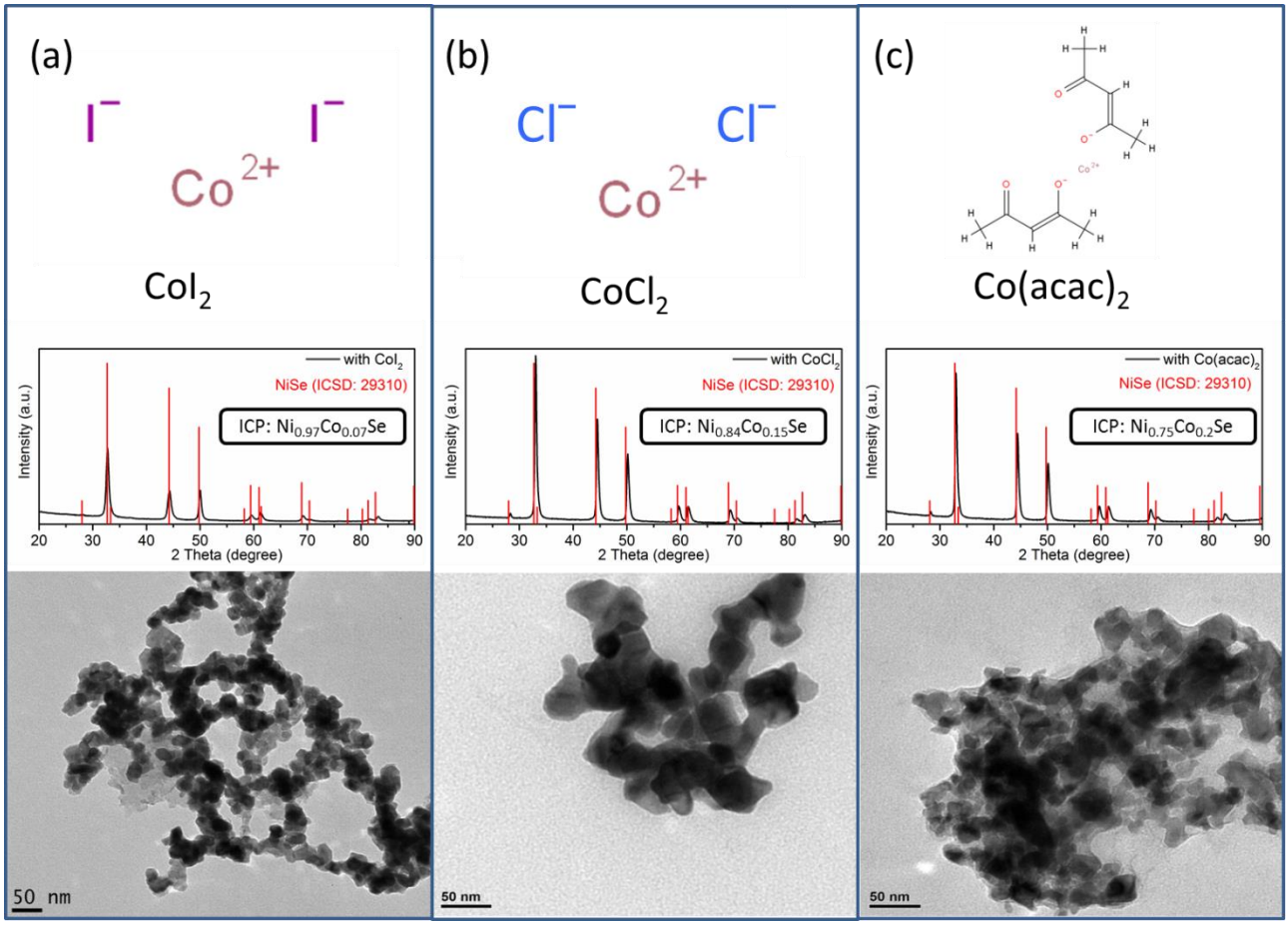

Figure 3.3. Molecular structure of (a) CoI_2, (b) $CoCl_2$ and (c) $Co(acac)_2$, XRD patterns and TEM images of samples used (a) CoI_2, (b) $CoCl_2$ and (c) $Co(acac)_2$ as Co precursors. Other experimental parameters: 0.5 mmol of $NiCl_2$, 0.5 mmol of Co precursor, 5 mL of ODE, 6 mL of OAm. After degassing 1 mmol of OAm-Se was injected in the mixture, the reaction was heated up to 250 °C for 30 min.

3.2.3 Influence of Ni Precursor

Similar as the strategy of studying the influence of Co precursor, Ni salts with different basicity of anions such as $NiCl_2$ and $Ni(acac)_2$ were chosen to study the influence of the Ni precursors. Meanwhile, the other experimental parameters remain the same. The characterizations of the samples are shown in Figure 3.4. Briefly, the XRD pattern of the sample produced using $NiCl_2$ matches with that of bulk hexagonal NiSe, while the sample produced with $Ni(acac)_2$ contains the hexagonal $NiCoSe_2$ and Co_9Se_8, a phase with more ratio of metal compared to $NiCoSe_2$. This result was confirmed by the elemental analysis ($Ni_{0.67}Co_{0.6}Se$), in which the ratio of metal/selenium is 1.27:1. This is expected since $Ni(acac)_2$ is more active than $NiCl_2$. Surprisingly, although the phase of the sample used as $Ni(acac)_2$ as Ni precursor is not pure, the Ni/Co ratio is more balanced than the sample used $NiCl_2$ as Ni precursor. This might be because the Cl^- in $NiCl_2$

can influence the activity of Co^{2+} and result in a lower ratio of Co in the final product. Therefore, actually $Ni(acac)_2$ and $Co(acac)_2$ are the best combination to tune the composition easily in the current system, but the tuning of the crystal structure remains a problem.

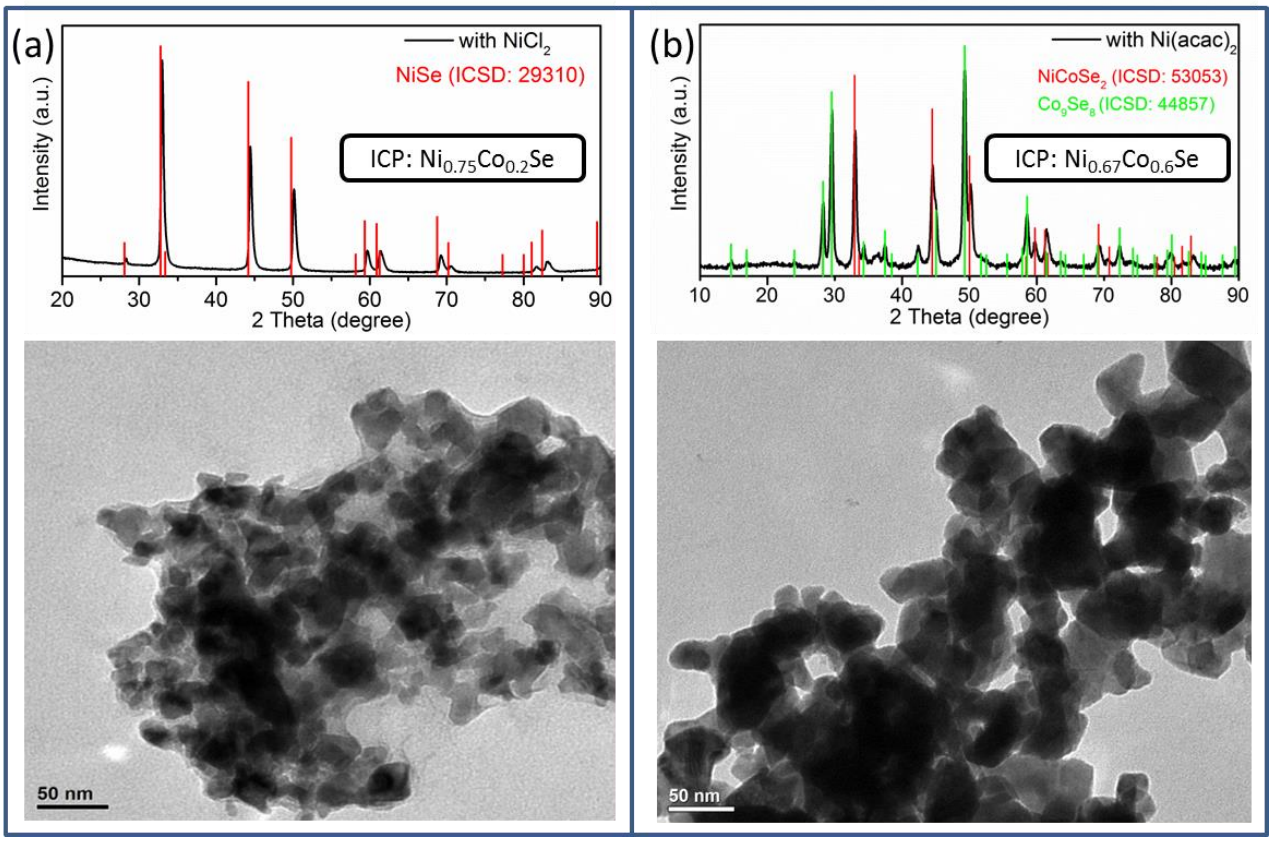

Figure 3.4. XRD pattern and TEM image of sample with (a) $NiCl_2$ and (b) $Ni(acac)_2$ as precursor. Other experimental parameters: 0.5 mmol of Ni precursor, 0.5 mmol of $Co(acac)_2$, 5 mL of ODE, 6 mL of OAm. After 1 mmol of OAm-Se was injected in the mixture, the reaction was heated up to 250 °C for 30 min.

3.2.4 Influence of Solvents

Different types of solvents are also tested in the hope of obtaining samples with better morphology and more pure phase. According to the previous results, since the combination of $Ni(acac)_2$/$Co(acac)_2$ may produce a mixture in crystal structure, the $NiCl_2$/$Co(acac)_2$ couple is chosen as Ni and Co precursors. In order to study the role of different solvents in the synthesis of Ni-Co-Se NCs, in the following experiments ODE is replaced by commonly used solvents for colloidal synthesis such as octyl ether, TOPO and OAm. The conventional characterizations are shown in Figure 3.5. From the XRD patterns, samples obtained using ODE and octyl ether have the same crystal structure corresponding to the hexagonal NiSe with a slight shift to higher 2 theta

because of the alloying of Ni and Co. According to the elemental analysis the Ni/Co ratio is higher when the solvent is octyl ether, which means octyl ether is not helpful to increase the amount of Co inside the compound. As the solvent is changed to TOPO and OAm, a mixture of phases are formed. As to the morphology, the TEM images do not show clearly the improvement in morphology when the solvent are changed to octyl ether, TOPO and OAm. Thus the ODE is still chosen as the solvent in the future research.

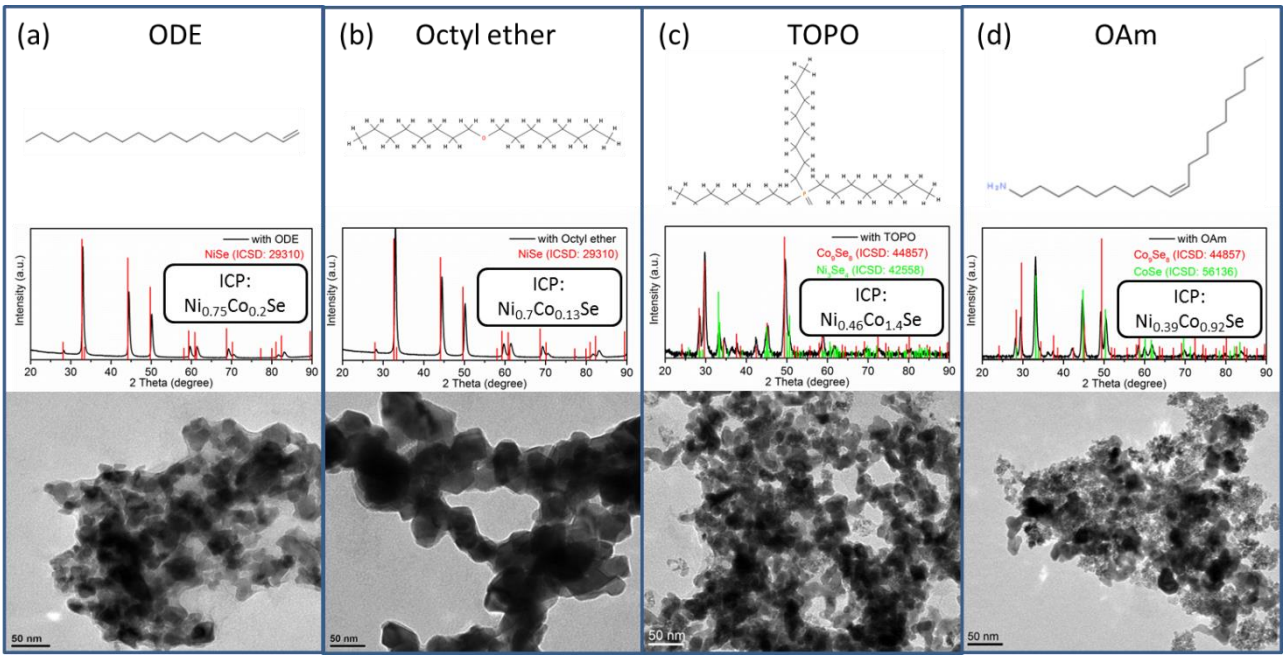

Figure 3.5. Molecular structures of the solvent (a) ODE, (b) octyl ether, (c) TOPO and (d) OAm. XRD patterns and TEM images of the samples by solvent (a) ODE, (b) octyl ether, (c) TOPO and (d) OAm. Other experimental parameters: 0.5 mmol of $NiCl_2$, 0.5 mmol of $Co(acac)_2$, 5 mL of solvents (3 g of TOPO because it is solid), 6 mL of OAm. After 1 mmol of OAm-Se was injected in the mixture, the reaction was heated up to 250 °C for 30 min.

3.2.5 Influence of Surfactants

A variety of commonly used surfactants was tested in order to improve the control over the size and shape of the final NCs. Figure 3.6 shows the TEM images of the samples synthesized with different kinds of surfactants. It is obvious that ODPA (Figure 3.6a) and HPA (Figure 3.6b) do not help to form the nanoparticles with smaller size and specific shapes. When OAc (Figure 3.6c) or a combination of OAc and OAm (Figure 3.6d) are used, the size of the particles is increased to around 100 nm and the morphology turns to round spheres. By using OAm, the size can be controlled to less than 50 nm (Figure 3.6e), but without any surfactant the size is also similar (Figure 3.6f). Moreover, these two samples have the same hexagonal structure and similar

composition, as shown in Figure 3.6g. Unfortunately, these five surfactants are not suitable for improving the size or morphology. When DDT was used as the surfactant, the size of the sample was decreased dramatically to around 10 nm. The XRD pattern shows that the structure was close to Ni_3S_4, while the elemental analysis shows an unrelated composition comparing to the XRD pattern. This is probably because DDT decomposed at 250 °C and released S for constructing the crystal structure. This system with DDT as a surfactant and reactant at the same time will be discussed further in chapter IV. To conclude, the surfactants tested in this work did not have any influence in the size and shape control of Ni-Co-Se NCs, under the current synthesis conditions.

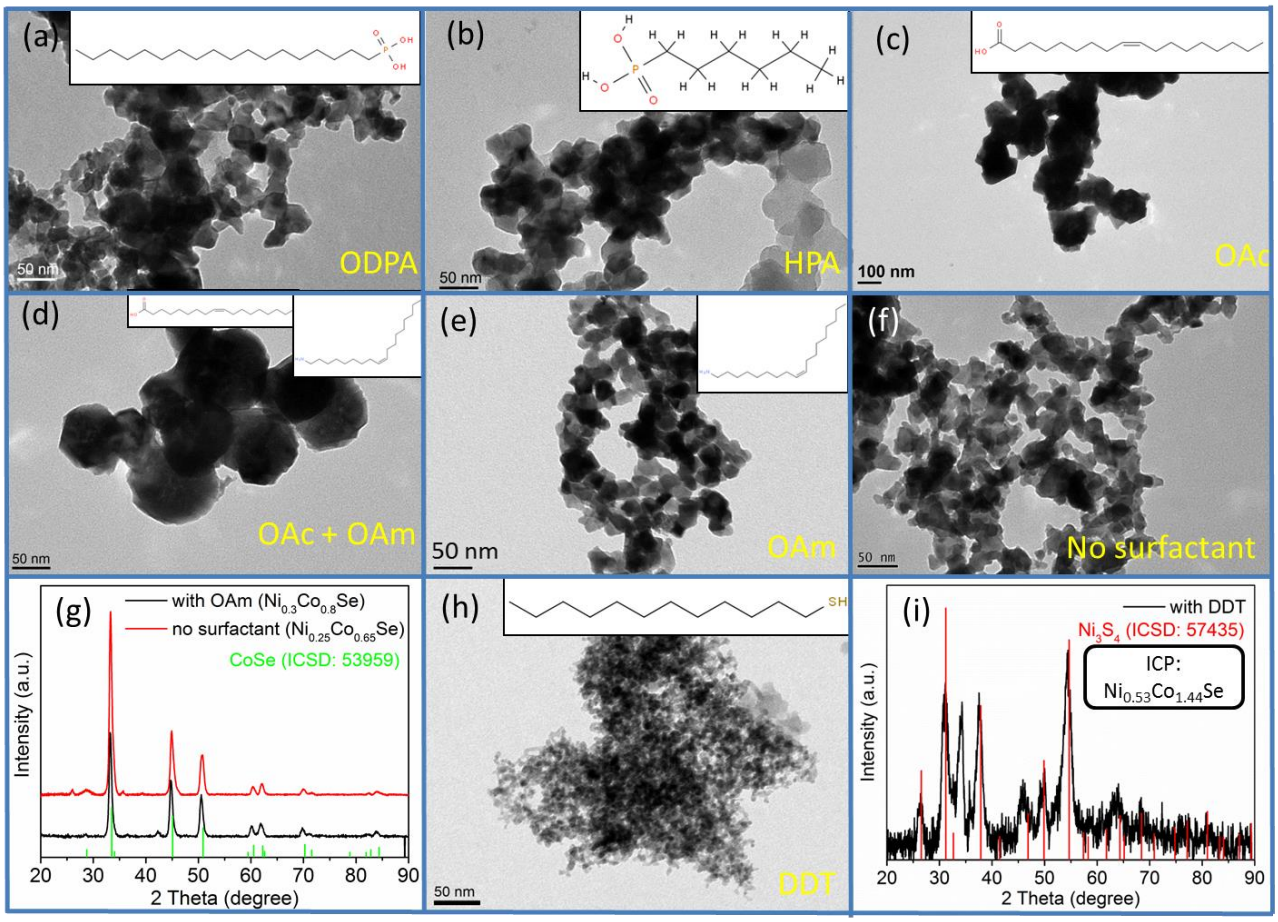

Figure 3.6. TEM images of samples with different kinds of surfactants: (a) ODPA, (b) HPA, (c) OAc, (d) OAc + OAm, (e) OAm, (f) no surfactants, (h) DDT. (g) XRD patterns of the samples using OAm as surfactant and without surfactant. (i) XRD pattern of the sample using DDT as surfactant. Other experimental parameters: 0.25 mmol of $NiCl_2$, 1 mmol of $Co(acac)_2$, 5 mL of ODE, some amount of surfactant ((a) 0.05g of ODPA, (b) 0.05 g of HPA, (c) 3 mL of OAc, (d) 3 mL of OAc + 3 mL of OAm, (e) 3 mL of OAm, (f) no surfactant and (h) 3 mL of DDT). After 1 mmol of OAm-Se was injected in the mixture, the reaction was heated up to 250 °C for 5 min.

3.2.6 Influence of Reaction Time

In order to study the influence of the reaction time, We arranged the reaction time from 1 min to 60 min. As expected, we found that the reaction time plays a key role in the experimental results. The following results are from this series of experiments to show how the reaction time affects the results (Figure 3.7). Figure 3.7a shows the dominating hexagonal CoSe phase (ICSD: 53959) after 1 min of reaction, together with a small amount of CoO or NiO (ICSD: 245320) impurities because the cubic CoO and NiO have similar XRD patterns. After 5 min, the phase becomes pure hexagonal CoSe phase (Figure 3.7b). After 30 min, a new metal-rich Co_9Se_8 phase (ICSD: 44857) appears from the CoSe phase (Figure 3.7c); After 60 min, the Co_9Se_8 phase totally replaced the CoSe one (Figure 3.7d). Since the elemental analysis shows a mixture of Ni and Co in these four experiments, it is possible that all the above-mentioned structures have alloyed cations. According to the XRD results and the published reports, it can be assumed that the process begins with the thermal decomposition of Ni and Co precursors to form oxide seeds.[26] The second step involves the decomposition of the oxides or the anion exchange from O^{2-} to Se^{2-} to form hexagonal CoSe structure. When the reaction time increases, more Co^{2+} or Ni^{2+} are added into the NCs and change the structure to cubic Co_9Se_8 phase (Figure 3.8).

The ICP results of samples of 1, 5, 30 and 60 min are $Ni_{0.45}Co_{0.42}Se$, $Ni_{0.41}Co_{0.46}Se$, $Ni_{0.45}Co_{0.73}Se$ and $Ni_{0.44}Co_{0.74}Se$, respectively. These results indicate that increasing the reaction time helps to increase the amount of Co in the crystals, but the influence of the reaction time is not as strong as the influence of the precursors and solvents. Besides, the ratio of (Ni + Co)/Se increases from 0.87 to1.18. These ICP results can match the results of XRD measurements except the first one, which should have shown (Ni + Co)/Se ratio more than 1 because of the existence of NiO and CoO. The reason why the sample has a (Ni + Co)/Se ratio of 0.87 may be because the oxide particles are surrounded by Se precursor, which might have a strong connection with the nanoparticles and is not easy to remove by washing with ethanol.

TEM images in Figure 3.7 indicate that increasing the reaction time from 1 min to 60 min, the size of the NCs enlarges slowly from 25 nm to 50 nm in this experimental system.

Therefore, in order to obtain sample with pure hexagonal phase and a balanced Ni/Co ratio inside, we need to set the reaction time at around 5 min. On the other hand, the reaction time should be less than 30 min otherwise the phase of the sample will change to Co_9Se_8 and the size of NCs will be large.

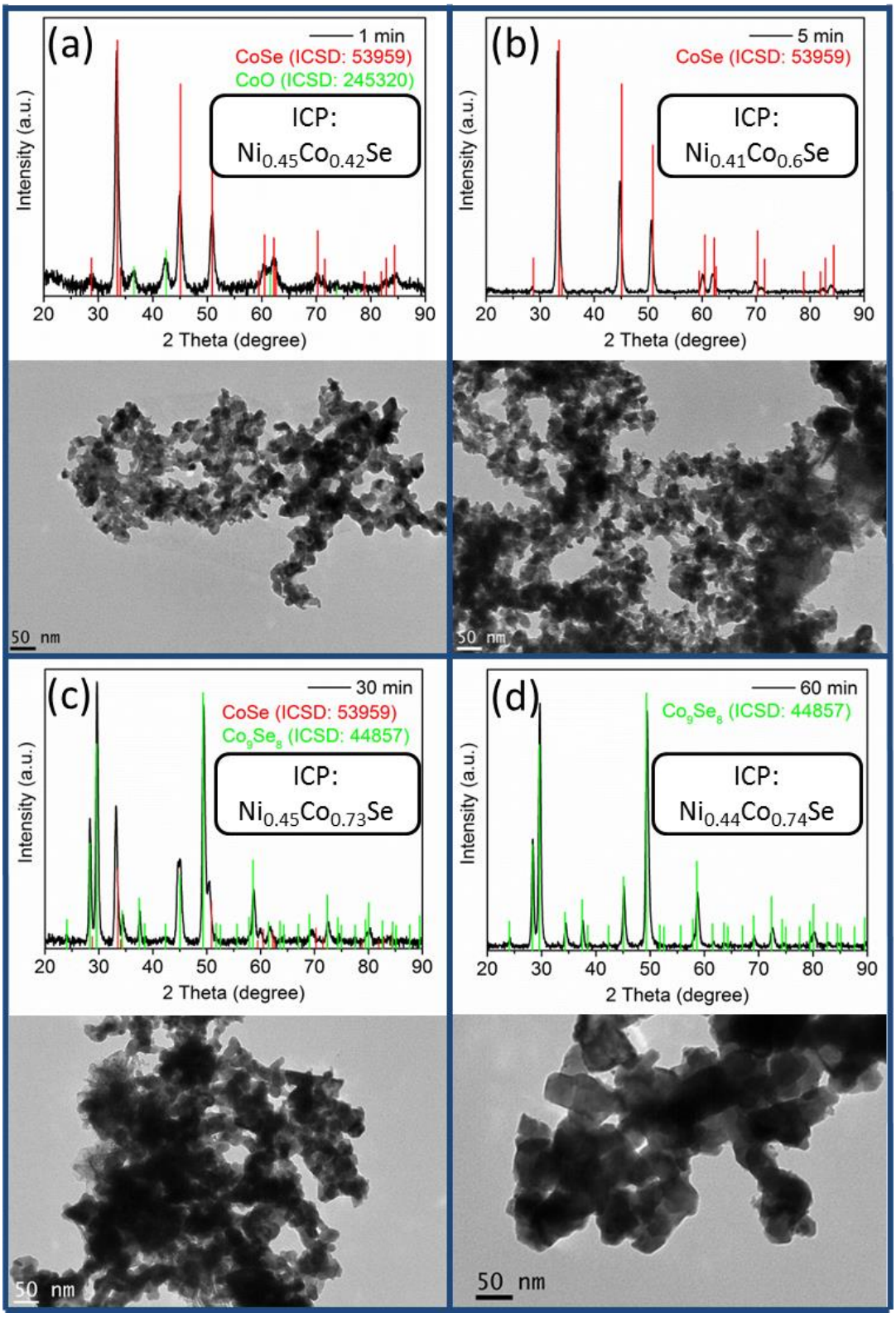

Figure 3.7. XRD patterns and TEM images of the samples after the reaction time of (a) 1 min, (b) 5 min, (c) 30 min and (d) 60 min. Other experimental parameters: 0.25 mmol of $NiCl_2$, 1 mmol of $Co(acac)_2$, 5 mL of ODE, 3 mL of OAm. After degas 1 mmol of OAm-Se was injected in the mixture, the reaction was heated up to 250 °C for the specific time.

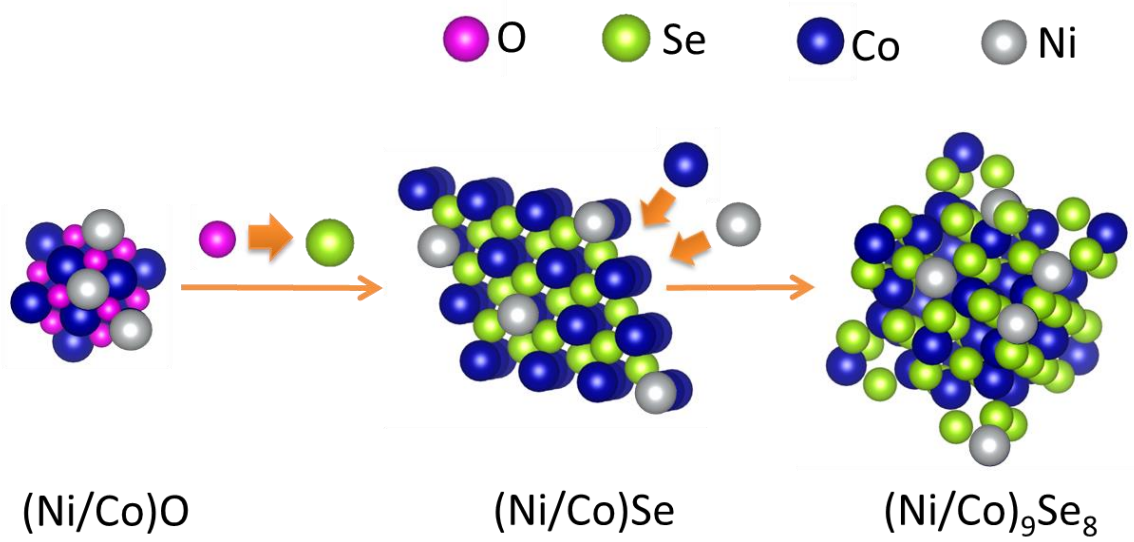

Figure 3.8. Schematic illustration of the probable change route of the chemical structures of the samples according to the reaction time.

3.2.7 Influence of Reaction Temperature

We studied the influence of the reaction temperature to have a further comprehension about this colloidal synthesis. From the XRD patterns, it is clear that different reaction temperatures lead to different crystal structures (Figure 3.9). Working at 150 °C the product consists of small CoO/NiO nanoparticles and a small amount of (Ni+Co)Se, as shown in Figure 3.9a. At 200 °C, there is still a mixture of oxides and selenides in the sample, and the ratio of the selenide in the mixture becomes dominating (Figure 3.9b). Working at 250 °C the resulting NCs have a hexagonal CoSe phase without any oxides impurities.

Besides, the elemental analysis shows an increase in Ni/Co ratio, which means that at higher temperature the reactivity of the Ni precursor is higher than that of the Co one.

Interestingly, the TEM image of very small NCs which are less than 5 nm for the sample obtained at 150 °C is shown in Figure 3.9a, and this is the morphology of the metal oxides. Figure 3.9c shows the TEM image of the samples obtained at 250 °C, and this images reveals the particle size of the selenides of around 25 nm, conforming that the size of selenides is quite different from the size of oxides. While in Figure 4.9b, both these two morphologies are observed, proving the mixture of oxides and selenides, which is in accordance with the XRD results.

These experiments prove that to get pure metal selenide NCs, the temperature should be higher than 200 °C, below which the Se precursor, most likely, doesn't thermally decompose fast enough to release Se, so Co^{2+} or Ni^{2+} ions tends to react first with the oxygen which is from the thermal

decomposition of $acac^-$ to form oxides. However, the Ni/Co ratio will increase when the reaction temperature increases, so the temperature should not be higher than 250 °C in order to control the Ni/Co ratio in the compound and acquire pure selenide structure at the same time.

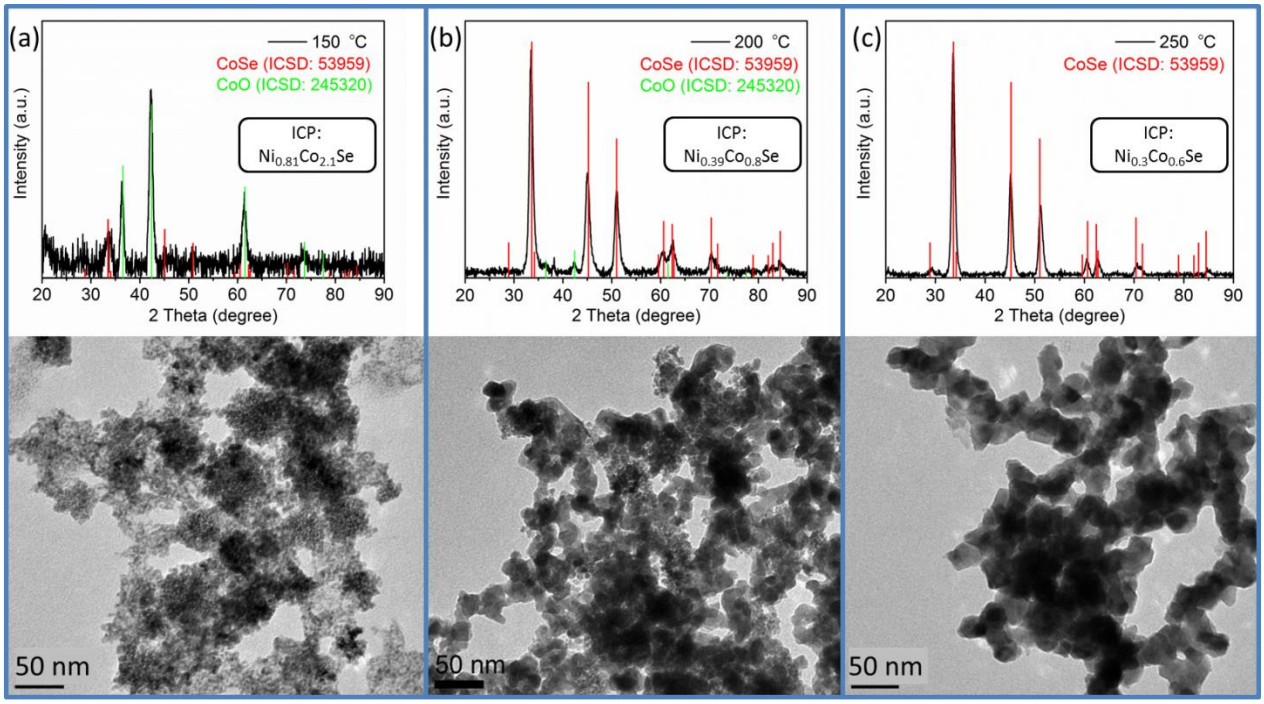

Figure 3.9. XRD patterns and TEM images of the samples under the reaction temperature of (a) 150 °C, (b) 200 °C and (c) 250 °C. Other experimental parameters: 0.25 mmol of $NiCl_2$, 1 mmol of $Co(acac)_2$, 5 mL of ODE, 3 mL of OAm. After 1 mmol of OAm-Se was injected in the mixture, the reaction was heated up to the target temperature for 5 min.

3.2.8 Influence of Hot Injection and Heat-up Procedure

Classical theory suggests that burst nucleation and diffusion-controlled growth are the most important factors for the control of the size distribution in colloidal synthesis.[27] Thus hot injection is chosen as a typical method used in colloidal synthesis with the aim to from smaller nuclei and better control the growth of the NCs. We also tried hot injection method to compare with heat-up approach while other experimental conditions were kept the same in the comparable experiments. The results are shown in Figure 3.10. According to the XRD patterns of the corresponding NC products (Figure 3.10b), with the hot injection method impurities are even induced impurities while the sample with the heat-up procedure remains a single hexagonal phase. The phase is also hard to control in other experiments with hot-injection procedure (Table 3.2). By comparing the two TEM pictures, it is obvious that the size does not decrease when we use hot injection method. Also in other synthesis

by hot-injection method, there is no observation of the improvement in the morphology (Figure 3.11). Unfortunately, the hot injection method is improper for optimizing the results.

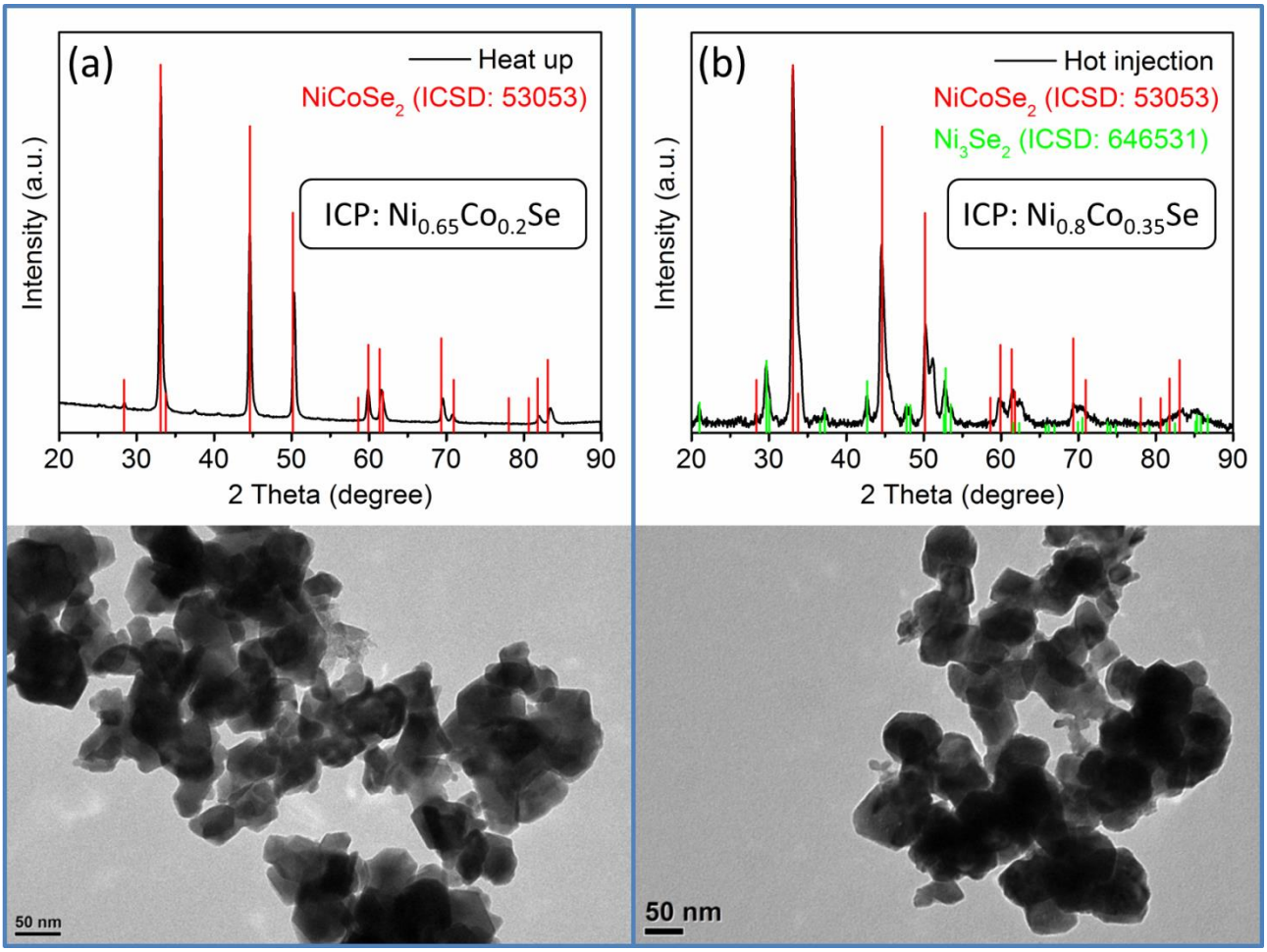

Figure 3.10. XRD and TEM images of samples with (a) heat-up process and (b) hot injection. Other experimental parameters: 0.5 mmol of $NiCl_2$, 0.5 mmol of $Co(acac)_2$, 1 mmol of Se:OAm, 5 mL of ODE, 3 mL of OAm, After 1 mmol of OAm-Se was injected in the mixture, the reaction was heated up to 250 °C for 5 min; or the temperature reached to 250 °C then 1 mmol of OAm-Se was injected and the reaction lasted for 5 min.

Table 3.2. Other experiments performed with hot-injection method.

Sample	**Ni precursor**	**Co precursor**	**Se precursor**	**Solvent**	**Surfactant**	**Reaction time**	**Reaction Temperature**	**Phase**
1	$NiCl_2$	$CoCl_2$	OAm-Se	ODE	OAm	5 min	250 °C	$NiCo_2Se_4$
	0.5 mmol	0.5 mmol	1 mmol	5 mL	6 mL			Ni_3Se_2
2	$NiCl_2$	$CoCl_2$	OAm-Se	ODE	OAm	30 min	250 °C	$NiCoSe_2$

Sample	Ni precursor	Co precursor	Se precursor	Solvent	Surfactant	Reaction time	Reaction Temperature	Phase
	0.5 mmol	0.5 mmol	1 mmol	5 mL	6 mL			Ni_3Se_2
3	$NiCl_2$	$Co(acac)_2$	TOP-Se	ODE	OAc 3 mL	60 min	200 °C	Ni_3Se_2
	1 mmol	1 mmol	2 mmol	5 mL				Ni_6Se_5
4	$Ni(acac)_2$	$Co(acac)_2$	OAm-Se	ocytl ether	OAm	60 min	250 °C	Ni
	0.5 mmol	0.5 mmol	1 mmol	5 mL	6 mL			Co_9Se_8
5		$CoCl_2$	TOP-Se	ODE	OAm	60 min	250 °C	Co_9Se_8
		0.5 mmol	1 mmol	5 mL	3 mL			Co
6	$NiCl_2$		TOP-Se	ODE	OAm	60 min	250 °C	$H_{12}C_{l2}NiO_6$
	1 mmol		1 mmol	5 mL	3 mL			

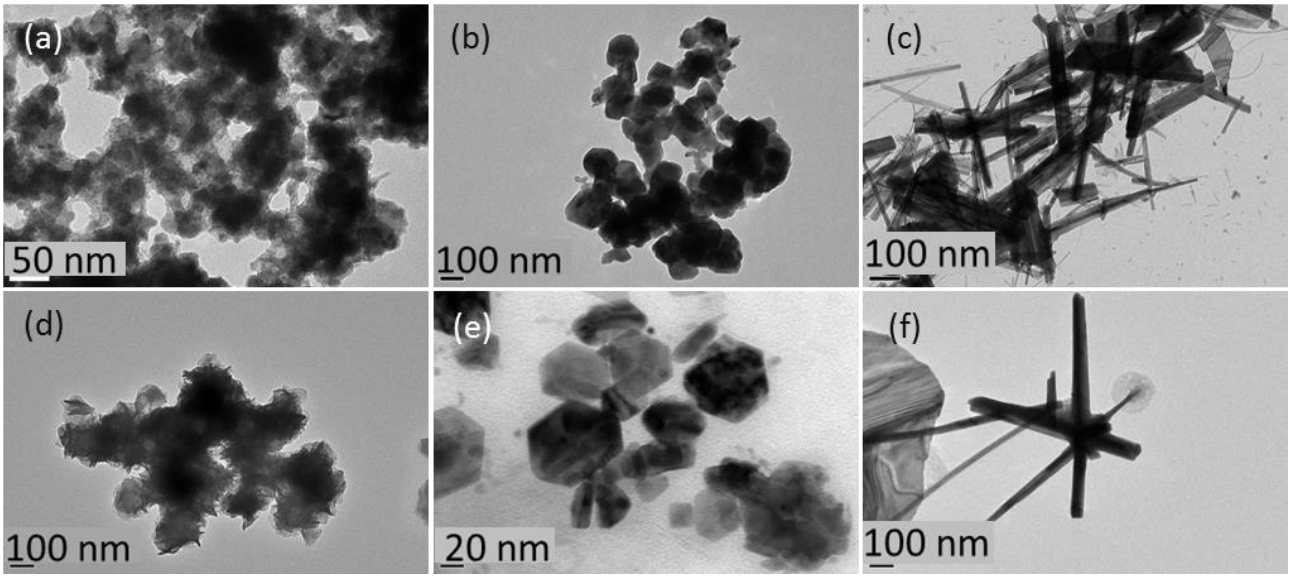

Figure 3.11. (a-f) TEM images of the six samples listed in Table 3.2.

3.2.9 Optimization of the Experimental Parameters

To conclude, the above experimental parameters can influence the formation of the Ni-Co-Se ternary NCs in terms of structure, composition and morphology. Table 3.3 gives a brief overview about how the parameters can influence the results. Therefore, to synthesize the ternary Ni-Co-Se NCs with pure hexagonal phase, controllable composition and as small size as possible, the following parameters are needed: suitable ratios of OAm-Se, $Co(acac)_2$, $Ni(acac)_2$ as Se, Co and Ni precursors, respectively, ODE as solvent, no surfactant, reaction time of 5 min, reaction temperature of 250 °C, using classical heat-up procedure as the synthesis method.

Table 3.3. Sumary of the influence of the experimental parameters.

Parameters		**Structure**	**Composition**	**Morphology**
Se precursor	TOP-Se	metal-rich	Ni/Co ↑	Rod, 5 μm length
	OAm-Se	hexagon	Ni/Co ↓	Sphere, 100 nm
Co precursor	CoI_2	hexagon	Ni/Co ↑	NCs, 50 nm
	$CoCl_2$	hexagon	Ni/Co —	NCs, 50 nm
	$Co(acac)_2$	hexagon	Ni/Co ↓	NCs, 30 nm
Ni precursor	$NiCl_2$	hexagon	Ni/Co ↑	NCs, 50 nm
	$Ni(acac)_2$	metal-rich	Ni/Co ↓	NCs, 50 nm
Solvent	**ODE**	hexagon	Ni/Co ↑	NCs, 50 nm
	Octyl ether	hexagon	Ni/Co ↑	NCs, 50 nm
	TOPO	metal-rich	Ni/Co ↓	NCs, 25 nm
	OAm	metal-rich	Ni/Co ↓	NCs
Surfactant	ODPA			NCs, 50 nm
	HPA			NCs, 50 nm
	OAc			sphere, 100 nm
	OAc + OAm			sphere, 100 nm
	OAm	hexagon	Ni/Co ↑	NCs, 30 nm
	No surfactant	hexagon	Ni/Co ↓	NCs,25 nm
	DDT	metal-poor	Ni/Co ↓	NCs, 10 nm
Reaction	1 min	oxide + hexagon	Ni/Co ↑	NCs, 25 nm
Time	**5 min**	hexagon	Ni/Co ↑	
	30 min	hexagon + metal-rich	Ni/Co —	
	60 min	metal-rich	Ni/Co ↓	
Reaction	150 °C	oxide (more) + hexagon	Ni/Co ↓	NCs, 5 nm
Temperature	200 °C	hexagon (more) + oxide	Ni/Co —	NCs, 5 nm and 25 nm
	250 °C	hexagon	Ni/Co ↑	NCs, 25 nm
Hot Injection Method		metal-rich		NCs, 50 nm

Based on the above analysis, the ratio of the Ni/Co precursors was tuned to obtain a group of Ni-Co-Se ternary NCs with a Ni/Co ratio arrange from 0 to 1. In a typical synthesis, a desired

amount of $Ni(acac)_2$ and $Co(acac)_2$ precursors (see Table 3.4 for details) was mixed with 10 mL of ODE in a 3-neck flask and dried under vacuum for 1 h at 120 °C. Subsequently, 1 mmol of the as-prepared OAm-Se solution was injected in an Ar atmosphere and the temperature was increased to 250 °C. After 5 min, the reaction mixture was immediately cooled down and quenched with toluene. The resulting NCs were washed twice by precipitation upon addition of ethanol followed by re-dispersion in toluene.

Table 3.4. Synthetic parameters used for the synthesis of binary NiSe and CoSe, ternary Ni-Co-Se NCs. The composition of the samples was measured by ICP.

Sample	$Ni(acac)_2$ (mmol)	$Co(acac)_2$ (mmol)
CoSe	0	1
$Ni_{0.3}Co_{0.74}Se$	0.25	0.75
$Ni_{0.52}Co_{0.56}Se$	0.4	0.6
$Ni_{0.78}Co_{0.28}Se$	0.7	0.3
NiSe	1	0

3.3 Exploration of the Experimental Parameters of Electrochemical Measurements

The electrochemical performance in HER and OER was studied separately to search for the suitable parameters for the as-synthesized electrocatalysts. Similar as the route of the last section, the relative parameters which can influence the results of the electrochemical measurement are performed in this section as well. Different substrates, inks, electrolytes, loading masses and annealing temperatures of the samples were tried to find the optimized combination of parameters for HER and OER.

3.3.1 Influence of Electrolyte

As we introduced in Chapter I, the pH of the electrolyte plays an important role in electrocatalysis as the process of HER and OER in acidic and alkaline solutions are different. In general, HER is more likely to happen in acid solution and OER more likely to happen in alkaline solution because in both cases the ionization of H_2O contributes little to the energy barrier of both the reactions. Here we choose $Ni_{0.52}Co_{0.56}Se$ for HER and CoSe NCs for OER. In HER measurement, 5 mg of $Ni_{0.52}Co_{0.56}Se$ NCs are mixed with 0.95 mL of H_2O and 0.05 mL of Nafion which is used as the dispersant for the sample in H_2O and decrease the resistance of the electrode.

The mixture is sonicated for more than 30 min to obtain uniform and thick ink. To fabricate the electrode, the FTO glasses are cut into 1×1.5 cm^2 squares, then 20 μL of the as-prepared ink is drop casted on the FTO substrate to form a layer of 1×1 cm^2. After all these preparations, the electrodes are used in the electrolyte including 0.5 M H_2SO_4 and 1 M KOH to measure LSV at a scan rate of 10 mV/s. The preparation process for OER is similar except that Ti foil is chosen as the substrate. To compare the results properly, the unit of voltage is converted to V vs. RHE.

Figure 3.12 shows polarization data for the sample in H_2SO_4 and KOH, respectively. Apparently, in H_2SO_4, the sample shows better performance in HER, while OER is prone to happen in KOH solution. These results are in accordance with the above-mentioned regulations that the acid electrolyte is good for HER and the alkaline solution is good for OER. However, the performance of these electrocatalysts is extremely low in either HER or OER, and other parameters should be changed to improve the activity.

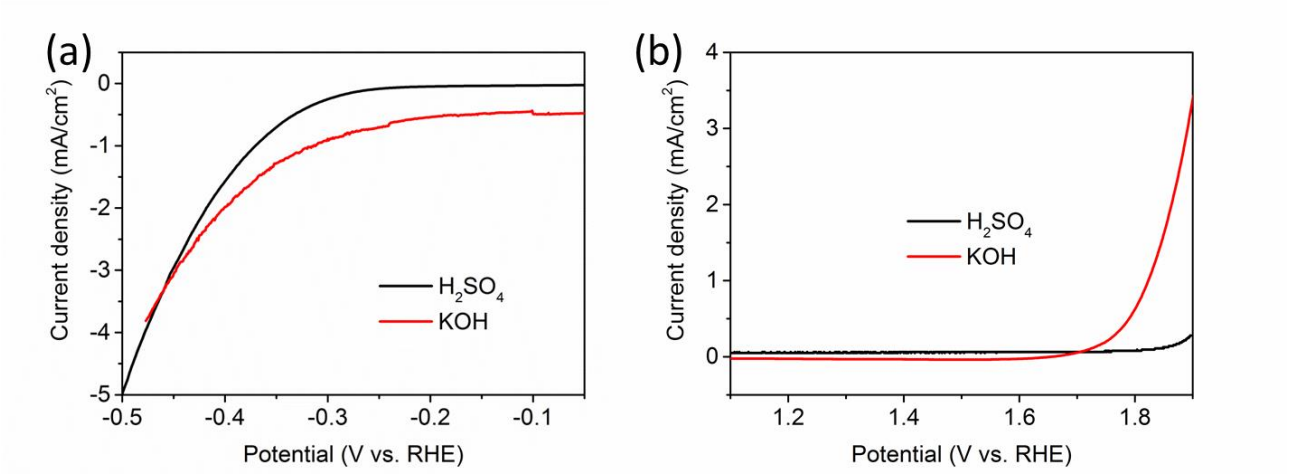

Figure 3.12. Polarization curves of (a) $Ni_{0.52}Co_{0.56}Se$ NCs with different electrolytes in HER and (b) CoSe NCs with different electrolytes in OER.

3.3.2 Influence of Substrate

Based on the known reports, Ti foil and FTO conductive glasses are commonly chosen as substrates in electrochemical measurements because of their excellent conductivity. $Ni_{0.52}Co_{0.56}Se$ NCs are used as the electrocatalyst for both HER and OER. The preparation of the electrocatalyst on the electrode is the same as that introduced in the previous section except that the substrates are different. Then 0.5 M H_2SO_4 and 1 M KOH are chosen as the electrolyte for HER and OER, respectively. The polarization curves shown in Figure 3.13a indicate that the sample with Ti foil as substrate has slightly better HER performance, while in Figure 3.13b, as to OER measurement, the sample with FTO substrate shows better property. The similar phenomena can be also found on

other samples but the reasons remain is not clear.

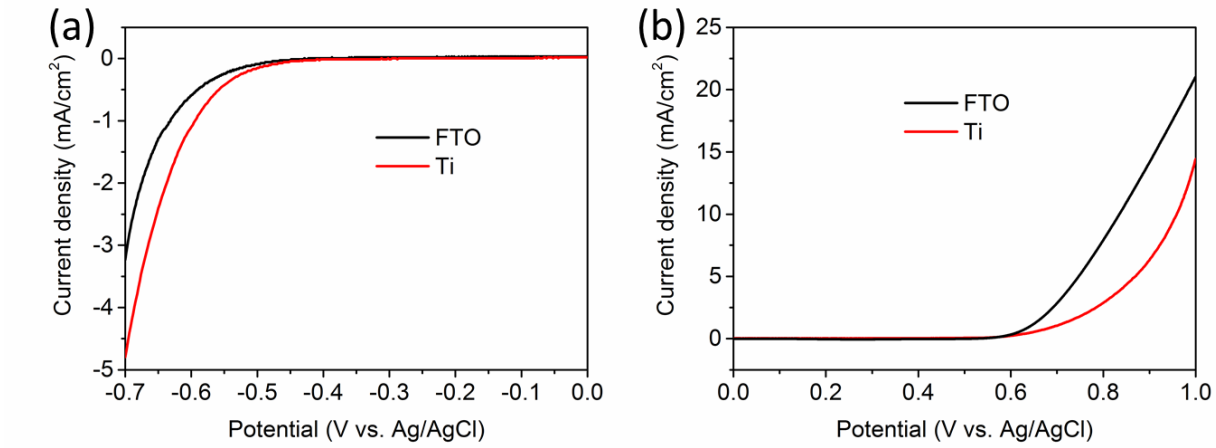

Figure 3.13. Polarization curves of $Ni_{0.52}Co_{0.56}Se$ NCs with different substrates in (a) HER and (b) OER.

3.3.3 Influence of Ink

A good ink should be helpful to disperse the electrocatalysts uniformly and form a homogeneous film on the substrate. Here we tried different types of inks using H_2O or organic liquids as the solvents of the ink. Table 3.5 lists the components of these inks which are commonly used in electrochemical measurements according to the literatures.[28-29] These different kinds of inks are used for HER and OER respectively and other experimental parameters remain the same. The results are shown in Figure 3.14. By comparison, it is obvious that Method 1 which contains only toluene is more suitable for OER and Method 2 which contains only ethanol is more suitable for HER.

Since the samples are from colloidal synthesis and the surface organic ligands are hydrophobic, the organic inks are better for the dispersion of the samples than H_2O, which is proved by the above tests that the sample the organic-based inks has better performance than the sample dispersed in H_2O.

Besides, mixture of conductive carbon with the samples was expected to decrease the resistance of the sample and enhance the activity (Method 4 and Method 5). In reality, the final performance is not improved probably because the sample and the conductive carbon are not able to have a compact connection with each other.

Table 3.5. Components of the inks.

Method	Sample	Solvent	Dispersant
Method 1	5 mg of sample	1 mL of toluene	No

Method	Sample	Solvent	Dispersant
Method 2	5 mg of sample	1 mL of ethanol	No
Method 3	5 mg of sample	0.95 mL of H_2O	0.05 mL of Nafion
Method 4	2.5 mg of sample + 2.5 mg of conductive carbon	1 mL of toluene	No
Method 5	2.5 mg of sample + 2.5 mg of conductive carbon	0.95 mL of H_2O	0.05 mL of Nafion

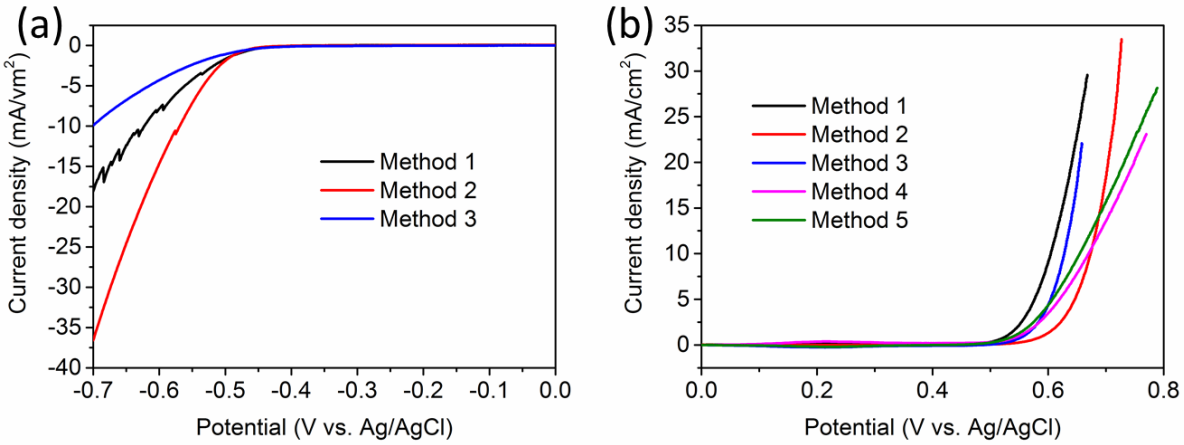

Figure 3.14. (a) Polarization curves of electrodes comprising of CoSe NCs for HER with various catalyst loading amounts. Other experimental parameters: Ti foil as substrate and 0.5 M H_2SO_4 as electrolyte. The loading mass is 250 μL. (b) Polarization curves of electrodes comprising of $Ni_{0.3}Co_{0.74}Se$ NCs for OER with various catalyst loading amounts. Other experimental parameters: FTO as substrate and 1 M KOH as electrolyte. The loading mass is 20 μL.

3.3.4 Influence of Loading Mass

Theoretically, the catalytic activity of HER and OER should increase linearly with the catalyst loading mass. In the present case, however, there is always an optimized loading mass corresponding to the best performance. This is because when the amount of the catalysts is not enough, the provided active sites are limited. If the amount exceeds the optimized amount, the catalysts might form a thick layer inside which no effective contact with the electrolyte takes place. On the other hand, too much amount of catalysts may have negative influence on the resistance of the system and decrease the charge transfer speed since the conductivity of the transition metal selenides is not very good compared to the conductive substrates.

Here we study the loading amount of the catalyst in HER and OER separately. In HER, CoSe is made into ink by Method 7. Then the ink is drop casted on the Ti substrates with the volume of 20, 50, 200, 250 and 300 μL, respectively. The catalytic activity toward HER is measured by the LVS at a potential scan rate of 10 mV/s in 0.5 M H_2SO_4 electrolyte. Figure 3.15a shows the

polarization curves of CoSe with different loading amounts. It is obvious that 200 µL and 250 µL of CoSe ink by Method 7 exhibit the lowest onset potential while CoSe with 250 µL has more current density comparing to CoSe with 200 µL. Thus 250 uL of inks of the samples is chosen as the best loading amount for HER.

In OER, the loading amount of 15 µL, 20 µL and 30 µL are tested for $Ni_{0.3}Co_{0.74}Se$ NCs which are made into ink my Method 1. The OER activity is investigated in 1 M KOH solution by the LVS with a scan rate of 1 mV/s. The polarization curve with the 20 µL of $Ni_{0.3}Co_{0.74}Se$ NCs on the electrode shows the smallest overpotential, thus this amount is chosen for further measurements (Figure 3.15b).

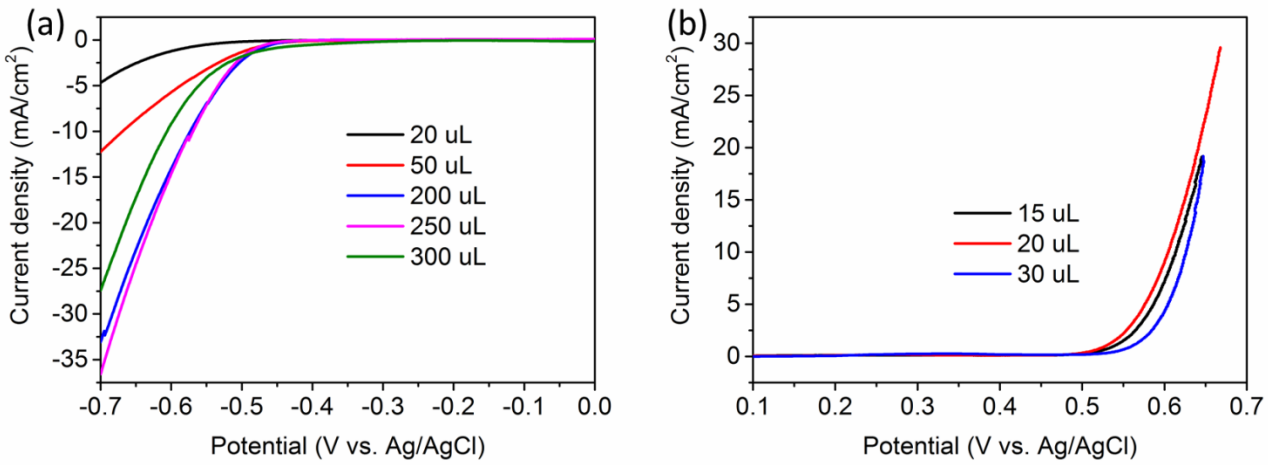

Figure 3.15. (a) Polarization curves of electrodes comprising of CoSe NCs for HER with various catalyst loading amounts. (b) Polarization curves of electrodes comprising of $Ni_{0.3}Co_{0.74}Se$ NCs for OER with various catalyst loading amounts.

3.3.5 Optimization of the Experimental Parameters

The results of our experiments evidence that the type of electrolyte, substrate, ink and the loading mass play an important role in the electrochemical measurement. The performance can be improved dramatically by choosing the right combination of parameters. In the case of HER, a suitable combination can be 0.5 M H_2SO_4, Ti foil, the ink with ethanol and 250 µL of loading mass; while in the case of OER of these system of samples, better performance can be gained by 1 M KOH, TFO glasses, the ink with toluene and 20 µL of loading mass. These parameters are used in all the samples for the next measurements.

3.4 Results of Electrochemical Measurements and Discussion

3.4.1 Conventional Characterization

In section 3.2, we synthesized binary and ternary Ni-Co-Se NCs with CoSe, $Ni_{0.3}Co_{0.74}Se$, $Ni_{0.52}Co_{0.56}Se$, $Ni_{0.78}Co_{0.28}Se$ and NiSe compositions, as revealed by our ICP elemental analysis (see Table 3.2). The TEM images of the samples, which are reported in Figure 3.16, indicated that the size of the NCs was around 10 nm in all cases except for NiSe NCs, which exhibited a mean diameter of 25 nm. Our XRD analysis revealed that all the NC products had the same hexagonal crystal structure, with no presence of secondary phases (see Figure 3.16f). In more detail, the XRD patterns of both NiSe and CoSe NCs well matched those of bulk hexagonal NiSe (ICSD number: 29310) and CoSe (ICSD number: 53959), respectively, while the reflections that were observed for Ni-Co-Se NCs were systematically located between those of the CoSe and NiSe hexagonal structures, suggesting the formation of alloyed NCs (see Figure 3.16f): the increase in the Ni content in Ni-Co-Se NCs led to a shift of the XRD peaks toward lower 2-theta values, indicating an expansion of the lattice parameters. This is in agreement with the larger unit cell of hexagonal NiSe (a=3.66 Å, c=5.33 Å) compared to that of CoSe (a=3.594 Å, c=5.277 Å).

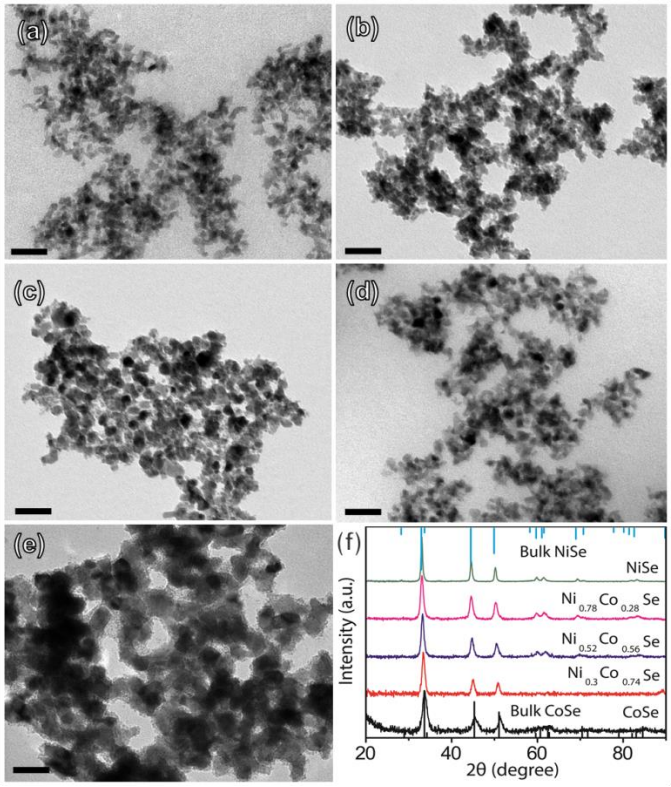

Figure 3.16. (a-e) TEM images and (f) XRD patterns of (a) CoSe, (b) $Ni_{0.3}Co_{0.74}Se$, (c)

$Ni_{0.52}Co_{0.56}Se$, (d) $Ni_{0.78}Co_{0.28}Se$ and (e) NiSe NCs. The scale bar in each panel is 50 nm. (f) The bulk reflections of hexagonal NiSe (ICSD number 29310) and CoSe (ICSD number 53959) are also reported by means of light blue and black bars, respectively.

3.4.2 HER

This group of samples is used for HER with the experimental parameters optimized in the previous section. The electrochemical results are evaluated by using LSV at a scan rate of 10 mV/s and the results can be seen in Figure 3.17. Surprisingly, binary CoSe and NiSe NCs show lower onset potentials and higher current density at the same potential level than the various ternary samples, which means the alloying of the cations is not helpful to improve the performance under the current experimental conditions. Then we tried other strategy to improve the performance which will be discussed in chapter V.

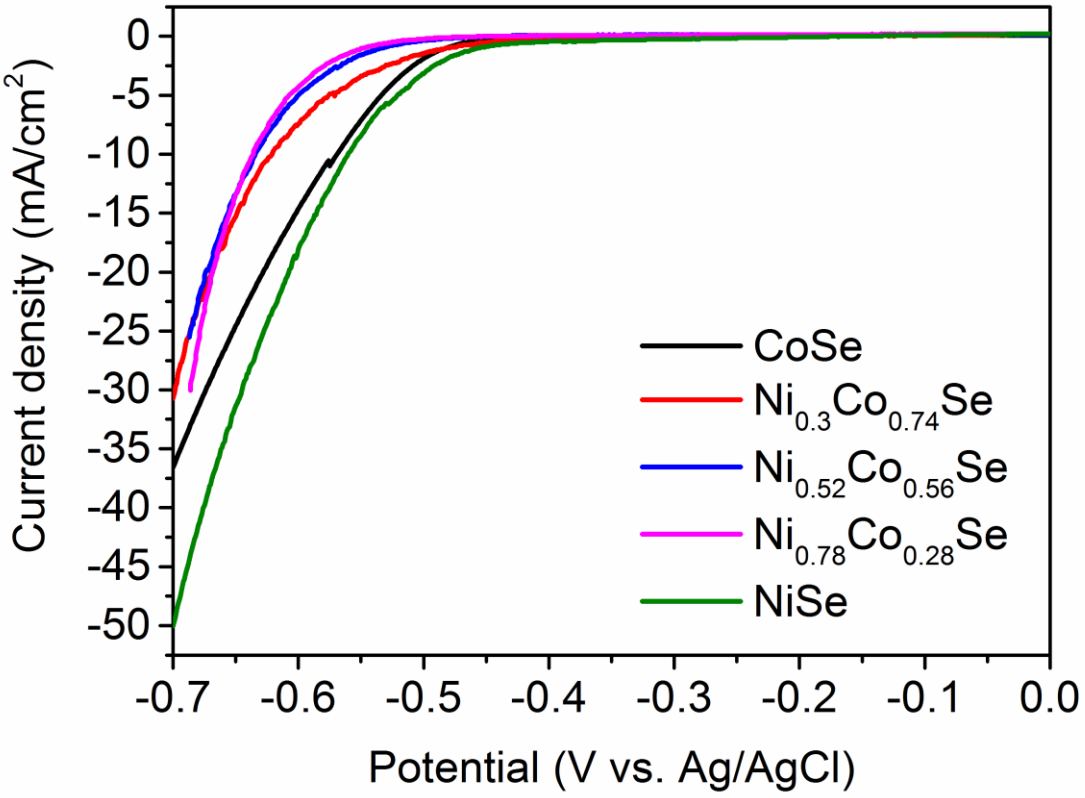

Figure 3.17. Polarization curves in HER of binary and ternary Ni-Co-Se NCs.

3.4.3 OER

The above group of samples were also used for OER with the optimized parameters concluded in section 3.3.

The synthesized NCs were deposited on FTO substrates and their electrocatalytic OER properties were evaluated (see the Experimental Section for details). The resulting polarization curves are reported in Figure 3.18a. It is evident that the onset potentials for the OER heavily depend on the composition of the NCs. In particular, NiSe NCs exhibited the highest onset potential, which systematically decreased when the amount of Co increased, reaching the lowest value of 272 mV in the $Ni_{0,3}Co_{0,74}Se$ composition (see Figure 3.18a, red curve). This value then raised to 317 mV in the samples with no Ni, i.e. in the CoSe NCs (see Figure 3.18a, black curve). In order to elucidate the underlying OER mechanism, the obtained LSV plots were fitted using the Tafel equation.[30-31] From the Tafel plots, which are reported in Figure 3.18b, the Tafel slopes for CoSe and $Ni_{0.3}Co_{0.74}Se$ were calculated to be ~67 and ~76 mV/dec, respectively, indicating that $Ni_{0.3}Co_{0.74}Se$ NCs have slightly slower OER kinetics than CoSe NCs. The Tafel slopes of the $Ni_{0.52}Co_{0.56}Se$, $Ni_{0.78}Co_{0.28}Se$ and NiSe samples were ~83, ~184 and ~286 mV/dec, respectively, i.e. they had slower OER kinetics than the $Ni_{0.3}Co_{0.74}Se$ and CoSe samples (see Table 3.6). It is worth to highlight here that since LSV measurements were conducted at a very low scan rate (1 mV/s), any capacitive contribution to the measured OER currents should be minimal. The specific activity of the catalysts was evaluated by TOF calculation, which refers to the rate of O_2 molecules that evolved per metal atom per second. Figure 3.18c and Table 3.6 demonstrate that the TOF improved up to three times upon the optimization of the ternary Ni-Co-Se NCs' composition. The CVs of samples measured at a sweep rate of 10 mV/s are provided in Figure 3.18d to better explain the observed improvements in the OER. It can be seen that the best performing sample shows the largest pseudocapacitive peaks, indicating the increase of the electrochemically active surface area of the catalyst. On the other hand, the NiSe NCs did not show any pseudocapacitive peak in the same range, indicating that no formation of Ni oxide species took place, thus explaining the observed poor performance of NiSe NCs in the OER.[32]

Furthermore, our impedance spectroscopy analyses indicated that the series resistance (R_s) of the samples decreased from 12.9 Ω for CoSe NCs to 11.2 Ω for $Ni_{0.3}Co_{0.74}Se$ NCs, before rising again at higher Ni contents (see Figure 3.18e, f and Table 3.6). Since all other parameters were kept constant in all cases, the observed R_s of the systems could be considered to be directly related to the electrical conductivity of the NCs. Thus, we concluded that the incorporation of an optimal amount of Ni in CoSe NCs (reaching a Ni/Co ratio of 1/2.5) led not only to an increase in the overall electrical conductivity of the sample, but also to a decrease of the onset potential for the OER. These results are in line with the study of Bates *et al*., in which they observed improvements in the OER properties when going from Ni-oxide to Ni, Co-oxide catalysts, most likely as a consequence of the better electrical conductivity of the latter.[33-35]

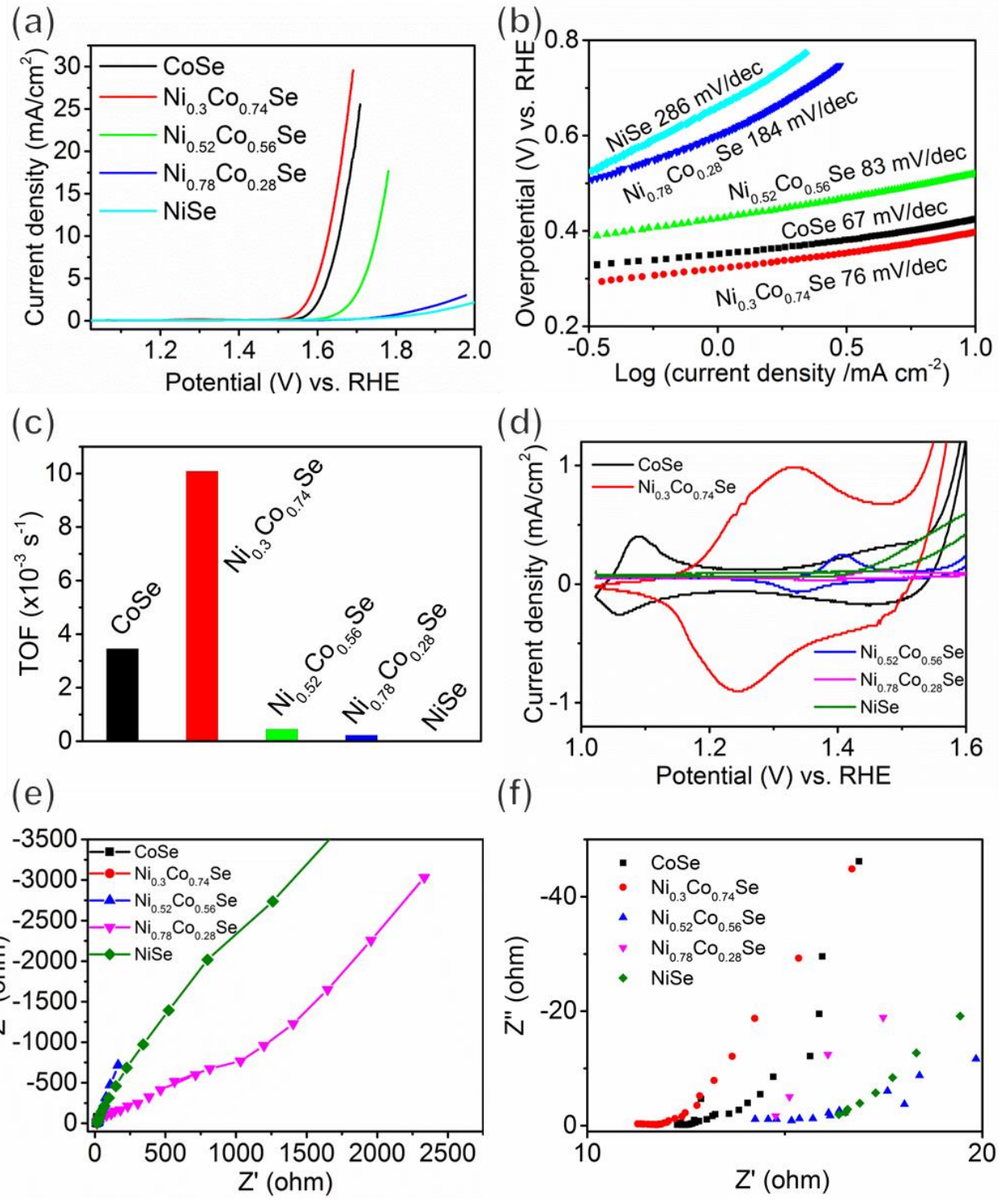

Figure 3.18. (a) LSVs measured at a sweep rate of 1 mV/s, (b) Tafel plots, (c) TOF values at η = 0.35 V, (d) CVs, (e) impedance spectra of electrodes measured at open circuit potential and (f) magnification of (e) in high frequency area of binary and ternary Ni-Co-Se NCs.

Table 3.6. Various electrochemical parameters of Ni-Co-Se-FTO electrodes.

Sample	Onset potential (mV)	η/mV at j = 10 mA/cm^2	Tafel slope (mV/dec)	Rs (Ω)/cm^2	TOF ($\times 10^{-3}$ s^{-1})
CoSe	317	425	67	12.9	3.46
$Ni_{0.3}Co_{0.74}Se$	277	397	76	11.2	10.09
$Ni_{0.52}Co_{0.56}Se$	383	520	83	14.2	0.45
$Ni_{0.78}Co_{0.28}Se$	504	-	184	14.8	0.23
NiSe	507	-	286	16.4	0.04

In order to better understand the composition and the structure of the actual active catalyst, we also carried out XRD and ICP elemental analyses of representative CoSe, $Ni_{0.3}Co_{0.74}Se$ and NiSe NC samples after performing the OER. The XRD patterns of the cycled CoSe and $Ni_{0.3}Co_{0.74}Se$ NCs exhibited no diffraction peaks, apart from those which were related to the substrate, while the NiSe NCs retained their hexagonal structure (see Figure 3.19). These results were consistent with what was observed during ICP elemental analysis: after the OER, NiSe NCs preserved their original stoichiometry, whereas no residual Se was found in the CoSe and $Ni_{0.3}Co_{0.74}Se$ samples, in which Co and/or Ni were the only elements detected. It should be noted that we measured the Ni/Co ratio of the $Ni_{0.3}Co_{0.74}Se$ NCs before and after the OER, and it was found to be constant.

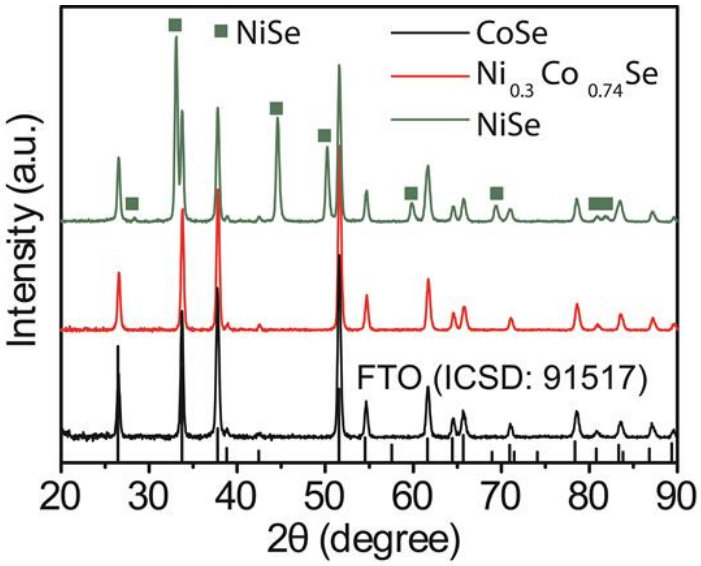

Figure 3.19. XRD patterns of CoSe, $Ni_{0.3}Co_{0.74}Se$ and NiSe NCs on FTO substrates after OER.

To have a better understanding of the chemical, structural and morphological evolution of the $Ni_{0.3}Co_{0.74}Se$ NC upon OER, we also performed HRTEM analyses. HRTEM micrographs of the starting $Ni_{0.3}Co_{0.74}Se$ sample (Figure 3.20b) indicated that the as synthesized NCs are monocrystalline and they exhibit the expected hexagonal crystal structure, as revealed by XRD (see Figure 3.16f and Figure 3.20a). Moreover, the STEM-EDS elemental mapping revealed a uniform distribution of Ni, Co and Se elements in the NCs (Figure 3.20c).

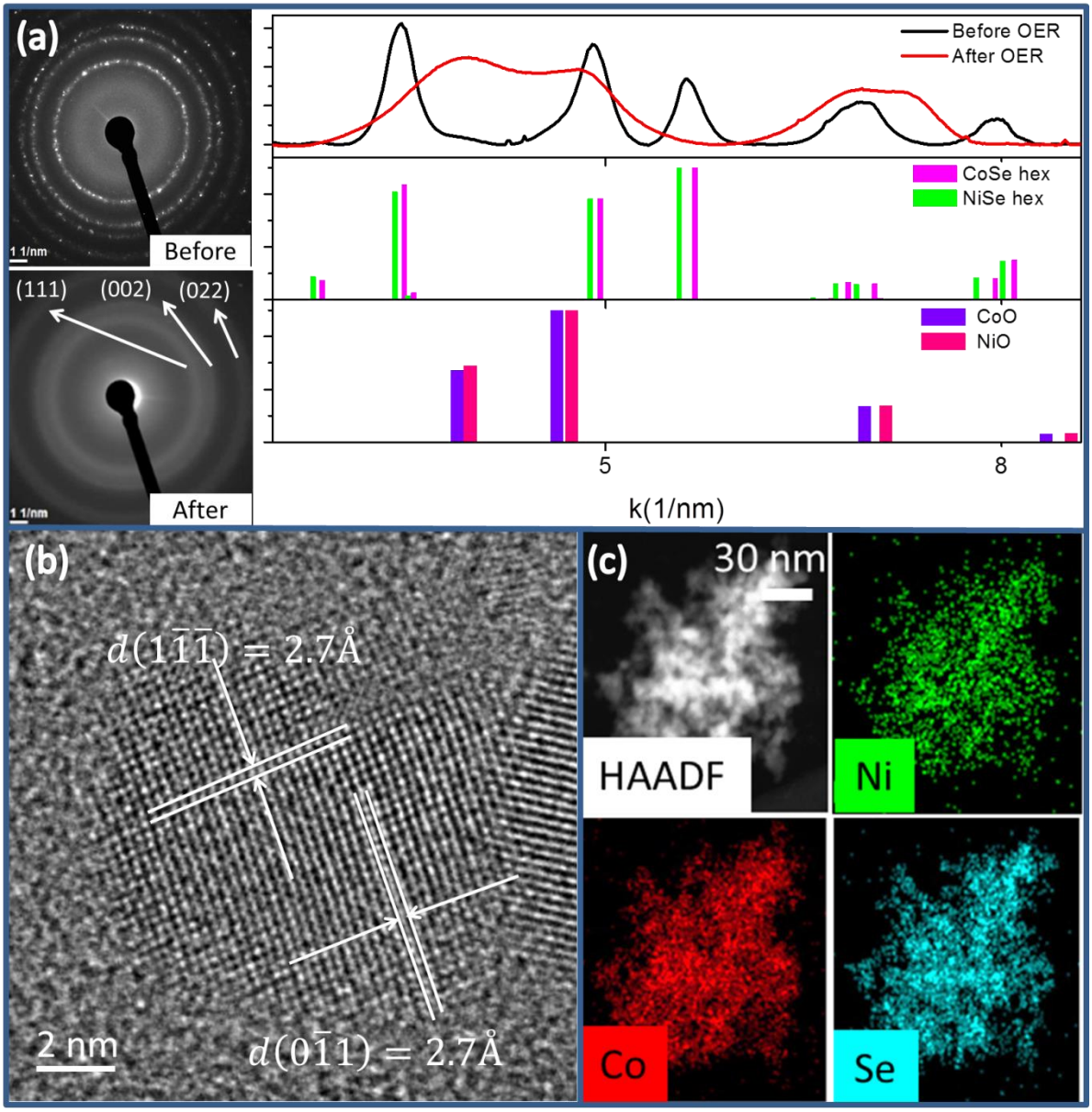

Figure 3.20. (a) SAED patterns of $Ni_{0.3}Co_{0.74}Se$ NCs before and after the OER. (b) HRTEM image of $Ni_{0.3}Co_{0.74}Se$ NCs before OER, exhibiting the expected hexagonal CoSe crystal structure and characterized by the absence of crystal defects. (c) EDS elemental mapping of a group of $Ni_{0.3}Co_{0.74}Se$ NCs before OER.

However, a profound restructuring of the NCs was observed after the OER: the HRTEM analyses evidenced the presence of a major fraction of amorphous Ni, Co- based nanoparticles and a minor fraction of NCs whose crystal structure could be ascribed either to cubic CoO or NiO (ICSD numbers: 9865 and 9866, respectively), as these two structures have similar lattice parameters (see Figure 3.21a, b and Figure 3.20a). Furthermore, STEM-EDS elemental mapping and spectra both revealed that these particles only contained Ni, Co and O (with a Ni/Co ratio of 1/2.5), but no Se, confirming what had already been measured by ICP (see Figure 3.21c and d). It should be also mentioned that no any Pt element was detect in the sample, which means the Pt counter electrode does not affect the performance.

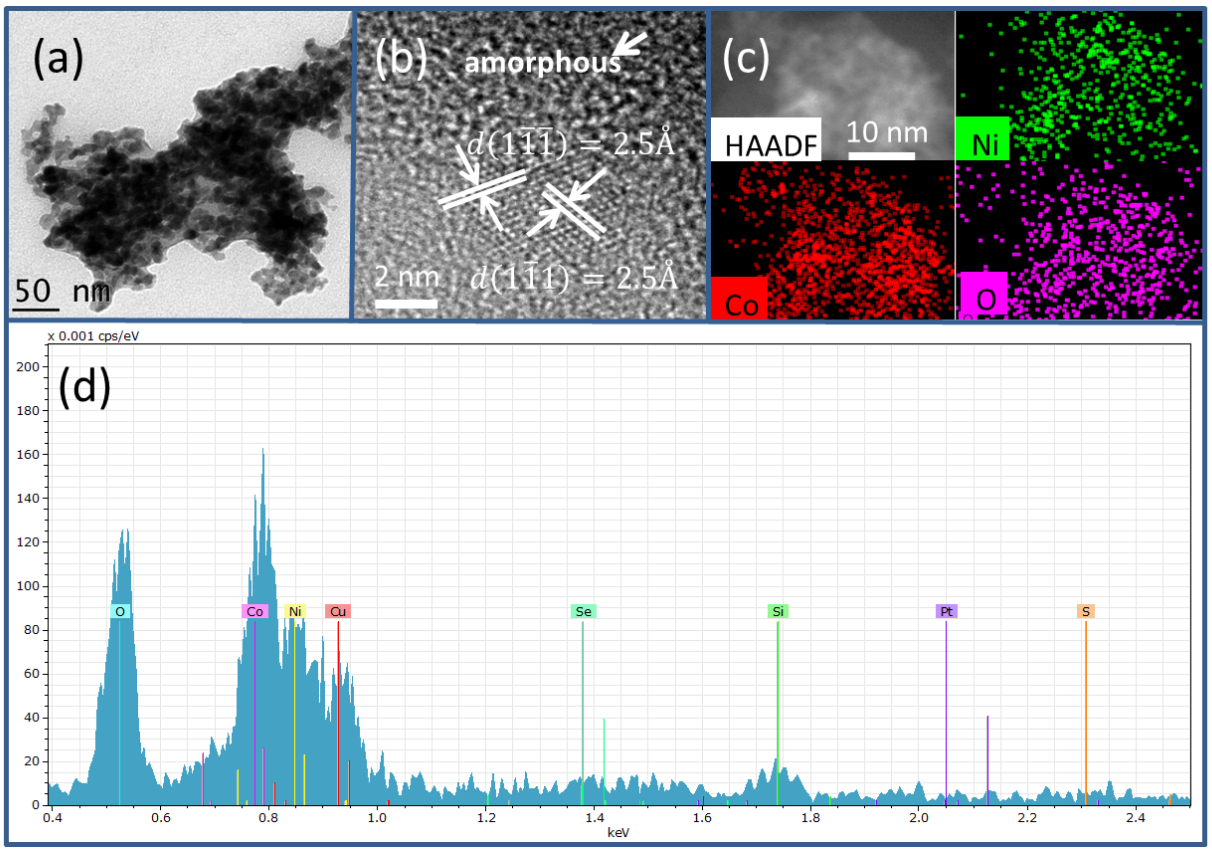

Figure 3.21. (a) TEM image and (b) HRTEM image of $Ni_{0.3}Co_{0.74}Se$ NCs after OER, showing the presence of both amorphous particles and a small fraction of tiny CoO or NiO NCs. (c) EDS elemental mapping and (d) EDS spectra of $Ni_{0.3}Co_{0.74}Se$ NCs after OER.

The XPS analysis of $Ni_{0.3}Co_{0.74}Se$ NCs before and after OER was performed. In Figure 3.22a, before OER, the as-made NCs exhibited mostly Ni^{2+} species on the surface with a weak shoulder peak at around 852.9 eV from metallic Ni. While after OER, the metallic peak disappeared totally, with only the Ni^{2+} peaks existing. Similar results are also observed in the case of Co (Figure 3.22b).

These results indicate that before OER, there are two oxidation states of Ni and Co inside the ternary selenides. However, for the metal oxides after OER, the only existing species are Ni^{2+} and Co^{2+}. XPS analyses of ternary NCs on Se 3d high-resolution spectra before and after OER further again confirmed our findings: while the Se signal disappeared upon OER, the position of the Ni and Co peaks shifted to higher binding energies, suggesting the evolution of the catalyst from Ni-Co-Se to Ni-Co oxide/hydroxide materials (see Figure 3.22c). These results are in agreement with those reported by different groups, who observed the transformation of MX nanostructures (MX, M = Co, Ni, Fe; X = S, Se, Te) into the corresponding metal oxides/hydroxides upon OER in alkaline conditions.[18-20, 36] The oxidation process, at the same time, was shown to affect the chalcogen anions, which are released from the starting nanostructures in the form of SeO_x species.[20, 36-39] Importantly, XPS analysis clearly demonstrates that Pt is not present at the surface of the Ni-Co-based electrodes after OER. Indeed, no Pt 4f peaks are detected in the typical energy range between 70 and 75 eV [NIST X-ray Photoelectron Spectroscopy Database, Version 4.1 (National Institute of Standards and Technology, Gaithersburg, 2012); http://srdata.nist.gov/xps/].

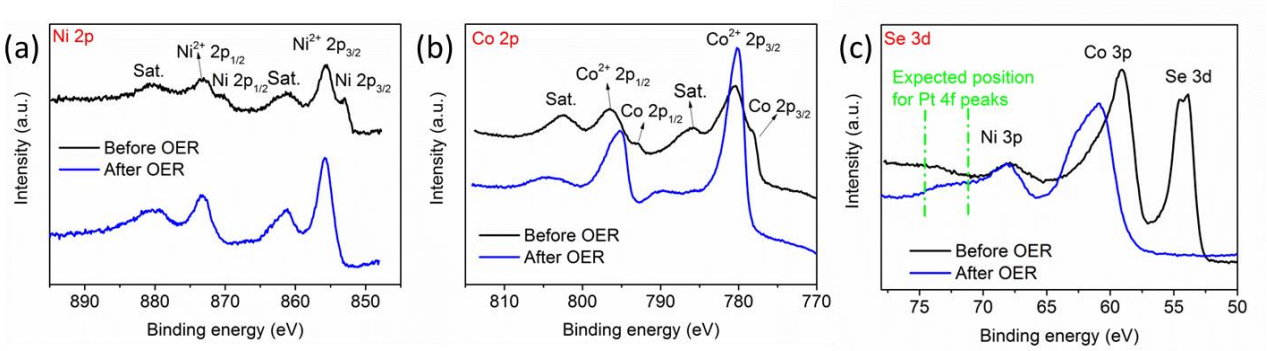

Figure 3.22. High-resolution (a) Ni, (b) Co and (c) Se spectra of $Ni_{0.3}Co_{0.74}Se$ NCs before and after OER.

In order to study the fate of organic ligands we performed a Fourier transform infrared spectroscopy study on a Ni-Co-Se NC film before and after five CVs of OER (see Figure 3.23 for details). We prepared two samples in order to acquire FTIR spectra of $Ni_{0.3}Co_{0.74}Se$ NCs before and after the OER. A first sample was obtained by mixing $Ni_{0.3}Co_{0.74}Se$ NCs with a KBr powder using a NCs/KBr ratio of 1% in weight (i.e. 0.5 mg of NCs and 50 mg of KBr). The resulting powder was put in a die and pressed for 3 minutes with 3 Tons, producing a 12 mm diameter disk. A second sample was obtained by scratching a film of $Ni_{0.3}Co_{0.74}Se$ NCs, which was previously subjected to five CVs of OER, and mixing it with KBr powder using a NCs/KBr ratio of 1% in weight. Also in this case the resulting powder was put in a die and pressed for 3 minutes with 3 Tons, producing a

12 mm diameter disk. The disks were analyzed using a FTIR Vertex 70v, running 128 scans per sample in the 4000-500 cm^{-1} range, with a resolution of 4 cm^{-1}.

In the FTIR spectra of $Ni_{0.3}Co_{0.74}Se$ NCs before and after five CVs of OER, it is possible to detect the presence of oleylamine, the surfactant used for the synthesis of Ni-Co-Se NCs: the peaks at 2846 and 2920 cm^{-1} can be assigned to the symmetric and asymmetric CH_2 stretching modes, respectively; the peak at 1642 cm^{-1} is due to the ν (C=C) stretching mode, the peak at 1591 cm^{-1} is due to the NH_2 scissoring mode.[40-41] Therefore, the native ligands (*i.e.* oleylamine) were present on our catalyst even after OER. This finding suggests that oleylamine molecules, which are not soluble in the electrolyte, most likely bind to Ni and Co oxide/hydroxide species that form upon the transformation of native Ni-Co-Se NCs.

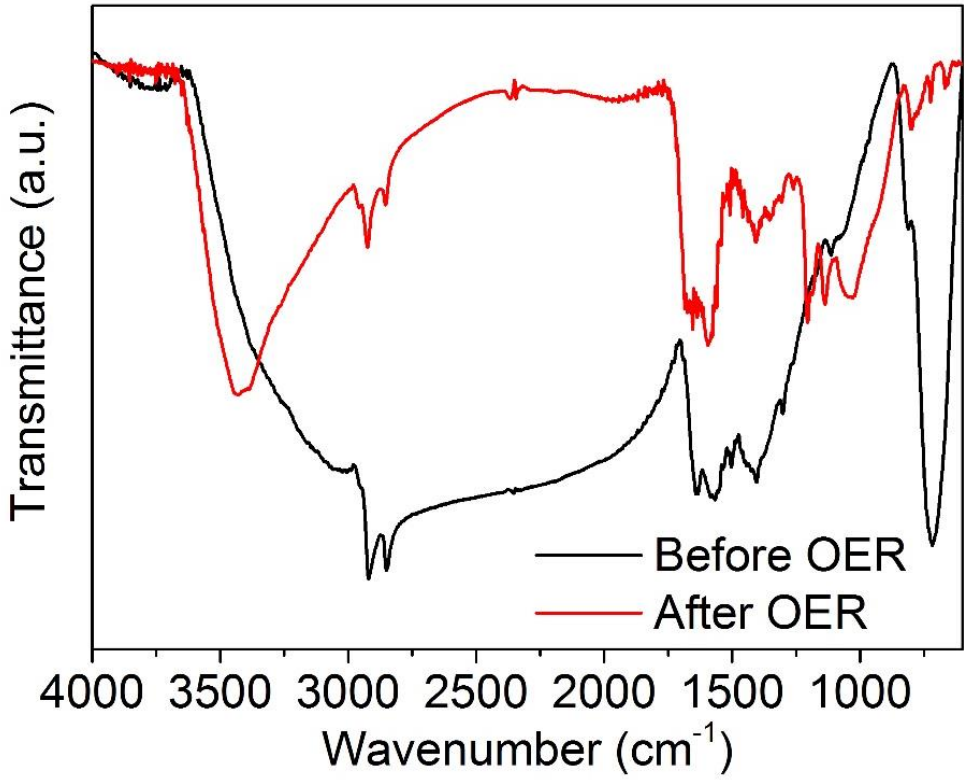

Figure 3.23. FTIR spectra of $Ni_{0.3}Co_{0.74}Se$ NCs before (black line) and after (red line) five CVs of OER.

Overall, our findings indicate that Ni-Co-Se NCs underwent a phase transformation under OER conditions, releasing Se anions and forming mainly amorphous Ni-Co oxide/hydroxide species, which were the actual catalytic materials.[18-20, 36, 42-48] The OER performance of such species depended on their relative composition: an optimal Ni/Co ratio was the key parameter not only to increasing the conductivity and the number of active sites of the final material, but also to lowering

its onset potential. However, the NiSe NCs did not undergo any phase changes and they retained their crystal structure under OER conditions. In this case, differently from what observed by other groups, no active Ni oxide/hydroxide species were found, explaining the poor performance of our NiSe NCs in the OER.[20, 36, 43, 49]

3.5 Conclusions

In conclusion, we have developed a colloidal synthesis method to produce binary NiSe, CoSe, ternary Ni-Co-Se NCs with controllable compositions and identical hexagonal crystal structures. First of all, we tried the HER performance of these samples but still the binary compounds have better activity, which means the alloy strategy is not helpful to promote the electrocatalytic activity in HER.

Then, we studied, in detail, variations in the OER catalytic activity of these NC systems as a function of their composition. We observed that, under OER conditions, ternary Ni-Co-Se NC samples underwent a complete chemical transformation, losing the chalcogen anions and forming Ni, Co hydroxides/hydroxide compounds, which are the actual catalytic species for OER. While the oxidation of metal chalcogenides upon OER has been reported by different groups, not much is known on how the composition and the structure of starting materials affect this process and the properties of the resulting active compounds. What we found is that the activity of the oxide/hydroxide products are strongly dependent on the composition of the starting NCs. In more detail, when working with Ni-Co-Se NCs, amorphous Ni, Co hydroxides/hydroxide nanoparticles were mainly produced. Interestingly, the activity of such species was found to be optimal at a Ni/Co ratio of 1/2.5.

References

1. Sivanantham, A.; Ganesan, P.; Shanmugam, S. Hierarchical $NiCo_2S_4$ Nanowire Arrays Supported on Ni Foam: An Efficient and Durable Bifunctional Electrocatalyst for Oxygen and Hydrogen Evolution Reactions. *Adv. Funct. Mater.* **2016,** *26*, 4661-4672.
2. Liu, B.; Zhao, Y. F.; Peng, H. Q.; Zhang, Z. Y.; Sit, C. K.; Yuen, M. F.; Zhang, T. R.; Lee, C. S.; Zhang, W. J. Nickel-Cobalt Diselenide 3d Mesoporous Nanosheet Networks Supported on Ni Foam: An All-pH Highly Efficient Integrated Electrocatalyst for Hydrogen Evolution. *Adv. Mater.* **2017,** *29*.
3. Faber, M. S.; Lukowski, M. A.; Ding, Q.; Kaiser, N. S.; Jin, S. Earth-Abundant Metal Pyrites (Fes_2, Cos_2, Nis_2, and Their Alloys) for Highly Efficient Hydrogen Evolution and Polysulfide Reduction Electrocatalysis. *J. Phys. Chem. C* **2014,** *118*, 21347-21356.
4. Liu, Q.; Jin, J.; Zhang, J. $NiCo_2S_4$@Graphene as a Bifunctional Electrocatalyst for Oxygen Reduction and Evolution Reactions. *ACS Appl. Mater. Interfaces* **2013,** *5*, 5002-8.
5. Xia, C.; Jiang, Q.; Zhao, C.; Hedhili, M. N.; Alshareef, H. N. Selenide-Based Electrocatalysts and

Scaffolds for Water Oxidation Applications. *Adv. Mater.* **2016,** *28*, 77-85.
6. Shinde, D. V.; Trizio, L. D.; Dang, Z.; Prato, M.; Gaspari, R.; Manna, L. Hollow and Porous Nickel Cobalt Perselenide Nanostructured Microparticles for Enhanced Electrocatalytic Oxygen Evolution. *Chem. Mater.* **2017,** *29*, 7032-7041.
7. Chi, J.-Q.; Yan, K.-L.; Xiao, Z.; Dong, B.; Shang, X.; Gao, W.-K.; Li, X.; Chai, Y.-M.; Liu, C.-G. Trimetallic Ni-Fe-Co Selenides Nanoparticles Supported on Carbon Fiber Cloth as Efficient Electrocatalyst for Oxygen Evolution Reaction. *Int. J. Hydrogen Energy* **2017,** *42*, 20599-20607.
8. Nikdov, I.; Darkaoui, R.; Zhecheva, E.; Stoyanova, R.; Dimitrov, N.; Vitanov, T. Electrocatalytic Activity of Spinel Related Cobaltites $M_xCo_{3-x}O_4$ (M = Li, Ni, Cd in the Oxygen Evolution Reaction. *J. Electroanal. Chem.* **1997,** *429*, 157-168.
9. Yang, Y.; Fei, H.; Ruan, G.; Xiang, C.; Tour, J. M. Efficient Electrocatalytic Oxygen Evolution on Amorphous Nickel-Cobalt Binary Oxide Nanoporous Layers. *ACS Nano* **2014,** *8*, 9518-9523.
10. Fang, W.; Liu, D.; Lu, Q.; Sun, X.; Asiri, A. M. Nickel Promoted Cobalt Disulfide Nanowire Array Supported on Carbon Cloth: An Efficient and Stable Bifunctional Electrocatalyst for Full Water Splitting. *Electrochem. Commun.* **2016,** *63*, 60-64.
11. Zhang, J.; Zhao, Z.; Xia, Z.; Dai, L. A Metal-Free Bifunctional Electrocatalyst for Oxygen Reduction and Oxygen Evolution Reactions. *Nat. Nanotechnol.* **2015,** *10*, 444-452.
12. Peng, Z.; Jia, D.; Al-Enizi, A. M.; Elzatahry, A. A.; Zheng, G. From Water Oxidation to Reduction: Homologous Ni-Co Based Nanowires as Complementary Water Splitting Electrocatalysts. *Adv. Energy Mater.* **2015,** *5*, 1402031.
13. Xu, Y.-Z.; Yuan, C.-Z.; Chen, X.-P. Co-Doped Nise Nanowires on Nickel Foam Via a Cation Exchange Approach as Efficient Electrocatalyst for Enhanced Oxygen Evolution Reaction. *RSC Adv.* **2016,** *6*, 106832-106836.
14. Swesi, A. T.; Masud, J.; Liyanage, W. P. R.; Umapathi, S.; Bohannan, E.; Medvedeva, J.; Nath, M. Textured $NiSe_2$ Film: Bifunctional Electrocatalyst for Full Water Splitting at Remarkably Low Overpotential with High Energy Efficiency. *Sci. Rep.* **2017,** *7*, 2401.
15. De Silva, U.; Masud, J.; Zhang, N.; Hong, Y.; Liyanage, W. P. R.; Asle Zaeem, M.; Nath, M. Nickel Telluride as a Bifunctional Electrocatalyst for Efficient Water Splitting in Alkaline Medium. *J. Mater. Chem. A* **2018,** *6*, 7608-7622.
16. Umapathi, S.; Masud, J.; Swesi, A. T.; Nath, M. $Feni_2se_4$-Reduced Graphene Oxide Nanocomposite: Enhancing Bifunctional Electrocatalytic Activity for Oxygen Evolution and Reduction through Synergistic Effects. *Adv. Sustainable Syst.* **2017,** *1*, 1700086.
17. Chen, W.; Liu, Y.; Li, Y.; Sun, J.; Qiu, Y.; Liu, C.; Zhou, G.; Cui, Y. In Situ Electrochemically Derived Nanoporous Oxides from Transition Metal Dichalcogenides for Active Oxygen Evolution Catalysts. *Nano Lett.* **2016,** *16*, 7588-7596.
18. Zhou, W.; Wu, X.-J.; Cao, X.; Huang, X.; Tan, C.; Tian, J.; Liu, H.; Wang, J.; Zhang, H. Ni_3S_2 Nanorods/Ni Foam Composite Electrode with Low Overpotential for Electrocatalytic Oxygen Evolution. *Energy Environ. Sci.* **2013,** *6*, 2921-2924.
19. Ma, Z.; Zhao, Q.; Li, J.; Tang, B.; Zhang, Z.; Wang, X. Three-Dimensional Well-Mixed / Highly-Densed NiS-CoS Nanorod Arrays: An Efficient and Stable Bifunctional Electrocatalyst for Hydrogen and Oxygen Evolution Reactions. *Electrochim. Acta* **2018,** *260*, 82-91.
20. Han, X.; Tong, X.; Wu, G.; Yang, N.; Guo, X.-Y. Carbon Fibers Supported NiSe Nanowire Arrays as Efficient and Flexible Electrocatalysts for the Oxygen Evolution Reaction. *Carbon* **2018,** *129*, 245-251.
21. Yin, Y.; Erdonmez, C. K.; Cabot, A.; Hughes, S.; Alivisatos, A. P. Colloidal Synthesis of Hollow Cobalt Sulfide Nanocrystals. *Adv. Funct. Mater.* **2006,** *16*, 1389-1399.
22. Zhang, H. T.; Wu, G.; Chen, X. H. Synthesis and Magnetic Properties of NiS_{1+X} Nanocrystallines. *Materials Letters* **2005,** *59*, 3728–3731.
23. Lee, H.; Holloway, P. H.; Yang, H.; Hardison, L.; Kleiman, V. D. Synthesis and Characterization of Colloidal Ternary ZnCdSe Semiconductor Nanorods. *J. Chem. Phys.* **2006,** *125*, 164711.
24. Liu, H.; Owen, J. S.; Alivisatos, A. P. Mechanistic Study of Precursor Evolution in Colloidal Group II-VI

Semiconductor Nanocrystal Synthesis. *J. Am. Chem. Soc.* **2007,** *129*, 305-312.
25. Shao, H.; Huang, Y.; Lee, H.; Suh, Y. J.; Kim, C. O. Cobalt Nanoparticles Synthesis from $Co(CH_3COO)_2$ by Thermal Decomposition. *J. Magn. Magn. Mater.* **2006,** *304*, e28-e30.
26. Sharma, H.; Pulugurtha, M. R.; Tummala, R. Chemical Synthesis of Low-Coercivity, Silica/Co Composites for High-Frequency Magnetic Components. *Mater. Chem. Phys.* **2016,** *175*, 46-53.
27. Kwon, S. G.; Hyeon, T. Formation Mechanisms of Uniform Nanocrystals Via Hot-Injection and Heat-up Methods. *Small* **2011,** *7*, 2685-702.
28. Liao, L.; Wang, S.; Xiao, J.; Bian, X.; Zhang, Y.; Scanlon, M. D.; Hu, X.; Tang, Y.; Liu, B.; Girault, H. H. A Nanoporous Molybdenum Carbide Nanowire as an Electrocatalyst for Hydrogen Evolution Reaction. *Energy Environ. Sci.* **2014,** *7*, 387-392.
29. Mendoza-Garcia, A.; Su, D.; Sun, S. Sea Urchin-Like Cobalt-Iron Phosphide as an Active Catalyst for Oxygen Evolution Reaction. *Nanoscale* **2016,** *8*, 3244-7.
30. Liu, T.; Liang, Y.; Liu, Q.; Sun, X.; He, Y.; Asiri, A. M. Electrodeposition of Cobalt-Sulfide Nanosheets Film as an Efficient Electrocatalyst for Oxygen Evolution Reaction. *Electrochem. Commun.* **2015,** *60*, 92-96.
31. Jin, Y.; Huang, S.; Yue, X.; Du, H.; Shen, P. K. Mo- and Fe-Modified $Ni(OH)_2$/NiOOH Nanosheets as Highly Active and Stable Electrocatalysts for Oxygen Evolution Reaction. *ACS Catal.* **2018,** *8*, 2359-2363.
32. Doyle, R. L.; Godwin, I. J.; Brandon, M. P.; Lyons, M. E. Redox and Electrochemical Water Splitting Catalytic Properties of Hydrated Metal Oxide Modified Electrodes. *Phys. Chem. Chem. Phys.* **2013,** *15*, 13737-83.
33. Bates, M. K.; Jia, Q.; Doan, H.; Liang, W.; Mukerjee, S. Charge-Transfer Effects in Ni–Fe and Ni–Fe–Co Mixed-Metal Oxides for the Alkaline Oxygen Evolution Reaction. *ACS Catal.* **2015,** *6*, 155-161.
34. Yang, J.; Fujigaya, T.; Nakashima, N. Decorating Unoxidized-Carbon Nanotubes with Homogeneous Ni-Co Spinel Nanocrystals Show Superior Performance for Oxygen Evolution/Reduction Reactions. *Sci. Rep.* **2017,** *7*, 45384.
35. Deng, X.; Ozturk, S.; Weidenthaler, C.; Tuysuz, H. Iron-Induced Activation of Ordered Mesoporous Nickel Cobalt Oxide Electrocatalyst for the Oxygen Evolution Reaction. *ACS Appl. Mater. Interfaces* **2017,** *9*, 21225-21233.
36. Tang, C.; Cheng, N.; Pu, Z.; Xing, W.; Sun, X. Nise Nanowire Film Supported on Nickel Foam: An Efficient and Stable 3d Bifunctional Electrode for Full Water Splitting. *Angew. Chem., Int. Ed. Engl.* **2015,** *54*, 9351-5.
37. Chen, W.; Liu, Y.; Li, Y.; Sun, J.; Qiu, Y.; Liu, C.; Zhou, G.; Cui, Y. In Situ Electrochemically Derived Nanoporous Oxides from Transition Metal Dichalcogenides for Active Oxygen Evolution Catalysts. *Nano Lett.* **2016,** *16*, 7588-7596.
38. Mabayoje, O.; Shoola, A.; Wygant, B. R.; Mullins, C. B. The Role of Anions in Metal Chalcogenide Oxygen Evolution Catalysis: Electrodeposited Thin Films of Nickel Sulfide as "Pre-Catalysts". *ACS Energy Lett.* **2016,** *1*, 195-201.
39. Chen, W.; Wang, H.; Li, Y.; Liu, Y.; Sun, J.; Lee, S.; Lee, J. S.; Cui, Y. In Situ Electrochemical Oxidation Tuning of Transition Metal Disulfides to Oxides for Enhanced Water Oxidation. *ACS Cent. Sci.* **2015,** *1*, 244-51.
40. Lee, D. H.; Condrate, R. A.; Lacourse, W. C. Ftir Spectral Characterization of Thin Film Coatings of Oleic Acid on Glasses Part II Coatings on Glass from Different Media Such as Water, Alcohol, Benzene and Air. *J. Mater. Sci.* **2000,** *35*, 4961-4970.
41. Erley, W.; Hemminger, J. C. Spectroscopic Identification of an HCNH Species on Pt(111). *Surf. Sci.* **1994,** *316*, L1025-L1030.
42. Burke, M. S.; Kast, M. G.; Trotochaud, L.; Smith, A. M.; Boettcher, S. W. Cobalt–Iron (Oxy)Hydroxide Oxygen Evolution Electrocatalysts: The Role of Structure and Composition on Activity, Stability, and Mechanism. *J. Am. Chem. Soc.* **2015,** *137*, 3638-3648.
43. Louie, M. W.; Bell, A. T. An Investigation of Thin-Film Ni–Fe Oxide Catalysts for the Electrochemical Evolution of Oxygen. *J. Am. Chem. Soc.* **2013,** *135*, 12329-12337.
44. Chang, J.; Xiao, Y.; Xiao, M.; Ge, J.; Liu, C.; Xing, W. Surface Oxidized Cobalt-Phosphide Nanorods as

an Advanced Oxygen Evolution Catalyst in Alkaline Solution. *ACS Catal.* **2015,** *5*, 6874-6878.

45. Zhao, X.; Yang, Y.; Li, Y.; Cui, X.; Zhang, Y.; Xiao, P. Nico-Selenide as a Novel Catalyst for Water Oxidation. *J. Mater. Sci.* **2016,** *51*, 3724-3734.

46. Friebel, D.; Louie, M. W.; Bajdich, M.; Sanwald, K. E.; Cai, Y.; Wise, A. M.; Cheng, M.-J.; Sokaras, D.; Weng, T.-C.; Alonso-Mori, R.; Davis, R. C.; Bargar, J. R.; Nørskov, J. K.; Nilsson, A.; Bell, A. T. Identification of Highly Active Fe Sites in (Ni,Fe)OOH for Electrocatalytic Water Splitting. *J. Am. Chem. Soc.* **2015,** *137*, 1305-1313.

47. Bates, M. K.; Jia, Q.; Doan, H.; Liang, W.; Mukerjee, S. Charge-Transfer Effects in Ni–Fe and Ni–Fe–Co Mixed-Metal Oxides for the Alkaline Oxygen Evolution Reaction. *ACS Catal.* **2016,** *6*, 155-161.

48. Smith, R. D. L.; Berlinguette, C. P. Accounting for the Dynamic Oxidative Behavior of Nickel Anodes. *J. Am. Chem. Soc.* **2016,** *138*, 1561-1567.

49. Xu, S.-M.; Yan, H.; Wei, M. Band Structure Engineering of Transition-Metal-Based Layered Double Hydroxides toward Photocatalytic Oxygen Evolution from Water: A Theoretical–Experimental Combination Study. *J. Phys. Chem. C* **2017,** *121*, 2683-2695.

Chapter IV Synthesis of Cation and Anion Alloyed Quaternary Ni-Co-S-Se NCs and Their Application in OER

4.1 Introduction

As introduced in chapter III, since the metal atoms are considered as the real active sites for HER and OER, the traditional strategy of the alloying is to mix the transition metals to tune the electron configuration in order to tune the absorption energy of the intermediates thus to decrease the energy barrier of every elemental reaction step in HER and OER. However, as it has been documented in two recent studies, another interesting feature that characterizes Ni and Co chalcogenide based materials is that a synergistic effect may arise from the presence of different kinds of anions like O, S, Se, N, C.[1-6] Duan *et al.* synthesized Co-Fe-P-O compounds with the modulated anions and cations as a bifunctional catalyst for both HER and OER, and the atomic modulation between cation and anion greatly expands the amount of the active sites.[7] This provides the evidence of the possibility to improve the electrocatalytic properties by mixing different kinds of anions. Therein, transition metal compounds containing a mixture of S and Se are synthesized and tested for electrocatalysis. Fang *et al.*, for example, showed that peapod-like $Co(S_xSe_{1-x})_2$ nanoparticles have higher OER and HER performances than pure CoS_2 and $CoSe_2$ ones.[1] Moreover, Hu and co-workers recently demonstrated that the decoration of (NiCo)S/OH nanosheets with elemental Se can improve their OER activity.[2] However, a complete understanding of the roles of S and Se with regard to the catalytic properties of the final materials is still lacking.

All these recent findings have motivated us to investigate not only if optimized OER performances could be achieved via both a cation and anion composition tuning of Ni-Co-S-Se catalysts, but also what the specific roles of the Ni, Co, S and Se elements are. As no quaternary Ni-Co-S-Se NC systems have been reported to date, inspired by the trials from the previous chapter (Fgure 3.6h), we developed the colloidal synthesis based on the previous ternary system and used DDT as S precursor and surfactant at the same time, which allowed us to produce quaternary Ni-Co-S-Se NCs which had the same crystal structure and comparable uniform particle sizes (see Scheme 4.1).

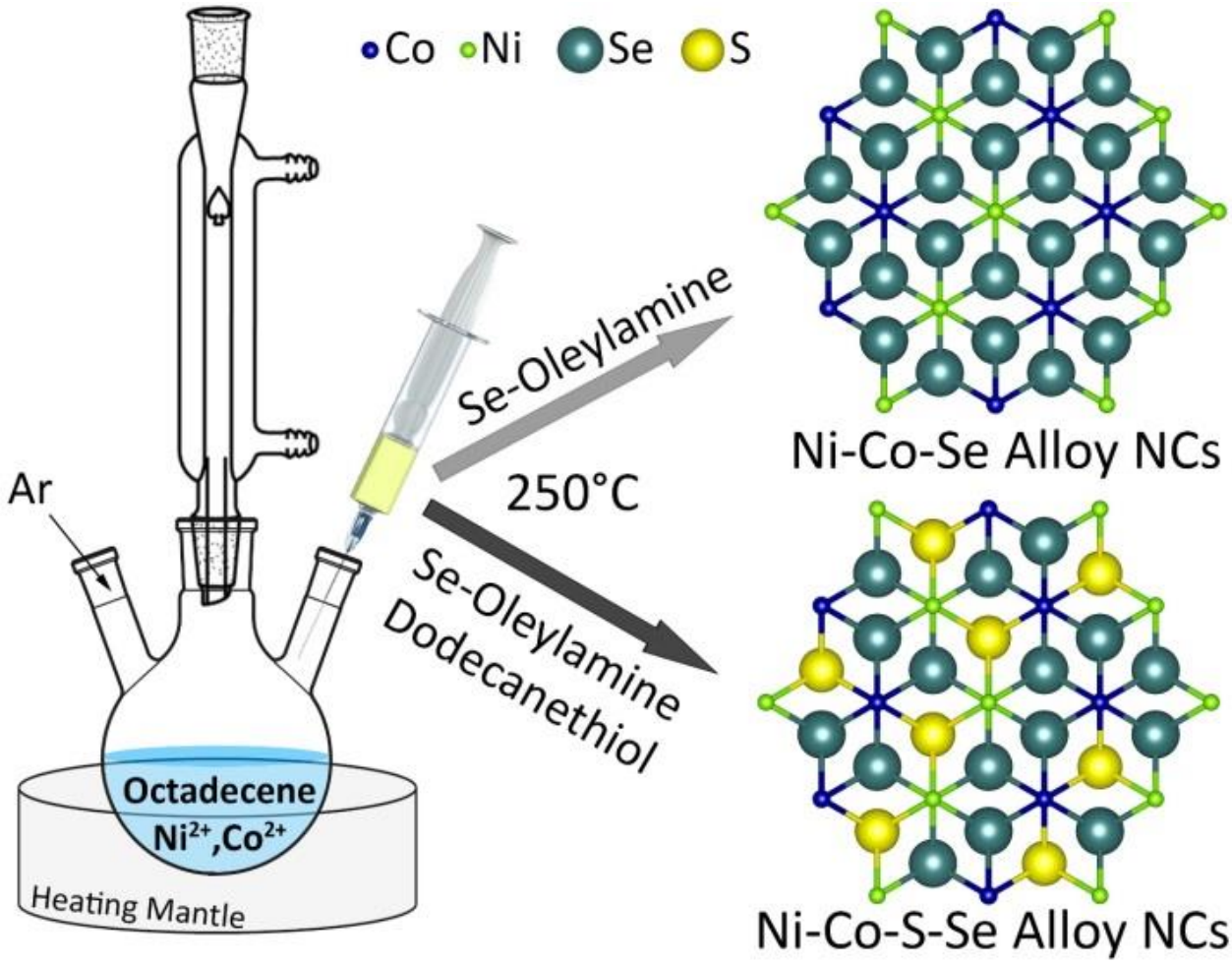

Scheme 4.1. Sketch of the Colloidal Synthesis of Ternary Ni-Co-Se and Quaternary Ni-Co-S-Se Alloy NCs Having the Same Hexagonal Crystal Structure.

Then, we systematically studied the OER catalytic properties and transformations of such NCs during OER under alkaline conditions. Our findings revealed that the insertion of S into Ni-Co-Se NCs, leading to Ni-Co-S-Se NCs, resulted in the formation of small Ni-Co oxide NCs (~1-2 nm in diameter) and $Co(OH)_2$ nanosheets (NSs) under OER conditions, and these had a higher activity than the ternary Ni-Co-Se NCs. We found that $Ni_{0.25}Co_{0.65}S_{0.4}Se_{0.6}$ was the optimal stoichiometry with regards to maximizing the final OER activity, with an onset potential of 262 mV and a OER current density of 10 mA/cm^2 at an overpotential of 358 mV. The TOF of that sample was measured to be 24.84 $\times 10^{-3}$ s^{-1} at an overpotential of 350 mV, which was ~7 times higher than that of the binary CoSe NCs.

4.2 Influence of S/Se

As introduced in Figure 3.6h and i, the use of DDT in the synthesis of Co-Ni-Se NCs can bring

dramatic improvement in decreasing the size as well as inserting S inside the NCs to form quaternary systems, as revealed by XRD, TEM and ICP measurements. Therefore, we decided to tune part of the experimental parameters based on the previous results.

4.2.1 Synthesis of Quaternary Ni-Co-S-Se NCs with Different S/Se Ratios

Influence of the reaction time. To investigate the influence of the reaction time on S/Se ratio, first we used the parameters which was used for synthesizing $Ni_{0.3}Co_{0.74}Se$ NCs and added 0.1 mL of DDT. Figure 4.1 presents the typical structure, morphology and composition of the samples, which are prepared with the reaction time changing from 5 to 120 min. The XRD confirmed the hexagonal phase structure (CoSe, ICSD: 53959) in all the samples (Figure 4.1a). However, when the reaction time is more than 90 min, there is another new hexagonal CoS phase (ICSD: 29305) which is separated from the main CoSe phase.

The ICP elemental analysis confirmed that before 30 min, the S/Se ratio is close to 3:7, while when the reaction time reaches 60 min, the S/Se ratio increases slowly to 4:6 and this ratio is not likely to increase even the time increases. Meanwhile, the Ni/Co ratio after 5 min is close to 1:1, which differs from the Ni/Co precursors ratio (1:3) and the Ni/Co ratio in the sample without S precursor (1:2.5). This means that the addition of DDT might help to increase the amount of Ni^{2+} or decrease the amount of Co^{2+} in the crystals. Fortunately, the Ni/Co ratio can be tuned by increasing the reaction time up to 60 min. When the time is more than 60 min, the Ni/Co ratio seems to increase as well. However, there is a mixture of the phases, it is difficult to calculate Ni/Co ratio in the main phase.

The TEM images reveal the uniform sizes in each sample (Figure 4.1b-f). Furthermore, the size of such NCs increases after 60 min from around 10 nm to 30 nm, indicating that the NCs grow bigger when the reaction time is longer.

Thus, taking into account the reasult from each characterization technique, we can summarize that the reaction time of 60 min is the best reaction time for the synthesis to obtain a similar structure, Ni/Co ratio and size as its corresponding ternary NCs.

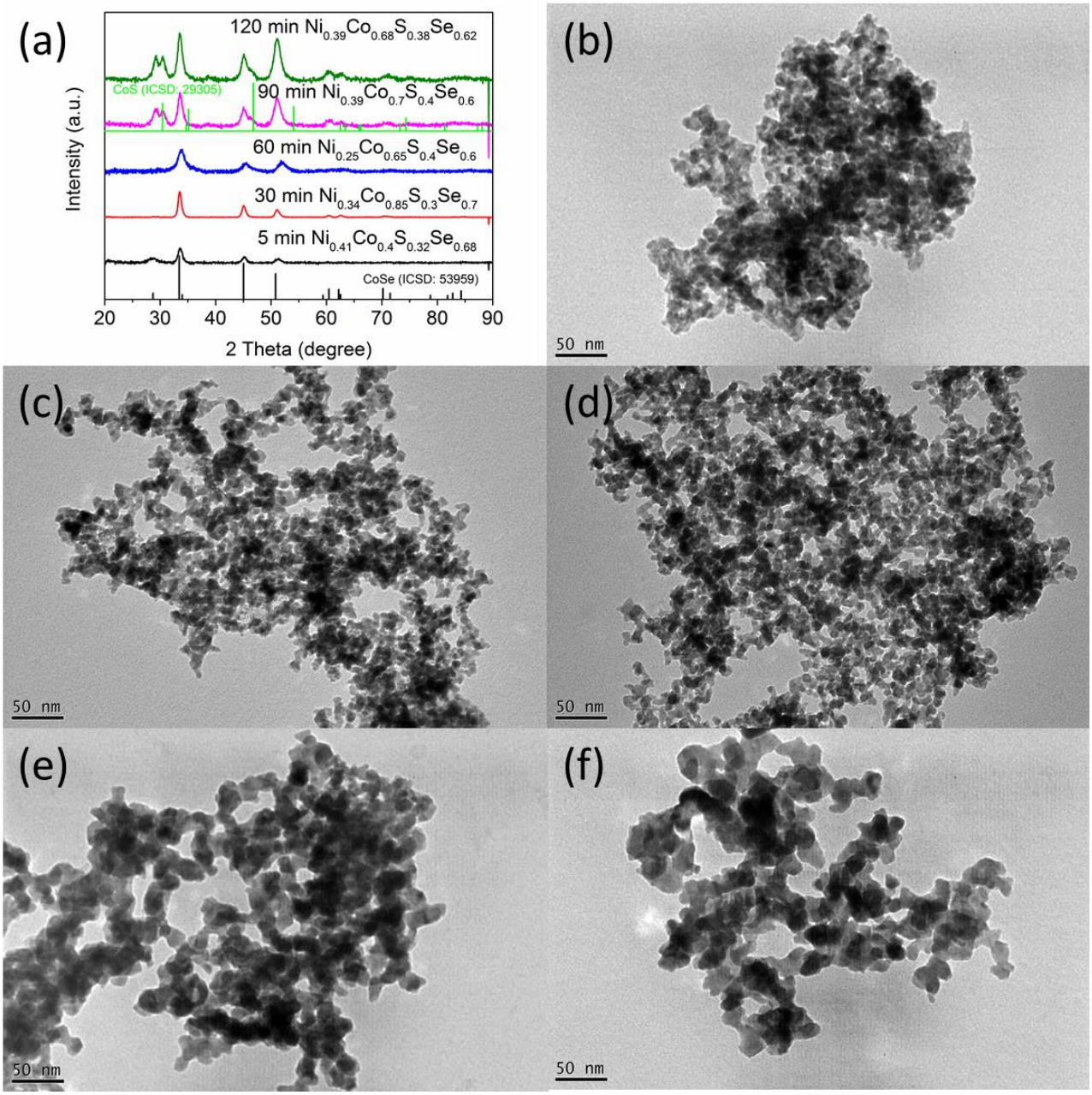

Figure 4.1. (a) XRD patterns of various quaternary Ni-Co-S-Se NCs after different reaction time. TEM images of the samples after (b) 5 min, (c) 30 min, (d) 60 min, (e) 90 min and (f) 120 min.

Influence of the S/Se precursor ratio. A group of synthesis was performed with only the S/Se precursor ratio changed and other parameters are the same. XRD patterns (Figure 4.2a) indicate a change in crystal structures when the S/Se precursor ratio changes from 0 to 1. The NCs tend to form metal-rich cubic phase M_9X_8 (M = Co/Ni; X = S/Se) when S/Se is low, while the structures are chalcogen-rich cubic phase M_3X_4 (M = Co/Ni; X = S/Se). It should be noticed that with the S/Se precursor ratio of DDT (0.1 mL)/ OAm-Se (3 mL), the phase shows the hexagonal structure, which

is comparable with the group of sample in Chapter III. The shift to the higher degree is because of the replacement of the smaller S (atomic radius 1.04 Å) with the larger Se (atomic radius 1.6 Å) in the crystal lattice.

The elemental analysis shows the composition of $Ni_{0.44}Co_{0.74}Se$, $Ni_{0.37}Co_{0.85}S_{0.21}Se_{0.79}$, $Ni_{0.25}Co_{0.65}S_{0.4}Se_{0.6}$, $Ni_{0.27}Co_{0.74}S_{0.68}Se_{0.32}$, $Ni_{0.2}Co_{0.77}S_{0.86}Se_{0.14}$ and $Ni_{0.15}Co_{0.82}S$ when using 3 mL of OAm-Se, 3 mL of OAm-Se + 0.05 mL of DDT, 3 mL of OAm-Se + 0.1 mL of DDT, 1 mL of OAm-Se + 0.25 mL of DDT, 1 mL of OAm-Se + 0.25 mL of DDT and 5 mL of DDT (Table 4.1). With the S/Se precursor ratio increasing, the S/Se ratio in the final samples increases consequently. Meanwhile, the Ni/Co ratio decreases from 1/1.68 to 1/5.46. This might come from the influence of the reaction time, as we discussed in Chapter III that increasing the reaction time may result in an increase of Ni/Co ratio.

Figure 4.2b-g show representative TEM images of the samples with different compositions. It is obvious that increasing the ratio of S precursor from 0 to 0.1 mL, the size decreases dramatically from more than 50 nm to about 10 nm (Figure 4.2b-d). However, when the amount of S precursor increases more than 0.1 mL, the control of the size is not apparent and the size of the NCs is around 10 nm (Figure 4.2e-g).

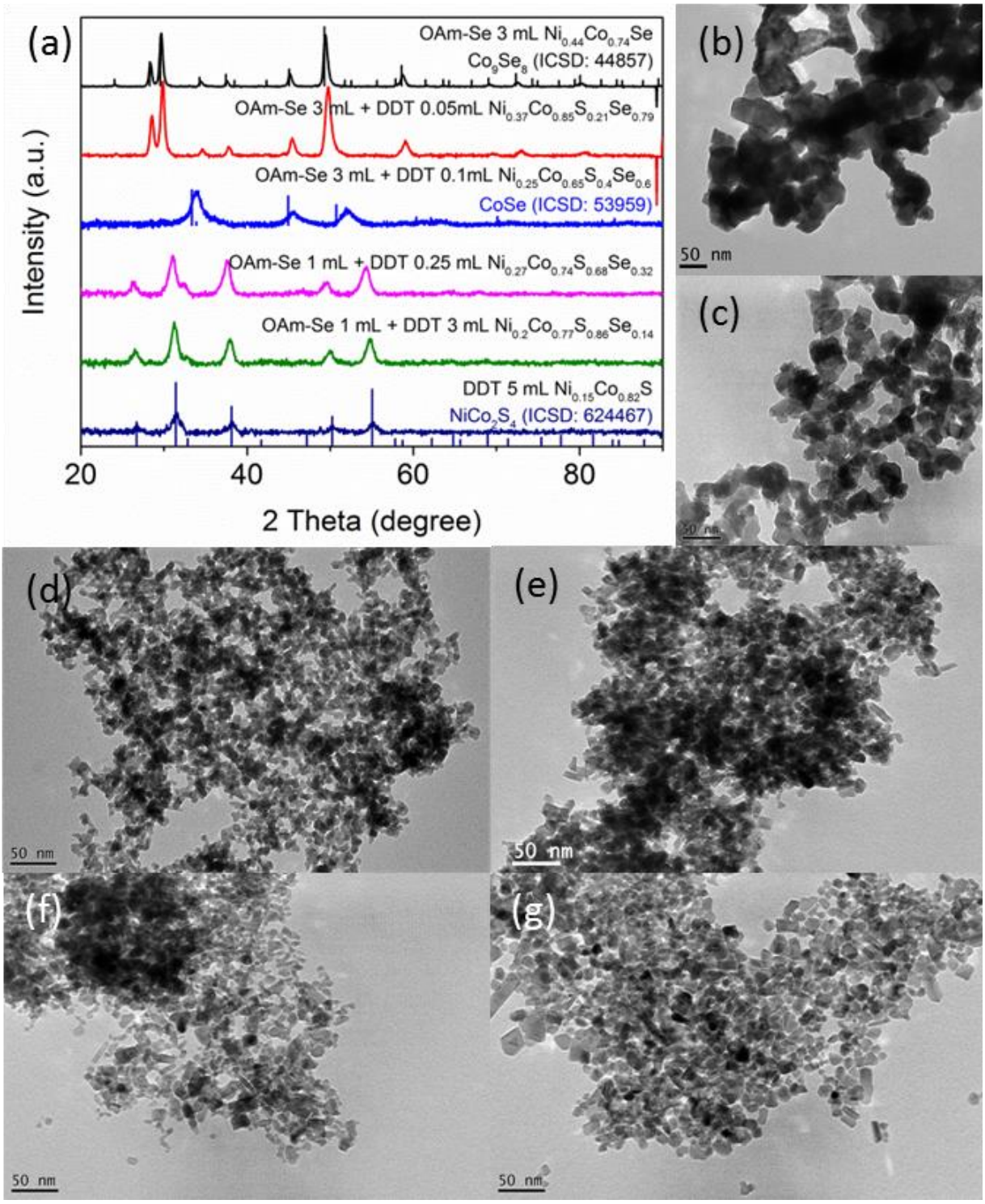

Figure 4.2. (a) XRD patterns of various quaternary Ni-Co-S-Se NCs with different S/Se ratio. TEM images of the samples with (b) 3 mL of OAm-Se, (c) 3 mL of OAm-Se + 0.05 mL of DDT, (d) 3 mL of OAm-Se + 0.1 mL of DDT, (e) 1 mL of OAm-Se + 0.25 mL of DDT, (f) 1 mL of OAm-Se + 0.25 mL of DDT and (g) 5 mL of DDT. Other experimental parameters: 0.25 mmol of $Ni(acac)_2$, 0.75 mmol of $Co(acac)_2$, 10 mL of ODE. After the injection of S/Se precursors, the reaction was heated up to 250 °C for 1 h.

Table 4.1. Amount of Se and S precursor, elemental analysis and XRD results of the quaternary samples synthesized with different S/Se precursor ratios.

Sample	OAm-Se (mL)	DDT (mL)	ICP	XRD
1	3	0	$Ni_{0,44}Co_{0,74}Se$	Co_9Se_8
2	3	0.05	$Ni_{0.37}Co_{0.85}S_{0.21}Se_{0.79}$	Co_9Se_8
3	3	0.1	$Ni_{0.25}Co_{0.65}S_{0.4}Se_{0.6}$	CoSe
4	1	0.25	$Ni_{0.27}Co_{0.74}S_{0.68}Se_{0.32}$	$NiCo_2S_4$
5	1	3	$Ni_{0.2}Co_{0.77}S_{0.86}Se_{0.14}$	$NiCo_2S_4$
6	0	5	$Ni_{0.15}Co_{0.82}S$	$NiCo_2S_4$

Eventually, from Chapter III we found that when the reaction time is reduced, the crystal structure can change from M_9X_8 to MX. Thus we also tried to reduce the reaction time in this quaternary system in order to obtain a group of samples with hexagonal phase and controllable S/Se ratios at the same time. The main experimental parameters are listed in Table 4.2 and the composition of the samples was determined by ICP analysis.

Table 4.2. Main experimental parameters of samples with various S/Se ratios.

Sample	$Ni_{0.3}Co_{0.74}Se$	$Ni_{0.3}Co_{0.73}S_{0.2}Se_{0.8}$	$Ni_{0.25}Co_{0.65}S_{0.4}Se_{0.6}$
$Ni(acac)_2$ (mmol)	0.25	0.25	0.25
$Co(acac)_2$ (mmol)	0.75	0.75	0.75
OAm-Se (mL)	3	3	3
DDT (mL)	0	0.05	0.1
ODE (mL)	10	10	10
Reaction time (min)	5	15	60
Reaction temperature (°C)	250	250	250

4.2.2 Conventional Characterization

The quaternary Ni-Co-S-Se NCs listed in Table 4.2 were then studied to investigate the effects of the presence of sulfur on the final OER performance. The S/Se ratio in the products changed from 0/1 to 2/3 while the Ni/Co ratio was fixed to 1/2.5, which was found to optimize the catalytic activity of Ni-Co-Se NCs. The produced Ni-Co-S-Se NCs had a mean size of 10 nm, as was

determined by TEM analysis (see Figure 4.3a, b), and the same hexagonal crystal structure as the binary and ternary Ni-Co-Se NCs (see Figure 4.3c). A systematic shift of the XRD peaks toward larger 2-theta values was observed when the relative amount of S inside the NCs was increased. This is consistent with the ionic radius of S, which is smaller than that of Se, suggesting the formation of alloyed structures. As discussed before, it is important to underline here that a further inclusion of S inside the alloy NCs, above the $Ni_{0.25}Co_{0.65}S_{0.4}Se_{0.6}$ composition, led to quaternary NCs having a cubic structure (see Figure 4.2a). However, these samples were excluded from our study since our final goal was to compare the catalytic properties of NC systems with different compositions but having the same crystal structure.

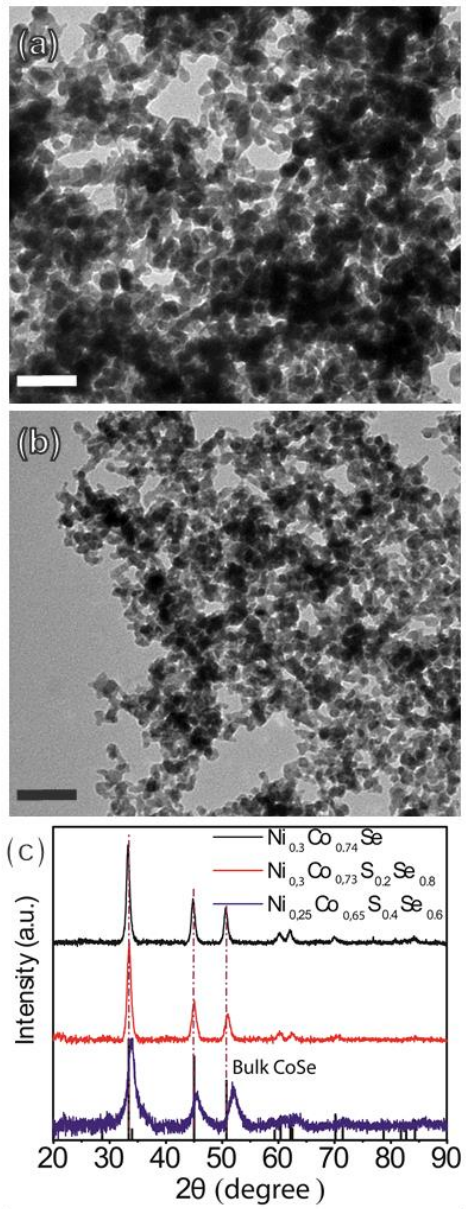

Figure 4.3. Low resolution TEM images of (a) $Ni_{0.3}Co_{0.73}S_{0.2}Se_{0.8}$ and (b) $Ni_{0.25}Co_{0.65}S_{0.4}Se_{0.6}$ NCs. The scale bar is 50 nm. (c) XRD patterns of $Ni_{0.3}Co_{0.74}Se$, $Ni_{0.3}Co_{0.73}S_{0.2}Se_{0.8}$ and $Ni_{0.25}Co_{0.65}S_{0.4}Se_{0.6}$ NCs. The pattern of $Ni_{0.3}Co_{0.74}Se$ NCs is also reported for a better comparison.

4.2.3 OER

The electrocatalytic OER properties of quaternary alloy NCs were evaluated by LSV, and the corresponding polarization curves are shown in Figure 4.4a. It is evident that the introduction of S inside the ternary Ni-Co-Se NCs resulted in an improved OER activity. The electrodes that were composed of $Ni_{0.3}Co_{0.73}S_{0.2}Se_{0.8}$ and $Ni_{0.25}Co_{0.65}S_{0.4}Se_{0.6}$ NCs exhibited a high activity for OER, with an onset overpotential of about 272 mV and 262 mV, respectively (see Table 4.3). The Tafel slopes of the $Ni_{0.3}Co_{0.73}S_{0.2}Se_{0.8}$ (64 mV/dec) and $Ni_{0.25}Co_{0.65}S_{0.4}Se_{0.6}$ (64 mV/dec) NCs were lower than that of the $Ni_{0,3}Co_{0,74}Se$ (76 mV/dec) NCs, suggesting that the quaternary systems had faster OER kinetics (see Figure 4.4b). Furthermore, the calculated TOF (Figure 4.4c) of the $Ni_{0.25}Co_{0.65}S_{0.4}Se_{0.6}$ NCs at an overpotential of 0.35 V was more than twice that of the $Ni_{0,3}Co_{0,74}Se$ NCs.

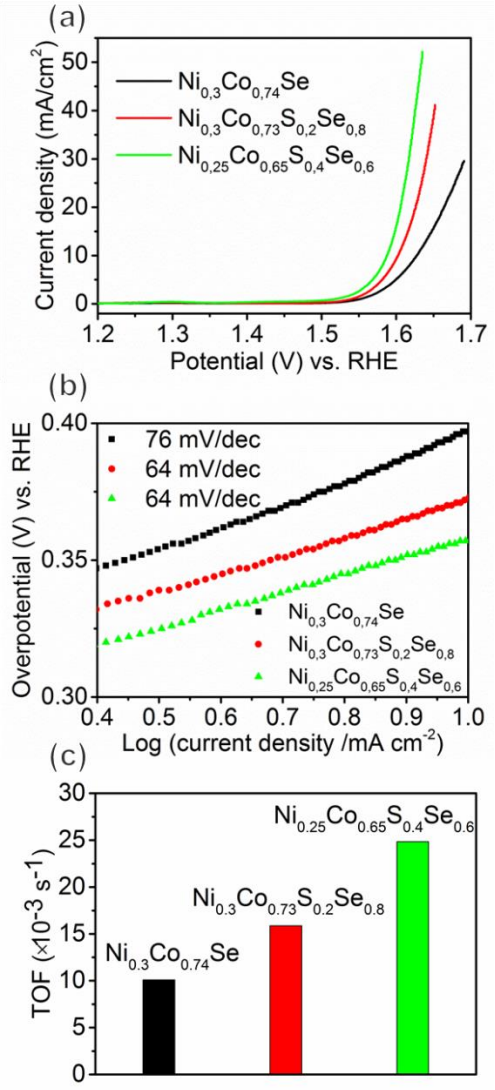

Figure 4.4. (a) LSVs measured at a sweep rate of 1 mV/s, (b) Tafel plots and (c) TOF values at η = 0.35 V of ternary and quaternary Ni-Co-S-Se NCs with various S/Se ratios.

In addition, the impedance analysis showed that the R_s of the $Ni_{0.3}Co_{0.73}S_{0.2}Se_{0.8}$ (8.9 Ω) and $Ni_{0.25}Co_{0.65}S_{0.4}Se_{0.6}$ (7.4 Ω) NCs were much smaller than that of the $Ni_{0,3}Co_{0,74}Se$ NCs (11.2 Ω), further supporting that quaternary systems are characterized by a faster charge transfer (see Figure 4.5 and Table 4.3).

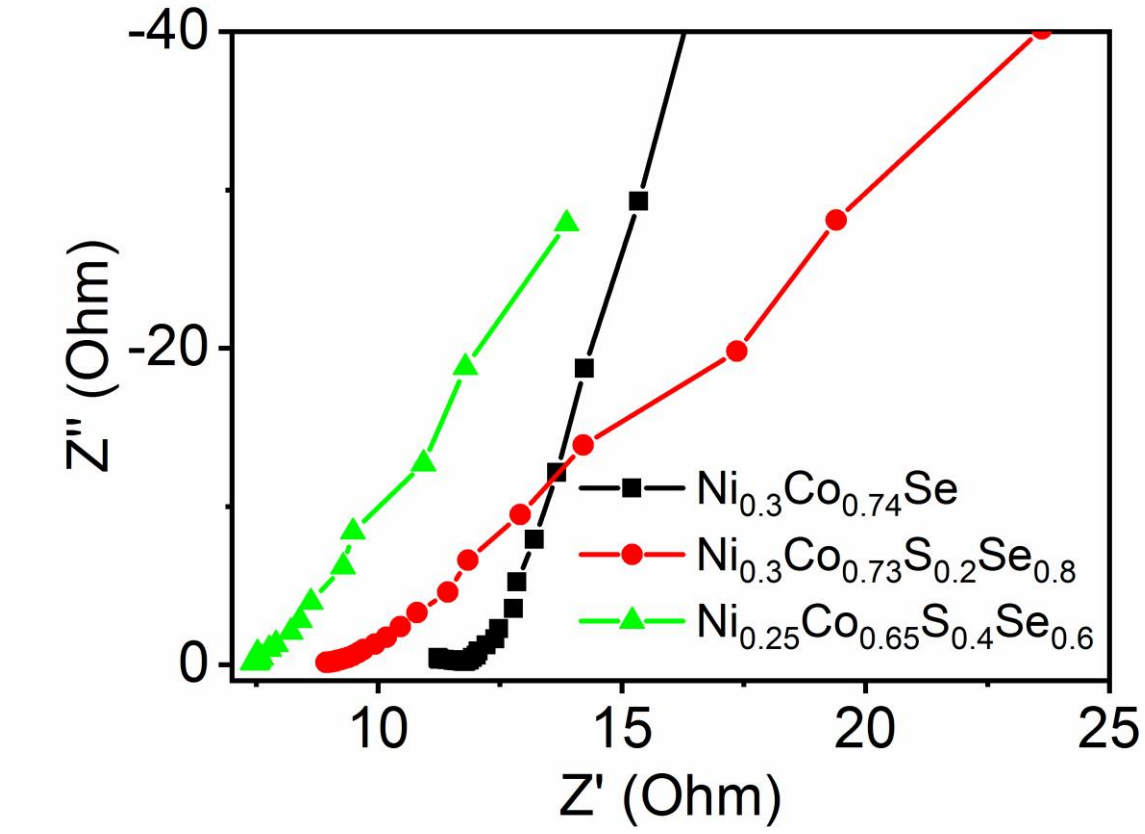

Figure 4.5. Impedance spectra of electrodes measured at open circuit potential of ternary and quaternary Ni-Co-S-Se NCs with various S/Se ratios.

To estimate the differences in electrochemically active surface areas of various catalysts, the cyclic voltammetry (CV) method was employed to measure the electrochemical double-layer capacitance (EDLC), C_{dl}. The potential range where no faradic current was observed was selected for accurate measurements of the large active surface area of the electrode (Figure 4.6a-c). CV curves were obtained at various scan rates (10, 20, 30, 40, 50 mV/s) at 0.02-0.08 V vs. Ag/AgCl region, and the corresponding C_{dl} values were calculated. The C_{dl} of $Ni_{0.3}Co_{0.73}S_{0.2}Se_{0.8}$ (0.42 mF/cm^2) and $Ni_{0.25}Co_{0.65}S_{0.4}Se_{0.6}$ (0.41 mF/cm^2) NCs are higher than $Ni_{0,3}Co_{0,74}Se$ (0.059 mF/cm^2) NCs, indicating that the addition of S inside the crystals may help to increase the active sites thus to improve the OER activity.

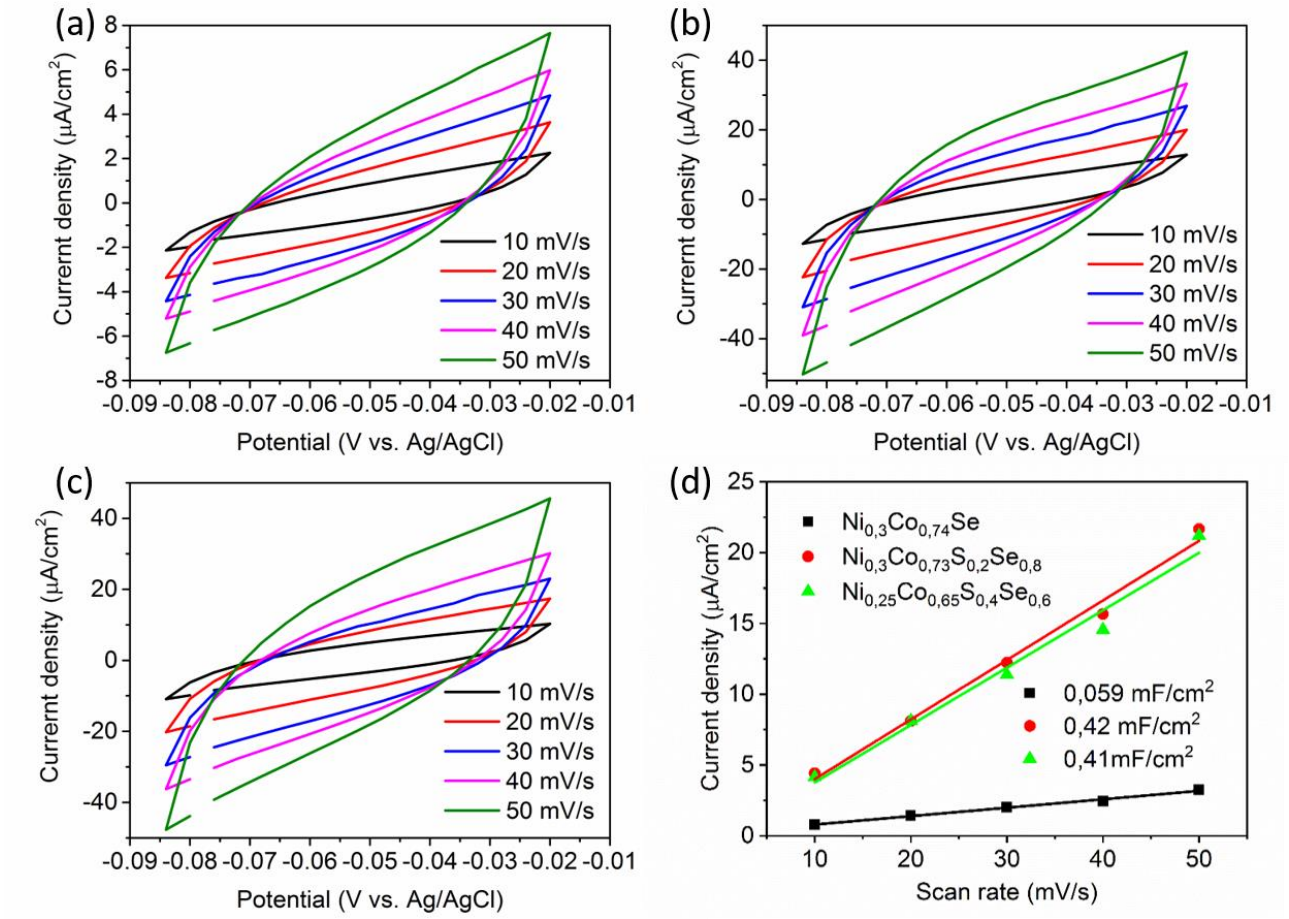

Figure 4.6. The EDLC measurements of (a) $Ni_{0,3}Co_{0,74}Se$, (b) $Ni_{0.3}Co_{0.73}S_{0.2}Se_{0.8}$ and (c) $Ni_{0.25}Co_{0.65}S_{0.4}Se_{0.6}$ NCs at different scan rates and the corresponding C_{dl} linear fitting and calculation (d).

These results confirmed that $Ni_{0.25}Co_{0.65}S_{0.4}Se_{0.6}$ NCs had the highest intrinsic catalytic activity among all the reported samples, and its stability is also remarkable (Figure 4.7). After 8 h of continuous electrolysis reaction, only a 30 mV increase in the overpotential was required to maintain OER current density of 10 mA/cm^2 (from 1.68 V to 1.71 V).

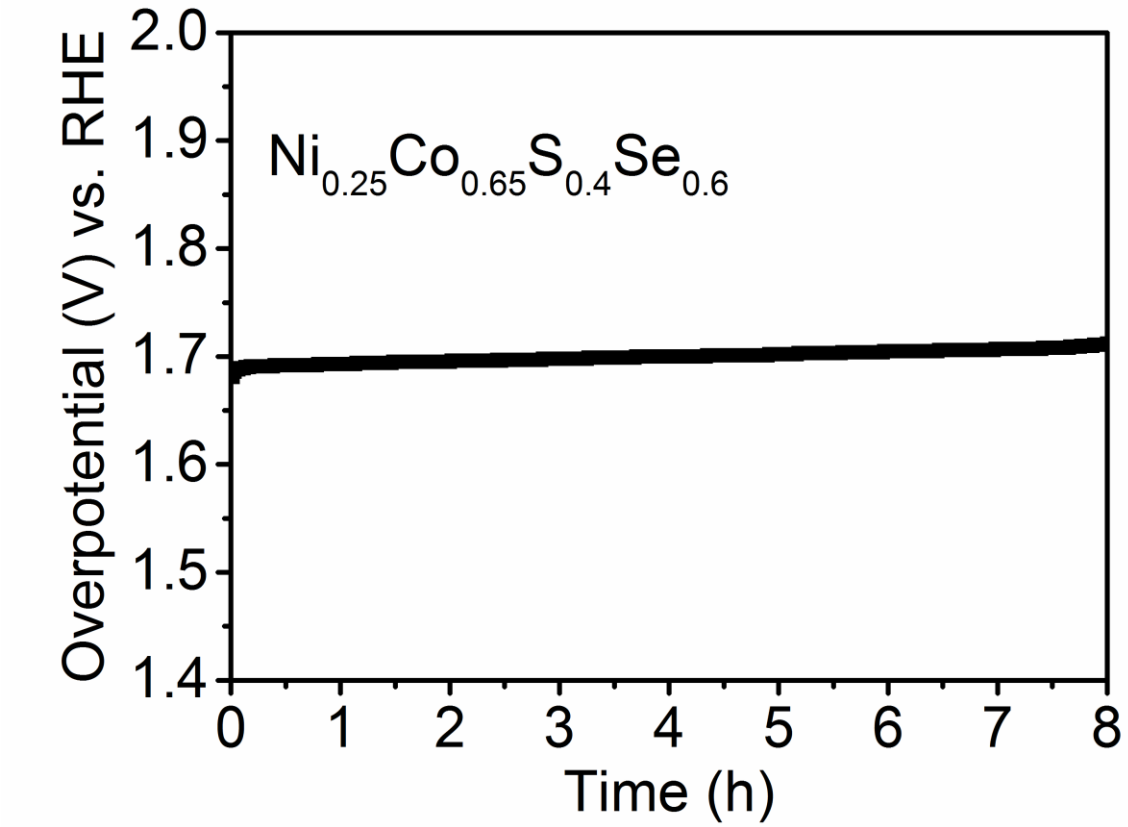

Figure 4.7. Chronopotentiometry measurement at a current density of 10 mA/cm^2 for $Ni_{0.25}Co_{0.65}S_{0.4}Se_{0.6}$ NCs electrode.

To further elucidate the reasons underlying the better OER performance of $Ni_{0.25}Co_{0.65}S_{0.4}Se_{0.6}$ NCs, polarization curves of all the samples were also collected between 1.0 and 2.0 V versus RHE at a scan rate of 10 mV/s. As shown in Figure 4.8, the CVs of all the samples were characterized by one broad anodic peak in the range of 1.2-1.4 V (versus RHE). As mentioned above in the discussion of the ternary Ni-Co-Se samples, the presence of this single peak stands for the oxidation of Ni^{II} to Ni^{III} or Ni^{IV}. The increase in the intensity of this redox peak when going from $Ni_{0,3}Co_{0,74}Se$ to $Ni_{0.25}Co_{0.65}S_{0.4}Se_{0.6}$ NCs suggested that quaternary NC samples are characterized by a higher amount of Ni^{II} sites which can undergo a reversible redox reaction to Ni^{III} or Ni^{IV}. These sites might act as catalytically active sites, which would explain the superior electrocatalytic performance of our quaternary samples.[8-9]

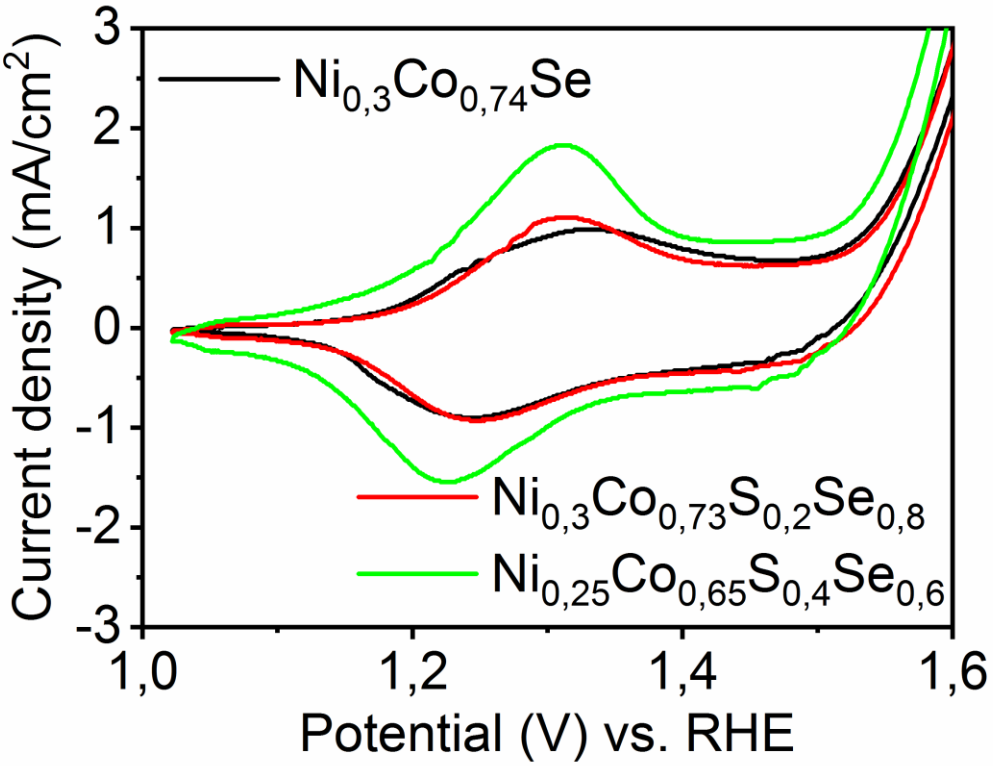

Figure 4.8. CVs of quaternary Ni-Co-S-Se NCs with various S/Se ratios.

Table 4.3. Summary of electrochemical OER parameters of quaternary Ni-Co-S-Se NC catalysts.

Sample	**$Ni_{0.3}Co_{0.74}Se$**	**$Ni_{0.3}Co_{0.73}S_{0.2}Se_{0.8}$**	**$Ni_{0.25}Co_{0.65}S_{0.4}Se_{0.6}$**
Onset potential (mV)	277	272	262
η/mV at j = 10 mA/cm^2	397	373	358
Tafel slope (mV/dec)	76	64	64
R_s (Ω)/cm^2	1.2	8.9	7.4
TOF ($\times 10^{-3}$ s^{-1})	10.05	15.88	24.84
ECSA (mF/cm^2)	0.059	0.42	0.41

HRTEM studies were carried out on $Ni_{0.25}Co_{0.65}S_{0.4}Se_{0.6}$ NCs before and after OER so that the chemical and structural evolution of the NCs could be further studied. Before OER, the NCs were found to have the expected hexagonal crystal structure and a homogeneous distribution of the four elements, with a mean composition of $Ni_{0.3}Co_{0.63}S_{0.4}Se_{0.6}$, which is in agreement with ICP results (see Figure 4.9a-c). Interestingly, our HRTEM analysis also revealed that quaternary NCs were characterized by a large amount of crystal defects including steps (see Figure 4.9d and g), twin

boundaries (see Figure 4.9b, e, f and h) and stacking faults (see Figure 4.9f). The formation of these defects is tentatively explained by the presence of S anions on the Ni-Co-Se hexagonal lattice, which could induce a compressive strain, since the ionic radius of S^{2-} is smaller than that of Se^{2-} (184 pm compared to 198 pm).

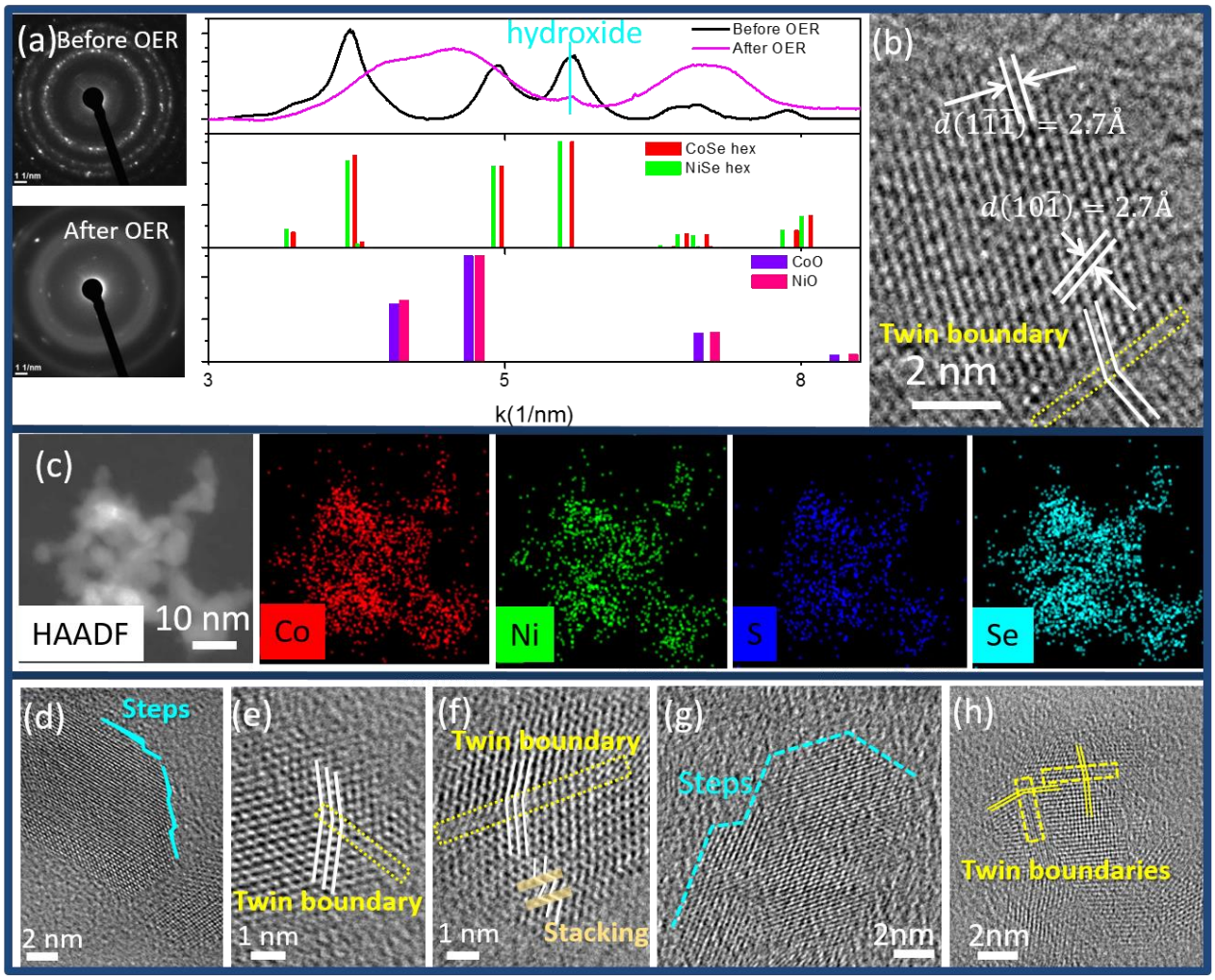

Figure 4.9. (a) SAED patterns of $Ni_{0.25}Co_{0.65}S_{0.4}Se_{0.6}$NCs before and after OER. (b, d-h) HRTEM images and (c) EDS elemental mapping of $Ni_{0.25}Co_{0.65}S_{0.4}Se_{0.6}$ NCs before OER. The NCs exhibit the expected hexagonal structure (ICSD number 53959) and they are characterized by a rich presence of defects.

However, a large number of small NiO or CoO NCs, amorphous Ni, Co oxide/hydroxide nanoparticles and $Co(OH)_2$ ultrathin nanosheets were detected after the OER by HRTEM analysis (see Figure 4.10a-f). Indeed, in Figure 4.10g-h, the STEM-EDS elemental mapping and EDS spectrum of the final sample confirmed the presence of Ni, Co and O elements, but there were almost no traces of S and Se (the ratio of (S+Se)/(Ni+Co) was 5.3%). Such findings were also

supported by the XRD analysis of the $Ni_{0.25}Co_{0.65}S_{0.4}Se_{0.6}$ NC sample after the OER, which revealed the presence of a fraction of crystalline $Co(OH)_2$ (ICSD number: 53994) (see Figure 4.10i).

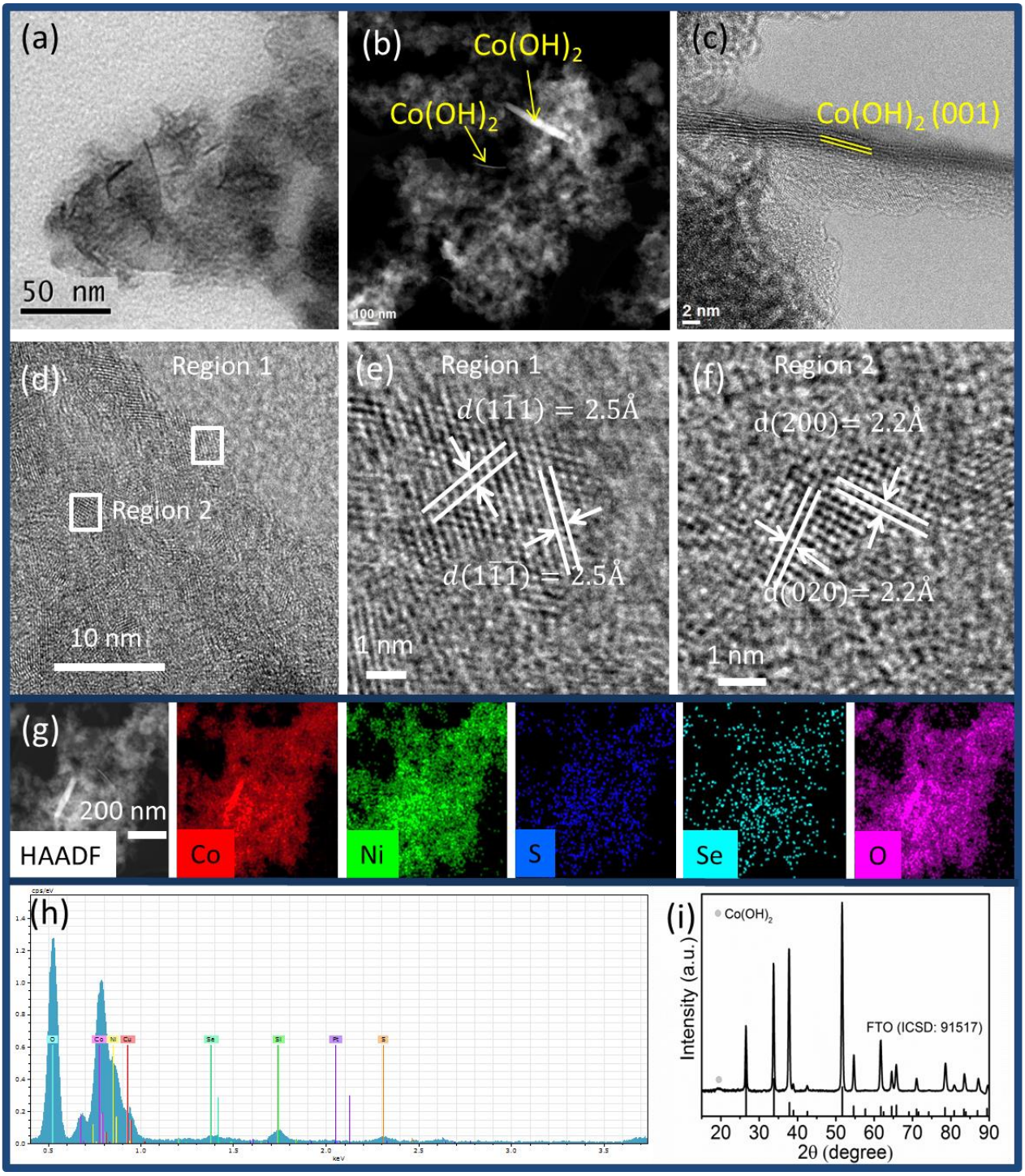

Figure 4.10. (a) TEM micrograph, (b) HAADF-STEM image and (c,d) HRTEM image of $Ni_{0.25}Co_{0.65}S_{0.4}Se_{0.6}$NCs after OER. (e,f) Two regions of panel (d) are magnified to show the lattice fringes of the oxide NCs, which matching either NiO (ICSD number 9866) or CoO (ICSD number 9865). (g) EDS elemental mapping of $Ni_{0.25}Co_{0.65}S_{0.4}Se_{0.6}$ NCs after OER. (h) EDS spectrum and (i)

XRD patterns on the FTO substrate of $Ni_{0.25}Co_{0.65}S_{0.4}Se_{0.6}$NCs after OER.

The maximum of Co 3p peaks shifted from (59.2±0.3) eV to (60.9±0.3) eV and the shoulder at approx. 66.6 eV disappeared in the Ni 3p binding energy region (Figure 4.11a, b). The observed shifts are consistent with an oxidation of both Co and Ni, thus corroborating the results coming from other techniques (evolution of the catalyst from Ni-Co chalcogenides to Ni-Co oxide/hydroxide species). Se 3d peaks at approx. 54 eV disappeared after OER (Figure 4.11d). Again, no Pt relative peaks are observed before and after OER, which means that Pt is not involved in the measurement. In the quaternary systems, also S 2p peaks (in the 160-165 eV binding energy region) disappeared after OER (Figure 4.11c).

XPS analyses of quaternary NCs before and after OER, also in this case corroborated our findings: while the S and Se signals disappeared upon OER, the position of Ni and Co peaks have a shift, suggesting the evolution of the catalyst from Ni-Co-Se-S to Ni-Co oxide/hydroxide species (see Figure 4.11). We believe that the preferential formation of such crystalline oxide/hydroxide nanoparticles could be directly correlated to the presence of crystal defects in the parent $Ni_{0.25}Co_{0.65}S_{0.4}Se_{0.6}$ NCs, which might act as preferential nucleation sites.

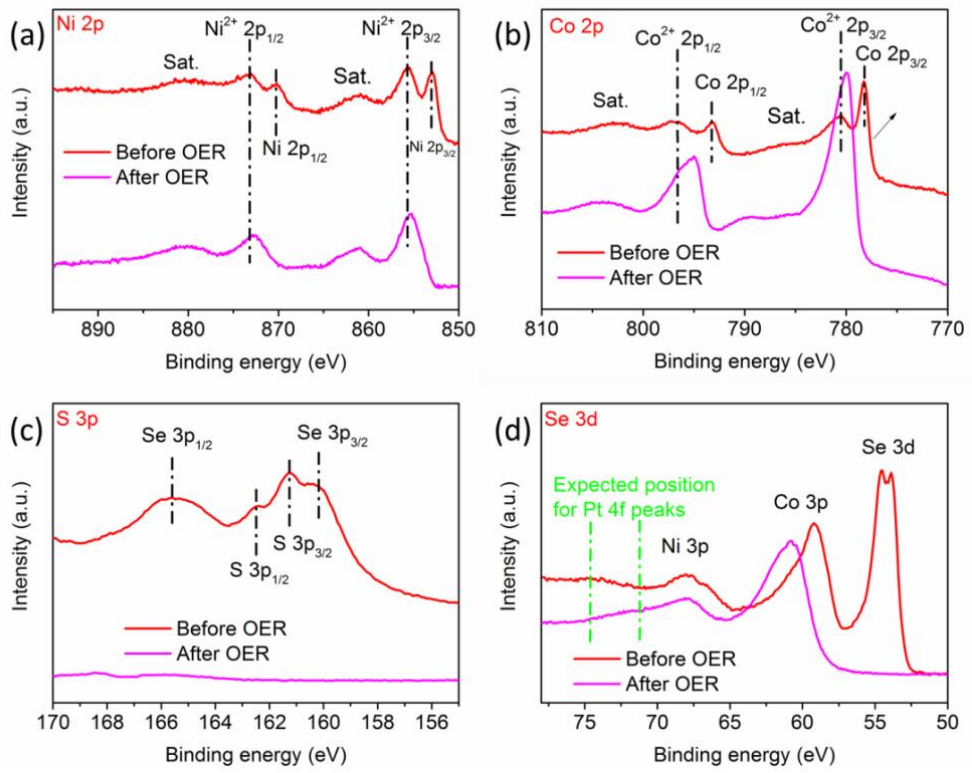

Figure 4.11. High-resolution (a) Ni, (b) Co, (c) S and (d) Se spectra of $Ni_{0.25}Co_{0.65}S_{0.4}Se_{0.6}$ NCs before and after OER.

Overall, our findings indicated that both ternary and quaternary Ni-Co-S-Se NCs undergo oxidation upon OER and transform *in situ* into Ni, Co oxide/hydroxide materials. Ternary samples were found to form active amorphous compounds, while quaternary NCs transformed mostly into small NiO/CoO NCs and ultrathin $Co(OH)_2$ nanosheets. Thus, we ascribe the superior OER performance of Ni-Co-S-Se NCs to the crystalline species which were experimentally found to promote the catalytic activity of the final catalyst.[10] It is also important to highlight here that our electrochemical results have been obtained using Pt counter electrodes in the experimental setup. Our ICP, STEM-EDS and XPS elemental analyses performed on both ternary and quaternary compounds before and after OER indicated the absence of Pt in both the catalyst and the electrolyte, excluding any influence of Pt on the catalytic properties and on the transformations of the NCs.

4.3 Influence of Ni/Co in Quaternary System

4.3.1 Conventional Characterization

The Ni/Co ratio can be easily tuned by changing the ratio of Ni and Co precursors. The reaction time is decreased from Co-S-Se to Ni-S-Se in order to synthesize a group of samples with comparable sizes. On the other side, since the reaction time can influence the S/Se ratio inside the NCs, the amount of S/Se precursor ratio is also tuned in order to obtain samples with a constant S/Se ratio. Table 4.4 lists the different experimental parameters and of the samples named by the compositions from ICP analysis, and the S/Se ratio is determined by the best $Ni_{0.25}Co_{0.65}S_{0.4}Se_{0.6}$ NCs in the above-mentioned section.

Table 4.4. Experimental parameters of the samples with various Ni/Co ratios.

Sample	$Co(acac)_2$ (mmol)	$Ni(acac)_2$ (mmol)	Reaction time (min)	DDT (mL)
$Co_{0,93}S_{0.39}Se_{0.61}$	1	0	60	0.1
$Ni_{0,25}Co_{0,65}S_{0,41}Se_{0,59}$	0.25	0.75	60	0.1
$Ni_{0.57}Co_{0.56}S_{0.38}Se_{0.62}$	0.6	0.4	5	0.2
$Ni_{0.78}Co_{0.24}S_{0.42}Se_{0.58}$	0.75	0.25	5	0.2
$NiS_{0,41}Se_{0,59}$	0	1	5	0.2

* Other experimental parameters: Se precursor 1 mmol, ODE 10 mL, reaction temperature 250 °C.

All the obtained samples exibithed the hexagonal CoSe (ICSD: 53959) phase as evinced from our XRD analyses (see Figure 4.12a). The peaks are shifted toward higher 2 theta values because of

the high amount of S. Although the Ni/Co ratio differs a lot from $Co_{0,93}S_{0.39}Se_{0.61}$ to $NiS_{0,41}Se_{0,59}$ NCs, there is no apparent peak shift between these samples. This is probably because of the similar atomic radius and chemical environment of Ni and Co. Also because of this reason, the value of Ni/Co ratio can be easily tuned from 0 to 1. The morphology and size of the as-synthesized samples were investigated via TEM analysis. All the as-synthesized samples exhibit similar size of around 10 nm (see Figure 4.12b-f).

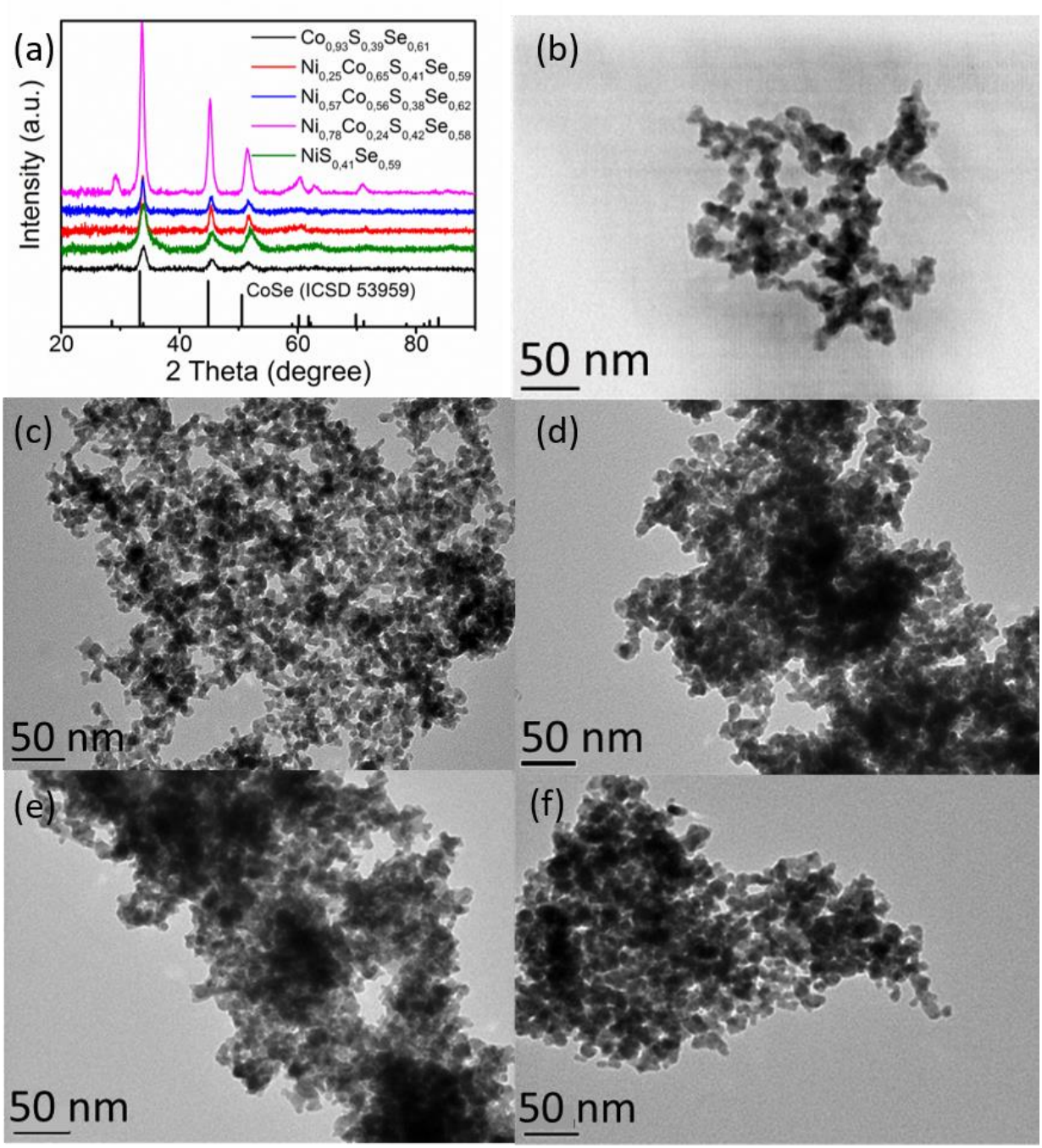

Figure 4.12. (a) XRD patterns and TEM images of (b) $Co_{0,93}S_{0.39}Se_{0.61}$, (c) $Ni_{0,25}Co_{0,65}S_{0,41}Se_{0,59}$, (d) $Ni_{0.57}Co_{0.56}S_{0.38}Se_{0.62}$, (e) $Ni_{0.78}Co_{0.24}S_{0.42}Se_{0.58}$ and (f) $NiS_{0,41}Se_{0,59}$ NCs.

4.3.2 OER

The LSV curves of the samples are shown in Figure 4.13a. The onset potentials of the samples from $Co_{0.93}S_{0.39}Se_{0.61}$ to $NiS_{0.41}Se_{0.59}$ are 317, 262, 324, 355 and 440 mV, respectively (see Table 4.5). Likewise, when the current density reaches 10 mA/cm^2, the potentials are 392, 358, 433, 515 and 694 mV, respectively, and the best result is comparable to the state-of-art transition metal chalcogenide electrocatalysts for OER (see Figure 1.6). These results demonstrate that the OER properties strongly depend on the composition of the NCs. The regulation is the same as the corresponding ternary system, namely, the sample has the Ni/Co ratio of 1/2.5 ($Ni_{0,25}Co_{0,65}S_{0,4}Se_{0,6}$), exhibits the highest catalytic activity compared to the other samples. Moreover, the quaternary NCs all show lower onset potential and overpotential at j = 10 mA/cm^2, which can result from the insertion of S. The OER kinetics of these catalysts was probed further by analyzing the Tafel plots as shown in Figure 4.13b. The resulting Tafel slopes were found to be 52, 64, 79, 146 and 201 mV/dec for $Co_{0.93}S_{0.39}Se_{0.61}$, $Ni_{0.25}Co_{0.65}S_{0.4}Se_{0.6}$, $Ni_{0.57}Co_{0.56}S_{0.38}Se_{0.62}$, $Ni_{0.78}Co_{0.24}S_{0.42}Se_{0.58}$, and $NiS_{0.41}Se_{0.59}$ NCs, respectively. It should be noted here that all the quaternary samples exhibit smaller Tafel slope compared to their ternary counterparts, confirming faster charge transfer in the quaternary system. Besides, the values also decrease when the Ni/Co ratio increases, the regulation of which is the same as the ternary system. The TOF values were found to be 52, 64, 79, 146 and 201 mV/dec, which are also higher than the ternary samples, indicating better OER activity of the NCs with the addition of S.

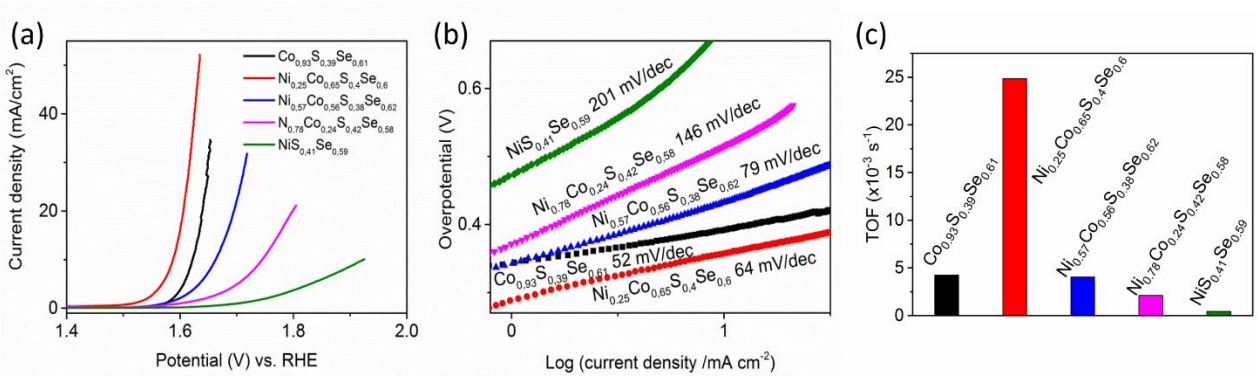

Figure 4.13. (a) LSVs measured at a sweep rate of 1 mV/s, (b) Tafel plots and (c) TOF values at η = 0.35 V of ternary and quaternary Ni-Co-S-Se NCs with various Ni/Co ratios.

To understand clearly the electrical properties of the as-prepared electrodes/solution interfaces, EIS is performed to investigate the electrode kinetics of the OER process. As shown in Figure 4.14, the impedance spectra reveal that the R_s of $Co_{0.93}S_{0.39}Se_{0.61}$, $Ni_{0.25}Co_{0.65}S_{0.4}Se_{0.6}$,

$Ni_{0.57}Co_{0.56}S_{0.38}Se_{0.62}$, $Ni_{0.78}Co_{0.24}S_{0.42}Se_{0.58}$, and $NiS_{0.41}Se_{0.59}$ NCs are approximately 11, 7.4, 9.6, 10.3 and 12.6 Ω, respectively (see Table 4.5). The $Ni_{0.25}Co_{0.65}S_{0.4}Se_{0.6}$ NCs possess the lowest R_s, and they are an excellent catalyst for OER. Again, the R_s of these quaternary samples is lower than the value of their ternary counterparts, confirming that the addition of S is an effective method to obtain electrocatalysts with better performance. The R_s is also influenced by the Ni/Co ratio. It is verified again that the synergistic effect reaches maximum when the Ni/Co ratio is 1/2.5, following the same trend as how Ni/Co ratio influences the R_s of the ternary NCs.

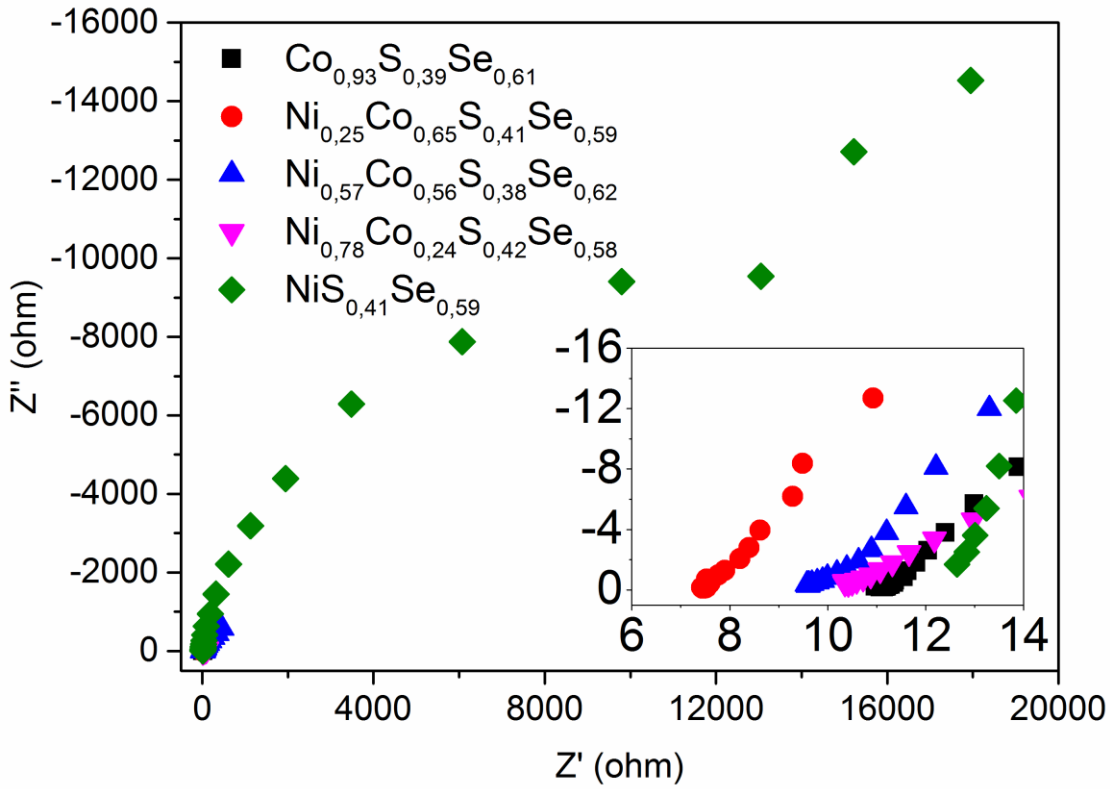

Figure 4.14. Impedance spectra of electrodes measured at open circuit potential of ternary and quaternary Ni-Co-S-Se NCs with various Ni/Co ratios.

C_{dl}, which is believed to be positively proportional to the ECSA, has also been determined by measuring the CV curves in the potential range from -0.02 ~ -0.08 V vs. Ag/AgCl without redox processes. As can be seen, like the samples with different S/Se ratios, although these 5 samples have similar size and morphology according to the TEM pictures in Figure 4.12, their value of C_{dl} has a big difference, the highest ($Co_{0.93}S_{0.39}Se_{0.61}$: 0.8 mF/cm^2) and lowest ($NiS_{0.41}Se_{0.59}$: 0.005 mF/cm^2) are not even on the same scale (see Figure 4.15 and Table 4.5). Besides, the ECSA is not the only factor to influence the OER activity. The ternary $Co_{0.93}S_{0.39}Se_{0.61}$ NCs actually have the largest

ECSA among all the samples instead of the best-performing $Ni_{0.25}Co_{0.65}S_{0.4}Se_{0.6}$ NCs (0.41 mF/cm^2), which means that $Co_{0.93}S_{0.39}Se_{0.61}$ NCs have more active sites than $Ni_{0.25}Co_{0.65}S_{0.4}Se_{0.6}$ NCs. However, $Ni_{0.25}Co_{0.65}S_{0.4}Se_{0.6}$ NCs have higher TOF and R_s which results in faster charge transfer, thus the OER performance of $Ni_{0.25}Co_{0.65}S_{0.4}Se_{0.6}$ NCs are better than $Co_{0.93}S_{0.39}Se_{0.61}$ NCs. As to the rest three samples $Ni_{0.57}Co_{0.56}S_{0.38}Se_{0.62}$ (0.15 mF/cm^2), $Ni_{0.78}Co_{0.24}S_{0.42}Se_{0.58}$ (0.005 mF/cm^2), and $NiS_{0.41}Se_{0.59}$ (0.002 mF/cm^2) NCs, the C_{dl} is quite low and not comparable to the first two samples, which means that there are no enough active sites for OER thus hindering their activity in the OER.

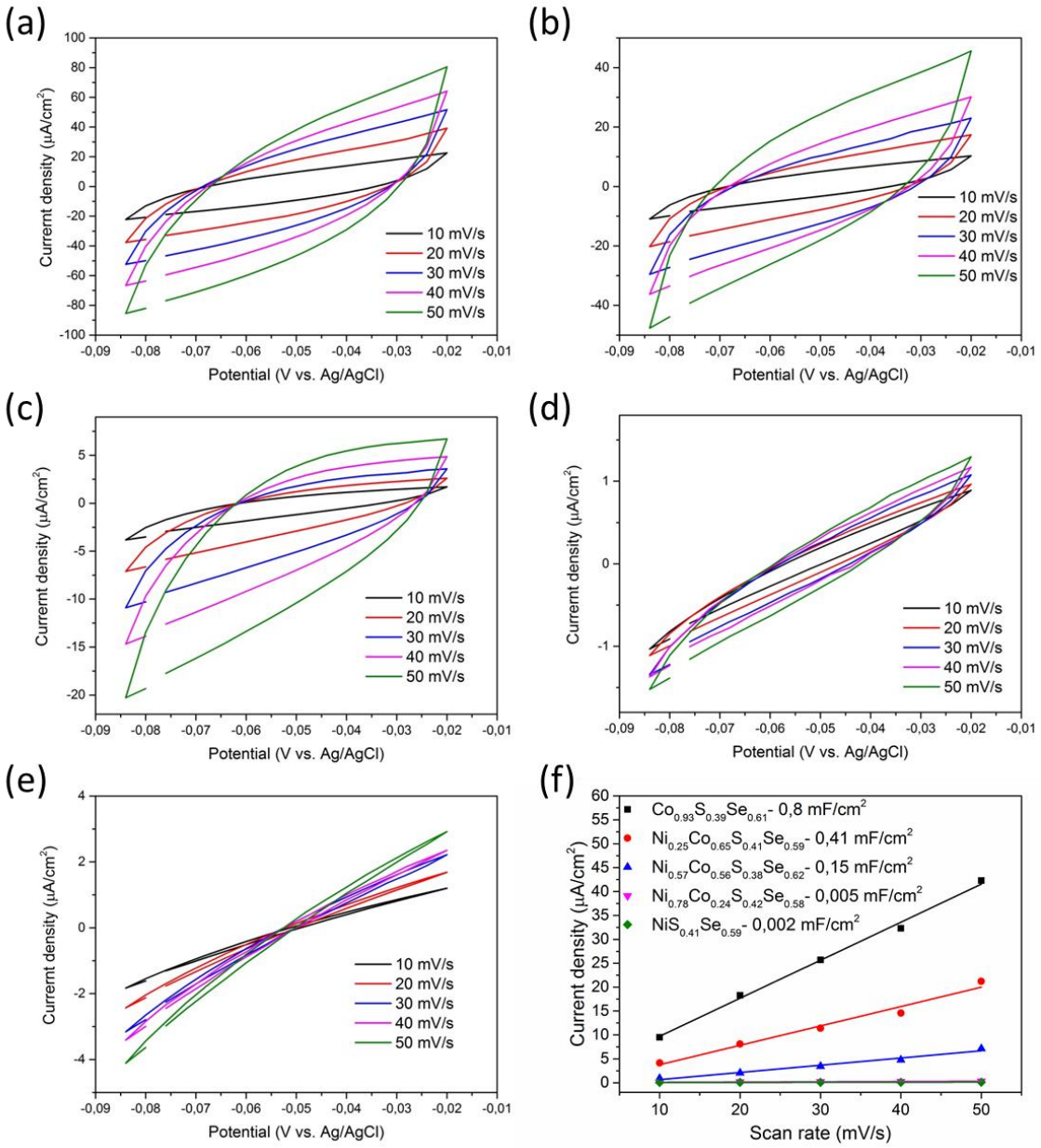

Figure 4.15. The EDLC measurements of (a) $Co_{0.93}S_{0.39}Se_{0.61}$, (b) $Ni_{0.25}Co_{0.65}S_{0.4}Se_{0.6}$, (c) $Ni_{0.57}Co_{0.56}S_{0.38}Se_{0.62}$, (d) $Ni_{0.78}Co_{0.24}S_{0.42}Se_{0.58}$, and (e) $NiS_{0.41}Se_{0.59}$ NCs at different scan rates and the corresponding C_{dl} linear fitting and calculation (f).

Table 4.5. Various electrochemical parameters of Ni-Co-S-Se on FTO electrodes.

Sample	Onset potential (mV)	η/mV at j = 10 mA/cm^2	Tafel slope (mV/dec)	R_s (Ω)/cm^2	TOF ($\times10^{-3}$ s^{-1})	ECSA (mF/cm^2)
$Co_{0.93}S_{0.39}Se_{0.61}$	317	392	52	11	4.23	0.8
$Ni_{0.25}Co_{0.65}S_{0.4}Se_{0.6}$	262	358	64	7.4	24.84	0.41
$Ni_{0.57}Co_{0.56}S_{0.38}Se_{0.62}$	324	433	79	9.6	4.06	0.15
$Ni_{0.78}Co_{0.24}S_{0.42}Se_{0.56}$	355	515	146	10.3	2.11	0.005
$NiS_{0.41}Se_{0.59}$	440	694	201	12.6	0.43	0.002

Figure 4.16 presents the CV curves of this group of samples. Similar as the regulation concluded from the ternary Ni-Co-Se group, the position and the intensity of the redox peaks heavily depend on the Ni/Co ratio. Higher Ni/Co ratio result in the closer position to Ni oxidation peak and lower intensity. In case of $Co_{0.93}S_{0.39}Se_{0.61}$ NCs, two separated peaks appearing at around 1.1 and 1.45 V vs. RHE stand for the oxidation peak of Co^{II} to Co^{III} and Co^{III} to Co^{IV}. These results are the same as the corresponding ternary system except that all the quaternary samples have higher peak intensity compared to their ternary counterparts. While in case of $NiS_{0.41}Se_{0.59}$ NCs, the absence of redox peaks indicates that there is no formation of oxidation of Ni, which is similar as its binary counterpart NiSe.

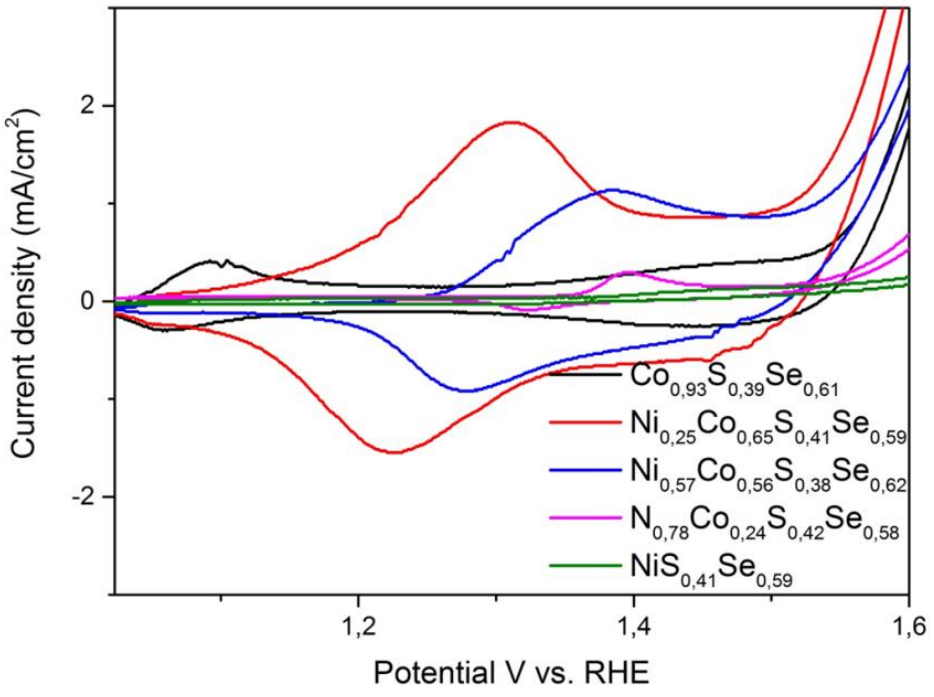

Figure 4.16. CVs of quaternary Ni-Co-S-Se NCs with various S/Se ratios.

In addition, since the best $Ni_{0.25}Co_{0.65}S_{0.4}Se_{0.6}$ NCs after OER are already analyzed in the above section, $Co_{0.93}S_{0.39}Se_{0.61}$ and $NiS_{0.41}Se_{0.59}$ NCs were chosen to be analyzed after OER to further study the influence of individual Ni and Co. From Figure 4.17a, it is clear that after OER the $Co_{0.93}S_{0.39}Se_{0.61}$ is totally converted to $Co(OH)_2$, while $NiS_{0.41}Se_{0.59}$ NCs remain the original NiSe structure. According to the TEM pictures of these three samples, the morphology of all the samples is changed (Figure 4.17b-c). From these results we can speculate that samples with relatively more content of Co, like $Co_{0.93}S_{0.39}Se_{0.61}$ and $Ni_{0.25}Co_{0.65}S_{0.4}Se_{0.6}$, can form $Co(OH)_2$ which is helpful to improve the OER activity. However, it seems $NiS_{0.41}Se_{0.59}$ is not able to be oxidized to $Ni(OH)_2$ which is also an active material good for OER.

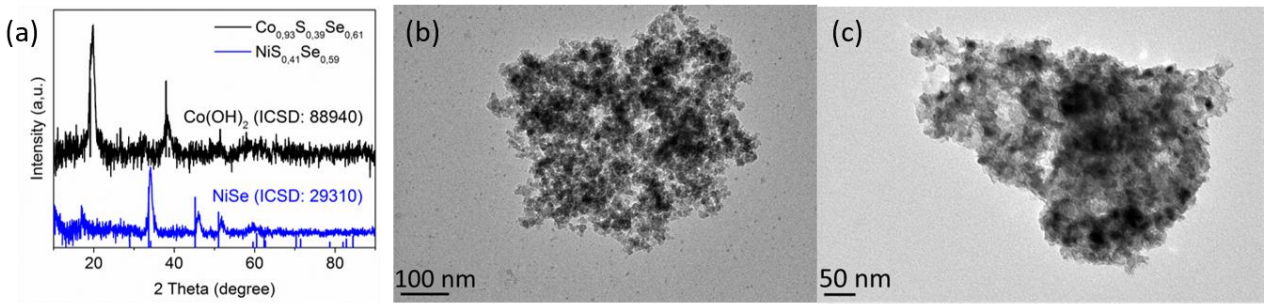

Figure 4.17. (a) XRD patterns and TEM images of (b) $Co_{0.93}S_{0.39}Se_{0.61}$ and (c) $NiS_{0.41}Se_{0.59}$ NCs after OER.

These results and with the ternary system encourage us to investigate more details of the relationship between the redox peaks and the chemical transformation. For comparison, nine samples are chosen according to their composition and classified into three groups by the type of the cations. As shown in Figure 4.18a-c, the XRD patterns show the phases of different metal chalcogenides without any impurities. All these samples are used for OER and the CVs before OER are shown in Figure 4.18d-f. It is obvious that the redox peaks depend on the type of the cations despite the types of the chalcogens and the phases, since these peaks belong to the oxidation peaks of the metals. Specifically, all the Co chalcogenides samples are characterized by two peaks at around 1.1 and 1.45 V vs. RHE which can be attributed to the oxidation of Co^{II} to Co^{III} and Co^{III} to Co^{IV}, which was analyzed in Chapter III. The XRD patterns of all the samples on FTO substrates also provide the evidence that all the samples were oxidized to $Co(OH)_2$ (Figure 4.18g). Ni-Co chalcogenides all have one strong broad peak which is arises as a consequence of the synergistic effect of Ni and Co, while almost no peaks are detected after OER because probably these three samples form mostly amorphous or very small oxides (Figure 4.18h, 4.10 and 3.19). Interestingly, no redox peaks are detected for NiSe, $NiS_{0.41}Se_{0.59}$ and Ni_3S_2, which means that these chalcogenides

do not oxidize under OER operational conditions. The XRD patterns on FTO substrates after OER also prove that the phases of all the Ni chalcogenides remain original (Figure 4.18i). The reason of the difference in transformation of the chemical structure is unknown. According to the current results, it might be related to the kind of the transition metals. On the other side, the lack of transformation into chemical structure among Ni chalcogenides also leads to the poor performance in OER of Ni chalcogenides, as the oxides provides large amount of active sites according to theliteratures.[11-13]

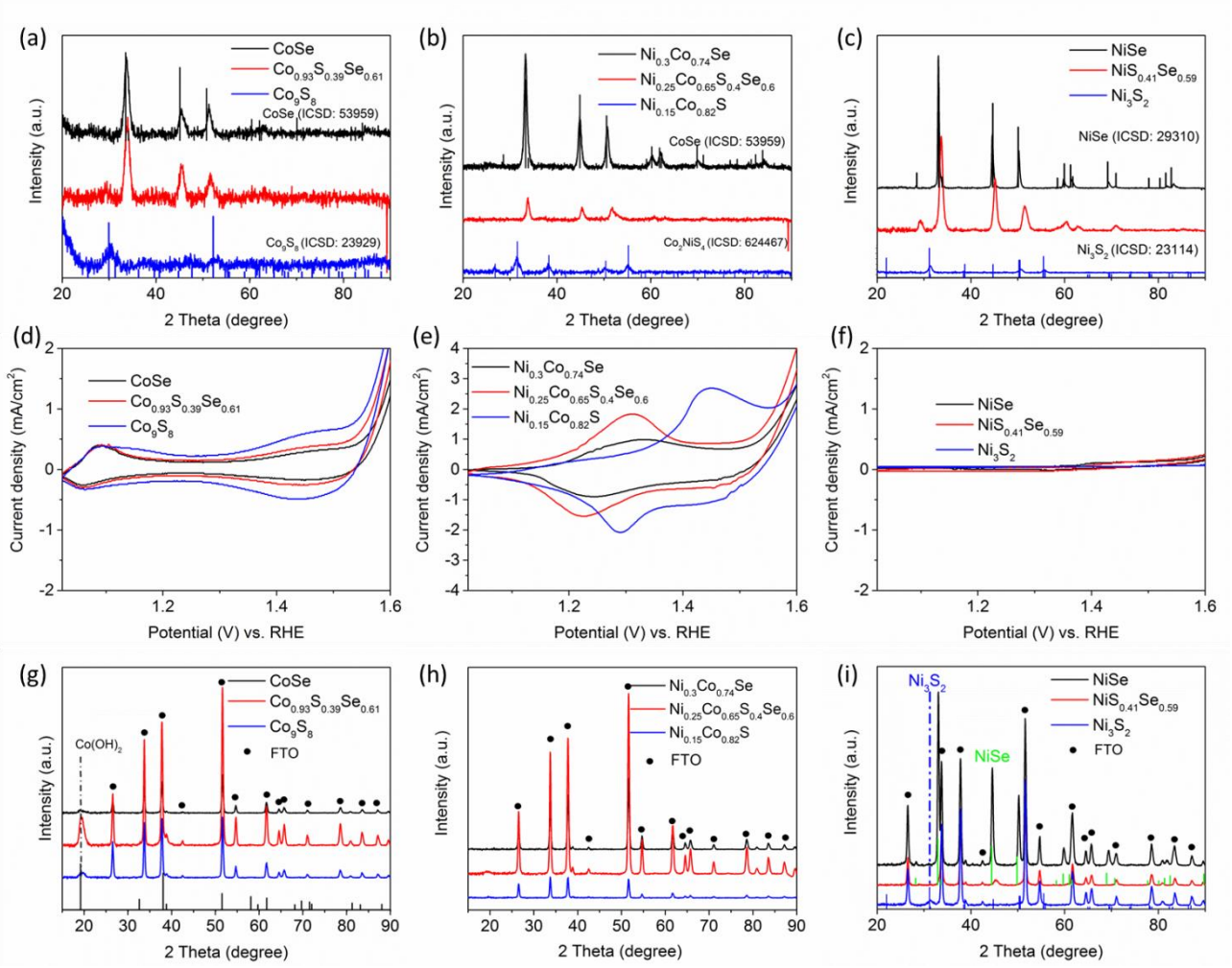

Figure 4.18. XRD patterns of (a) Co chalcogenides, (b) Ni-Co chalcogenides and (c) Ni chalcogenides. CVs of (d) Co chalcogenides, (e) Ni-Co chalcogenides and (f) Ni chalcogenides. XRD patterns on FTO substrates after OER of (g) Co chalcogenides, (h) Ni-Co chalcogenides and (i) Ni chalcogenides. Parameters of Co_9S_8: 1 mol of $Co(acac)_2$, 0.3 mL of DDT and 10 mL of ODE. 250 °C for 1 h. Parameters of Ni_3S_2: 1 mol of $Ni(acac)_2$, 0.3 mL of DDT and 10 mL of ODE. 250 °C for 1 h.

4.4 Conclusions

In conclusion, we have developed a colloidal synthesis route to produce quaternary Ni-Co-S-Se NCs with controllable compositions and hexagonal crystal structure.

Then we used the quaternary NCs to test the OER performance. It is found that the addition of S to the ternary compounds, thus forming quaternary alloy Ni-Co-S-Se NCs, led to a systematic improvement in the final OER activity. We found that the presence of S resulted in the formation of crystal defects inside the alloy NCs. Such defects, in turn, acted as preferential nucleation sites for the formation of small NiO-CoO NCs and ultrathin $Co(OH)_2$ nanosheets during the OER, and these species/compounds are believed to have promoted the final OER performance of the catalyst. Moreover, the quaternary Ni-Co-S-Se NCs with tunable Ni/Co ratios have the same trend in the OER activity but better activity than their ternary counterparts. The results provide more evidence that the addition of S can improve the OER activity remarkably.

References

1. Fang, L.; Li, W.; Guan, Y.; Feng, Y.; Zhang, H.; Wang, S.; Wang, Y., Tuning Unique Peapod-Like $Co(S_xSe_{1-x})_2$ Nanoparticles for Efficient Overall Water Splitting. *Adv. Funct. Mater.* **2017,** *27* (24), 1701008.
2. Hu, C.; Zhang, L.; Zhao, Z. J.; Li, A.; Chang, X.; Gong, J., Synergism of Geometric Construction and Electronic Regulation: 3D Se-$(NiCo)S_x/(OH)_x$ Nanosheets for Highly Efficient Overall Water Splitting. *Adv. Mater.* **2018,** *30* (12), 1705538.
3. Gong, Q.; Cheng, L.; Liu, C.; Zhang, M.; Feng, Q.; Ye, H.; Zeng, M.; Xie, L.; Liu, Z.; Li, Y., Ultrathin $MoS_{2(1-x)}Se_{2x}$ Alloy Nanoflakes For Electrocatalytic Hydrogen Evolution Reaction. *ACS Catal.* **2015,** *5* (4), 2213-2219.
4. Jin, H.; Wang, J.; Su, D.; Wei, Z.; Pang, Z.; Wang, Y., In situ Cobalt-Cobalt Oxide/N-doped Carbon Hybrids as Superior Bifunctional Electrocatalysts for Hydrogen and Oxygen Evolution. *J. Am. Chem. Soc.* **2015,** *137* (7), 2688-94.
5. Xu, K.; FengmeiWang; ZhenxingWang; Zhan, X.; QishengWang; Cheng, Z.; Safdar, M.; He, J., Component-Controllable $WS_{2(1-x)}Se_{2x}$ Nanotubes for Efficient Hydrogen Evolution Reaction. *ACS Nano* **2014,** *8*, 8468–8476.
6. Wang, Z. L.; Hao, X. F.; Jiang, Z.; Sun, X. P.; Xu, D.; Wang, J.; Zhong, H. X.; Meng, F. L.; Zhang, X. B., C and N Hybrid Coordination Derived Co-C-N Complex as a Highly Efficient Electrocatalyst for Hydrogen Evolution Reaction. *J. Am. Chem. Soc.* **2015,** *137* (48), 15070-3.
7. Duan, J.; Chen, S.; Vasileff, A.; Qiao, S. Z., Anion and Cation Modulation in Metal Compounds for Bifunctional Overall Water Splitting. *ACS Nano* **2016,** *10* (9), 8738-45.
8. Monteverde Videla, A. H. A.; Stelmachowski, P.; Ercolino, G.; Specchia, S., Benchmark Comparison of Co_3O_4 Spinel-Structured Oxides with Different Morphologies for Oxygen Evolution Reaction under Alkaline Conditions. *J. Appl. Electrochem.* **2017,** *47* (3), 295-304.
9. Friebel, D.; Louie, M. W.; Bajdich, M.; Sanwald, K. E.; Cai, Y.; Wise, A. M.; Cheng, M. J.; Sokaras, D.; Weng, T. C.; Alonso-Mori, R.; Davis, R. C.; Bargar, J. R.; Norskov, J. K.; Nilsson, A.; Bell, A. T., Identification of Highly Active Fe Sites in (Ni,Fe)OOH for Electrocatalytic Water Splitting. *J. Am. Chem. Soc.* **2015,** *137* (3), 1305-1313.

10. Yan, D.; Li, Y.; Huo, J.; Chen, R.; Dai, L.; Wang, S., Defect Chemistry of Nonprecious-Metal Electrocatalysts for Oxygen Reactions. *Adv. Mater.* **2017,** *29* (48), 1606459.
11. McKendry, I. G.; Thenuwara, A. C.; Sun, J.; Peng, H.; Perdew, J. P.; Strongin, D. R.; Zdilla, M. J., Water Oxidation Catalyzed by Cobalt Oxide Supported on the Mattagamite Phase of $CoTe_2$. *ACS Catal.* **2016,** *6* (11), 7393-7397.
12. Swesi, A. T.; Masud, J.; Liyanage, W. P. R.; Umapathi, S.; Bohannan, E.; Medvedeva, J.; Nath, M., Textured $NiSe_2$ Film: Bifunctional Electrocatalyst for Full Water Splitting at Remarkably Low Overpotential with High Energy Efficiency. *Sci. Rep.* **2017,** *7* (1), 2401.
13. Gao, Q.; Wang, X.; Shi, Z.; Ye, Z.; Wang, W.; Zhang, N.; Hong, Z.; Zhi, M., Synthesis of Porous $NiCo_2S_4$ Aerogel for Supercapacitor Electrode and Oxygen Evolution Reaction Electrocatalyst. *Chem. Eng. J.* **2018,** *331*, 185-193.

Chapter V Colloidal Ru-Decorated Binary Selenide Nanocrystals with Enhanced Hydrogen Evolution Reaction

5.1 Introduction

With rising concerns about an energy crisis, present efforts are aimed at finding clean and renewable energy resources to lessen our reliance on fossil fuels. Hydrogen is considered as an ideal fuel for the future as it is the most abundant element in the universe and it burns without producing toxic species.[1] Among various approaches to generate hydrogen, the electrolysis of water is the most attractive one as it is cheap and environmentally sustainable.[2-3] In the past decades, tremendous efforts have been made to develop efficient hydrogen evolution reaction (HER) catalysts based on both noble and non-noble elements.[4-5] Examples are noble metals (platinum,[6] iridium,[7] gold,[8] ruthenium[9] and their alloys[10]), transition metal chalcogenides (MoS_2,[11-12] FeS_2,[13] WS_2,[14] CoS_2,[15] CoSe,[16-17] NiS,[18-19] and NiSe[20]), metal carbides (Mo_2C[21]),[22] metal borides (MoB),[23] metal nitrides ($CoMoN_x$[24]),[22] and metal phosphides (Ni_5P_4,[25] CoP,[26] FeP,[27] MoP[28] and WP[29]) which were shown to be good HER catalysts.

However, among them, the best catalytic materials for the HER are still expensive noble-metal-based materials. In order to reduce the cost and reserve the electrocatalytic activity meanwhile as much as possible, the exploration of noble metal nanoparticles supported by matrixes which can provide large surface area, increase conductivity or achieve synergetic effect with the noble metal nanoparticles, is currently a hot research topic.[30-31] Carbon materials such as carbon nanotubes[32] and graphene are widely used as supports due to the high electrical conductivity and huge surface area. But it is proved that these carbon-based supports are not electrocatalytically active.[33] Moreover, the N or P doping carbon materials which function as eletrocatalysts are considered as more effective supports than the pure carbon materials, but the doping procedure requires high reaction temperature (around 1000 °C) and multistep process.[34] Besides, transition metal chalcogenides are also reported as support for noble metal nanoparticles and provide active sites for HER as well.[30, 35] However, the stability of these noble metal and transition metal chalcogenides combinations remains a problem because of the corrosion from the electrolyte and the aggregation from during HER. Thus to search for a suitable support which is able to optimize

the electrocatalytic property of the noble metals becomes a new strategy for discovering efficient electrocatalysts.

On the other hand, Ru has been recently employed and studied in HER electrocatalytic applications since it possesses a similar bond strength with hydrogen (~0.4 eV) compared to platinum, which is still the most efficient electrocatalyst for HER.[36] Although metallic Ru is active in catalyzing the HER, the dissolution of Ru during the catalytic reaction results in the low stability of pure Ru.[37] Therefore, the combination of Ru and other materials as heterostructures, alloys or hybrids becomes an new strategy to sustain the stability for Ru catalyst. For example, Liu *et al.* demonstrated that Ni@Ni_2P−Ru heterostructures show better HER performance than pure Ru NCs.[36] Su *et al.* synthesized alloyed Ru-Co NCs encapsulated in nitrogen-doped graphene as active electrocatalysts in HER.[34] Nong *et al.* dispersed Ru NCs in mesoporous TiO_2 as an advanced electrocatalyst for HER.

Motivated by such findings, we decided to use cobalt selenide, which is also an efficient and stable electrocatalyst for HER and easy to synthesize according to our previous report, as our support for Ru NCs. We developed a simple one-pot colloidal synthesis approach in order to incorporate a small ratio of Ru decorated with CoSe and to study the corresponding HER activity. Interestingly, the Ru-CoSe NCs exhibited a dramatically accelerated HER kinetics in acidic electrolyte and an overpotential as low as 152 mV at the current density of 10 mA/cm^2, which are better than the pure CoSe support. More specifically, the HER activity of the NCs even surpasses that of Pt/C at sufficiently high overpotentials. Moreover, this electrocatalyst was observed to undergo chemical transformation in the acidic electrolyte and form a Ru-cobalt oxide-cobalt selenide system, which is the real catalyst with a synergistic effect to enhance the electrocatalytic property. These results, strongly suggest that Ru decoration of transition metal chalcogenide NCs represents an interesting direction toward efficient electrocatalysts and new idea of designing the electrocatalysts in HER.

5.2 Colloidal Synthesis of Ru Decorated CoSe and its Application in HER

5.2.1 Colloidal Synthesis of Ru Decorated CoSe (Ru-CoSe) NCs

The Ru-CoSe NCs were produced by a colloidal synthesis approach. Typically, 0.05 mmol of $RuCl_3$ and 1 mmol of $Co(acac)_2$ were mixed with 10 mL of ODE in a 25 mL round bottom flask with an electromagnetic stirring. The mixture was degassed under vacuum at 120 °C for 1 hour to remove moisture and oxygen. After that, 1 mmol of Se precursor was injected into the flask under a

flow of Ar. The mixture was heated to 250 °C and maintained at that temperature for 5 min under stirring. The black product was cleaned twice by redispersion in toluene and precipitation by the addition of ethanol. Eventually the product was dispersed in toluene. For comparison, "bare" CoSe NCs, that is without any Ru decoration, were also synthesized using the same procedure, but without any Ru precursor. The synthesis protocol is shown in Scheme 5.1.

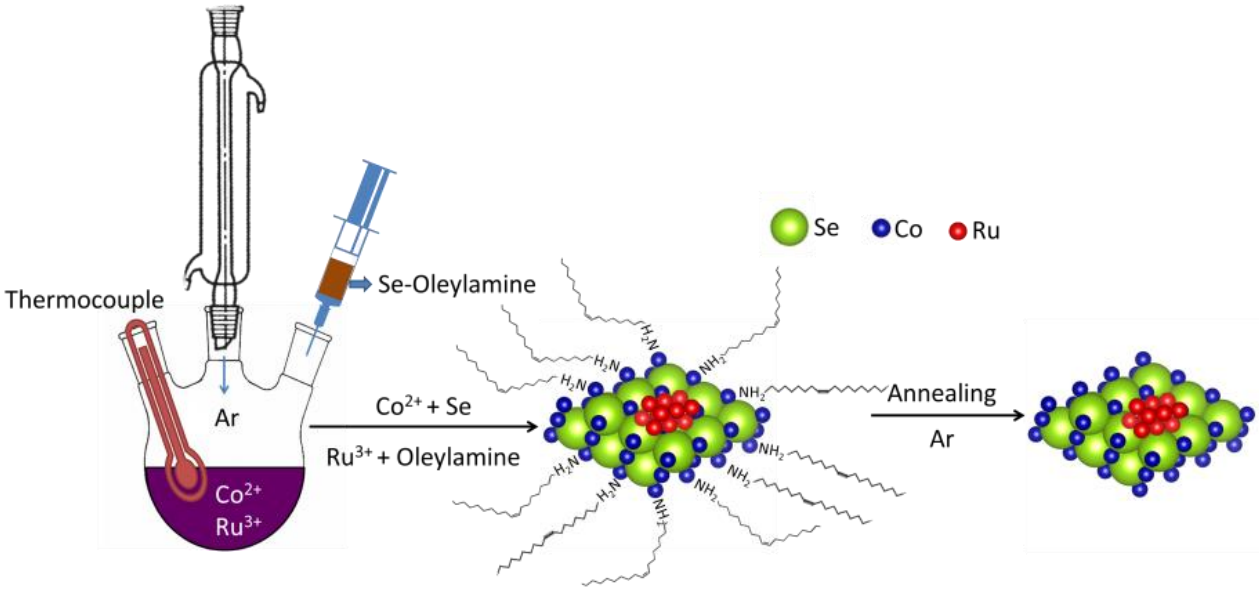

Scheme 5.1. Reaction Protocols for the synthesis of Ru-CoSe NCs.

Electrode Preparation. The NCs dispersed in ethanol can be directly used as an ink to coat on Ti foil substrates. 1.25 mg of NCs dispersion was drop-casted on 1 cm × 1 cm of Ti substrates. Then the electrodes were dried in air and annealed at 400 °C for 30 min under Ar atmosphere to remove the organic ligands on the surface of the samples.

5.2.2 Conventional Characterization

In order to test the effects of the incorporation of Ru inside CoSe, we synthesized both CoSe and Ru-decorated CoSe NCs (see the experimental part for details). After the synthesis, both samples were annealed at 300°C for 30 min under Ar with the aim of removing the native ligands (see the experimental part for details). Figure 5.1 shows the XRD patterns of Ru-CoSe and "bare" CoSe NCs indicating that the crystal phase of both NC products can be indexed with the hexagonal CoSe (ICSD number 53959) phase. However, the elemental analysis of CoSe and Ru-CoSe samples, performed via ICP-AES, showed atomic ratios of Co/Se are 1.06 and 0.96, suggesting a

composition of CoSe.

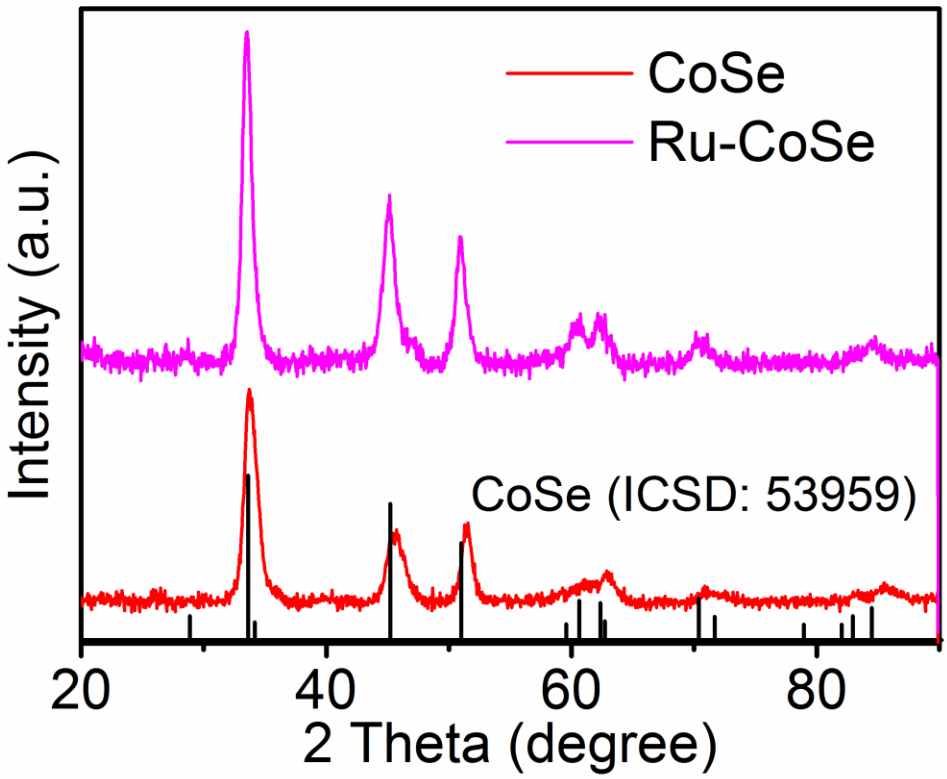

Figure 5.1. XRD patterns of CoSe and Ru-CoSe NC samples together with the bulk reflections of hexagonal CoSe (ICSD: 53959)

To further investigate the microstructure and chemical composition of our samples, we performed TEM and HRTEM characterizations. From the TEM micrographs the size of CoSe and Ru-CoSe NCs (Figure 5.2a, b) is around 10 nm. Figure 5.2c, d show HRTEM images of Ru-CoSe NCs in which the lattice fringes with spaces of 1.96 Å were observed, consistent with the distance of both (01-2) and (1-1-2) plane of the hexagonal CoSe phase (Figure 5.2e). The STEM-EDS mapping and line scan of Ru-CoSe NCs (Figure 2f, g) revealed that Ru was uniformly distributed inside CoSe NCs, with a Ru:Co ratio of 1.6:40 (4%).

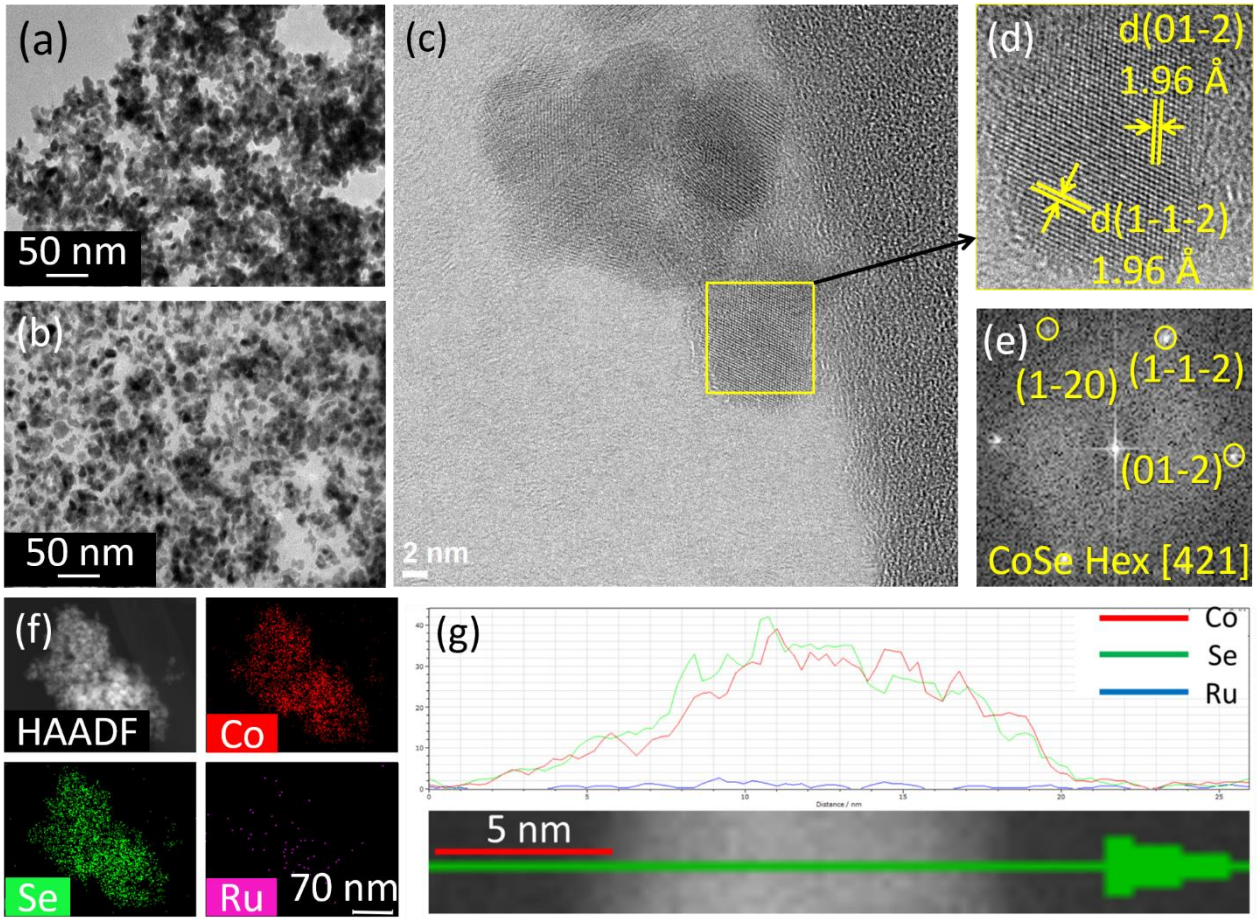

Figure 5.2. TEM images for (a) CoSe and (b) Ru-CoSe. (c) HRTEM image, (d) a region magnified of panel (c) and (e) the corresponding FFT pattern, (f) STEM-HAADF image and elemental maps of Ru, Co, and Se. (g) EDX line scan over a single NC of Ru-CoSe NCs.

To better elucidate the chemical composition of the samples we also performed XPS measurements, which are displayed in Figure 5.3a. In both CoSe and Ru-CoSe NC samples, four binding energies, Co $2p_{3/2}$, Co^{2+} $2p_{3/2}$, Co $2p_{1/2}$ and Co^{2+} $2p_{1/2}$ at 778, 781.2, 793 and 797 eV respectively, were observed in the high-resolution Co 2p spectrum, suggesting the existence of +2 and 0 oxidation states of Co (Figure 5.3b). As regarding CoSe NCs, two peaks appearing at 53.9 eV and 54.7 eV are related to the Se $3d_{5/2}$ and Se $3d_{3/2}$. Meanwhile, the broad peak at 59 eV is a mixture of SeO_x and Co 3p, which is in accordance with previous report,[38] implying the presence of SeO_2 on the surface of CoSe.[39] Se 3d in Ru-CoSe NCs has the similar condition compared to the oxidation state of Se 3d of CoSe NCs (Figure 5.3c). The Ru 3d peaks (blue line) in the Ru-CoSe NC sample were located at 280 and 284.2 eV are, indicating that Ru^{3+} ions were reduced to Ru(0) during the synthesis (Figure 5.3d), most likely conducted by the OAm.[40] Interestingly, the amount of Ru detected by XPS in Ru-CoSe NCs was around 8%, which suggests, if compared to what emerged

from the EDS analyses (4%), that probably Ru atoms are localized on the surface of the NCs as small clusters as metallic oxidation state, which are also analyzed in the CoP system.[31]

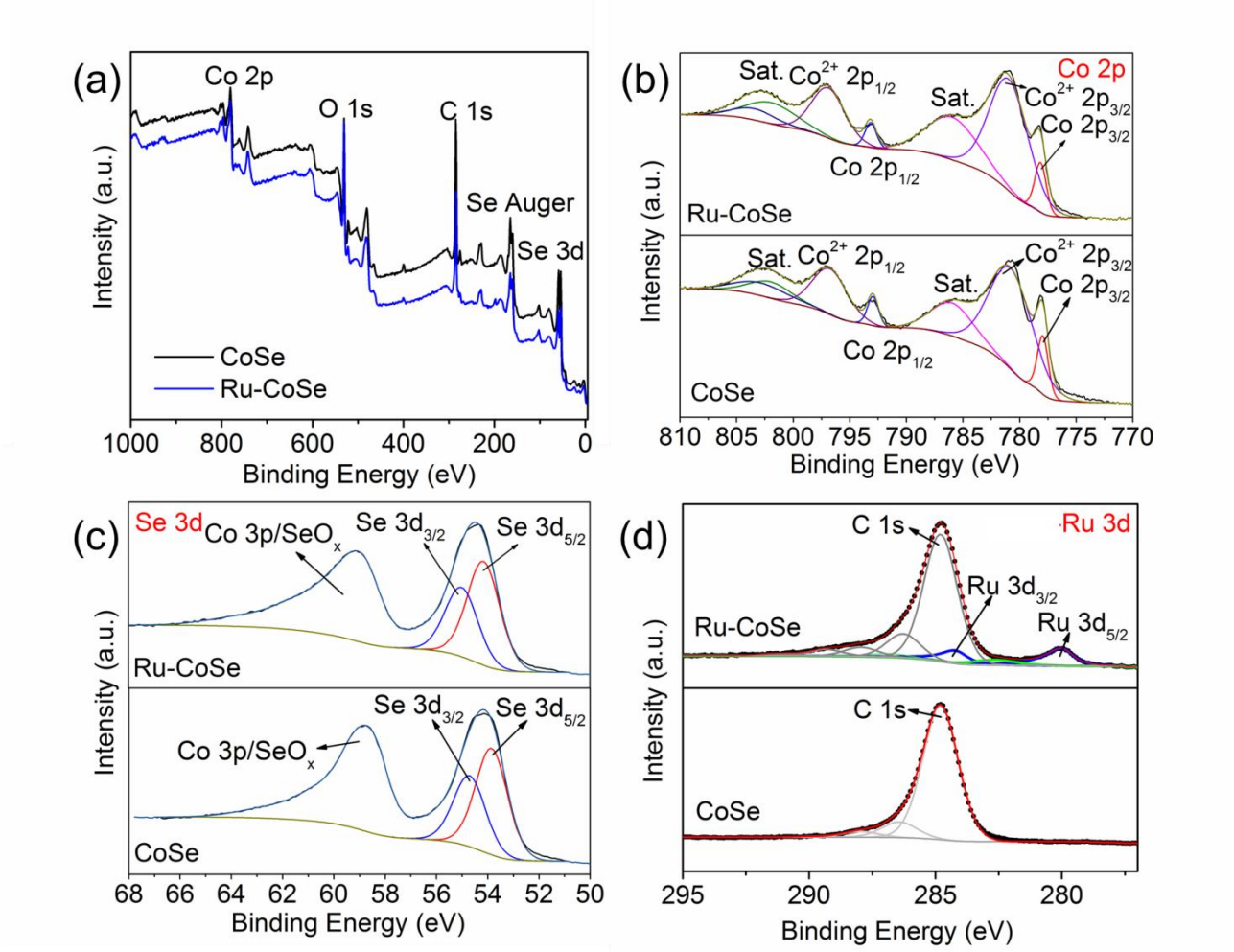

Figure 5.3. (a) XPS survey spectra of CoSe and Ru-CoSe NCs. XPS high resolution spectra of Co 2p (b), Se 3d (c) and Ru (d) for CoSe and Ru-CoSe NCs.

5.2.3 HER

To explore the effects of the presence of Ru on the electrocatalytic properties of CoSe NCs, the HER activities of both Ru-CoSe and CoSe NCs were characterized in detail. The polarization curves with the *iR* correction are illustrated in Figure 5.4a: the Ru-CoSe NCs exhibit an excellent HER performance with a low overpotential of 152 mV (to achieve 10 mA/cm^2), which is considerably lower than that of pristine CoSe NCs (228 mV). In order to understand the intrinsic HER activities of the electrocatalysts, we calculated the Tafel slopes from the corresponding polarization curves (see Figure 5.4b). The Tafel slope of Ru-CoSe NCs was as low as 37 mV/dec, close to the value of the Pt/C reference electrode (35.5 mV/dec), while CoSe NCs had a higher slope of 46 mV/dec. This indicates that hybridizing a small amount of Ru with CoSe indeed

substantially helps to accelerate the HER kinetics. The low Tafel slope of Ru-CoSe NC sample suggested that the HER kinetics employing this catalyst could be explained taking into account two steps of reactions: an initial Volmer step ($H^+ + e^- \rightarrow H_{ads}$) followed by a combination of Heyrovsky reaction ($H_{ads} + H^+ + e^- \rightarrow H_2$) and Tafel reaction ($2H_{ads} \rightarrow H_2$). The second step, in which adjacent adsorbed or ionic H combine to form H_2 molecule, was found to be the rate limiting step in this HER as the value of the Tafel slope is between 30 mV/dec (when Tafel reaction is dominating) and 40 mV/dec (when Heyrovsky reaction is dominating). EIS measurements performed on our HER catalysts, revealed that the presence of Ru on CoSe NCs support lowered the overall charge-transfer resistance (R_{ct}) than both CoSe and Pt/C NCs, suggesting a facile kinetics toward hydrogen evolution. (see Figure 5.4c). Furthermore, we calculated the TOF values which reflect the intrinsic electrocatalytic activity of a catalyst. As shown on the left of Figure 4d, the TOF values at different overpotentials for each active site of Ru-CoSe NCs and Pt/C NCs in acidic solution were calculated considering Ru and Pt as active sites, finding 0.5, 1.25 and 2.07 H_2 s^{-1} for Ru-CoSe NCs at 200, 250 and 300 mV, and 1.28, 1.65 and 2.1 H_2 s^{-1} for Pt/C NCs. It is interesting to see that the TOF is improved dramatically by the Ru clusters, and the value is comparable to Pt/C NCs under higher overpotential, indicating excellent H_2 production efficiency on each active site of Ru-CoSe NCs. Besides, the mass activity of the HER normalized to Ru (for Ru-CoSe NCs) and Pt (for Pt/C NCs) loading was calculated at 200, 250 and 300 mV, respectively. Remarkably, the mass activity of the Ru-CoSe NCs exceeds that of Pt/C NCs at 250 mV, and is 2 times higher than Pt/C NCs. These findings suggest that the Ru element in Ru-CoSe NCs can significantly increase the activity at higher overpotential in comaparison to the Pt element in the Pt/C compound.

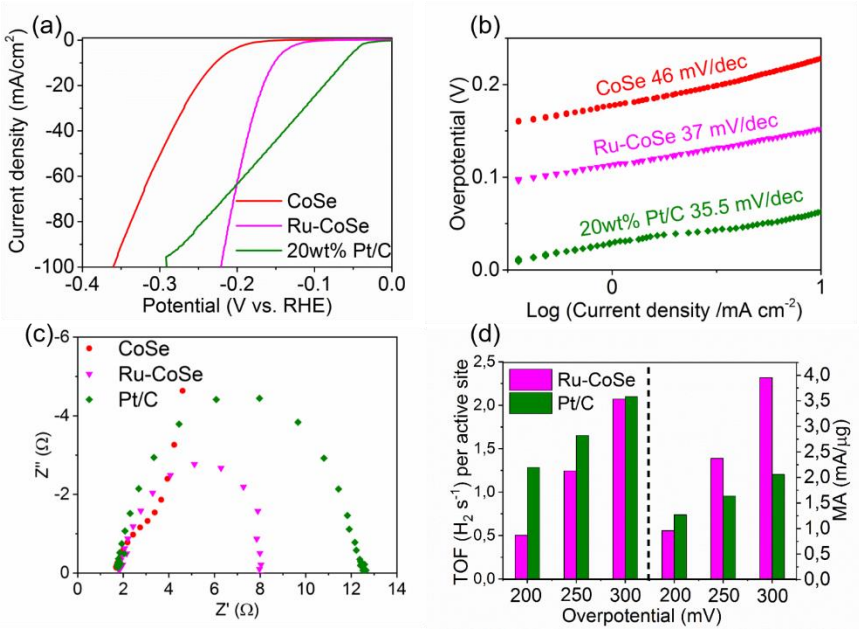

Figure 5.4. (a) LSV polarization curves, corresponding (b) Tafel plots, (c) EIS Nyquist plots and

(d) TOF and mass activity (MA) values of Ru-CoSe and Pt/C NCs.

These findings suggested that the addition of Ru in CoSe NCs does not lead to an increase in the number of active sites, but it strongly enhances the charge transfer speed. As it is well known, the metal–hydrogen (M–H) bond plays an important role in the HER: a strong M–H bond facilitates an easy adsorption of intermediate hydrogen and a difficult product desorption, while a weak M–H bond promotes the product desorption but restrains the adsorbed hydrogen. According to the literature, it is known that Ru has a weaker M-H bond (~0.245 eV) than Co (~0.41 eV).[40-44] Since for both CoSe and Ru-CoSe NCs the Heyrovsky reaction is the rate limiting step, it is possible that the function of Ru in CoSe is to accelerate the H_2 desorption from the surface of the catalyst, which is also supported by the TOF values measured for Ru-CoSe (0.5 H_2 s^{-1}) and CoSe (1.94×10^{-3} H_2 s^{-1}) at the overpotential of 200 mV. Although CoSe NCs have a larger C_{dl} (1.52 mF/cm^2) than Ru-CoSe NCs (0.87 mF/cm^2), that means they are characterized by more active sites, probably the adsorption of intermediate hydrogen and desorption of H_2 are faster on the surface of Ru-CoSe NCs, thus Ru-CoSe still has better kinetics though it has less C_{dl}.

5.2.4 Mechanism of HER of Ru-CoSe NCs

Moreover, in order to understand the mechanism of HER on Ru-CoSe NCs, we also performed CV measurement and the XRD characterization after 20 and 40 cycles. The results of the analysis are reported in Figure 5.7. Ru-CoSe NCs went through a chemical transformation from hexagonal CoSe (ICSD number: 53959) to monoclinic Co_3Se_4 (ICSD number: 99990) after 20 cycles of CV, then the Co_3Se_4 phase finally transformed to cubic $CoSe_2$ (ICSD number: 624998) structure after 40 cycles (Figure 5.7a-b), which was corroborated by the ICP elemental analysis (Table 5.1). This was further confirmed by the elemental analysis of the electrolyte used for the HER which was characterized by a Co/Se ratio as high as 2.79. This suggested that the Co extracted from the NCs during the chemical transformation from the CoSe to the $CoSe_2$ composition, was eventually solubilized in the electrolyte. It should be mentioned that Ru is not detected in the electrolyte, which suggests that Ru particles remain on the electrode. The corresponding CV curves in Figure 5.7c showed that the HER activity was improved when the chemical structure was changed from CoSe to Co_3Se_4 after 20 cycles. While after 40 cycles, a slight increase of the overpotential was observed. This might result from the delamination of the catalyst from the substrate after CV cycles since both Co and Se were detected in the electrolyte (see Table 5.1).

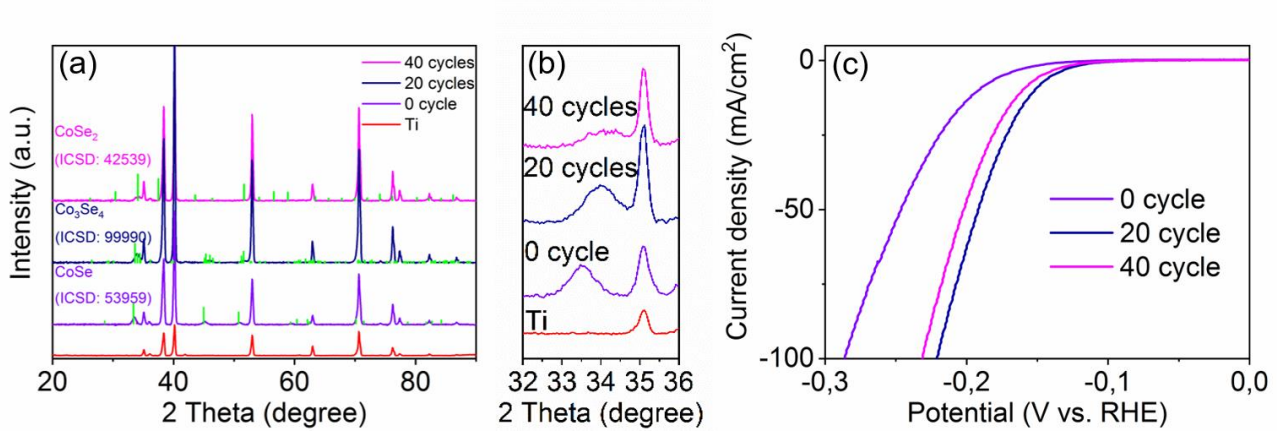

Figure 5.5. (a) XRD patterns, (b) the magnification of the XRD patterns from 32 to 36°, and (c) CV polarization curves on Ti substrates of Ru-CoSe NCs after 0, 20 and 40 cycles.

Table 5.1. Elemental analysis of Ru-CoSe NCs under annealing temperature of 400 °C after 40 cycles of CVs.

Sample	**Ratio of Co/Se**	**Ratio of Ru/Co**
Ru-CoSe	0.53	0.1
Electrolyte	2.79	0

The morphology, structure and composition of Ru-CoSe NCs after HER were further analyzed by TEM and HRTEM. The TEM image (Figure 5.6a) of the sample shows that the separated nanoparticles (Figure 5.2b) are aggregated and "covered" by the "cloud". The corresponding SAED pattern reveals the phase of $CoSe_2$ (ICSD number: 624998), which is consistent with the XRD result (Figure 5.5a-b). To deeper observe the element of the sample, the HAADF-STEM and the corresponding EDS elemental mapping were carried out. Figure 5.6c clearly confirms the Co, Se and Ru are still distributed uniformly throughout the NCs and the atomic ratio of Co/Se is 0.5 and Ru/Co is 0.1, which are in accordance with the ICP elemental analysis. Surprisingly, a large ratio of O (atomic ratio 24% among all the elements tested) is also found among the NCs, which means probably some oxides or hydroxides are formed among the NCs. The HRTEM image in Figure 5.6d shows that the crystals are surrounded by the amorphous substances which are probably Co hydroxides, as in the amorphous area some layers can be assigned to $Co(OH)_2$ (ICSD number: 53994). Another lattice-resolved HRTEM image taken from the NCs shows that the Ru-CoSe NCs after HER (Figure 5.6e) shows that the area has two systems of overlapped lattice fringes which can be indexed to the fringes from Ru (ICSD number: 40354, the yellow area) and $CoSe_2$ (ICSD number: 624998, the red area). This analysis is also proved by the corresponding fast Fourier

transform image in Figure 5.6f. Besides, the layered structure which can be $Co(OH)_2$ is also found beside the crystals. A linear EDX spectrum over a single NC shows also a small Ru nanoparticle of around 1 nm beside the $CoSe_2$ NC, which idcan be another evidence of the formation of Ru nanoparticles. These observations reveal that after HER, Co hydroxide layers are formed on the surface of the NCs, and the Ru-CoSe NCs undergo a composition transformation from hexagonal CoSe phase to cubic $CoSe_2$ phase with the extraction of Co from the lattice. Meanwhile, probably some Ru clusters decorated on the surface of the cobalt selenides are aggregated since Ru nanoparticles are found by HRTEM image (Figure 5.6e) and EDX spectrum (Figure 5.6g).

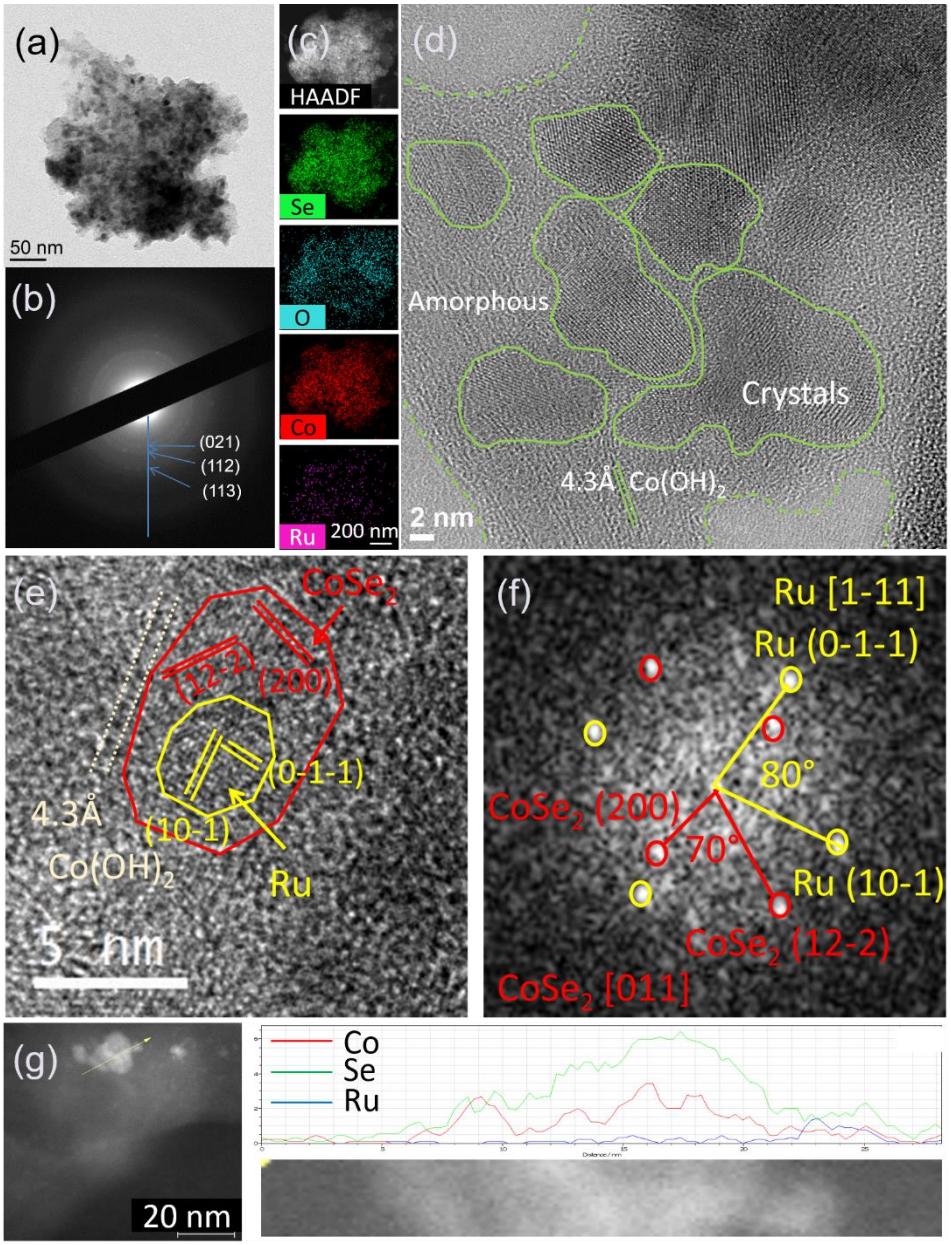

Figure 5.6. (a) TEM and (b) SAED pattern, (c) EDS mapping and (d-e) HRTEM of Ru-CoSe NCs

after HER. (f) Fast Fourier transform image of region (e). (g) EDX line scan over a single NC of the Ru-CoSe NCs after HER.

Then we tested the chemical composition and the valance state of Co, Se and Ru elements on the surface of the Ru-CoSe NCs after HER. As shown in Figure 5.7a, the dominant peaks in the Co 2p XPS spectrum at 781.8 and 797.3 eV assigned to Co^{2+} $2p_{3/2}$ and Co^{2+} $2p_{1/2}$ are from Co^{2+} coordinated to O^{2-} or OH^- ions, and are shifted to the higher binding energy compared to the Co^{2+} peaks from the CoSe phase of the sample before HER (Figure 5.3b). This is probably due to the oxidation on the surface of the samples during the HER.[24] Besides, the metallic Co can be seen at 778.7 (Co $2p_{3/2}$) and 795.5 eV (Co $2p_{1/2}$) and these peaks are attributed to the metallic nature of in the $CoSe_2$ phase.[11] The intensity of these peaks is weak compared to the Co^{2+} peaks, which reveals that the Co hydroxides are more on the surface and probably $CoSe_2$ is covered by these oxides. The fitting of Se 3d data reveals Se $3d_{5/2}$ (56 eV) and Se $3d_{3/2}$ (55 eV) states, which are assigned to the Se in the $CoSe_2$ phase (Figure 5.7b). The observed mixture of valance states of SeO_x and Co 3p at around 59 eV shows more intensive peak than the peaks from Se $3d_{5/2}$ and Se $3d_{3/2}$, which is on the opposite to the results of the sample before HER (Figure 5.3c). This increase of intensity is probably from Co 3p due to the Co hydroxides layer on the surface. XPS analysis in the Ru 3d region is shown in Figure 5.7c. It can be seen that no any peak related to Ru species was observed in this region. This might be because the amount of Ru is quite low and some of the Ru particles are covered by the Co hydroxide layers. Besides, the composition determined from the XPS analysis suggests that the sample surface is enriched in Co (Co/Se ratio is 72/28), which verifies again the existence of Co hydroxide layers on the surface.

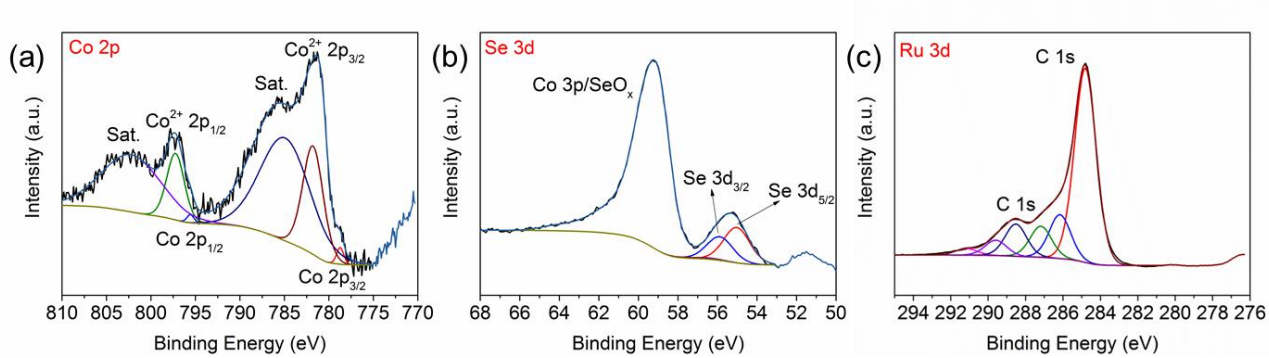

Figure 5.7. XPS spectra for the Ru-CoSe NCs after HER in the (a) Co 2p, (b) Se 3d and (c) Ru 3d regions.

The thermodynamic stability of these cobalt selenide compounds in water with an applied bias might explain the CoSe → $CoSe_2$ transformation occurring in our catalyst under HER operational

conditions. As reported, the standard Gibbs free energies of formation (1 bar of pressure and 25 °C) of CoSe and $CoSe_2$ are −56.3 ± 6.5 and −100.4 ± 15.0 kJ/mol, respectively, indicating that $CoSe_2$ is more stable than CoSe at ambient conditions.[45] Meanwhile, a potential-pH diagram (Pourbaix diagram) of Co-Se-H_2O system was plotted in Figure 5.8, where it is possible to see that when the applied bias is negative, the only stable phase in the pH rage from 0 to 14 is $CoSe_2$ (trogtalite) only. Moreover, since the H* species on the surface are consumed to form H_2, the remaining OH* are released into the electrolyte creating a temporary liquid layer with high pH value close to the surface of the electrocatalysts (Figure 5.9). Under such high pH value, it is possible that the surface of the $CoSe_2$ catalyst is oxidized to form Co hydroxide species.

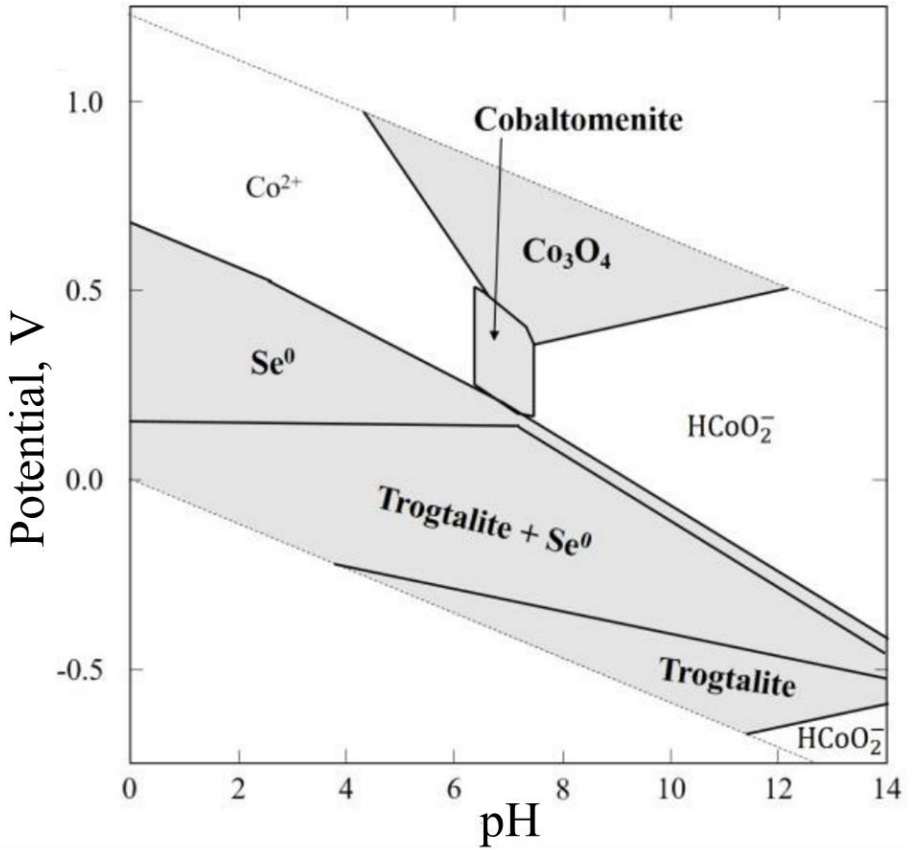

Figure 5.8. Potential–pH diagram of the system Co–Se–H_2O at 25 °C and the activities of the components: $a_{\Sigma Se} = 10^{-4}$, $a_{\Sigma Co} = \cdot 10^{-3}$.[46]

Our results indicated that, overall, the final actual catalyst was composed of a mixture of Ru-decorated $CoSe_2$ NCs surrounded by a Co oxide/hydroxide matrix (see Scheme 5.2). Thus, in order to explain the high HER performance of our catalyst, we propose a concerted interaction of OH^- with Co hydroxide species and H^+ with Ru NCs in which Co hydroxides help in water adsorption

and dissociation by forming H* species that are adsorbed on adjacent Ru atoms. Two H* on Ru sites then combine to evolve H_2, similar to what has been previously shown in the case of Cu-TiO_2 catalyst reported by our group and Li^+-$Ni(OH)_2$-Pt system reported by Markovic and co-workers.[47-48] The $CoSe_2$ which has an intimate connection with Co hydroxides can enhance the charge transfer speed on Co hydroxides since the conductivity of $CoSe_2$ is greater than the Co hydroxides. This enhancement can accelerate the water adsorption and dissociation speed on the surface of Co hydroxides thus provide more H* species per unit time. This synergistic effect of Co hydroxides, Ru nanoparticles and $CoSe_2$ NCs promotes the HER activity eventually.

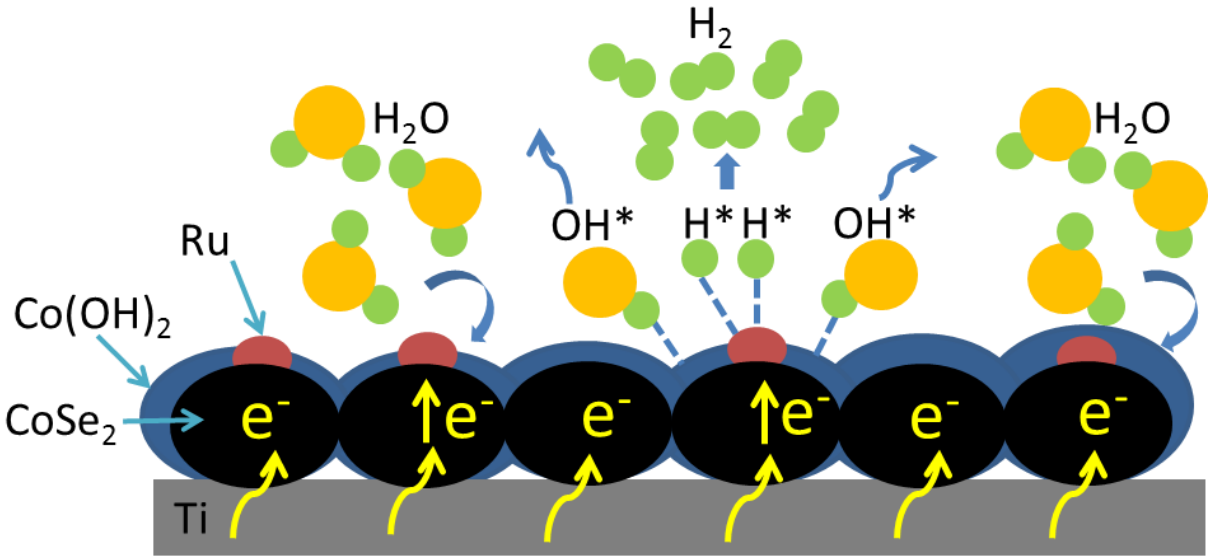

Scheme 5.2. Schematic illustration of the mechanism of Ru-$Co(OH)_2$-$CoSe_2$ electrocatalysts for HER.

5.2.5 Influence of the Annealing

We hypothesized that the main effect of the annealing was to remove the surface ligands, which are known as hindrance of the electrocatalytic properties of colloidal NCs.[49] Indeed, as organic ligands bind metal cations on the surface of NCs, they can reasonably hinder the formation of M-H bonds.[50] In order to test our hypothesis, we performed TGA and FTIR measurements to study the desorption temperature of ligands and if they are present on our catalysts after the annealing step. As shown in Figure 5.9a, the thermogravimetric scans of Ru-CoSe NCs reach a plateau at around 400 °C, and the ligand stripping process involves a total weight loss of around 14%. As shown in Figure 5.9b, before annealing, Ru-CoSe NCs shows strong IR peaks at 2853 and 2922 cm^{-1}, which are due to the symmetric and asymmetric CH_2 stretching modes, respectively. A weak peak at 1459 cm^{-1} could be ascribed to the NH_2 scissoring mode,[51-52] suggesting, thus, that in

both samples the NCs are passivated by OAm. After annealing the samples at 400 °C, we observed the complete disappearance of absorption features in the FTIR spectrum of Ru-CoSe NCs, confirming the complete removal of organic ligands from such sample.

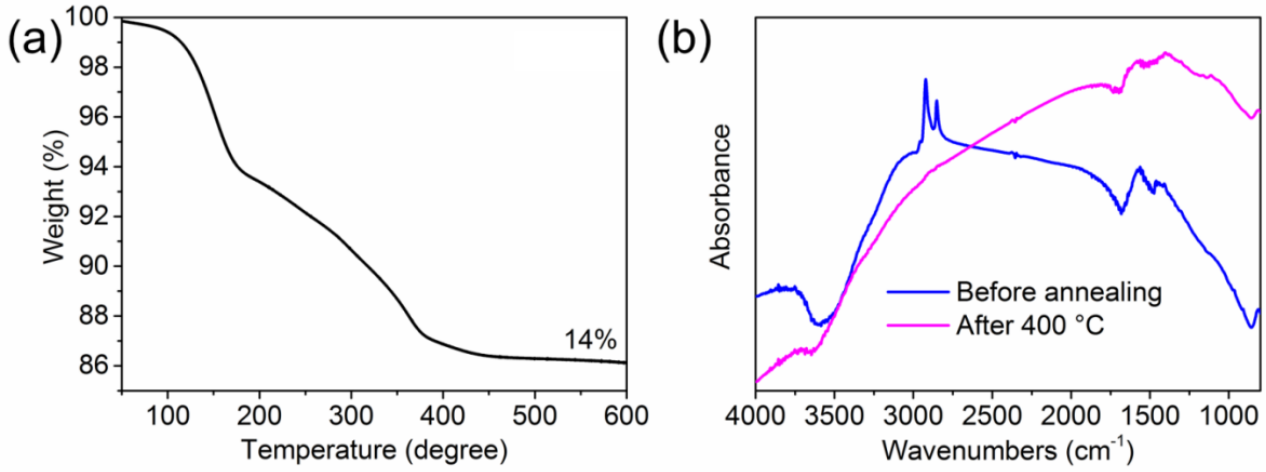

Figure 5.9. (a) Thermogravimetric scans for Ru-CoSe NCs. (b) FTIR spectra of Ru-CoSe NCs before and after annealing at 400 °C. The FTIR spectra were normalized to the amount of absorbing material.

The comparison in electrocatalytic properties of Ru-CoSe NCs before and after annealing is distinct. Figure 5.10a shows the LSVs at a scan rate of 10 mV/s for Ru-CoSe NCs before and after annealing. Before annealing, the Ru-CoSe exhibits a larger overpotential of 247 mV at 10 mA/cm^2 than the potential after annealing (152 mV). For further insight into the HER activity, Tafel plots are shown in Figure 5.10b. The fitting calculation shows a Tafel slope of 68 mV/dec for Ru-CoSe before annealing, which is larger than that of the sample after annealing (37 mV/dec). To gain a better understanding of the HER kinetics occurring at the electrode/electrolyte interface, EIS measurements were carried out with a potential of -0.2 V vs. RHE. The corresponding Nyquist plots are shown in Figure 5.10c. The R_{ct} of the sample was observed to be reduced after the annealing, implying a remarkable improvement in HER kinetics. In addition, the C_{dl} is used for representing the ECSA and the calculated capacitance of Ru-CoSe NCs before and after annealing is 0.25 and 0.87 mF/cm^2, respectively (Figure 5.10d). This implies that the surface area is enlarged by annealing. At last, by calculating the TOF at η = 350 mV, we found that annealing is helpful to increase the H_2 production efficiency by levels from 0.012 to 0.21 H_2 s^{-1}.

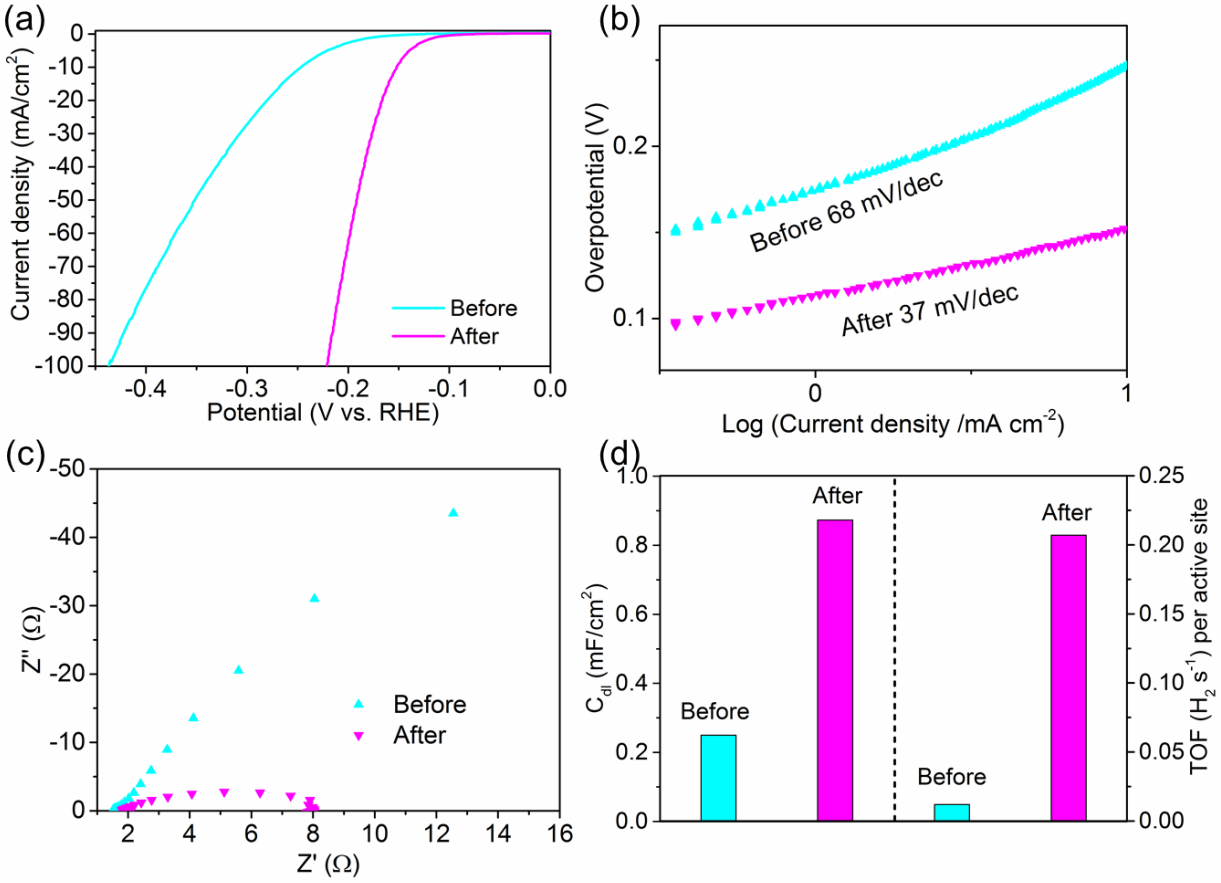

Figure 5.10. (a) LSV polarization curves, corresponding (b) Tafel plots, (c) EIS Nyquist plots and (d) C_{dl} and TOF values of Ru-CoSe NCs before and after annealing.

5.2.6 Stability

Finally, we tested the long-term stability of the Ru-CoSe catalyst by chronopotentionmetry at an applied current density of -10 mA/cm^2 for more than 80 h (Figure 5.11). In the initial 20 h, the potential gradually decreased: this could be explained considering that, initially, the electrocatalyst goes through a composition transformation from CoSe to $CoSe_2$. Meanwhile the surface of the catalyst is oxidized gradually to Co hydroxides. These changes can reconstruct a better system for HER as we discussed above. After 20 h, the catalyst showed an excellent stability, with an increase of the potential of only 0.04V at -10 mA/cm^2 after 80 h. This slight increase in the potential is probably caused by the drop of the NCs from the electrode, since Co and Se is detected by ICP measurement in the electrolyte after the stability test.

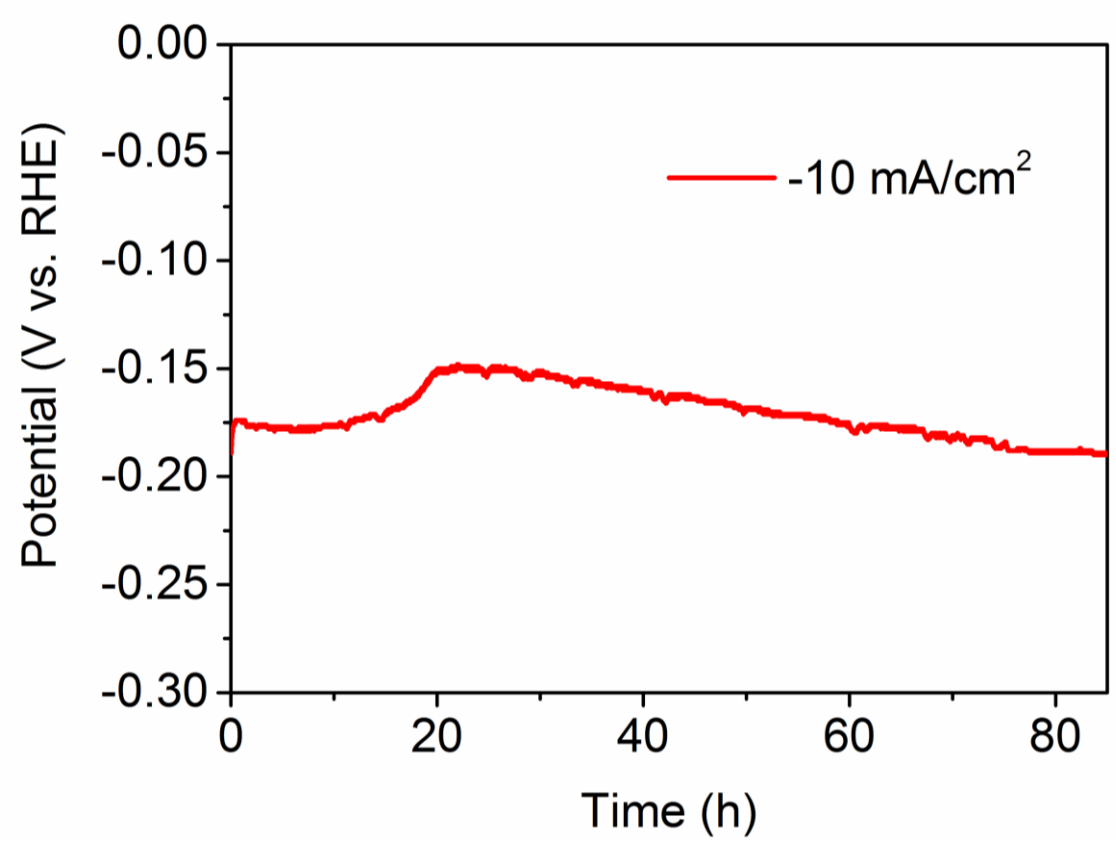

Figure 5.11. Chronopotentionmetry plot at a constant cathodic current of -10 mA/cm^2.

5.3 Colloidal Synthesis of Ru Decorated NiSe and its Application in HER

Synthesis of Ru decorated NiSe (Ru-NiSe) NCs. Typically, 0.05 mmol of $RuCl_3$ and 1 mmol of $Ni(acac)_2$ were mixed with 10 mL of ODE in a 25 mL round bottom flask with an electromagnetic stirring. The mixture was degassed under vacuum at 120 °C for 1 hour to remove moisture and oxygen. After that, 1 mmol of Se precursor was injected into the flask under a flow of Ar. The mixture was heated to 250 °C and maintained at that temperature for 5 min under stirring. The black product was cleaned twice by redispersion in toluene and precipitation by the addition of ethanol. Eventually the product was dispersed in toluene. For comparison, "bare" CoSe NCs, that is without any Ru decoration, were also synthesized using the same procedure, but without any Ru precursor.

Electrode Preparation. Typically, 5 mg of NCs were dispersed in 2 mL of solution (ethanol + 0.25 wt% of Nafion® 117 solution) and used as an ink. The performance with this kind of ink is better than the direct ethanol solution for Ru-NiSe (Figure 5.12). 0.625 mg of NCs dispersion was drop-casted on 1 cm × 1 cm Ti substrates. Then the electrodes were dried in air and annealed at 300 °C for 30 min under Ar atmosphere to remove the organic ligands on the surface of the

samples.

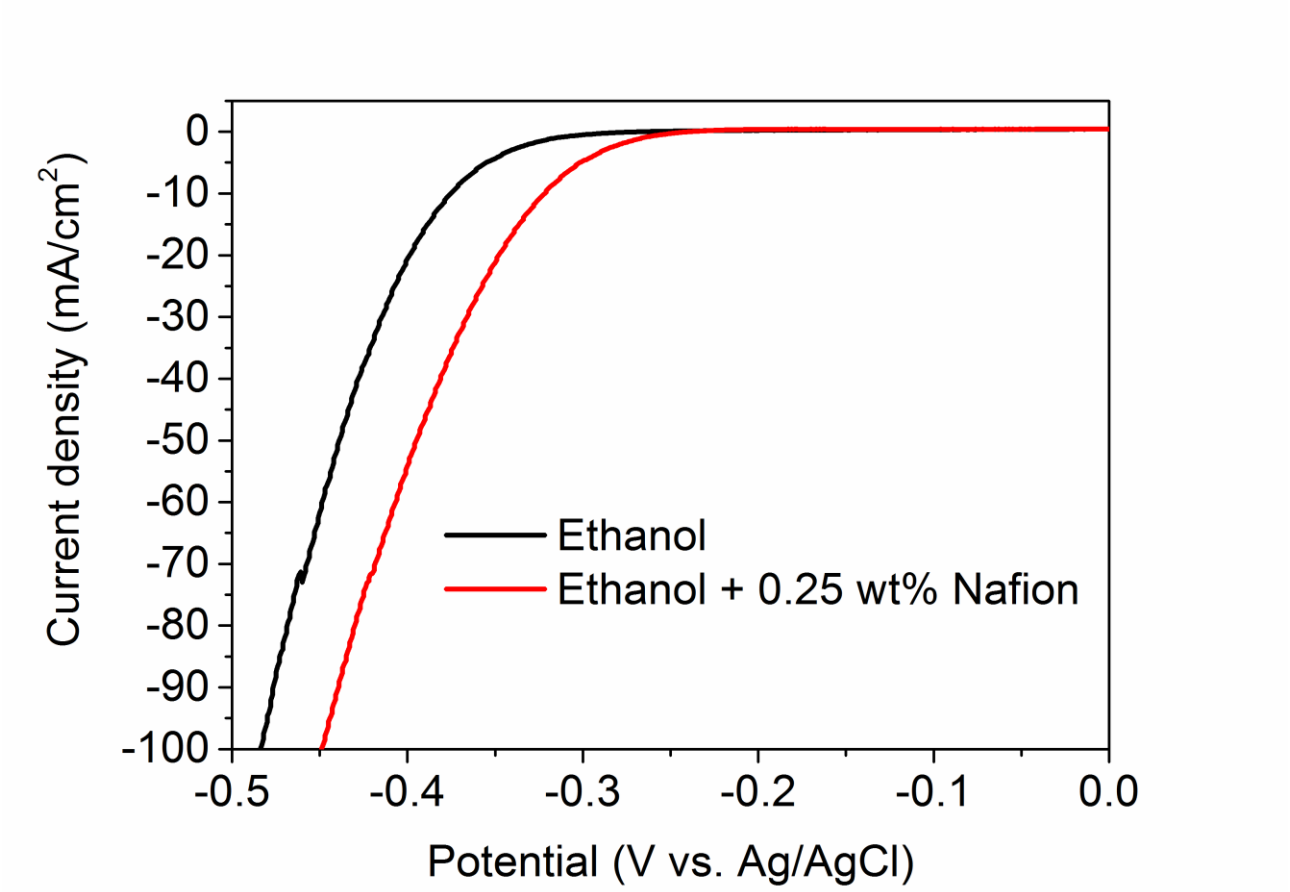

Figure 5.12. Comparison of the HER performance of Ru-NiSe with different inks.

Conventional characterization. The as-prepared NiSe and Ru-NiSe NCs were prepared according to the experimental procedure and annealed at 400 °C for 30 min under Ar atmosphere. The XRD patterns of the samples were shown in Figure 5.13a, exhibiting that both of NiSe and Ru-NiSe NCs inherited the hexagonal NiSe structure (ICSD number: 29310) except that Ru-NiSe has a small amount of cubic Ni_3Se_2 phase (ICSD number: 655498). The corresponding TEM images are illustrated in Figure 5.13b-c. The images of both NC samples showed an average particles size of around 40 nm. As shown in Figure 5.13d, the images of elemental mapping from SEM showed that all the elements including Ru (atomic ratio 0.64%), Ni (atomic ratio 45.75%) and Se (atomic ratio 53.6%) were uniformly distributed among the NCs, further providing the evidence that Ru might decorate without aggregation on the surface of NiSe NCs.

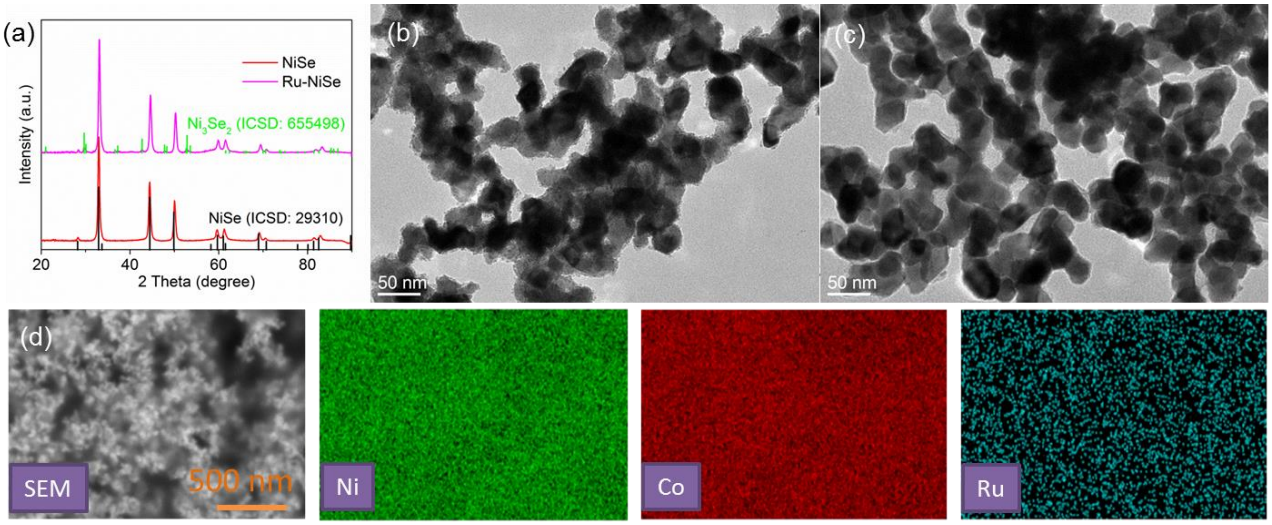

Figure 5.13. (a) XRD patterns of NiSe and Ru-NiSe NCs. TEM images of (b) NiSe and (c) Ru-NiSe NCs. (d) EDS mapping of Ru-NiSe NCs.

Electrochemical characterization. The electrocatalytic HER performance of Ru-NiSe NCs was evaluated and compared to that of NiSe NCs and the "reference" 20% Pt/C catalyst. Figure 5.14a shows the LSV curves of the different catalysts in 0.5 M H_2SO_4: a decrease in the HER activity (based on the onset potential) was observed in the following order: 20% Pt/C > Ru-NiSe >> NiSe. Besides, the overpotential at current density equal to -10mA/cm^2 for Ru-NiSe is 125 mV, which is much lower than that of NiSe NCs. Additionally, Ru-NiSe has a Tafel slope of 32.3 mV/dec, even smaller than that of 20% Pt/C (35.5 mV/dec) and much better than that of NiSe (122 mV/dec), indicating that Ru-NiSe has faster catalytic kinetics than the individual NiSe (Figure 5.14b). The EIS showed that Ru-NiSe had a much lower R_{ct} than NiSe, indicating the electron transfer rates in HER was much faster in the presence of Ru-NiSe than NiSe (Figure 5.14c). Also, the calculated TOF is 0.25 H_2 s^{-1} at overpotential of 350 mV if all the Ni and Ru are considered as the active sites, outperforming NiSe without Ru decoration (Figure 5.14d).

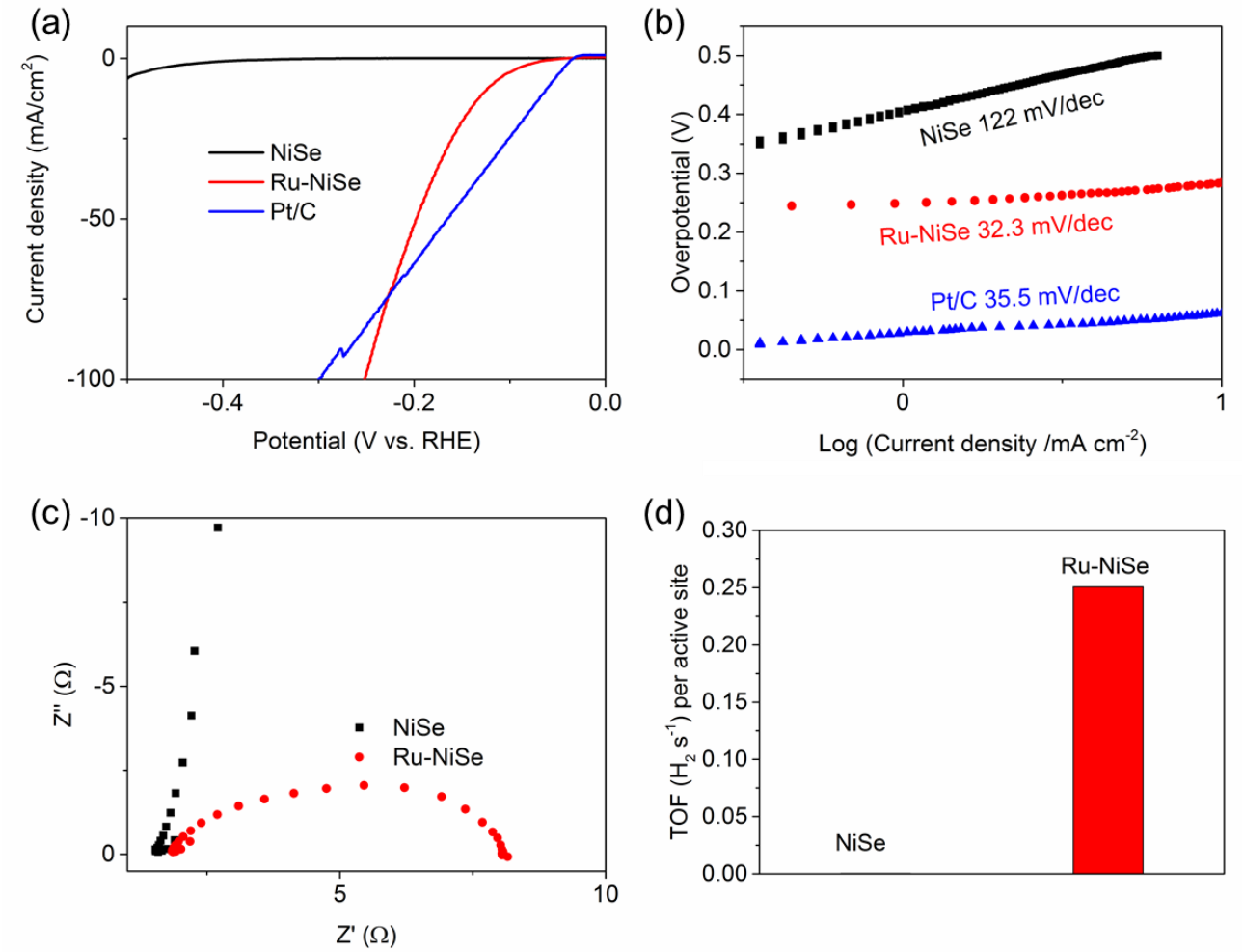

Figure 5.14. (a) LSV polarization curves, corresponding (b) Tafel plots, (c) EIS Nyquist plots and (d) C_{dl} and TOF values of Ru-CoSe NCs before and after annealing.

All of these electrochemical characterizations prove that a small amount of Ru, which acts as the decoration, can improve the activity of NiSe dramatically. This might be because the addition of Ru can modify the adsorption free energy of intermediate thus enhancing the performance.[36] Besides, the synergistic effect from a mixture of NiSe and Ni_3Se_2 phases can be another reason why Ru-NiSe has better performance according to other literatures.[53-54]

5.4 Conclusion

In summary, we synthetized Ru-decorated CoSe and NiSe NCs which exhibited excellent activity for the HER. The catalyst was produced by a simple and cheap one-step colloidal method in which $Co(acac)_2$ or $Ni(acac)_2$ and $RuCl_3$ were reacted with a OAm-Se complex at 250 °C. The presence of Ru was observed to strongly enhance the electrocatalytic properties of CoSe and NiSe NCs, mainly by improving the kinetics, resistance, and efficiency of H_2 production (TOF).

Besides, by studying the influence of the annealing, it is found that the long-chain amine ligands have a negative influence on HER properties and can be removed by annealing at 400 °C in Ar atmosphere. This is an efficient way to improve the HER activity of the materials from colloidal synthesis. Moreover, a chemical structure conversion was observed from CoSe to $CoSe_2$, the surface was oxidized and aggregated Ru nanoparticles were formed during HER. Such processes are beneficial for enhancing the charge transfer speed and leading to a boost in HER. This present work highlights that the coupling a small ratio of Ru with the transition metal chalcogenides could improve the performance and the Ru-NiSe is also an example. The synthetic strategy may also be extended to incorporate other similar noble metals into metal chalcogenide NCs.

References

1. Liang, J.; Yang, Y.; Zhang, J.; Wu, J.; Dong, P.; Yuan, J.; Zhang, G.; Lou, J. Metal Diselenide Nanoparticles as Highly Active and Stable Electrocatalysts for the Hydrogen Evolution Reaction. *Nanoscale* **2015,** *7*, 14813-6.
2. Zheng, Y.; Jiao, Y.; Vasileff, A.; Qiao, S. Z. The Hydrogen Evolution Reaction in Alkaline Solution: From Theory, Single Crystal Models, to Practical Electrocatalysts. *Angew. Chem., Int. Ed. Engl.* **2018,** *57*, 7568-7579.
3. Gao, M. R.; Xu, Y. F.; Jiang, J.; Yu, S. H. Nanostructured Metal Chalcogenides: Synthesis, Modification, and Applications in Energy Conversion and Storage Devices. *Chem. Soc. Rev.* **2013,** *42*, 2986-3017.
4. Zou, X.; Zhang, Y. Noble Metal-Free Hydrogen Evolution Catalysts for Water Splitting. *Chem. Soc. Rev.* **2015,** *44*, 5148-5180.
5. Moutet, J.-C., Electrocatalytic Hydrogenation on Hydrogen-Active Electrodes. A Review. *Org. Prep. Proced. Int.* **1992,** *24*, 309-325.
6. Ding, Q.; Song, B.; Xu, P.; Jin, S., Efficient Electrocatalytic and Photoelectrochemical Hydrogen Generation Using MoS_2 and Related Compounds. *Chem* **2016,** *1*, 699-726.
7. Lamy-Pitara, E.; Barbier, J., The Electrocatalytic Reactions of Oxidation and Evolution of Hydrogen on Iridium Electrodes Modified by Sulphur Adsorption. *J. Electroanal. Chem.* **1996,** *416*, 47-51.
8. Xu, Y., The Hydrogen Evolution Reaction on Single Crystal Gold Electrode. *Int. J. Hydrogen Energy* **2009,** *34*, 77-83.
9. McCoustra, M. R., Water at Interfaces. *Phys. Chem. Chem. Phys.* **2008,** *10*, 4676-7.
10. Greeley, J.; Norskov, J. K.; Kibler, L. A.; El-Aziz, A. M.; Kolb, D. M., Hydrogen Evolution over Bimetallic Systems: Understanding the Trends. *Chemphyschem* **2006,** *7*, 1032-5.
11. Shinde, D. V.; Trizio, L. D.; Dang, Z.; Prato, M.; Gaspari, R.; Manna, L. Hollow and Porous Nickel Cobalt Perselenide Nanostructured Microparticles for Enhanced Electrocatalytic Oxygen Evolution. *Chem. Mater.* **2017,** *29*, 7032-7041.
12. Merki, D.; Hu, X. Recent Developments of Molybdenum and Tungsten Sulfides as Hydrogen Evolution Catalysts. *Energy Environ. Sci.* **2011,** *4*, 3878-3888.
13. Faber, M. S.; Lukowski, M. A.; Ding, Q.; Kaiser, N. S.; Jin, S. Earth-Abundant Metal Pyrites (FeS_2, CoS_2, NiS_2, and Their Alloys) for Highly Efficient Hydrogen Evolution and Polysulfide Reduction Electrocatalysis. *J. Phys. Chem. C* **2014,** *118*, 21347-21356.
14. Yang, J.; Voiry, D.; Ahn, S. J.; Kang, D.; Kim, A. Y.; Chhowalla, M.; Shin, H. S. Two-Dimensional Hybrid Nanosheets of Tungsten Disulfide and Reduced Graphene Oxide as Catalysts for Enhanced Hydrogen

Evolution. *Angew. Chem. Int. Ed. Engl.* **2013,** *52*, 13751-13754.
15. Zhang, H.; Li, Y.; Zhang, G.; Xu, T.; Wan, P.; Sun, X. A Metallic CoS_2 Nanopyramid Array Grown on 3D Carbon Fiber Paper as an Excellent Electrocatalyst for Hydrogen Evolution. *J. Mater. Chem. A* **2015,** *3*, 6306-6310.
16. Li, Y.; Polakovic, T.; Curtis, J.; Shumlas, S. L.; Chatterjee, S.; Intikhab, S.; Chareev, D. A.; Volkova, O. S.; Vasiliev, A. N.; Karapetrov, G.; Snyder, J. Tuning the Activity/Stability Balance of Anion Doped CoS_xSe_{2-X} Dichalcogenides. *J. Catal.* **2018,** *366*, 50-60.
17. Zhang, M.; Hu, A.; Liu, Z.; Xu, Y.; Fan, B.; Tang, Q.; Zhang, S.; Deng, W.; Chen, X. Synergistic Effect of Three-Dimensional Cobalt Diselenide/Carbon Nanotube Arrays Composites for Enhanced Hydrogen Evolution Reaction. *Electrochim. Acta* **2018,** *285*, 254-261.
18. Jiang, N.; Tang, Q.; Sheng, M.; You, B.; Jiang, D.-e.; Sun, Y. Nickel Sulfides for Electrocatalytic Hydrogen Evolution under Alkaline Conditions: A Case Study of Crystalline NiS, NiS_2, and Ni_3S_2 Nanoparticles. *Catal. Sci. Technol.* **2016,** *6*, 1077-1084.
19. Feng, L. L.; Yu, G.; Wu, Y.; Li, G. D.; Li, H.; Sun, Y.; Asefa, T.; Chen, W.; Zou, X. High-Index Faceted Ni_3S_2 Nanosheet Arrays as Highly Active and Ultrastable Electrocatalysts for Water Splitting. *J. Am. Chem. Soc.* **2015,** *137*, 14023-6.
20. Liu, P. F.; Zhang, L.; Zheng, L. R.; Yang, H. G. Surface Engineering of Nickel Selenide for an Enhanced Intrinsic Overall Water Splitting Ability. *Mater. Chem. Front.* **2018,** *2*, 1725-1731.
21. Liu, Y.; Yu, G.; Li, G. D.; Sun, Y.; Asefa, T.; Chen, W.; Zou, X. Coupling Mo_2C with Nitrogen-Rich Nanocarbon Leads to Efficient Hydrogen-Evolution Electrocatalytic Sites. *Angew. Chem., Int. Ed. Engl.* **2015,** *54*, 10752-7.
22. Chen, W.-F.; Muckerman, J. T.; Fujita, E. Recent Developments in Transition Metal Carbides and Nitrides as Hydrogen Evolution Electrocatalysts. *Chem. Commun.* **2013,** *49*, 8896-8909.
23. Scanlon, M. D.; Bian, X.; Vrubel, H.; Amstutz, V.; Schenk, K.; Hu, X.; Liu, B.; Girault, H. H. Low-Cost Industrially Available Molybdenum Boride and Carbide as "Platinum-Like" Catalysts for the Hydrogen Evolution Reaction in Biphasic Liquid Systems. *Phys. Chem. Chem. Phys.* **2013,** *15*, 2847-57.
24. Cao, B.; Veith, G. M.; Neuefeind, J. C.; Adzic, R. R.; Khalifah, P. G. Mixed Close-Packed Cobalt Molybdenum Nitrides as Non-Noble Metal Electrocatalysts for the Hydrogen Evolution Reaction. *J. Am. Chem. Soc.* **2013,** *135*, 19186-92.
25. Lai, C.; Liu, X.; Deng, Y.; Yang, H.; Jiang, H.; Xiao, Z.; Liang, T. Rice-Shape Nanocrystalline Ni_5P_4: A Promising Bifunctional Electrocatalyst for Hydrogen Evolution Reaction and Oxygen Evolution Reaction. *Inorg. Chem. Commun.* **2018,** *97*, 98-102.
26. Xiao, X.; Tao, L.; Li, M.; Lv, X.; Huang, D.; Jiang, X.; Pan, H.; Wang, M.; Shen, Y. Electronic Modulation of Transition Metal Phosphide Via Doping as Efficient and pH-Universal Electrocatalysts for Hydrogen Evolution Reaction. *Chem. Sci.* **2018,** *9*, 1970-1975.
27. Wang, F.; Yang, X.; Dong, B.; Yu, X.; Xue, H.; Feng, L. A FeP Powder Electrocatalyst for the Hydrogen Evolution Reaction. *Electrochem. Commun.* **2018,** *92*, 33-38.
28. Wang, T.; Du, K.; Liu, W.; Zhu, Z.; Shao, Y.; Li, M. Enhanced Electrocatalytic Activity of MoP Microparticles for Hydrogen Evolution by Grinding and Electrochemical Activation. *J. Mater. Chem. A* **2015,** *3*, 4368-4373.
29. McEnaney, J. M.; Chance Crompton, J.; Callejas, J. F.; Popczun, E. J.; Read, C. G.; Lewis, N. S.; Schaak, R. E. Electrocatalytic Hydrogen Evolution Using Amorphous Tungsten Phosphide Nanoparticles. *Chem. Commun.* **2014,** *50*, 11026-11028.
30. Zeng, Z.; Tan, C.; Huang, X.; Bao, S.; Zhang, H., Growth of Noble Metal Nanoparticles on Single-Layer TiS_2 and TaS_2 nanosheets for Hydrogen Evolution Reaction. *Energy Environ. Sci.* **2014,** *7*, 797-803.
31. Xu, J.; Liu, T.; Li, J.; Li, B.; Yuefeng Liu; Xiong, D.; Amorim, I.; Li, W.; Zhang, B.; Liu, L., Boosting the Hydrogen Evolution Performance of Ruthenium Clusters through Synergistic Coupling with Cobalt Phosphide. *Energy Environ. Sci.* **2018,** *11*, 1819-1827.
32. Pan, Y.; Chen, Y.; Lin, Y.; Cui, P.; Sun, K.; Liu, Y.; Liu, C., Cobalt Nickel Phosphide Nanoparticles Decorated Carbon Nanotubes as Advanced Hybrid Catalysts for Hydrogen Evolution. *J. Mater. Chem. A* **2016,**

4, 14675-14686.
33. Mazanek, V.; Luxa, J.; Matejkova, S.; Kucera, J.; Sedmidubsky, D.; Pumera, M.; Sofer, Z., Ultrapure Graphene Is a Poor Electrocatalyst: Definitive Proof of the Key Role of Metallic Impurities in Graphene Based Electrocatalysis. *ACS Nano* **2019**.
34. Su, J.; Yang, Y.; Xia, G.; Chen, J.; Jiang, P.; Chen, Q. Ruthenium-Cobalt Nanoalloys Encapsulated in Nitrogen-Doped Graphene as Active Electrocatalysts for Producing Hydrogen in Alkaline Media. *Nat. Commun.* **2017,** *8*, 14969.
35. Kim, J.; Byun, S.; Smith, A. J.; Yu, J.; Huang, J., Enhanced Electrocatalytic Properties of Transition-Metal Dichalcogenides Sheets by Spontaneous Gold Nanoparticle Decoration. *J Phys Chem Lett* **2013,** *4*, 1227-32.
36. Liu, Y.; Liu, S.; Wang, Y.; Zhang, Q.; Gu, L.; Zhao, S.; Xu, D.; Li, Y.; Bao, J.; Dai, Z. Ru Modulation Effects in the Synthesis of Unique Rod-Like Ni@Ni_2P-Ru Heterostructures and Their Remarkable Electrocatalytic Hydrogen Evolution Performance. *J. Am. Chem. Soc.* **2018,** *140*, 2731-2734.
37. Cherevko, S.; Geiger, S.; Kasian, O.; Kulyk, N.; Grote, J.-P.; Savan, A.; Shrestha, B. R.; Merzlikin, S.; Breitbach, B.; Ludwig, A.; Mayrhofer, K. J. J., Oxygen and Hydrogen Evolution Reactions on Ru, RuO_2 , Ir, and IrO_2 Thin Film Electrodes in Acidic and Alkaline Electrolytes: A Comparative Study on Activity and Stability. *Catalysis Today* **2016,** *262*, 170-180.
38. Li, H.; Qian, X.; Zhu, C.; Jiang, X.; Shao, L.; Hou, L. Template Synthesis of $CoSe_2$/Co_3Se_4 Nanotubes: Tuning of Their Crystal Structures for Photovoltaics and Hydrogen Evolution in Alkaline Medium. *J. Mater. Chem. A* **2017,** *5*, 4513-4526.
39. Ge, P.; Zhang, C.; Hou, H.; Wu, B.; Zhou, L.; Li, S.; Wu, T.; Hu, J.; Mai, L.; Ji, X. Anions Induced Evolution of Co_3X_4 (X = O, S, Se) as Sodium-Ion Anodes: The Influences of Electronic Structure, Morphology, Electrochemical Property. *Nano Energy* **2018,** *48*, 617-629.
40. Can, H.; Metin, Ö. A Facile Synthesis of Nearly Monodisperse Ruthenium Nanoparticles and Their Catalysis in the Hydrolytic Dehydrogenation of Ammonia Borane for Chemical Hydrogen Storage. *Appl. Catal., B* **2012,** *125*, 304-310.
41. Wu, X.; Han, S.; He, D.; Yu, C.; Lei, C.; Liu, W.; Zheng, G.; Zhang, X.; Lei, L. Metal Organic Framework Derived Fe-Doped $CoSe_2$ Incorporated in Nitrogen-Doped Carbon Hybrid for Efficient Hydrogen Evolution. *ACS Sustainable Chem. Eng.* **2018,** *6*, 8672-8678.
42. Wu, Z.; Fang, B.; Wang, Z.; Wang, C.; Liu, Z.; Liu, F.; Wang, W.; Alfantazi, A.; Wang, D.; Wilkinson, D. P. MoS_2 Nanosheets: A Designed Structure with High Active Site Density for the Hydrogen Evolution Reaction. *ACS Catal.* **2013,** *3*, 2101-2107.
43. Mahmood, J.; Li, F.; Jung, S. M.; Okyay, M. S.; Ahmad, I.; Kim, S. J.; Park, N.; Jeong, H. Y.; Baek, J. B. An Efficient and pH-Universal Ruthenium-Based Catalyst for the Hydrogen Evolution Reaction. *Nat. Nanotechnol.* **2017,** *12*, 441-446.
44. Zhang, Z.; Li, P.; Feng, Q.; Wei, B.; Deng, C.; Fan, J.; Li, H.; Wang, H. Scalable Synthesis of Ruthenium-Based Electrocatalyst as a Promising Alternative to Pt for Hydrogen Evolution Reaction. *ACS Appl. Mater. Interfaces* **2018,** *10*, 32171-32179.
45. Krivovichev, V. G.; Charykova, M. V.; Vishnevsky, A. V. The Thermodynamics of Selenium Minerals in Near-Surface Environments. *Minerals* **2017,** *17*, 188.
46. Liu, B.; Zhao, Y. F.; Peng, H. Q.; Zhang, Z. Y.; Sit, C. K.; Yuen, M. F.; Zhang, T. R.; Lee, C. S.; Zhang, W. J. Nickel-Cobalt Diselenide 3D Mesoporous Nanosheet Networks Supported on Ni Foam: An All-pH Highly Efficient Integrated Electrocatalyst for Hydrogen Evolution. *Adv. Mater.* **2017,** *29*.
47. Shinde, D. V.; Dang, Z.; Petralanda, U.; Palei, M.; Wang, M.; Prato, M.; Cavalli, A.; De Trizio, L.; Manna, L. In Situ Dynamic Nanostructuring of the Cu-Ti Catalyst-Support System Promotes Hydrogen Evolution under Alkaline Conditions. *ACS Appl. Mater. Interfaces* **2018,** *10*, 29583-29592.
48. Subbaraman, R.; Tripkovic, D.; Strmcnik, D.; Chang, K.-C.; Uchimura, M.; Paulikas, A. P.; Stamenkovic, V.; Markovic, N. M. Enhancing Hydrogen Evolution Activity in Water Splitting by Tailoring Li^+-$Ni(OH)_2$-Pt Interfaces. *Science* **2011,** *334*, 1256-1260.
49. Henckel, D. A.; Lenz, O.; Cossairt, B. M. Effect of Ligand Coverage on Hydrogen Evolution Catalyzed

by Colloidal WSe_2. *ACS Catal.* **2017,** *7*, 2815-2820.
50. Wang, M.; Dang, Z.; Prato, M.; Shinde, D. V.; De Trizio, L.; Manna, L. Ni-Co-S-Se Alloy Nanocrystals: Influence of Their Composition on Their in Situ Transformation and Electrocatalytic Activity for the Oxygen Evolution Reaction. *ACS Appl. Nano Mater.* **2018**, *1*, 5753-5762.
51. Zhu, Y. P.; Xu, X.; Su, H.; Liu, Y. P.; Chen, T.; Yuan, Z. Y. Ultrafine Metal Phosphide Nanocrystals in Situ Decorated on Highly Porous Heteroatom-Doped Carbons for Active Electrocatalytic Hydrogen Evolution. *ACS Appl. Mater. Interfaces* **2015,** *7*, 28369-76.
52. Shi, Y.; Zhang, B. Recent Advances in Transition Metal Phosphide Nanomaterials: Synthesis and Applications in Hydrogen Evolution Reaction. *Chem. Soc. Rev.* **2016,** *45*, 1529-41.
53. Zhang, F.; Pei, Y.; Ge, Y.; Chu, H.; Craig, S.; Dong, P.; Cao, J.; Ajayan, P. M.; Ye, M.; Shen, J. Controlled Synthesis of Eutectic NiSe/Ni_3Se_2 Self-Supported on Ni Foam: An Excellent Bifunctional Electrocatalyst for Overall Water Splitting. *Adv. Mater. Interfaces* **2018,** *5*, 1701507.
54. Zhang, X.; Zhen, M.; Bai, J.; Jin, S.; Liu, L. Efficient NiSe-Ni_3Se_2/Graphene Electrocatalyst in Dye-Sensitized Solar Cells: The Role of Hollow Hybrid Nanostructure. *ACS Appl. Mater. Interfaces* **2016,** *8*, 17187-93.

Chapter VI Summary and Perspective

This PhD project mainly focuses on designing and synthesizing novel electrocatalysts by economic transition metal chalcogenides to replace rare metal materials. The achievements and innovation points of the project are listed as follows:

Firstly, we created a facile colloidal synthesis route to produce nanocrystals of ternary Ni-Co-Se and quaternary Ni-Co-S-Se transition metal chalcogenides. By tuning the experimental parameters such as the type and ratio of precursors and solvents, the reaction time and temperature we could control the structure, composition and size of the resulting nanocrystals.

Secondly, we synthesized a ternary $Ni_{1-x}Co_xSe$ NCs with control over the composition and we tested their performance in the OER. In the alkaline electrolyte (1 M KOH), we found that the OER activity has a close relationship with the Ni/Co ratio. The sample with the smallest onset potential (277 mV) was the one having (or being characterized with) a Ni/Co ratio of 1/2.5. By analyzing the material after OER, we found that the chalcogenide NCs were changed to mostly amorphous oxides, which function as the real catalyst.

Thirdly, we alloyed also the cations and synthesized quaternary Ni-Co-S-Se NCs with different S/Se and Ni/Co ratios. It is found that S/Se ratio can only arrange from 0 to 2/3 if the crystal structures maintain the hexagonal structure because of the discrepancy in size between S and Se. Moreover, $Ni_{0.25}Co_{0.65}S_{0.4}Se_{0.6}$ NCs are the best electrocatalysts among all the prepared chalcogenides. During the OER, the chalcogens are lost and the $Ni_{0.25}Co_{0.65}S_{0.4}Se_{0.6}$ NCs are totally oxidized. The good performance probably results from the final small NiO/CoO NCs and ultrathin $Co(OH)_2$ nanosheets formed from the defect-rich NCs. Besides, the group of the quaternary NCs with different Ni/Co ratios has the same trend with their ternary counterparts but better performance. This proves again the affinity between Ni/Co ratio and the OER activity.

At last, we applied doping strategy on the binary chalcogenides. The doping of CoSe and NiSe NCs with a small amount of Ru (4% in CoSe and 0.64% in NiSe) can improve the charge transfer efficiency of the NCs and, thus, their HER performance. The mechanism is investigated in Ru-CoSe NCs. The oxidation of the surface, the composition transformation from CoSe to $CoSe_2$ and the formation of Ru nanoparticles during HER are found beneficial for boosting the electrocatalytic activity. Besides, annealing is found to be another crucial factor to remove the ligands and improve the performance.

Besides, a suitable surfactant is necessary to control the shape of the NCs, and this is a problem to be solved in the future in the methodology of the synthesis.

By using different strategies to improve the electrocatalytic properties of transition metal

chalcogenides, the above achievements are obtained after a lot of trials and errors. During this research on the mechanism of electrocatalysis, we found that all these different strategies are helpful to improve the properties of the electrocatalysts thus optimize the electrocatalytic activity. All of these efforts are significant for designing efficient inexpensive electrocatalysts for HER and OER and carrying forward their applications in the industry field.

Acknowledgements

Time flies as fast as light and it is already close to the end of my PhD life. To review these three more years, I can see frustration when experiments are not successful, confusion when the direction is not clear, difficulties during the exploration, and finally confidence when the project is finished. All these negative and positive moments construct my precious experience during this period, and this unforgettable experience will stimulate the rest of my life no matter where I will go or which kind of career I will choose in the future.

To leave China and pursue my PhD career far away in this beautiful and mysterious country would not be an easy choice for me without the help of all my supervisors, friends, colleagues and families. Therefore, I would like to express my most sincere thanks to them.

Firstly I would like to thank Prof. Liberato Manna, who gives me this chance to open my horizon both on work and life and provides a perfect environment which enables me to focus on my scientific work with all my attention and finish the work in the best way I can do. I am extremely thankful to Dr. Luca De Trizio who gives me a lot of supervision in my scientific work and a lot of help to adjust to the life in Italy. With him I improved a lot in my thought and organization of my project, which makes me feel closer to the wonderful science. Also I had a comprehensive idea about Italian culture with his passionate introduction, which is also my valuable experience except the work. Then I would like to thank Dr. Dipak V. Shinde with my honest respect. He taught me full of patience from zero the knowledge of electrocatalysis and without him would not be able to finalize my project.

Meanwhile I would like to offer my gratitude to my dearest friends Lea, Cansunur and Tathiana. With them I want to share all the joyful moment of my life. They are always by my side during my bad times, giving me a lot of warm courage and making me feel that I am not alone. With them I become more confident to face my difficulties and be myself. Besides, I am also graceful that I make a lot of Chinese friends like Yao, Lin, Haiyan, Chunzheng, Renyong, Mengying, Zhiya, Xue, Tao, Shi, Qinqi, Zhuoqi, Yingqi, Jian'an, Boyang, Xiangping, Tianwen, Anda, Yiming, Yue and so on. They offered me a lot of help during my PhD and make me feel at home.

Also I would like to thank all my lovely and clever colleagues in this institute. They provide me a lot of help in all the aspects and my project goes more smoothly with these help. I had a wonderful time working together with them and I really enjoyed working with them in this friendly and efficient atmosphere.

Last but not least, I would like to express my gratitude to my parents, who always support me without hesitation and teach me to be strong in front of difficulties. My respect and gratitude are also for my grandparents, who gave me a cheerful childhood and taught me to be a kind person. All these teachings are the "key factors" of who I am and guide me to make my choice and insist on the choice of my life. Also I would like to thank my brother who is always kind and positive and influences me in a good way.

List of Publications

I. **Wang, M.;** Dang, Z.; Prato, M.; Shinde, D. V.; De Trizio, L.; Manna, L. Ni–Co–S–Se Alloy Nanocrystals: Influence of the Composition on Their in Situ Transformation and Electrocatalytic Activity for the Oxygen Evolution Reaction. *ACS Appl. Nano Mater.* **2018,** *1*, 5753-5762.

II. Shinde, D. V.; Dang, Z.; Petralanda, U.; Palei, M.; **Wang, M.;** Prato, M.; Cavalli, A.; De Trizio, L.; Manna, L. In Situ Dynamic Nanostructuring of the Cu-Ti Catalyst-Support System Promotes Hydrogen Evolution under Alkaline Conditions. *ACS Appl. Mater. Interfaces* **2018,** *10*, 29583-29592.

III. Imran, M.; Caligiuri, V.; **Wang, M.;** Goldoni, L.; Prato, M.; Krahne, R.; De Trizio, L.; Manna, L. Benzoyl Halides as Alternative Precursors for the Colloidal Synthesis of Lead-Based Halide Perovskite Nanocrystals. *J. Am. Chem. Soc.* **2018,** *140*, 2656-2664.

IV. **Wang, M.;** Dang, Z.; Prato, M.; Shinde, D. V.; De Trizio, L.; Manna, L. Colloidal Ru-Decorated Cobalt Selenide Nanocrystals with Enhanced Hydrogen Evolution Reaction. **2019** (under preparation).